Development of magnetic resonance imaging techniques for mouse models of Alzheimer's Disease

James Martin O'Callaghan

Ph.D. Thesis

Submitted for the degree of Doctor of Philosophy,

University College London,

October 2015

Declaration

I, James Martin O'Callaghan confirm that the work presented in this thesis is my own. Where information has been derived from other sources, I confirm that this has been indicated in the thesis. This work is based on research that I carried out at the Centre for Advanced Biomedical Imaging, University College London, UK, between September 2011 and September 2015.

James O'Callaghan

Publications arising from this thesis

Is Your System Calibrated? MRI Gradient System Calibration for Pre-Clinical, High-Resolution Imaging.

PLoS ONE 2014; 9(5):e96568.

J O'Callaghan, *J Wells, S Richardson, H Holmes, Y Yu, S Walker-Samuel, B Siow, MF Lythgoe.*

In-Vivo Imaging of Tau pathology using Multi-Parametric Quantitative MRI

NeuroImage, 2015, 111(0): 369-378

J Wells, **J O'Callaghan*** , H Holmes, N Powell, R Johnston , B Siow, F Torrealdea , O Ismail, S Walker-Samuel, X Golay, M Rega , S Richardson, M Modat, M Cardoso, S Ourselin, A Schwarz, Z Ahmed, T Murray, M O'Neill, E Collins, N Colgan, M F Lythgoe*
*Joint first authors

Acknowledgements

work would never have come to pass. Her love, inspiration, support, and self sacrifice have made it possible to get to this point and I therefore dedicate this thesis to her, Tiffany O'Callaghan, the love of my life.

Abstract

Due to increasing life expectancy in western societies, a rise in the prevalence of Alzheimer's Disease (AD) is expected to have adverse social and economic consequences. The success of emerging treatments for AD relies heavily on the ability to test their efficacy. Sensitive biomarkers are required that provide information specific to the therapeutic targets. Through manipulation of the genome, transgenic mice have been bred to exhibit particular pathological features of AD in isolation. Magnetic Resonance Imaging (MRI) of these mouse models can be used to observe phenotypic abnormalities *in-vivo* in a controlled environment. As summarised in the introductory chapter, the aim of this work was to develop MRI techniques for inclusion in multi-parametric protocols to characterise AD models *in-vivo*.

Structural MRI has become an increasingly popular tool in the measurement of atrophy of brain tissue over time and requires both accuracy and stability of the imaging system. In chapter 3, a protocol for the calibration of system gradients for high resolution, pre-clinical MRI is described. A structural phantom has been designed and 3D printed for use in a 9.4T small bore MRI and micro CT system. Post processing software is used to monitor gradient stability and provide corrections for scaling errors and non-linearity.

Diffusion Tensor Imaging (DTI) and Quantitative Susceptibility Mapping (QSM) are MRI techniques that have shown sensitivity to changes in white matter regions of the brain. QSM may also provide a non invasive method for measurement of increased iron concentration in grey matter tissue observed in AD. Chapters 4 and 5 evaluate the utility of these measurements as imaging biomarkers in a mouse model that exhibits tau pathology associated with AD. Discrepancies between transgenic and wild-type groups were identified for both MRI techniques indicating the potential benefit of their inclusion in a multi-parametric *in-vivo* protocol.

Contents

Figures

11

Tables

Abbreviations

AD	Alzheimer's Disease
ADC	Analogue to Digital Converter / Apparent Diffusion Coefficient
APOE	Apolipoprotein E
APP	Amyloid Precursor Protein
ASL	Arterial Spin Labelling
Aβ	Amyloid-beta
BOLD	Blood Oxygen Level Dependent
CABI	Centre for Advanced Biomedical Imaging
CAD	Computer Aided Design
CMB	Cerebral Microbleeds
CNR	Contrast to Noise Ratio
CSF	Cerebrospinal Fluid
CT	Computed Tomography
DA	Axial Diffusivity
DFT	Discrete Fourier Transform
DNA	Deoxyribonucleic Acid
DR	Radial Diffusivity
DSV	Diameter of Spherical imaging Volume
DTI	Diffusion Tensor Imaging
DW	Diffusion Weighted
EM	Electron Microscopy
EPI	Echo Planar Imaging
ES	Echo Spacing
FA	Fractional Anisotropy
FDG	Fluorodeoxyglucose
FDR	False Discovery Rate
FID	Free Induction Decay
fMRI	functional MRI
FOV	Field Of View
FT	Fourier Transform
GE	Gradient Echo
GRE	Gradient Recalled Echo
hAPP	human APP
htau	human tau
MAPT	Microtubule Associated Protein Tau
MCI	Mild Cognitive Impairment
MD	Mean Diffusivity
MMSE	Mini Mental State Examination
MR	Magnetic Resonance
MRI	Magnetic Resonance Imaging
MRS	Magnetic Resonance Spectroscopy
MTF	Modulation Transfer Function

NAA	N-acetylaspartate
NFT	Neurofibrillary Tangle
NMR	Nuclear Magnetic Resonance
NRR	Non Rigid Registration
NSA	Number of Signal Averages
PDF	Projection onto Dipole Fields
PE	Phase Encode
PET	Positron Emission Tomography
Pib	Pittsburgh compound B
ppb	parts per billion
ppm	parts per million
PSAPP	Presenilin 1/ APP
PSEN1	Presenilin 1
PSEN2	Presenilin 2
PSF	Point Spread Function
QA	Quality Assurance
QSM	Quantitative Susceptibility Mapping
RF	Radio Frequency
RO	Readout
ROI	Region Of Interest
ROS	Reactive Oxygen Species
SD	Standard Deviation
SE	Spin Echo
SGRE	Spoiled Gradient Recalled Echo
SHARP	Sophisticated Harmonic Artifact Reduction for Phase data
SNR	Signal to Noise Ratio
SPECT	Single Photon Emission Computed Tomography
SPM	Statistical Parametric Mapping
SS	Slice Select
SWI	Susceptibility Weighted Imaging
TBM	Tensor Based Morphometry
TBV	Total Brain Volume
TE	Time to Echo
TKD	Thresholded K-space Division
TR	Time to Repeat
TR	Transgenic
WMD	White Matter Disease
WT	Wild-Type

1 Alzheimer's Disease

1.1 A brief history

In 1901 Alois Alzheimer(Figure 1a) admitted a patient suffering memory loss, confusion and other symptoms of a neurological disorder to Frankfurt Hospital(1,2). When Auguste D. died four years later, Alzheimer conducted a post mortem investigation of her brain. As well as finding plaques that had been described previously(3), Alzheimer became the first to discover tangle pathology using silver stains(Figure 1b). In 1906 he presented his findings at the 37th meeting of the Society of Southwest German Psychiatrists, defining the characteristic clinical and neuropathological features of a disease that would come to bear his name. It was not until 1979 that the first Alzheimer's Disease (AD) association was formed in the USA to attract funding for the necessary pursuit of an understanding of the biology of the disease. In the intervening years, a clinicopathological distinction was developed between senile dementia patients (onset > 65 years of age), many of whom exhibited AD pathology, and pre-senile dementias (onset < 65 years of age), which include conditions such as Picks disease and Creuzfeldt-Jakob disease. The discovery of familial forms of the disease by Schottky in 1932(4) seeded a genetic avenue of scientific research in AD. This work has fused with studies of the molecular composition of proteinaceous aggregates in the brain over the last three decades to provide some insight into the etiology of the disease.
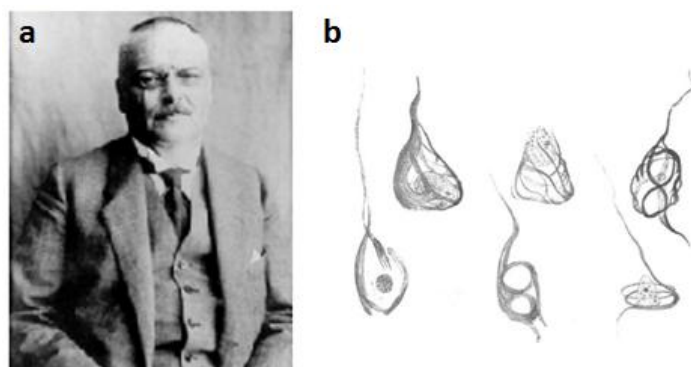
Figure 1.   **Alzheimer's disease historical images**

Photograph of Alois Alzheimer(a), and his sketch of stained tangle pathology(b) from his 1911 publication(5,6).

Neuritic plaques that accompany the tangle pathology discovered by Alzheimer had been reported previously in 1898 by Redlich(2). Preliminary electron microscopy (EM) investigations of post mortem tissue in the 1960s(7,8) revealed abnormal plaque filaments located in the extracellular space, whilst tangles appeared in helical filaments within cell bodies and in neurites as well as at the periphery of plaques(1). It was another 20 years before the identification of Amyloid-Beta(Aβ), formed from the cleavage of Amyloid Precursor Protein (APP), as a major component of plaques though biochemical analysis(2,9). The primary function of APP remains unclear but it is thought to have an impact on neuronal development and function through its involvement in a range of biological activities(10). The role of tau protein, detected within tangle pathology, is to act as a microtubule binding and stabilising agent. Hyperphosphorylation processes are thought to be responsible of the manifestation of tau in its tangled filamentous form in AD, sometimes described as neurofibrillary tangles (NFTs) (2).

NFTs in dementia cases are not homogeneously spread throughout the brain but display a characteristic pattern(11). A progressive spread of tau pathology was identified in 1991 that has become known as 'Braak Staging'(11). Six stages were defined corresponding to the level of infiltration across distinct brain regions. In the mildest cases, NFTs are restricted to the transentorhinal region (stages 1 and 2). In the limbic stages (3 and 4), pathology builds up and also spreads to the hippocampus. The low density of tau tangles present in the isocortex during the limbic stages increases in the final stages with a heavy burden throughout the aforementioned regions of the brain. Comparisons with cognitive tests have indicated that the transentorhinal stages are clinically silent(12). Mild stages of AD memory impairment are associated with NFT spread to the limbic regions, with severe memory loss occurring in the final Braak stages. Furthermore, studies of neuronal cell death and tissue atrophy also follow Braak staging patterns(13-16). In contrast, the regional distribution of plaques remains fairly consistent as accumulation occurs over time and post mortem analyses show variability in the density of plaques between patients that exhibit mild clinical symptoms of AD. Therefore, although amyloid pathology appears to occur early in disease, its utility as a method by which to stage the time course of AD with close affinity to clinical symptoms is limited.

The vast majority of AD cases are of the sporadic form with autosomal dominant(familial) cases accounting for less than 1%(1). This subset of cases often present with symptoms

before the age of 65, known as early onset, and is a more rapidly progressing form of the disease. The first links between genetics and pathology were made between plaque deposition and mutations and duplications of the APP gene(2). Discoveries of mutations in Presenilin 1 (PSEN1) and Presenilin 2 (PSEN2) genes on chromosome 14 in familial AD followed. The proteins encoded by these genes are involved in the processing of APP and Aβ(17) with PSEN1 mutations being the most common cause of autosomal dominant AD. The over expression of Aβ generated in these cases is described as a disease trigger in what is known as 'amyloid cascade' hypothesis(1). This suggests that the appearance of tangles, neurodegeneration, and dementia are downstream events of the disease. Mutations of the Microtubule Associated Protein Tau(MAPT) gene are not implicated in AD but have been associated with fronto-temporal dementia linked to chromosome 17(1). The APOEε4 allele on chromosome 19 has been identified as a genetic risk factor for late onset AD and is associated with mild cognitive impairment(MCI)(17). MCI is a clinical term used to describe patients at an intermediate stage between normal cognition and dementia. Functional independence is retained in MCI sufferers but the likelihood of developing AD, relative to non-sufferers at a similar age, is increased(18). Studies have associated APOEε4 with both MCI and its progression to AD(17).

Alzheimer's Disease is now the most common type of dementia contributing 60-70% of the 36 million cases worldwide(19). Lifestyle choices such as diet, exercise and intellectual stimulation, are thought to offer protective benefits to developing AD. However, the inescapable process of aging is by far the greatest risk factor, with incidence of AD doubling every five years after the age of 60(18). The toll that decline into AD takes on both sufferers and their carers is immense with loss of memory and cognitive abilities affecting every facet of daily life. The increasing life expectancy of the population suggests the prevalence of AD will increase to 115 million by 2050(20). A recent study has suggested that these projections may be an overestimation since they do not take into account other changing factors such as improvements to living conditions, education, and general health of the population(21). Nevertheless, there is already an urgent need to develop therapeutic treatments to alleviate the burgeoning social and economic burden of AD.

The connection made between the genetic mutations in familial forms and Aβ in plaque pathology provide an obvious target for pharmaceutical development. Strategies implemented in mouse models of familial AD have attempted to block Aβ production by

immunisation or by modulating the cleavage process in APP processing using secretase inhibitors. The complete inhibition of these proteases may have potential harmful side effects due to the multiple functions they serve and in the case of the γ secretase, this is toxic(2,22). Partial suppression of secretase activity has been shown to reduce Aβ levels in the brain and cognitive decline in animals and in the case of β secretase, some inhibitors are currently at an advanced stage in clinical trials(23). Aβ immunotherapies have been shown to reduce plaque load in the brain in clinical studies of AD but the cognitive benefits are less certain(24). These treatments are also associated with a number of amyloid-related side effects including increased severity of cerebral amyloid angiopathy, thought to be exacerbated by the removal of plaques(24).

Besides amyloid, other aspects of the AD pathogenesis have been targeted using anti inflammatory drugs, metal chelators, antioxidants, tau phosphorylation inhibitors, and compounds to lower cholesterol(2). The recent use of tau immunotherapies in mouse models has demonstrated efficacy in reducing tangle pathology and cognitive decline and may offer another promising target for AD pharmaceutical development(25,26). The translation of promising preclinical results to viable therapies has been impeded in some cases by findings of adverse side effects. It is also suspected that improvement in the design of clinical trials is necessary to better detect the positive effects of drugs, especially with regards to the stage of disease progression at which the treatments are administered(27). To this end, researchers in the field see the development of *in-vivo* biomarkers sensitive to disease pathology essential to guiding and facilitating drug development(27).

1.2 Biomarkers

The Mini Mental State Examination(MMSE), is a clinical tool widely used to screen for dementia and is thought to successfully discriminate sufferers from healthy patient groups(28). However, it lacks specificity to AD and is insensitive to MCI (29). These tests may result in a diagnosis of 'probable AD', with post-mortem analysis necessary to confirm dementia type. In 2007, the International Working Group for New Research Criteria for the Diagnosis of AD proposed a frame work that combined episodic memory tests and the use of biomarkers for the *in-vivo* diagnosis of AD as differentiated from other dementias(30). The use of biomarkers to take biochemical, pathological or anatomical measurements may

improve early detection and allow staging of disease providing longitudinal measurements by which therapeutic effects can be evaluated. Techniques developed offer sensitivity to different factors in the multifaceted pathogenesis of AD and can be broadly divided in to biofluid sampling and medical imaging categories.

The measurement of protein concentrations in sampled Cerebrospinal Fluid (CSF) is the most developed biofluid analyte technique(18). Depressed levels of Aβ have been detected in MCI and AD patients, although the relationship with plaque deposition is unclear(17). Conversely, CSF concentrations of total tau and phosphorylated tau are elevated in AD and have been shown to rise with disease severity(18,31). Variability between studies indicate there may be other factors influencing levels of tau in CSF(32) and the specificity to AD is lacking, with similar increases observed in other tauopathies(33,34). The cycle of Aβ production by platelets and deposition in the brain maintains a constant level of Aβ in the blood in healthy individuals(17). Detection of disruptions to this status quo in disease has been attempted by analysing plasma samples. While blood Aβ levels increase in familial AD have been reported, findings in studies of sporadic forms are inconclusive(17).

Imaging biomarkers offer a method by which to probe tissue vitality and pathology and unlike biofluid markers provide spatial localisation of abnormalities. The measurement of atrophy using MRI and plaque burden using amyloid positron emission tomography (PET) are two of the most frequently used techniques for the clinical study of AD(18). The resolution and soft tissue contrast generated using MRI can be used to measure subtle volumetric changes in brain structures. Atrophy occurs in normal aging and is accelerated in a number of conditions. In AD, volume decreases in brain structures measured using MRI appear closely linked to both severity and rate of impairment in cognitive function(35,36). Hippocampal reductions and brain-wide distribution of volume changes have been shown to correlate with the Braak stages of NFT pathology in AD(37).

Plaque burden may be measured using amyloid PET which uses Pittsburgh Compound B as a tracer (sometimes called PiB PET). It binds to plaques and the increased signal observed in AD has been shown to correspond with Aβ burden at post mortem and is inversely correlated with CSF Aβ(17). A recent hypothetical model suggests the sensitivity of these techniques is such that cases may be detected prior to the appearance of clinical symptoms(38). However, some studies have identified pathology indicative of AD at autopsy in almost one third of healthy subjects which is similar to the proportion of

abnormal scans in cognitively normal individuals reported in amyloid PET studies(18). Therefore, although sensitive to *in-vivo* levels of Aβ, amyloid PET may not be the most accurate predictor of the development of clinical symptoms. More recently, fluorine based tracers that bind to amyloid have been developed that can successfully differentiate AD cases from healthy controls. These compounds may prove more popular than PiB due to their greater availability(18). Additional AD PET targets include reduced cerebral glucose metabolism detected by FDG-PET, and microglial activation detected using molecular imaging probes. SPECT probes have been developed primarily to target dopamine transporters or receptors and may find application in the development of neuroprotective treatments in AD by providing a measure of neuronal population (17).

When envisaging the future of routine clinical care in AD, and the role that imaging might play, the completely non-invasive nature of MRI is a favourable attribute. This confers a considerable comfort benefit to patients receiving regular monitoring of their condition and may be especially important in AD where subjects are likely to be elderly. MRI includes the spatial information lacking in biofluid analytes and offers increased spatial resolution compared to nuclear imaging methods. Besides structural methods, MRI measurements of diffusion, perfusion and spectroscopy are emerging as techniques that may provide sensitivity to the deleterious effects of the condition. The disruption to the highly ordered microstructure of white matter tracts is thought to occur early in AD and in MCI, which causes measureable alterations in Diffusion Tensor Imaging (DTI) indices(39). Arterial Spin Labelling(ASL) is an MRI method used to measure blood perfusion in the brain and has shown deficits in AD that correspond to impaired cerebral metabolism in FDG-PET scans(18). It can both differentiate between MCI and AD cases as well as predict transition from the MCI to AD(17,40). Magnetic Resonance Spectroscopy(MRS) of hydrogen can be used to detect cellular metabolite levels. AD patients exhibit reduced N-acetylaspartate(NAA), thought to reflect decreases in neuronal population, in early neurodegeneration. Neuronal activity can be probed, albeit indirectly, using fMRI and studies have been carried out for both task based and resting state paradigms. There is a decreased BOLD signal in the hippocampus of AD patients during cognitive tasks(41) and in the resting state, disruptions to the default mode network can be detected that differentiate normal cases from AD and MCI(40). The endogenous nature of MRI contrast means that an assortment of measures of tissue composition, integrity and function may be gathered in a single, non-invasive, imaging session. A number of studies have used

Multi-parametric MRI protocols to acquire data in MCI and AD patient cohorts(39,42-46). Many of these studies have collected structural MRI and DTI and report that an increased diagnostic accuracy is achieved through a combination of parameters(42,43,46).

The biomarkers described in this section are not in current clinical use due to a lack of standardisation and questionable effects on disease outcomes given the absence of an effective treatment. The use of animal models of AD can be used to expedite the optimisation of imaging markers for clinical use. Pathology develops in a much shorter timeframe than in humans, typically over a few months, enabling a high throughput of biomarker testing. Genetic mutations in transgenic mice can produce different 'AD like' pathophysiological features in isolation. Therefore, biomarkers can be tested in a controlled environment and sensitivity to biological changes can be validated using histology.

1.3 Mouse models of disease

Early in the twenty-first century, in a testament to the value of big science, the sequencing of the human genome was completed. This opened the floodgates for a plethora of scientific investigations into gene function and profiling. Relationships between phenotypes and the DNA instructions detailing their architecture could now be defined. The benefits of genetic testing are being reaped clinically providing robust diagnostic testing for a growing number of conditions. The mouse was the first animal to have its genome sequenced which was found to be very similar to that of humans. Powerful genetic techniques have been developed that can introduce abnormalities into the mouse genome to generate AD models. There are now a number of mice lines available that exhibit 'human like' plaque and tau pathology. Low variability in phenotypes can be achieved using inbred strains, and the low costs and rapid maturation of these animals allows a high experimental throughput(47).

Mouse models may vary in both the specific genes that are targeted as well as the way in which they are manipulated. Genes can be inactivated known as knocking out, introduced known as knocking in, and mutated using chemical processes. The earliest models of AD are based around the known genetic mutations in familial forms and are therefore associated with abnormal Aβ processing. These mice develop plaques, cognitive deficits, and in some cases atrophy of brain tissue to varying degrees(48). The different mutations

and promoters - DNA sequences that define where transcription begins, can be used to vary the regional distribution of pathology and age at which phenotypic changes occur. Transgenic mouse lines have been bred to over express normal hAPP (human APP) which causes reduced density in presynaptic terminals but not the accompanying plaque pathology observed in models expressing the mutated form(49). Mutations in the presenilin gene produce an increase in Aβ levels(50) without cognitive deficits and plaque formation(48) that are only observed when crossed with mice expressing hAPP mutations to form a PSAPP model(51). Interestingly, plaques occur at an earlier age compared to hAPP models(52), and appear after measurable cognitive deficits are detected in this double transgenic line(53).

The full pathological profile of AD incorporates both plaque and tangle pathology. NFTs accumulate in a progressive manner with age in mice with the P301L htau (human tau) mutation along with motor and behavioural deficits that are similar to the human condition(54). The tau pathology in these mice is more severe when crossed with a hAPP model implying that amyloid deposition may intensify NFT formation(55). Tau models expressing wild-type human tau display neuronal dysfunction without the aggregation and NFT formation in mutant forms(48). In a study where mice with no endogenous tau alleles were crossed with a hAPP line, an improvement in memory and learning was observed but there was no decrease in amyloid pathology(56). Combined with the result from the P301L/hAPP double transgenic experiment, these findings suggest that tau aggregation may be a downstream event from plaque formation in line with the amyloid cascade hypothesis. However, these studies do highlight a detrimental effect of both mutated and wild-type human tau on neuronal vitality that is not observed in models expressing mutated hAPP only. Models that can replicate tau deregulation and aggregation in human AD therefore have an important place in the ongoing investigation of the disease.

The increasing number of models available means that it is crucial to make an appropriate choice as part of the experimental design process. In the case of drug development, the well documented time course of appearance of plaques and cognitive impairments in different models(48,57) should aid selection when targeting a specific stage of AD related pathology. The administration of a pharmaceutical at discrepant timepoints in mouse models relative to AD patients may lead to failure to translate successful tests in mice to the clinic. *In-vivo* biomarkers that provide spatial distribution and density of NFT pathology

could be used stratify the Braak stage of the disease and provide homologues between pre-clinical and clinical studies. Other important considerations include the fact that transgenic mice do not model sporadic AD in which there are differences in clinical and pathological symptoms compared to the relatively small population of familial forms. Drug delivery is complicated by the large disparity in pharmacokinetics and the difficulty in equating doses in humans to those in mice(48). These factors may have played a role in the failure of amyloid targeting drugs in human trials that had previously shown success in transgenic mice.

The benefits of mouse models in the study of AD so far are undeniable: correlative relationships in degenerative processes observed in humans have been replicated and validated in mice; potential therapies developed; and the powerful isolation of amyloid and tau pathologies have demonstrated that they both have important roles in AD. The failure of candidate amyloid modulating drugs to arrest cognitive decline in clinical trials to date has caused a shift in interest to alternative therapeutic pathways(2). The more recent availability of mouse models that develop tau pathology that mimics the human condition may provide a new target for diagnostic imaging and therapeutic development.

1.4 Pre-clinical imaging biomarkers

Histological staining of *ex-vivo* tissue in cross sectional studies has provided quantification of the plaque and tangle pathology in mouse models of AD. The age and severity at which deposits appear varies between lines, as does the extent of cognitive impairment observed. Imaging biomarkers offer the potential to track pathological changes over time in longitudinal studies and in many cases have analogous human protocols. The repeated examination of the same subjects generates both group and individual comparison data that is both cheaper and reduces animal use. This can expedite the testing and validation of new imaging techniques for clinical applications in AD. External effects such as lifestyle choices are controlled for in animal studies and composite influences from multiple pathological processes can be dissected to provide new insights into mechanisms of disease.

Pib-PET studies in mice with APP mutations have previously reported poor retention of the tracer(58,59) but more recently PSAPP mice have displayed a correlation between uptake and Aβ pathology(60). Using a fluorine based tracer(florbetapir), thought to bind better to

fibrillar amyloid, excellent uptake can be achieved in PSAPP mice(61) and brain regions with plaque pathology are differentiated in PET images(62). Decreases in FDG-PET signal have also been observed in PSAPP mice indicating the reduced metabolic activity associated with AD(52). Methods specific to NFT pathology are under development(63) but PET has been shown to detect increases in tracers sensitive to reactive microglia in mice with a tau mutation(64). The limited resolution of PET relative to the size of the mouse brain is a major drawback of the technique which can make accurate delineation of signal from specific structures challenging(65).

The sophisticated methods of structural MRI analysis developed for measurements of volumetric changes in the human brain have been adapted for mice. Studies in both Amyloid and Tau models have detected volumetric reductions in specific brain structures relative to wild-type controls(66-70) as well as measuring longitudinal changes(71). Plaques can be visualised in hAPP and PSAPP mice using high resolution T2 and T2* weighted imaging which may be due to the presence of iron(72-78). Deficits in cerebral blood flow and white matter abnormalities have also been observed in amyloid models using ASL and DTI respectively(79-82). The decrease in NAA levels associated with AD also occur in MRS of hAPP and PSAPP models(83). This effect has been shown to be attenuated after administration of anti-inflammatory drugs(84). In a study that used manganese enhanced MRI to probe axonal transport transgenic mice that develop amyloid and tau pathology, deficits were observed prior to the age at which plaques and tangles appear(85).

Tau pathology in AD progresses through the brain in a region-by-region manner described by Braak staging(11). Imaging methods sensitive to the regional spread of NFTs over time would constitute a powerful marker of disease severity for longitudinal clinical assessment and pharmaceutical testing. Due to the lack of an identified tau mutation in autosomal dominant forms of AD, mouse models are selected for the likeness of the pathological characteristics they develop to that of the human form. One such model is the rTg4510 model of tauopathy which expresses human tau with the P301L mutation. The soluble tau expressed, co migrates with a hyperphosphorylated tau species observed in NFTs in the human disease(86). In the rTg4510, aggregated Tau and NFTs accumulate in an increasing age dependent manner in parallel with memory impairment, neuronal cell loss and atrophy(87). The calmodulin kinase II promoter system is used to direct expression to frontal brain structures causing high concentrations of tau pathology in the cortex and

24

hippocampus with gliosis(87). The prevalence of NFTs appears to be independent of neuronal cell death in agreement with findings in clinical studies of AD(86,87). As with Braak staging, a progressive regional spread of pathology is observed with age in the rTg4510(although this regional pattern is different to that observed in sporadic AD sufferers). NFTs first appear in the cortex at 2.5 month before spreading to the limbic structures at 5 months(87). At 8.5 months, high NFT density is observed throughout the forebrain structures and is accompanied by neuronal cell loss with gross atrophy apparent in visual comparisons of histology at 10 months(86).

Prior to this work, a volumetric MRI study of the rTg4510 at five months showed early sensitivity to reductions in the hippocampus and cortex relative to wild-type controls. This study also included proton MRS data that showed increases in myo-inositol to creatine ratios, indicative of glial activity in the hippocampus(70). Investigations using manganese enhanced MRI revealed a reduction in neural activity in regions associated with memory formation at six months of age(88). These early studies provide an indication of the sensitivity of MRI to pathology and degeneration in the rTg4510. Investigation into techniques that probe other distinct aspects of AD pathophysiology such as perfusion, microstructure, and protein aggregation may provide a more complete characterisation of the rTg4150 phenotype.

1.5 Summary and thesis aims

In this introductory chapter, a brief overview of some of the major events in the discovery of AD is provided. There is a need for this debilitating disease to be better understood. One method by which to achieve this may be to use mice as reductionist tools to observe and analyse individual known biological factors that may be tracked using biomarkers. In this way, MRI may provide a tool to evaluate therapeutics and also elucidate new mechanisms in the pathogenesis. The real power of this non-invasive modality may lie in the combination of data from the application of multiple techniques that are directly translatable to the clinic, providing a holistic approach to describe the neurodegenerative process. In comparison to studies of mouse models of plaque pathology, there is paucity of pre-clinical studies into the role of tau in AD.

To aid the development of pharmaceuticals that target tau pathology in AD, a collaboration was born between CABI and Eli-Lilly & Co. Ltd. with the aim of developing an *in-vivo* multi-

parametric MRI protocol sensitive to pathology in the rTg4510. In addition to structural MRI, the goal was to develop new techniques that provide sensitivity to other degenerative aspects of the disease to complement the information from this established biomarker. Total scan time is restricted by limits of anaesthesia duration in the mouse. Development of time efficient acquisitions are necessary to collect multiple MRI metrics sequentially in a single session.

Magnetic field gradients used for spatial localisation of signal are central to most MRI techniques. Imperfections can cause distortions in structural MRI data used for volumetric analysis, and errors in diffusion estimates from DTI protocols. The first aim of this work was to develop a novel calibration protocol that could be used to perform quality assurance by monitoring the accuracy of the system gradients of the MRI scanner. This is described in chapter 3 and provided a foundation for the acquisition of consistent multi-parametric data. Secondly, the primary aims of this thesis focussed on the development of MRI protocols that would provide sensitivity to white matter degeneration in AD mouse models. Diffusion Tensor Imaging and Quantitative Susceptibility Mapping protocols suitable for multi-parametric acquisition are designed, systematically optimised, and implemented in the rTg4510 mouse in Chapters 4 and 5 respectively. In the next chapter, the theoretical MRI concepts applied in this thesis are outlined.

2 Magnetic resonance imaging theory and methodology

2.1 Chapter summary

In the first chapter, an overview of the current understanding of Alzheimer's Disease was provided. A case was made for the great potential of emerging MRI techniques to provide biomarkers of the various pathological traits of the disease and to aid in the development of new therapies. In this chapter, the fundamental principles of MRI and the theory behind the relevant MRI techniques that have been applied in this thesis are described. Firstly, the physics of NMR signal generation is outlined as well as basic pulse sequences and MR relaxation time constants that are referred to throughout this work. Chapter three describes a technique developed to calibrate gradients so key concepts involved in the spatial encoding of the MRI signal are covered. In the latter sections of this chapter, methods of Diffusion Tensor Imaging and Quantitative Susceptibility Mapping are detailed to provide the reader with some understanding of steps involved in the protocols applied in chapters 4 and 5.

2.2 NMR signal generation

The signal in Nuclear Magnetic Resonance(NMR) can be described theoretically using a mixture of classical physics and quantum mechanics with each providing an explanation of different aspects of the phenomenon. Whereas quantum mechanics is useful for describing the interaction of magnetic fields with individual atomic nuclei, a classical treatment is more helpful in understanding the cumulative behaviour of a population. Electromagnetic radiation travels in waves consisting of packets of energy known as quanta. The relationship between these wave and quantal properties of radiation are described by the equation

$$\varepsilon = h\upsilon$$

<div align="right">**Equation 1**</div>

where ε is the energy of a quantum, h is Planck's constant and υ is the frequency of the electromagnetic wave. The interaction between magnetic radiation and molecules can

involve absorption or emission of a quantum of energy. This will result in a molecular energy level transition that is of equal energy to the quanta. This interaction between matter and radiation is central to the quantum mechanical theory of MRI.

The ^{1}H nucleus imaged in MRI is a member of a class of nuclei that possess the property of spin. The nucleus of such atoms is often referred to simply as a 'spin' in NMR and gyrates around its own axis generating an angular momentum(Figure 2) like a spinning top. The hydrogen nucleus consists of a single proton giving it positive electric charge. In the manner of a circulating electrical current in a loop of wire, the spinning motion of this positively charged nucleus generates a magnetic field. When placed in an external magnetic field, a turning moment acts on this 'nuclear dipole'. This is known as the magnetic moment, μ, and is associated with the angular momentum, of the spin. This angular momentum, p, can only take discrete values specified by quantum number I and is calculated as(89)

$$p = \hbar\{I.(I+1)\}^{1/2}$$

Equation 2

where $\hbar = h/2\pi$
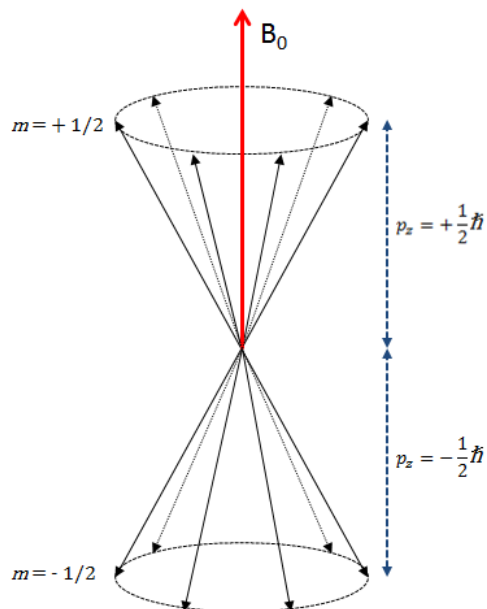
Figure 2.   **Spin angular momentum**

Schematic of various orientations of the angular momentum vector of a nucleus labeled with z components p_z and quantum number m. *Figure adapted from* (89).

I can take integral or half integral values based on the number of protons and neutrons in the nucleus in question. In the case of the ^{1}H nucleus, $I = 1/2$. In MRI we are interested in the component of angular momentum in the direction of the main magnetic field (B_0). The angular momentum is a vector quantity and therefore has both magnitude and direction. Another quantum number, m, can be used to define the component in the direction of the magnetic field (z) as(89)

$$p_z = m.\hbar = \pm\frac{1}{2}\hbar$$

<div align="right">**Equation 3**</div>

reflecting two possible spin states. The interaction between the magnetic moment and the B_0 field causes the nucleus to acquire an energy, E, given by(89)

$$E = -\gamma m \hbar B_0$$

<div align="right">**Equation 4**</div>

where γ is the gyromagnetic ratio (approximately 2.68×10^8 rad/s/T for the hydrogen proton in water). A difference in energy between the two possible values of ±1/2 that m can take can be calculated as

$$\Delta E = \gamma \hbar B_0$$

<div align="right">**Equation 5**</div>

The NMR signal is generated through the transition of spins between the two energy states described by Equation 4. This is achieved through the absorption of energy from an oscillating magnetic field, B_1, generated using Radio Frequency (RF) pulses. To induce transitions, the frequency of oscillation, v_0 , must be such that

$$\Delta E = h v_0$$

<div align="right">**Equation 6**</div>

where

$$\omega_0 = 2\pi v_0$$

<div align="right">**Equation 7**</div>

Equations 5,6, and 7 can be combined to give

$$\omega_0 = \gamma B_0$$

This relationship defines the frequency, known as the Larmor frequency, that nuclei of a particular gyromagnetic ratio, will precess at in a magnetic field. It is also the frequency that is required for the oscillating magnetic field, B_1, to induce spins to undergo transitions between energy levels.

One of the factors governing the amount of signal available in MRI is the difference in the number of nuclei in the higher N_+ and lower N_- energy states at equilibrium. This is described by the Boltzmann distribution which gives the relative populations of spin states in a sample(89)

$$\frac{N_-}{N_+} = e^{\left(\frac{-\gamma \hbar B_0}{kT}\right)}$$

where k is the Boltzmann constant and T is the temperature in Kelvin. The spins in the positive energy state are in parallel alignment with the main magnetic field and have less energy than those in the negative energy state that are in anti parallel alignment. The lower energy state is more populated at equilibrium and there is a net absorption of energy when an oscillating B_1 field is applied at the Larmor frequency. If energy state populations were equal, there would be equal transitions in both directions and no signal would be generated. The population difference that gives rise to the NMR signal is very small and is responsible for the limited sensitivity of NMR. As indicated by Equation 9, a greater discrepancy in spin states can be generated at greater B_0 values, and SNR is increased with magnetic field strength.
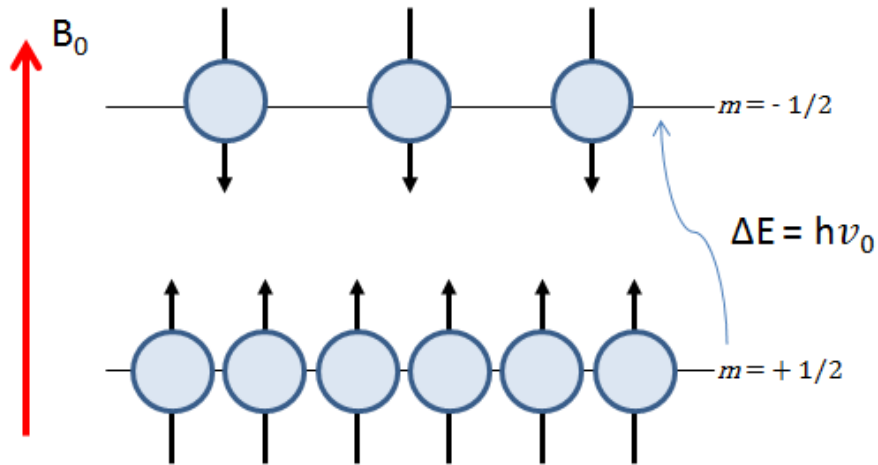
Figure 3.   **Spin energy states**

Spins with their magnetic moment aligned parallel and anti parallel to the magnetic field. Energy equal to ΔE must be absorbed to transition from the lower energy state (m=+1/2) to the higher energy stat(m=-1/2). Figure adapted from (89).

This quantum mechanical description indicates that the source of the measured signal is born from the difference in the populations between the two spin energy states. From here on, a more classical physics approach will be taken in describing the properties of the cumulative magnetic contributions from the signal generating proton population i.e. only those that transition to the higher energy state during a particular RF excitation. When placed in a magnetic field, the angular momentum of a spin causes it to process about the field at the Larmor frequency. At equilibrium, the precessing protons are all out of phase with each other and the angles made between their magnetic moments and B_0 are distributed randomly. By taking the vector sum of the magnetic vectors we can describe the proton ensemble by a net magnetization vector, M, which is at equilibrium is aligned along the direction of the main field, z(Figure 4a).   The cancelling of components perpendicular to the z axis means that, "at rest", there is no magnetisation in the xy plane (known as the transverse plane), M_{xy}, necessary for signal detection.

The equilibrium magnetisation, M_0, can be rotated towards the xy plane using an RF pulse applied perpendicular to the B_0 direction at the Larmor frequency. The net magnetisation vector will precess around the direction of the B_1 field generated by the RF pulse. This causes it to tip away from the z axis direction towards the xy plane. The angle subtended between the magnetisation and the z axis directly after the pulse is switched off is known

as the flip angle(Figure 4b). In the case of 'hard pulses' which are simply switched on and the off, the flip angle(α) is defined by(89)

$$\alpha = \gamma B_1 \, t_p$$

<div align="right">**Equation 10**</div>

where B_1 is the strength of the magnetic field applied and t_p is the pulse duration. Considering the case where a pulse is applied with a flip angle of 90^0, all magnetisation is now aligned with the transverse plane and the z component is zero(Figure 4c).   As soon as the pulse is switched off, the protons once again precess around the static B_0 field and there is now an M_{xy} component known as transverse magnetisation because the spins precess in phase. The M_{xy} component rotates round the z axis and can be detected using a receiver coil. An electromotive force is induced in the receiver coil that oscillates at the Larmor frequency that is further processed by the receiver hardware to produce the NMR signal.
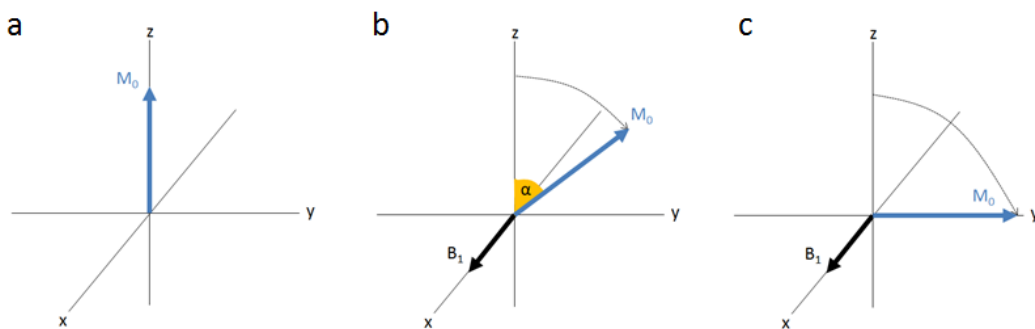
Figure 4.   Rotation of the net magnetic vector

Net magnetic vector in the rotating frame at equilibrium(a), after application of a B_1 field along x to tip the magnetization by flip angle, α,(b), and when tipped 90^0 into the transverse plane aligned with the y axis(c).

The signal received is known as the free induction decay (FID) since over time the M_{xy} component is reduced to zero again and the M_z component recovers to its initial value equal to M_0. The mechanisms governing the evolution of each component after excitation are different. The M_z component recovers through spin-lattice relaxation described by the T1 time constant, sometimes called T1 relaxation. During this process, energy absorbed through RF excitation is transferred to the lattice. The M_{xy} signal decays without energy transfer and is caused by dephasing and loss of coherence of the magnetic vector

contributions of individual protons. This decay is driven by spin-spin relaxation, described by the T2 time constant, in addition to the T2' time constant which describes dephasing caused by inhomogeneities in the main magnetic field. These two parameters are often combined to give the time constant T2* as

$$\frac{1}{T2^*} = \frac{1}{T2} + \frac{1}{T2'}$$

<div align="right">**Equation 11**</div>

The recovery over time, t, of the magnetisation following the excitation pulse along the z axis to its initial value, M_0, is given by

$$M_z(t) = M_0(1 - e^{-t/T_1})$$

<div align="right">**Equation 12**</div>

And the decay of the transverse signal can be calculated as

$$M_{xy}(t) = M_0 e^{-t/T_2^*}$$

<div align="right">**Equation 13**</div>

The T2* decay of the magnitude of the FID signal induced in the receiver coil over time is depicted in Figure 5. The net magnetic vector of the transverse magnetisation rotates around the z axis with an angular frequency that can be described in terms of phase angle as

$$\varphi = \omega_0 t$$

<div align="right">**Equation 14**</div>

i.e. frequency is the rate of phase change with respect to time, t. Differences in frequency between spins will generate a difference in phase over time. In the case of the FID, the effect of a 90^0 phase difference on the signal can be observed in Figure 5 . Frequency differences can be induced by gradients in the B_0 magnetic field across the spin population which will give rise to phase differences that can be exploited for spatial encoding or contrast purposes.
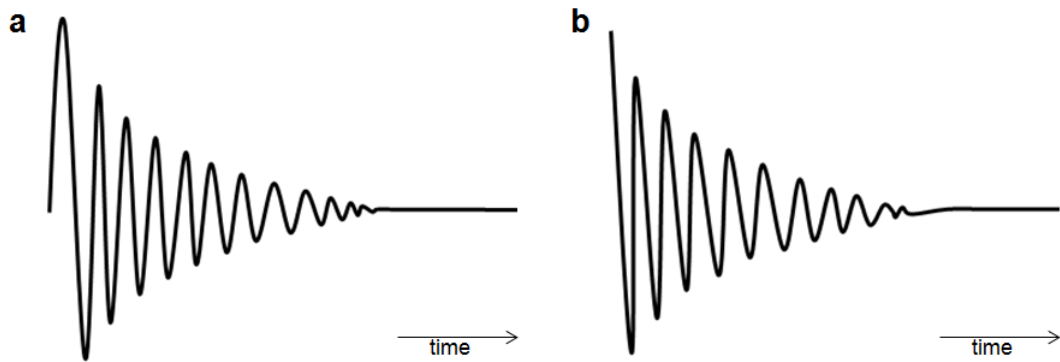
Figure 5. **Free Induction Decay**

Two FIDs that are approximately 90^0 out of phase with each other, at time zero the FID in (a) has minimum signal whilst the FID in (b) has maximum signal. Figure adapted from (89).

2.3 Echo formation

An alternative method to sampling the FID is to further manipulate the NMR signal to form what is known as an 'echo', which is more commonly acquired in MRI. The two most basic sequences used to generate signal in this format are called gradient echo and spin echo sequences (Figure 6). Whereas gradient echoes are formed using magnetic field gradients, spin echoes require an additional RF pulse.

To form a spin echo, spins are left to dephase in the transverse plane after excitation using a 90^0 RF pulse. At a time equal to half of the time to echo(TE), a 180^0 refocusing RF pulse is used generate a B_1 field in the y direction(orthogonal to the 90^0 pulse) in the rotating frame, to flip the spins in the xy plane such that it reverses the sign of the phase difference they have accumulated relative to the Larmor frequency. The spins precessing at a higher frequency now have a phase lag and will catch up with those precessing at a lower frequency in the second half of the TE to form a spin echo(Figure 6a). The effects of field inhomogeneities will be reversed by the refocusing pulse and therefore spin echoes are unaffected by T2' relaxation. The dephasing caused by spin-spin relaxation does occur and spin echoes are therefore described by the T2 time constant. In the case of a spin echo, the transverse magnetisation decay over time can be calculated by substituting the T2* term for T2 in Equation 13. Images can be generated through the repeated acquisition of echoes combined with spatial encoding using magnetic field gradients which is discussed in section 2.5. This time between excitations is known as the time to repeat (TR) and controls

the amount of signal recovery in the longitudinal plane (M_z). The signal from a spin isochromat(group of spins precessing at the same frequency) using a spin echo sequence is given by

$$S = S_0(1 - e^{-TR/T_1})e^{-TE/T2}$$

Equation 15

where S_0 is the signal measured with infinitely long TR and infinitely short TE.
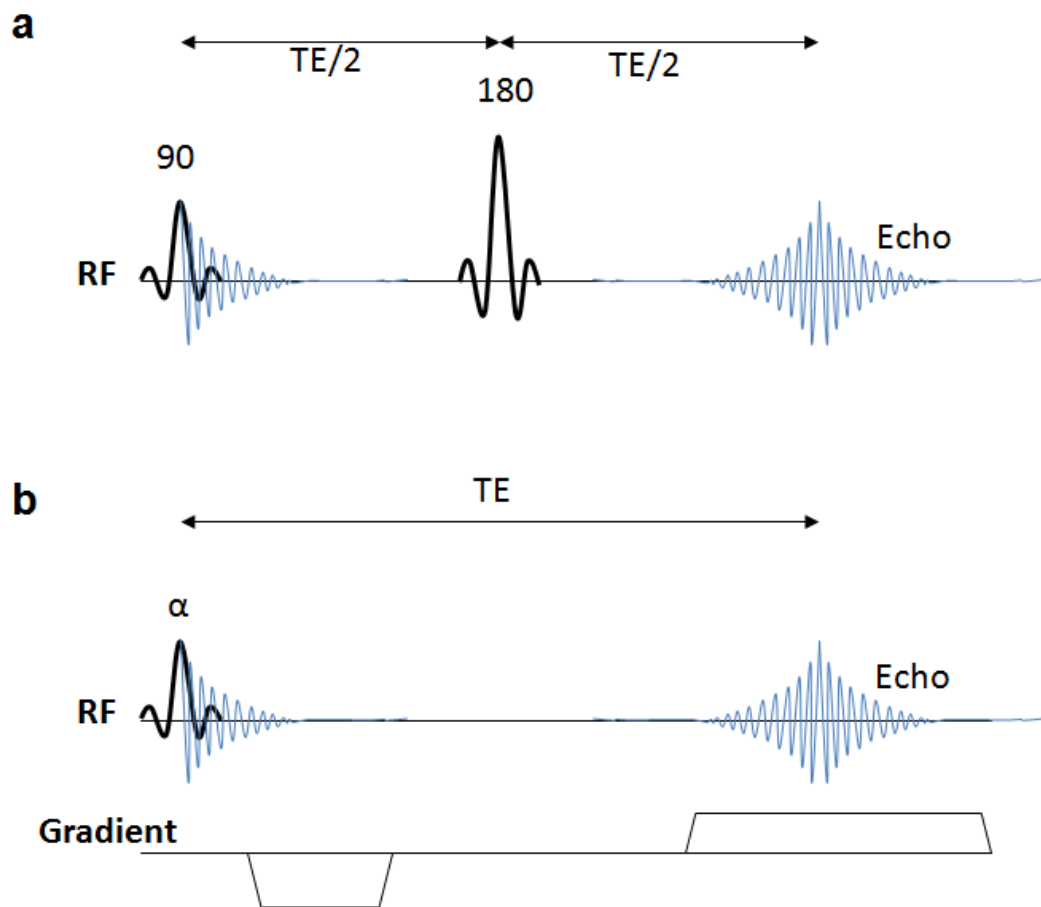
Figure 6.   **Echo formation**

Echo formation using a spin echo sequence(a) and a gradient echo sequence(b).

In the case of gradient echo acquisitions, a magnetic field gradient is applied after RF excitation that causes rapid dephasing of the transverse magnetisation (Figure 6b). This gradient field is then reversed so spins experience an equal and opposite magnetic field and frequency change. This has the effect of rephasing the transverse signal forming an echo at a time equal to TE. Both field inhomogeneities and spin-spin relaxation will

35

contribute to the loss of phase coherence over a TE and will not be eliminated in the process of echo formation. The decay of the transverse magnetisation at echo time is driven by T2* and can be calculated using Equation 13. The lack of a refocusing pulse means that flip angles other than 90^0 may be used in gradient echo sequences. The use of lower flip angles increases the longitudinal magnetisation retained after excitation allowing a quicker recovery of signal and rapid acquisitions using lower TRs. Therefore in addition to the parameters of TE and TR that control the signal in spin echo sequences, gradient echo acquisitions can be manipulated using the flip angle. The relationship between these three controllable parameters in gradient echo sequences is described by(90)

$$ S = S_0 (\sin \alpha \, e^{-TE/T_2^*}) \frac{(1 - e^{-TR/T_1})}{(1 - \cos \alpha \, e^{-TR/T_1})} $$

Equation 16

2.4 Relaxometry

The measurement of relaxation time constants T1, T2, and T2* can be performed using variations of the spin echo and gradient echo pulse sequences. In the case of T2*, measurement of a multi echo gradient echo sequence can be used to capture the transverse decay curve. Bipolar gradients can be used sequentially after excitation to rephase the transverse magnetisation and a monoexponential fit (Figure 7) can be used to estimate T2* using Equation 13. A similar process can be used to measure T2 by fitting the decaying signal using a multi echo spin echo sequence using 180^0 RF pulses to continuously refocus spins to generate echoes of decreasing magnitude.

36
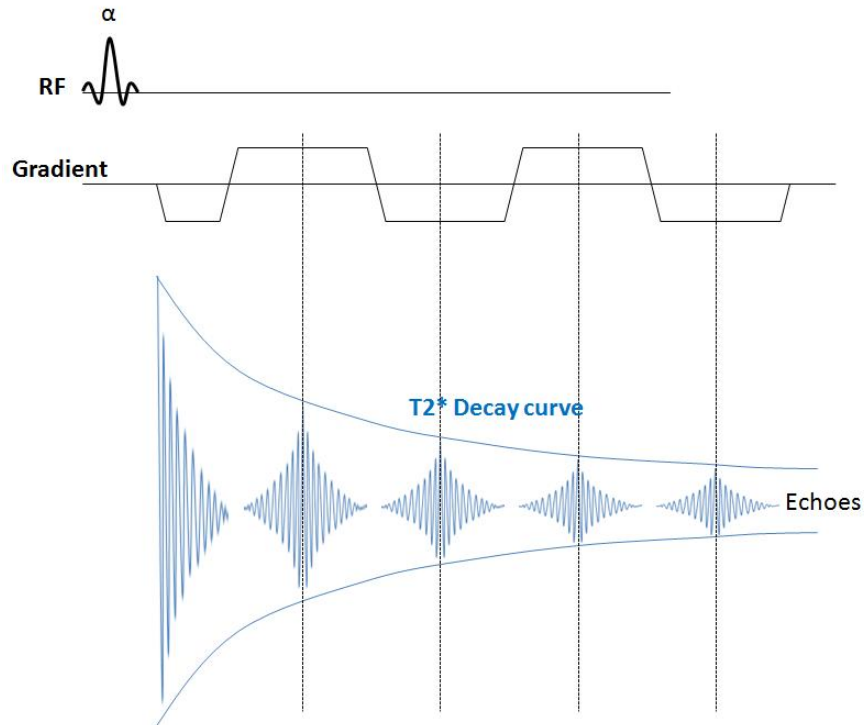
Figure 7.   **T2* measurement**

Formation of echoes using a multi echo gradient echo sequence. Rephasing of the transverse signal generates echoes of decaying magnitude that can be used for monoexponential fitting to estimate T2*.

A popular method by which to measure T1 is using an inversion recovery sequence. A 180^0 RF pulse is used to invert the longitudinal magnetisation(in the negative direction in the z axis) which then recovers towards its equilibrium value. A time after inversion(TI) a 90 degree pulse can be used to tip the magnetisation into the transverse plane to allow a measurement of the longitudinal magnetisation recovery.   Repeating this process at multiple TIs provides multiple measurements of the T1 recovery curve that can be fit using a monoexponential function to estimate the T1 recovery constant.   The signal for an inversion recovery spin echo acquisition is given by(91)

$$S = S_0(1 - 2e^{-\left(\frac{TI}{T_1}\right)} + e^{-\left(\frac{TR}{T_1}\right)})e^{-TE/T_2}$$

Equation 17

2.5 Spatial encoding

To generate images using the NMR signal, spatial encoding is required to separate components from the different locations in a sample. In MRI this is accomplished by introducing inhomogeneities in the main magnetic field using gradient coils. The spatially varying magnetic field causes the frequency of spin precession to change with position. The signal strength at a particular position can then be determined via measurement at the corresponding frequency. The spatial frequencies are mapped in three dimensions by application of pulsed gradients in the three axes of the scanner frame of reference. These can be described mathematically as

$$G_x = \frac{\partial B_z}{\partial x} \qquad G_y = \frac{\partial B_z}{\partial y} \qquad G_z = \frac{\partial B_z}{\partial z}$$

Equation 18

Where G_i is the gradient magnitude in axis i, B_z is the strength of the magnetic field in the z direction and x,y, and z are displacements in the direction of the respective axes.

The raw MRI data acquired is arranged to form a spatial frequency domain known as 'k-space' which can be transformed into an image space using a mathematical tool called the Fourier Transform(FT). To reconstruct images from sampled data a special version of this technique is used called the discrete Fourier transform(DFT). In order to resolve spin isochromats precessing at different frequencies, the DFT requires that they must possess a phase difference of at least 2π radians in the sampled signal(92). The spatial dependence of frequency in the presence of an applied gradient in the x direction is given by

$$\omega(x) = \gamma(B_0 + x \cdot G_x)$$

Equation 19

And using Equation 14 we can express this relationship in terms of signal phase :

$$\varphi(x) = \gamma(B_0 + x \cdot G_x).t$$

Equation 20

So the phase at position x is dependent on both the magnitude of the gradient along the x axis as well at its duration, t. It is the product of the gradient amplitude and gradient duration that determines the phase offsets between spin isochromats and therefore the

final spatial resolution. Sampling the MR signal as time increases in the presence of a gradient field provides information about smaller and smaller volumes in the final image. In k-space this corresponds to filling locations further and further out from the centre which represent higher spatial frequencies. The cumulative gradient time product, known as k is defined as

$$k_i = \gamma \int G_i(t)dt$$

<div align="right">**Equation 21**</div>

Where i denotes both the axis on which the gradient was applied and the axis along which the k-space matrix is filled with the sampled spatial frequency data. By sampling in multiple directions, a matrix representing the distribution of spins at various spatial frequencies can be produced that yield an imaging slice(2D) or volume(3D) after Fourier transformation. The conventional methods of spatial localisation of signal in 2D MRI acquisitions involve application of linear gradients for slice selection, frequency encoding, and phase encoding. These gradients, are applied in a 2D gradient echo sequence as shown in Figure 8.
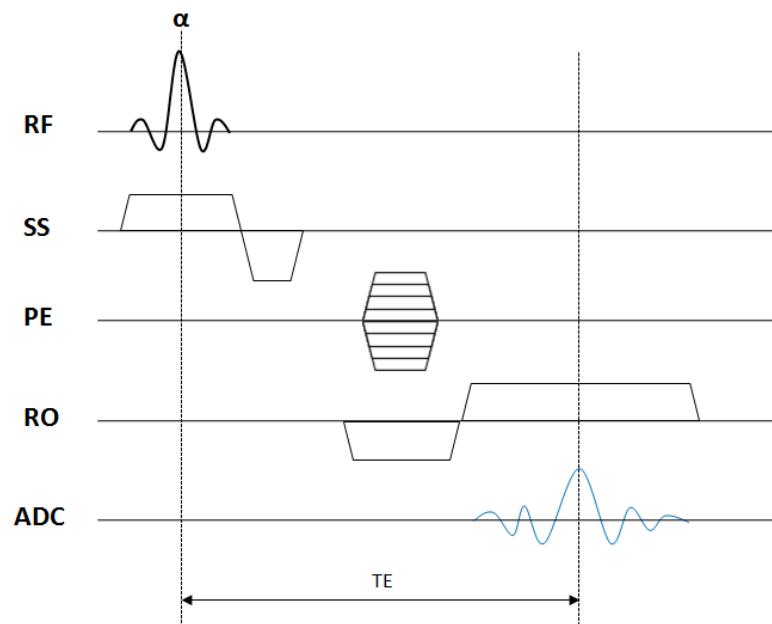
Figure 8.   2D Gradient Echo pulse sequence

2D gradient echo pulse sequence with slice select(SS), phase encode(PE), readout(RO) gradients.

A slice of the volume to be imaged is acquired by simultaneous application of a linear gradient along the desired axis (z in this case) and excitation using a frequency selective RF pulse. The position of the slice is determined by the centre frequency(ω_{rf}) of this RF pulse which corresponds to a point in space along direction of the applied gradient where spins are precessing at this frequency, This relationship is described by

$$\omega_{rf} = \ \omega_0 + \gamma z G_z$$

Equation 22

and the slice thickness, Δz, is dependent on bandwidth of the pulse(Δω), given by

$$\Delta z = \frac{\Delta \omega}{\gamma G_z}$$

Equation 23

After slice selection, the combination of frequency encoding and phase encoding in the remaining two orthogonal axes (in this case, x and y respectively) is used to produce 'in plane' k-space data. In the frequency encoding or 'readout' direction, the MR signal is sampled in the presence of a pulsed gradient with position encoded as in Equation 19. The zeroth gradient moment is equal to zero at the central point of k-space and represents a component of the acquired signal that is uniform throughout the volume. The filling of Cartesian k-space follows the pattern similar to that depicted in Figure 9. For each line in the readout direction a dephase gradient is applied prior to acquisition to move to one edge of k-space. A rephase gradient is then applied in the opposite direction and the MR signal is sampled as the whole width of k-space is traversed.
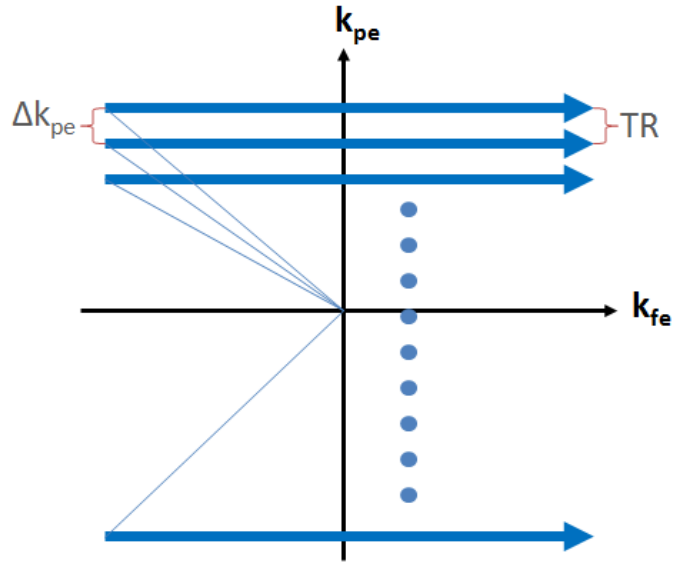
Figure 9.   K-space

Example of k-space being filled from left to right by sampling the echo during a rephase readout gradient (thick blue arrows). The phase encode gradient and the dephase readout gradients are used to traverse to the start point (thin blue lines) before acquisition. Figure adapted from (92).

In the axis perpendicular to readout, known as the phase direction, data is acquired by application of a relatively short pulsed gradient prior to readout. This generates an accumulation of phase by the time of acquisition that is position dependent described by Equation 20. The magnitude and duration of this phase encode gradient determine the point on the phase k-space axis that is traversed during signal readout. Due to the decay of the signal due to relaxation processes, the signal is refreshed for each line of k-space in the phase encode direction after one TR. The whole of k-space can be filled by varying the phase encoding gradient for each TR.

The spacing between points in k-space determines the Field of View (FOV) imaged. The relationship between spatial frequency resolution Δk_i and the image domain is described by the following equations(92)

$$\Delta k_x = \Upsilon G_x \Delta t = \frac{1}{FOV_x}$$

Equation 24

$$\Delta k_y = \maltese \Delta G_y t = \frac{1}{FOV_y}$$

<div align="right">**Equation 25**</div>

where $\maltese = \gamma/2\pi$.

We can rewrite these equations in terms of image domain resolution:

$$\Delta i = \frac{FOV_i}{N_i} = \frac{1}{k_i}$$

<div align="right">**Equation 26**</div>

where i can be substituted for x,y, or z axes.

For 3D MRI acquisition, the slice selection is applied to the whole volume in the required FOV, referred to as 'slab selection'. This is followed by the application of phase encoding gradients in the slice selection axis and k-space can be extended to a third dimension that is traversed a similar manner to the in-plane phase encoding dimension in 2D acquisition.

2.6 Echo Planar Imaging

2.6.1 Single and multi-shot acquisitions

The filling of k-space line by line in the conventional MRI acquisition described in the previous section is accomplished by refreshing the transverse magnetisation over multiple TRs. Advances in modern hardware performance allow faster switching of gradients with larger amplitudes and rapid sampling of the MR signal. This has enabled k-space to be completely traversed after a single excitation using Echo Planar Imaging (EPI). The readout gradient is repeatedly switched to rephase the transverse magnetisation which can be sampled many times before decaying away. EPI sequences commonly use 'blipped' phase encoding gradients to step through k-space in the phase direction incrementally. A gradient echo single shot or 'true' EPI pulse sequence is shown in Figure 10 along with the trajectory in k-space.
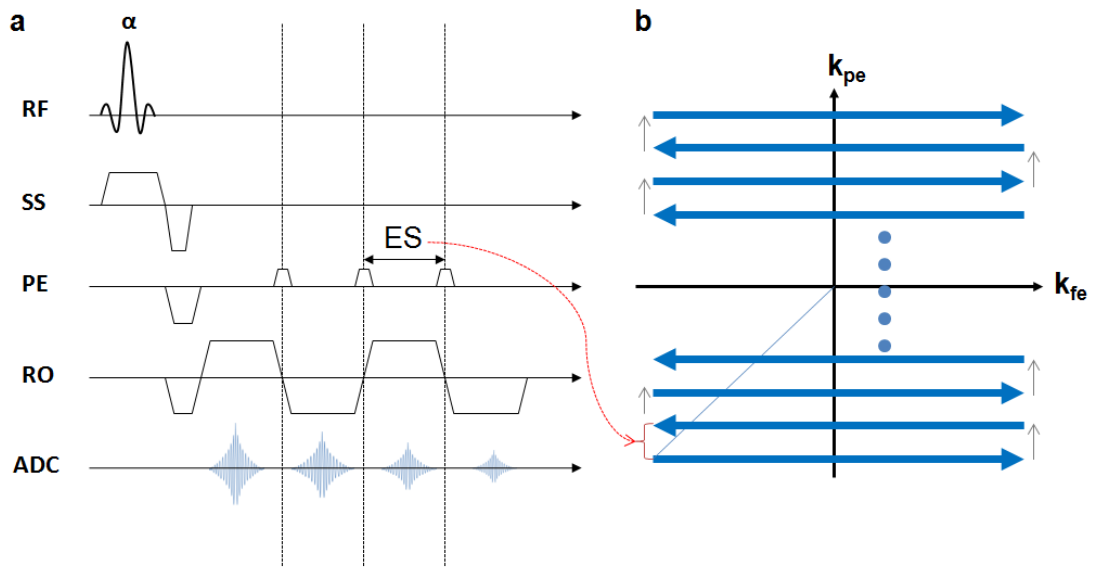
Figure 10.   **Single shot EPI**

Pulse sequence for single shot EPI (a) and diagram describing trajectory through k-space(b). Figure adapted from (92).

The long readout time in EPI makes the resultant images vulnerable to distortion from magnetic field inhomogeneities and signal drop out from $T2^*$ decay. The limitations on the amplitude and slew rates of the gradients both limit the achievable resolution as well as preventing reductions in readout time to minimize susceptibility effects. An alternative approach is to take an interleaved multi-shot approach to fill k-space using multiple excitations (Figure 11). Although less time efficient and more sensitive to artifacts from motion, less demands are placed on the gradients so a greater spatial resolution can be achieved. Multi shot approaches have shorter readouts and are therefore less affected by $T2^*$ effects and artifacts arising from low bandwidth in the PE direction in true EPI are reduced.
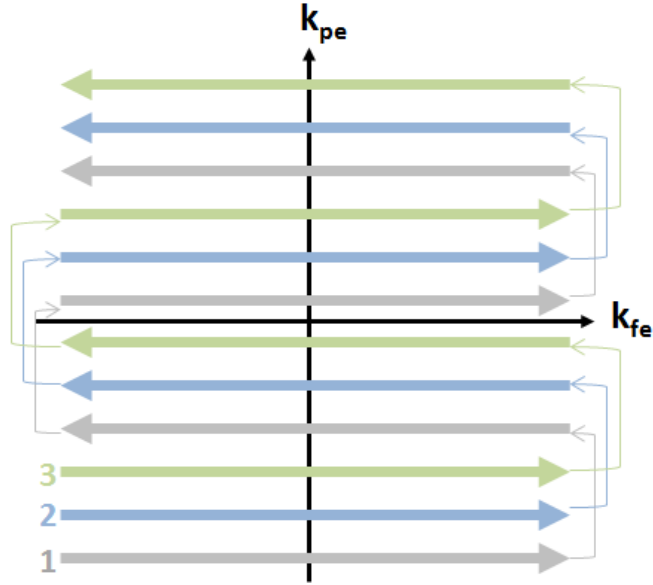
Figure 11.   **Multi shot EPI**

Diagram of k-space trajectory of a multi shot EPI acquisition with three excitations. Figure adapted from (92).

2.6.2 Artifacts

The time between signal samples in the PE direction in EPI is equal to the time between echoes formed from consecutive rephrase gradients, known as echo spacing(ES)(Figure 10a). This sampling occurs at a much lower rate than in the frequency encoding direction and the bandwidth per pixel in the PE direction can be calculated by

$$bw_{pe} = \frac{1}{N_{pe}ES}$$

Equation 27

which is lower than the bandwidth per pixel in the frequency encoding direction by approximately a factor of approximately N_{pe} .   This is particularly important when considering the effects of the chemical shift phenomenon in MRI.   The electronic environment of nuclei can modulate the magnetic field experienced by a spin (B_{eff}) given by

$$B_{eff} = B_0(1 - \sigma)$$

Equation 28

Where σ is the shielding constant and is approximately 3.3ppm for fat. Consequently, the protons in fat will precess at a shifted frequency that may cause mislocalisation of the signal to neighbouring voxels. The size of the spatial displacement of the signal is inversely proportional to bandwidth per pixel and may be calculated by

$$\Delta_{pe} = \frac{\gamma \sigma B_o}{bw_{pe}}$$

<div align="right">**Equation 29**</div>

The use of an interleaved multi-shot sequence means that k-space is traversed at an increased rate and combining Equation 27 with Equation 29 it is apparent that reducing N_{pe} will reduce the pixel shift of fat by a factor of $1/N_{shot}$, where N_{shot} is the number of shots used in the EPI acquisition. The spatial shift of fat in tissue can cause significant artifacts in EPI images and further measures may need to be taken such as the use of frequency selective RF pulses to saturate the fat signal prior to excitation.

EPI images can often suffer from geometric distortion caused by sources of magnetic susceptibility differences between regions in the volume of interest. The magnitude of distortion, *d*, is increased in the PE direction due to low bandwidth and is given by(92)

$$d = \frac{\Delta\chi B_0}{G} = \frac{\Delta\chi B_0 \gamma \Delta y}{bw_{pe}}$$

<div align="right">**Equation 30**</div>

where *G* is magnitude of the PE gradient blips and Δy is the resolution in image space in the phase encode direction. The k-space steps in the PE direction in multi shot EPI are larger than in single shot acquisitions as can be seen in Figure 11. The gradient-time product of the blips must therefore be greater, and as shown by Equation 30, this will have the effect of decreasing distortion.

Gradients arising from magnetic field inhomogeneities may cause signal loss and blurring in addition to geometric distortion. Consequently, the pulse train length is limited by T2* decay which is given by

$$\frac{1}{T_2^*} = \frac{1}{T_2} + \gamma\Delta B$$

<div align="right">**Equation 31**</div>

45

The readout time in single shot EPI is long relative to the T2* of tissue making it more sensitive to effects of signal dephasing when compared with the truncated echo trains used in multi shot acquisitions.

Both single shot and multi shot EPI acquisitions are susceptible to N/2 or nyquist ghosting artifacts. These are caused by misalignments of echoes along the PE k-space axis which manifest in images as faint 'ghost' images displaced by half of the field of view. This problem stems from the necessity to acquire each consecutive line of k-space with read gradients of alternating polarity. Echoes acquired with negative gradients are reversed with respect to time and effects of eddy currents and processing of the signal by the RF receiver produces differences between odd and even lines in k-space(Figure 12).

The rapid switching of gradients in the MRI scanner causes a fluctuating magnetic field that may induce electrical currents into conducting scanner components known as eddy currents. These eddy currents cause a lag between the current in the coil and the gradient field and this delay causes the rephasing of the echo to be time shifted with respect to the centre of the acquisition window. After time reversal of the odd echoes, this shift is in the opposite direction in k-space creating a zigzag pattern along the phase encode axis in k space. If the eddy currents induced are asymmetric, B_0 field modulation occurs and echo delays are not consistent across the field of view. This may be caused by misalignments between the gradient coil and the structures in which eddy currents occur. Another source of time delay is introduced during the low pass filtering of the signal in the receiver to remove noise from the MR signal.
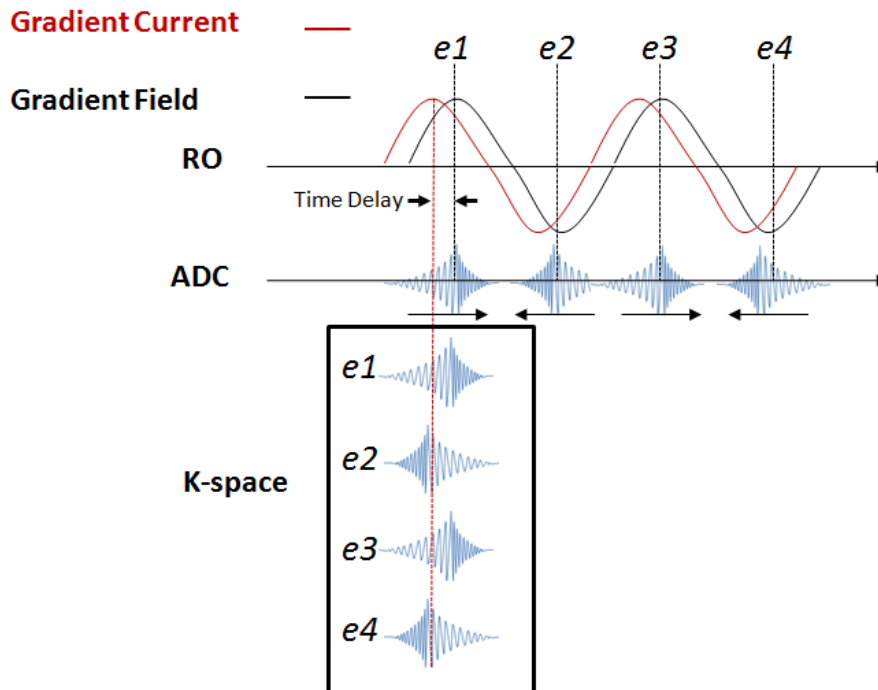
Figure 12. **Echo misalignment**

Echo misalignment in k-space caused by time delay between gradient current and gradient waveform. A discrepancy between echo peaks in k-space is caused by time reversal of even echoes. Figure adapted from(92).

2.6.3 Nyquist ghost reduction

The effects of eddy currents on the gradient waveforms may be reduced by scanner manufacturers through the use of pre-emphasis of the gradient waveforms as well as hardware to actively shield the gradient coils. However, further techniques are required to remove the residual offsets of odd and even echoes in EPI. A simple method is to delay to the start of the signal acquisition by a time that is equal to the lag between the current and the gradient waveform. This aligns the echoes with the centre of the acquisition window. Reference scans are an alternative method used to correct for phase and time shifts between odd and even echoes. Navigator echoes are acquired without phase encoding and the position of the echo peaks are detected. Phase and timing adjustments are then calculated to align echoes along the PE k-space axis. In the case of full reference scans, navigator echoes are collected for all lines of k-space in the EPI image which also has the effect of doubling the scan time.

2.7 Diffusion MRI

2.7.1 Diffusion weighting of the MR signal

Diffusion is a process by which molecules travel from areas of high concentration to areas of low concentration by way of random thermal motion. Ficks first law describes the net flux of particles from regions of high concentration to low concentration[93]:

$$J = -D\nabla C$$

<div align="right">**Equation 32**</div>

Where J is the net particle flux, C is the particle concentration, and D is the diffusion coefficient. Einstein later related the mean displacement of an ensemble of particles that occurs as a result of Brownian motion to the diffusion coefficient by the equation[93]

$$<x^2> = 6D\Delta$$

<div align="right">**Equation 33**</div>

Where $<x^2>$ is the mean-squared displacement of the ensemble, and Δ is the time over which diffusion occurs, known as 'diffusion time'. Diffusion weighted (DW) MRI is used to measure the amount of displacement of water molecules in tissue. This can be achieved by the addition of 'diffusion weighting' gradients to a standard sequence. In the simple case of a spin echo sequence, two identical DW gradients can be added, one between the 90 degree excitation and the 180 degree refocusing RF pulses, and one after the 180 degree pulse(Figure 13). This method developed by Stejskal and Tanner is known as a pulsed gradient spin echo sequence.
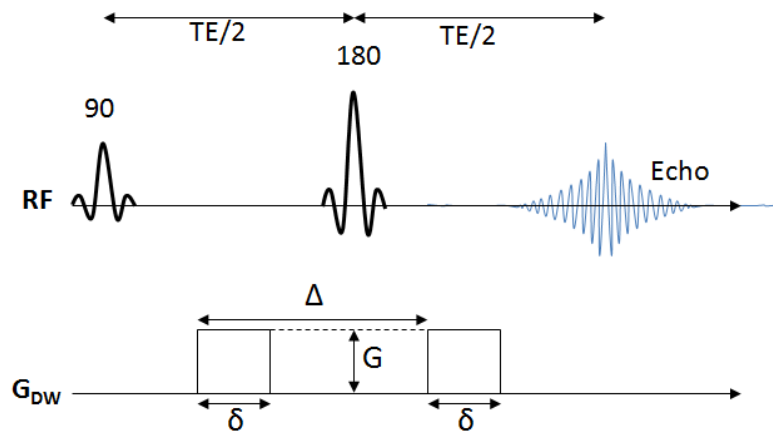
Figure 13.   **Pulsed gradient spin echo pulse sequence**

Stejkal and Tanner diffusion weighted sequence. Pulsed gradients are added to a spin echo sequence to generate diffusion weighting.

The effects of these additional gradients can be best understood in a 'narrow pulse' regime, where the separation between the two pulses(Δ), is much greater than the pulse duration (δ). Under these circumstances, diffusion taking place during the pulses is ignored, and the calculation describing the attenuation of the MR signal of a populations of spins caused by diffusion is much simplified(94). The application of the first pulsed gradient will induce a spatially dependent phase shift, Φ_1, in the transverse component of the MR signal of a spin that can be described by

$$\Phi_1 = \gamma.G.z_1.\delta$$

Equation 34

where G and δ are the magnitude and duration of the gradient pulses and z_1 is the position of the spin along the z axis in this example. Likewise, the phase accumulation, Φ_2, of a spin generated by the second diffusion gradient is given by

$$\Phi_2 = \gamma.G.z_2.\delta$$

Equation 35

The effect of the 180^0 RF refocusing pulse is to reverse the direction of the phase induced by the second gradient, and therefore the aggregate accumulated phase caused by diffusion weighting using this sequence is

$$d\varPhi = \varPhi_2 - \varPhi_1 = \gamma.G.\delta(z_2 - z_1)$$

<div align="right">**Equation 36**</div>

It is apparent from this relationship that stationary spins will experience zero net phase change. Since the phase accumulation from the first gradient is flipped in polarity by the refocusing pulse, the second gradient has the effect of generating an equal and opposing phase change. Spins that experience a displacement component in the direction of the gradient between the pulsing of the gradients will not experience equal phase shifts and will therefore have a net phase change at echo time. The incomplete cancellation of induced phase increments will cause a spread of phases that will attenuate the cumulative transverse MR signal of a population of spins. This effect can be described by signal attenuation, A, which is equal to the diffusion-attenuated signal, S, divided by the unweighted signal, S_0, which can be expressed as(94)

$$A = \frac{S}{S_0} = \int \rho(z_1) \int e^{i\gamma\delta G(z_2 - z_1)} P(z_2, z_1, \Delta) \, dz_2 dz_1$$

<div align="right">**Equation 37**</div>

The term $\rho(z_1)$ is the spin density at the time of the first gradient pulse and describes the inital concentration of spins at location z_1. $P(z_2, z_1, \Delta)$ is called the diffusion propagator and is the conditional likelihood that a spin at location z_1 will have diffused to location z_2, in diffusion time Δ. Where D is the diffusion coefficient, and diffusion is isotropic(94) :

$$P(z_2, z_1, \Delta) = \frac{1}{\sqrt{4\pi\Delta D}} . e^{\frac{-(z_2 - z_1)^2}{4\Delta D}}$$

<div align="right">**Equation 38**</div>

By combining Equation 37 with Equation 38 the attenuation can be calculated as

$$A = e^{-(\gamma\delta G)^2 \Delta D}$$

<div align="right">**Equation 39**</div>

Sometimes all gradient effects are summarised using a term known a 'b value' or 'b factor' which describes the magnitude of diffusion weighting :

$$A = e^{-bD}$$

<div align="right">**Equation 40**</div>

In practical situations, the 'narrow pulse' assumption is violated and diffusion will occur during the application of diffusion gradients. The diffusion time then becomes less trivial to define although ($\Delta - \delta/3$) is commonly used instead of Δ. The b-value is therefore calculated as(94)

$$b = \gamma^2 . G^2 . \delta^2 . (\Delta - \delta/3)$$

Equation 41

Attenuation of the MR signal may be calculated by division of MRI images acquired with diffusion weighting gradients by spatially corresponding unweighted images, known as B0 images in DW-MRI. The pulsed gradient parameters can then be used to provide an estimate of Diffusion Coefficient. When applied to measurements in tissue, this is referred to as the Apparent Diffusion Coefficient (ADC) and can be used to infer the presence of structures that restrict diffusion. In some cases where microstructural arrangements in tissue cause highly anisotropic diffusion of spins, sampling in multiple directions may be necessary to characterise the environment.

2.7.2 Diffusion Tensor Imaging

Some tissues such as the white matter in the brain, have shown diffusion estimates to be highly dependent on direction (95) due to the highly ordered nature of their diffusion restricting structures. The spin diffusivity in these environments is direction dependent and cannot be fully characterised using the scalar ADC value. The diffusion tensor model (96,97), was developed to describe diffusion in three dimensions. The diffusion tensor, given below, is a 3 x 3 matrix describing displacement in three dimensions, which can be calculated at each voxel in the images acquired.

$$D = \begin{bmatrix} D_{xx} & D_{xy} & D_{xz} \\ D_{xy} & D_{yy} & D_{yz} \\ D_{xz} & D_{yz} & D_{zz} \end{bmatrix}$$

Equation 42

The 'on diagonal' elements D_{xx}, D_{yy}, and D_{zz} indicate the diffusivity along each of the three principle orthogonal axes(x,y,z), and the off-diagonal elements give a measure of the correlation between them. The diffusion tensor can be described in terms of an ellipsoid (Figure 14), the surface of which represents the distances from the origin that a molecule will diffuse. The principle axes of the ellipsoid are given by the eigenvectors of the tensor and diffusion distance along each axis over time t is given by the eigenvalues. In an isotropic medium with equal diffusion in all directions, this ellipsoid will be spherical. For environments where diffusion is more favourable in a particular direction, the ellipsoid will become more stretched in this direction. Since the tensor is symmetric, there are only six unknown elements to determine and therefore, we need to image with diffusion weighted gradients applied in six different directions to generate the six simultaneous equations necessary to solve using linear algebra.
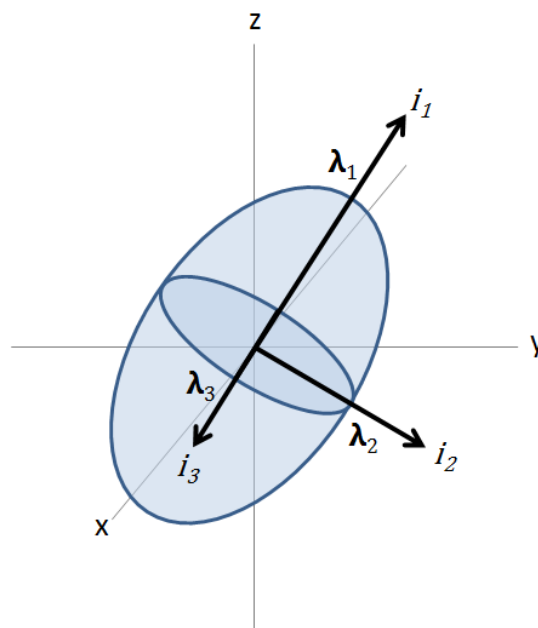
Figure 14.   The diffusion tensor ellipsoid

A depiction of the ellipsoid representation of the diffusion tensor labeled with eigen vectors,*i*, and eigenvalues,**λ**. Figure adapted from (93).

A number of clinically useful measures can be derived from the diffusion tensor that are rotationally invariant. The Mean Diffusivity (MD) is simply the mean of the diagonal

elements of the tensor, known as the trace of the tensor, and gives a scalar value of the average diffusivity in a voxel(93):

$$MD = \frac{Tr(D)}{3}$$

Equation 43

The MD can be used in combination with eigenvalues of the tensor to provide a measure of the anisotropy of diffusion in the voxel that is rotationally invariant. The most popular anisotropy measure used in the literature is Fractional Anisotropy (FA), which normalizes the variance of the eigenvalues to the magnitude of the tensor and is scaled to take values in the range zero to 1. It gives a measure of the fraction of the tensor that can be attributed to anisotropic diffusion and is given by(93)

$$FA = \frac{\sqrt{3}}{\sqrt{2}} \cdot \frac{\sqrt{(\lambda_1 - MD)^2 + (\lambda_2 - MD)^2 + (\lambda_3 - MD)^2}}{\sqrt{\lambda_1{}^2 + \lambda_2{}^2 + \lambda_3{}^2}}$$

Equation 44

where λ_1, λ_2, and λ_3 are the primary, secondary, and tertiary eigenvalues of the diffusion tensor. In white matter tracts of the brain, where highly anisotropic diffusion is observed, these eigenvalues can be interpreted as measures of axial diffusivity in the direction of the fibres and radial diffusivity perpendicular to fibres across the tract(98). Axial diffusivity(DA) is given by

$$DA = \lambda_1$$

Equation 45

and Radial diffusivity(DR) is calculated as

$$DR = (\lambda_2 + \lambda_3)/2$$

Equation 46

2.8 Quantitative Susceptibility Mapping

2.8.1 Magnetic susceptibility

Magnetic susceptibility, χ, is a quantitative property which determines a materials tendency to interact with and distort a magnetic field. A materials magnetization, M, is linearly related to the applied magnetic field, H, by the formula

$$M = \chi H$$

Equation 47

Diamagnetic materials have χ < 0 and paramagnetic materials have χ >0, with ferromagnetic materials having χ >> 1. In the case of human tissue, values of |χ| << 1 are typical in MRI, with values close to that of water (χ~-9ppm).

2.8.2 Magnetic susceptibility from the phase of the MR signal

The phase of a gradient echo MRI signal at echo time(TE) is sensitive to magnetic susceptibility effects that cause variations in the main magnetic field, B_0. This relationship is described by

$$\Delta\Phi = -\gamma . \Delta B . \text{TE}$$

Equation 48

Where ΔΦ is the difference observed in the phase of the net magnetic vector (relative to larmor frequency) and ΔB is the difference in magnetic field from the scanner B_0 field strength. Equation 48 can be used to calculate changes in the magnetic field, which have a functional dependence on the magnetic susceptibility distribution, using the phase of the MR signal. It has been shown that signal phase can be calculated through the convolution of the magnetic susceptibility distribution with a magnetic dipole field(99,100).

$$\Phi(x, y, z) = -\gamma . B_0 . \text{TE} . \text{FT}^{-1}\left(\frac{1}{3} - \frac{k_z^2}{K^2}\right) * (\chi(x, y, z))$$

Equation 49

Where K is the k-space vector, and

$$K^2 = k_x^2 + k_y^2 + k_z^2$$

<div align="right">**Equation 50**</div>

This convolution becomes a pointwise multiplication in the Fourier domain and by rearrangement of the Equation 49 we can express the magnetic susceptibility in terms of the measured MRI phase signal.

$$\chi(x, y, z) = FT^{-1}\left[FT\left(\frac{\Phi(x, y, z)}{-\gamma . B_0 . TE}\right) . F\right]$$

<div align="right">**Equation 51**</div>

where
$$F = \frac{1}{\left(\frac{1}{3} - \frac{k_z^2}{K^2}\right)}$$

<div align="right">**Equation 52**</div>

This method of calculation of the magnetic susceptibility distribution from the image phase is underdetermined as the k-space filter, F, requires a division by zero on the surface of a cone at the magic angle in the Fourier domain. The simplest method by which to remove the division by zero is by regularisation using a thresholded K-space division(TKD) technique(101), which sets the value of the filter to a constant at these discontinuities. Thresholded k-space division provides a computationally efficient method of calculating the susceptibility distribution in an imaging volume from the phase of the MRI signal generating a Quantitative Susceptibility Map (QSM).

By thresholding the K-space filter, magnetic susceptibility maps can be reconstructed from phase field maps that have had background contributions removed. However, unfavourable side effects of the regularisation include streaking artifacts, noise amplification and systemic underestimation of magnetic susceptibility. In the case of the underestimation errors, this can be corrected using a method suggested by schweser et al(102). By dividing the original k-space filter (F) by the thresholded version (F'), the modulation transfer function(MTF) of the filter modification can be calculated as

$$MTF = \frac{F}{F'}$$

Equation 53

The point spread function (PSF) is equal to the Fourier transform of the modulation transfer function which can then be deconvolved with the susceptibility map to perform the correction. The PSF can be approximated by a delta function, scaled by a factor dependent on the TKD threshold, t_F. The Fourier transform of a delta function is a constant value. A property of the FT is that point-wise division in the Fourier domain is equivalent to deconvolution in the spatial domain. Therefore the correction can be applied by a simple rescaling of susceptibility estimates from TKD by a factor calculated using the TKD threshold,t_F, to approximate the PSF.

2.8.3 Phase unwrapping

3D gradient echo is currently the most commonly used pulse sequence for acquisition of data to perform QSM[103,104]. Complex data is reconstructed from the acquired k-space matrix using a 3D discrete Fourier transformation. The signal phase, Φ, can then be calculated as

$$\Phi = \arctan\left(\frac{\text{Im}(Z)}{\text{Re}(Z)}\right)$$

Equation 54

where Z is the complex reconstructed imaging data. A volume of phase values called a field map is generated from this calculation that can take values in the limited range $[-\pi, \pi]$ radians for which the arctan function is defined. The phase of a spin is dependent both on the magnetic field experienced at its location and the time period over which it is measured as indicated in Equation 20. Therefore, the presence of field gradients across the field of view due to large field inhomogeneities or poor shimming will cause phase values to fall outside of this range giving rise to 'phase wraps' in the image. Where a phase value exceeds $\pm\pi$ it will be aliased back to this range by effectively adding or subtracting multiples of 2π(Figure 15). This causes the appearance of fringe lines across the image where phase wrapping occurs.
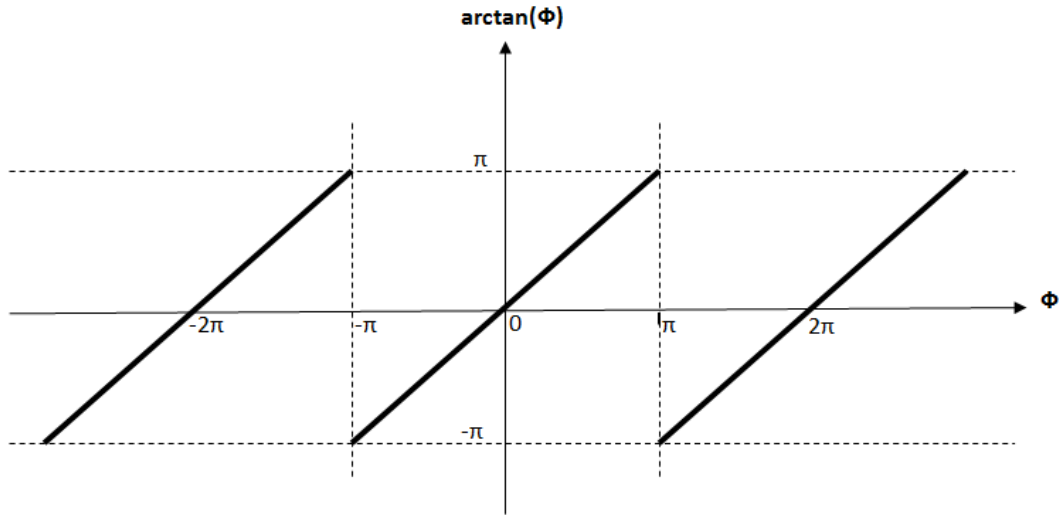
Figure 15.   **Phase aliasing**

A plot of true phase vs. output from the arctan function. Values of true phase that fall outside of [-π, π] are aliased back into the range. Figure adapted from (90).

Path based and laplacian based algorithms are commonly used to spatially unwrap aliased images. In the path based approach, as the name suggests, unwrapping is done by following a discrete path adding or subtracting multiples of 2π where aliasing is encountered. These algorithms unwrap regions of 'high quality' voxels first to prevent error propagation in the unwrapping process. The quality of a voxel may be established using multiple criteria such as estimated noise levels and spatial connectivity. Unwrapping by taking the Laplacian of the phase can be accomplished using properties of Fourier transforms with trigonometric functions as described by Schofield and Zhu(105)

$$\nabla^2 \Phi = \cos \Phi_w . \nabla^2 \sin \Phi_w - \sin \Phi_w . \nabla^2 \cos \Phi_w$$

Equation 55

where Φ_w is the wrapped field map and the laplacian terms can be calculated using the properties of Fourier transforms(106). In chapter 5, both path based and laplacian methods are applied and evaluated for *in-vivo* and *ex-vivo* field maps in the mouse brain.

2.8.4 Removal of background field contributions

Field maps of unwrapped phase can be considered to contain both data sensitive to the magnetic susceptibility of tissue in the volume of interest as well as what are known as

background field contributions. These unwanted effects come from field inhomogeneities that may occur from sources such as boundaries between air and tissue such as the sinuses in the head. In Susceptibility Weighted Imaging(SWI), homodyne (high pass) filtering is a popular way of separating the low frequency background contributions from the high frequency local susceptibility distribution in tissue. However, this technique is prone to through plane banding artifacts and struggles to remove background effects from tissue boundaries of large susceptibility difference(104). More sophisticated methods of background field removal have been developed recently called Projection onto dipole fields (PDF) and sophisticated harmonic artifact reduction for phase data (SHARP) that make use of the fact that the background field is harmonic within the region of interest.

The PDF method requires the generation of a mask around the region of interest. All voxels outside of this ROI are assumed to be responsible for the harmonic background susceptibility distribution inside, χ_B. The strength of a magnetic dipole is then fit at each of the voxels outside of the ROI using a weighting matrix W(107):

$$\chi_B^* = argmin \ \chi_B \|W(b - d \otimes \chi_B)\|_2^2$$

Equation 56

Where b is the total field and d is the unit dipole field. The background field is then calculated as $d \otimes \chi_B^*$ and removed.

The harmonic nature of the external field contributions inside the ROI, χ_B , means that it satisfies Laplace's equation(108):

$$\nabla^2 \chi_B = 0$$

Equation 57

In SHARP, the background field is removed from the local field, b_L, by convolving the total field, b, with the Laplace operator, L. Next an eroded mask, M, is applied to the data to remove unreliable convolution results around the edge of the brain. In the final step, an inverse Laplacian operator, L^{-1}, is applied to the data to compensate for the signal loss caused to the local field by the original convolution. This process can be described by the following equation(108):

$$b_L = L^{-1}MLb$$

<div align="right">**Equation 58**</div>

After removal of the background contributions from the field map by either PDF or SHARP methods, quantitative susceptibility maps can be generated using thresholded k-space division described in section 2.8.2.

2.9 References

The following texts were used extensively in the MRI theory descriptions, equations and generation of figures in this chapter.

Gadian, David G. *NMR and its applications to living systems*. Vol. 7. Oxford: Oxford University Press, 1995.

McRobbie, Donald W., et al. *MRI from Picture to Proton*. Cambridge university press, 2006.

Johansen-Berg, Heidi, and Timothy EJ Behrens, eds. *Diffusion MRI: from quantitative measurement to in vivo neuroanatomy*. Academic Press, 2013.

Schmitt, Franz, Michael K. Stehling, and Robert Turner. *Echo-planar imaging*. Springer Science & Business Media, 1998.

3 Development of a gradient calibration protocol for pre-clinical imaging at high resolution

3.1 Overview

As outlined in chapter 1, the study of animal models of AD *in-vivo* using MRI may offer new insights into disease progression and therapeutic response. This chapter will describe a calibration protocol that was developed to ensure accuracy and consistency in the system imaging gradients for acquisition of longitudinal multi-parametric MRI data in the mouse brain. The 9.4T MRI scanner at the Centre for Advanced Biomedical Imaging (CABI) was calibrated using this technique and data was acquired to evaluate the stability of the system. The importance of such quality assurance protocols for high resolution, pre-clinical imaging is demonstrated. This work lays the foundation for development and robust *in-vivo* acquisition of MRI techniques that are highly sensitive to errors in imaging gradients, such as Diffusion Tensor Imaging which is the subject of Chapter 4.

3.2 Background

Pre-clinical, high-field MRI systems are now widely used to provide high-resolution images of animal models of human disease. Such phenotyping studies have enhanced our understanding of numerous disease processes and, when used in combination with advanced computational methods, have been used to detect subtle differences in tissue structure, particularly in the brain (109). To perform accurate, longitudinal, phenotyping studies, both *in-vivo* and *ex-vivo*, requires careful calibration of the MRI scanner, in particular of imaging gradients, so that microscopic changes in tissue structure can be robustly measured.

Imaging gradients are generally calibrated via linear scaling factors in each principal imaging axis, and any error in their values results in a global compression or expansion of acquired images. Furthermore, imaging gradients are assumed to be spatially linear, and complex image distortions can be introduced by gradient non-linearity, which rapidly

manifest with increasing distance from the magnet isocentre. Gradient calibration is typically performed annually during routine maintenance by the scanner manufacturers. Scaling factors and linearity are assessed using a structural phantom. Distances between structures are measured on a single slice of an MRI image of the phantom and compared to those of the original CAD design. This approach is highly vulnerable to error due to operator variability, the small number of measurements taken and the large slice thickness (1 mm) used. Neither drift of applied gradients over time due to hardware instability between maintenance visits nor deformations in the phantom structure over time are accounted for. Additionally, acceptance limits specified (≤5% linearity over a 40 mm diameter of spherical imaging volume (DSV)) are potentially unsuited to the degree of accuracy required for phenotyping studies.

Whilst several strategies for calibrating imaging gradients have been proposed for clinical scanners (110-113), these may not translate to pre-clinical scanners which differ from clinical scanners in several fundamental ways. For example, the maximum imaging gradient strengths are typically an order of magnitude greater than those found on a clinical system, scanners have a much smaller bore size, and field strengths are typically between 7 and 11.7 T, compared with 1.5 or 3 T for clinical systems. Due to the challenging design considerations, large distortions can be observed in pre-clinical gradient sets. In these scenarios, control point or spot matching algorithms employed in clinical protocols to unwarp distorted images have been shown to fail and require operator intervention(114). Furthermore, the level of accuracy required for phenotyping studies (of the order of 10s of microns) outweighs that typically required for clinical *in-vivo* studies.

The aim of this work was to develop a gradient calibration and quality assurance protocol for pre-clinical MRI scanners, which can be customised to individual systems and RF coils, and that aims to reduce geometric distortions and ensure stability over time in both *in-vivo* and *ex-vivo* longitudinal phenotyping studies. Moreover, studies using imaging techniques that also rely on accurate gradients (such as diffusion MRI) would also benefit.

The protocol is based on a structural phantom that was constructed and designed in-house. 3D printing was used to construct the phantom which is a fast, straightforward and cost-effective method to build bespoke components(115), particularly of the size required for pre-clinical systems. Materials were chosen to be susceptibility matched, robust, and

usable in successive studies. CAD plans for the phantom are open-source, and have been published online: https://www.ucl.ac.uk/cabi/publications/open_source.

The calibration protocol consists of two stages: i) a system calibration method for absolute scaling of imaging gradients; ii) a post-processing correction of gradient non-linearity, achieved through non-rigid image registration. All post-processing software is feely available to download (*NifTK,* http://cmic.cs.ucl.ac.uk/home/software/), making this simple protocol easy to adopt as part of a pre-clinical quality assurance (QA) procedure.

In the following sections, the protocol is introduced and it is evaluated to what extent it can improve the accuracy of imaging gradients, compared with the values derived from the standard calibration procedure performed by the scanner manufacturer. The variation in the calibration parameters were monitored across a six-month period, alongside a serial assessment of the structural stability of the phantom.

Here follows, a brief, step-by-step description of the calibration protocol.

3.3 Gradient calibration protocol description

The calibration protocol is shown schematically in Figure 16. Firstly, a 3D grid phantom is constructed using 3D printing, with dimensions set according to the size of the RF coil and/or scanner bore to be used. The phantom is then scanned using X-ray CT to provide a set of image data that is free from image distortion(114,116,117) (although for 3D printers with a high printing accuracy, the CAD plans for the phantom could be used as a fall back option if an X-ray CT system is not available). Next, scaling errors in the imaging gradients are corrected by performing a linear system calibration (Figure 16a). Here, high-resolution, 3D gradient echo MR images of the grid phantom are acquired and are overlaid on the CT data using affine registration (i. e. scaling, translation, rotation and shearing). The registration parameters are then used to adjust the system gradient scaling values.

After system calibration of the scaling values, a second set of MR data is acquired, in order to perform a post-processing correction of gradient non-linearity. These data are translated into the CT imaging space using a rigid registration and then unwarped by non-rigid registration. This removes distortions caused by gradient non-linearity and any residual scaling errors that remain after the linear system calibration.
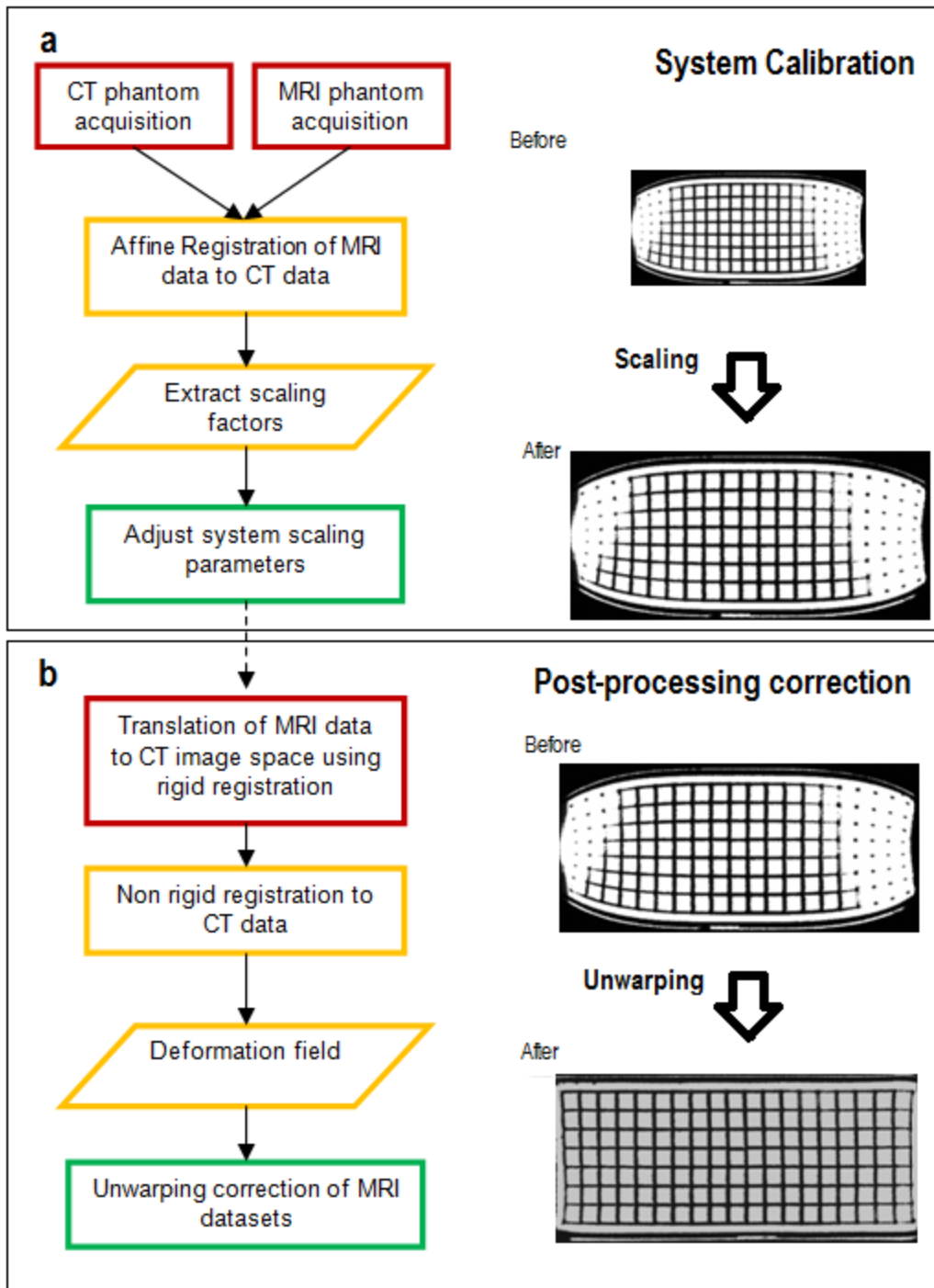
Figure 16. **Gradient calibration protocol flowchart**

Flowchart detailing the processes involved in the protocol and the order in which they should be implemented. The two major subdivisions of the technique are the system calibration (a) and the post-processing correction (b). Expected image deformations are illustrated using schematics.

3.4 Methods

3.4.1 3D Grid phantom

A phantom containing a three dimensional grid structure was designed in SolidWorks (DSS Corp, Concord, MA) computer aided design (CAD) software and was 3D printed using a Formiga P100 plastic laser-sintering system (EOS Electro Optical Systems Ltd., Warwick, UK) at a layer thickness of 100 µm. It was manufactured using fine polyamide (PA-2200 nylon), a material with low water absorption properties (0.41% over an initial 24hr period) and ability to withstand high mechanical and thermal load (EOS, PA 2200 Material Data Sheet). Nylon has a magnetic susceptibility that is close to that of water (< 3ppm) and so should not cause artifacts in either spin-echo or gradient-echo images (118).

For the current study, the dimensions of the phantom were 3D-printed to fit into a 35 mm birdcage coil that is routinely used for *in-vivo* phenotyping of mice (Rapid Biomedical GmbH, Germany). The grid pattern occupied 75% of the diameter of the coil and its length (60 mm) encompassed its entire sensitive region (50 mm) and extended beyond the 40mm DSV of linearity specified by the manufacturer. To enable removal of waste material generated during production, the phantom was formed in four pieces (Figure 17). After cleaning, the grid section was inserted into the outer chamber, where it was sealed by attaching a chamber cap with epoxy resin. Also incorporated into the phantom design is a positioner with a thread for a nylon screw that allows consistent placement within the coil.

The walls of the three-dimensional grid pattern in the phantom were 0.5 mm thick to enable adequate sampling at the imaging resolution, and spaced 2.5 mm apart. An irregular prism (Figure 17f) was included in the design of the phantom, at the centre of the grid, to aid orientation during post-processing. When inserted, the centre of the grid structure aligned with the isocentre of the magnet.

The phantom was filled with a solution of copper sulphate (1.25 g/L) and sodium chloride (5.3 g/L) in water (measured T_1, 245 ms). The filling tube contained an s-bend shape to ensure air bubbles that accumulated at the top when stored in its vertical position were prevented from travelling into the main chamber during imaging.
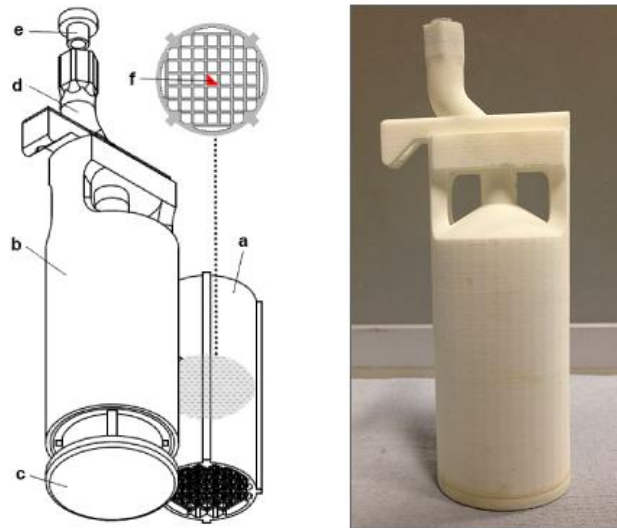
Figure 17.   3D grid phantom design

CAD drawing of phantom sections and photograph of the assembled phantom, which was created using 3D printing. To assemble, the grid section (a) was inserted into the outer chamber (b) which was sealed by the chamber cap (c). It can then be filled through the s-bend (d) and sealed using a cap (e). An irregular prism (f) in the centre of the grid structure aids in the orientation of images.

3.4.2 CT and MRI imaging

CT images of the phantom (Figure 18a,b) were acquired prior to filling with solution using a Bioscan nanoSPECT/CT system (Mediso, Budapest, Hungary). The Field of View (FOV) was selected to cover the whole grid section of the phantom and images were reconstructed using the vendor software to an isotropic resolution of 73 µm (system limit). To verify that the CT data were accurate, 10 manual measurements of the phantom were made using digital calipers and compared to CT data using NiftyView software (UCL, London, UK).

Prior to MRI acquisition, the phantom was filled and placed into the RF coil. An imaging gradient set with a 60 mm inner diameter (SGRAD 115/60/HD/S, Agilent Technologies UK Ltd., Berkshire, UK) was used in all experiments (unless stated otherwise), with a maximum gradient amplitude of 1 Tm^{-1}. The gradient set is specified by the manufacturer to have a gradient sub-system rise time of 130 µs and a linearity of ≤ 5% within a 40 mm DSV.

All measurements were performed using a 9.4 T Agilent scanner, and images were acquired using a 3D gradient echo sequence, optimized for high resolution imaging of *ex-vivo* murine brains (119). The FOV was set to 26x30x30 mm^3 in the central region of the phantom,

within the 40 mm DSV of specified linearity. Voxel size was set to 40 μm, isotropic, and the readout gradient was 0.09 Tm^{-1}, applied in the *Z* direction (parallel with the bore of the magnet). Other acquisition parameters included TR = 17 ms, TE = 4.54 ms, and a flip angle of 51°. Five averages were acquired, resulting in a total imaging time of 13 hours, 16 minutes. To investigate warping effects outside of the specified region of linearity and the possibility of reducing acquisition time for system calibration, data were also acquired at a reduced isotropic resolution of 100 μm over a larger FOV. The readout gradient was reduced to 0.04 Tm^{-1} and the FOV was 60x40x40 mm^3, imaging the whole grid structure (Figure 18c, d) in a reduced time of 3 hours, 46 minutes.
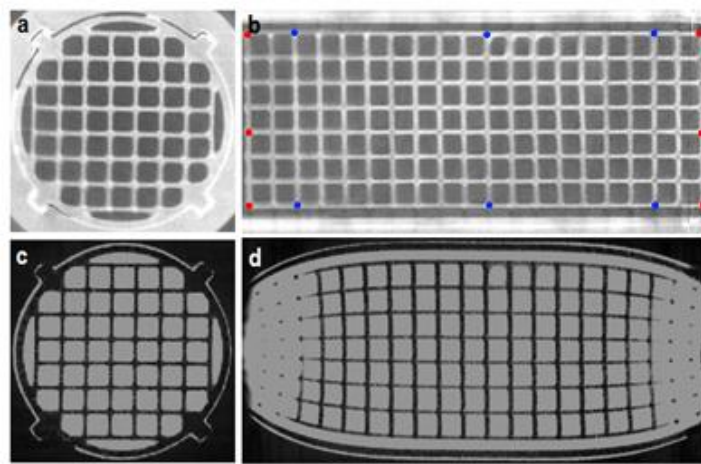
Figure 18.   CT and MRI images of phantom

Axial (a) and coronal (b) slices from CT data and corresponding axial (c) and coronal (d) slices from 3D gradient echo MRI data. Landmarks for distance measurements are shown (b) for Z axis (red) and Y axis (blue) (landmarks in X axis are orthogonal to those in the Y axis at same Z coordinates).

Shimming was performed manually at the start of each imaging session. The linewidth of the shim was monitored across imaging time points for consistency (40 ± 5 Hz) using a pulse and collect sequence and the temperature variation during a scan was measured by attaching a probe to the outer surface of the phantom.

To investigate warping effects that may be specific to the gradient echo sequence implemented, 3D Fast Spin Echo images of the phantom were acquired over the larger FOV with an isotropic resolution of 100 μm. Other acquisition parameters included TR = 200 ms, Echo Train Length = 4, Echo Spacing = 6.86 ms, Averages = 5, and a read gradient strength of 0.11 Tm^{-1} applied in the Z direction (Acquisition time of 11 hours, 7 minutes).

To maintain consistency in the comparison between sequences, gradient echo data was acquired at an isotropic resolution of 100 µm as detailed above with the read gradient strength increased to 0.11 Tm^{-1}.

3.4.3 System Calibration

NiftyReg software (120-122) was used for all image registration in this study. The affine and rigid registrations were carried out using the *reg_aladin* algorithm(120,121) which employs a two step process. A block matching algorithm provides a set of corresponding points between a target and source image before the transformation is evaluated using normalized cross-correlation(123). To reduce processing time, initial alignment is assessed based on down-sampled low resolution images before final registration using full resolution images.

Prior to registration, the CT data was cropped reducing the FOV to include the grid section of the phantom only, providing initial alignment of the MRI and CT images. An affine transformation matrix was output by the *reg_aladin* algorithm, which was decomposed into its constituent transformation parameters. The gradient scaling values stored in the MRI console software were then adjusted through multiplication with the scaling parameters from the registration in the *X*, *Y* and *Z* directions.

Phantom grid structures were segmented within MRI data by intensity thresholding to remove high signal intensity voxels occupied by the filling solution, and was further refined by manual segmentation to include only the grid structure.

To evaluate the improvement in gradient scaling afforded by the affine registration, dice coefficients (124) of the segmented grid structures were compared, before and after adjustment. The dice coefficient, *s*, was defined as

$$s = \frac{2| G_{MRI} \cap G_{CT} |}{| G_{MRI} | + | G_{CT} |}$$

Equation 59

where G_{MRI} and G_{CT} are the segmented grid structures of the MRI and the CT data. *s* ranges from 0 (indicating no overlapping voxels) to 1 (indicating that all voxels overlap completely).

3.4.4 Longitudinal assessment of calibration accuracy

After the initial system calibration, MRI acquisitions were repeated at monthly intervals over a period of six months to measure stability over time. Additionally, CT images of the phantom were acquired at the same time points to account for structural deformations. To investigate global volume changes in the phantom, affine registrations of the CT data at each time point to the CT data acquired at the first time point were implemented, again using Niftyreg. Distortion in the structure was evaluated by taking distance measurements (using NiftyView) between grid section landmarks in the CT data (Figure 18b), at three evenly spaced points along each axis. The measurements taken spanned the full diameter of the grid section in the *X*, and *Y* direction and the full length of the phantom in the *Z* direction. To test for a dependency between each of the measurements and longitudinal time point, a linear least squares regression analysis was performed to identify any significant correlation (*P*=0.05, *ANOVA*).

3.4.5 Scaling measurements for correction of Total Brain Volume estimates

Due to differences in experimental setup, structural imaging of the mouse brain *in-vivo* is carried out using a larger 120 mm diameter gradient set (SGRAD 205/120/HD/S, Agilent Technologies UK Ltd., Berkshire, UK) with a maximum gradient amplitude of 0.6 Tm^{-1}. The gradient set is specified by the manufacturer to have a gradient sub-system rise time of 180 μs and a linearity of ≤ 5% within a 80 mm DSV. The larger diameter facilitates use of a mouse bed with anaesthetic breathing apparatus and a two channel mouse brain surface coil (RAPID, Germany) for signal detection. Scaling of the gradient magnitude values for each of the gradient sets is done independently which may be a source of error when comparing data collected across multiple hardware configurations.

Prior to development of the protocol described here, *in-vivo* data was acquired in the larger diameter gradients that had been previously calibrated by the scanner manufacturers as part of an annual maintenance visit. *Ex-vivo* structural imaging of the same mice was carried out in the smaller diameter gradient set, post system calibration. To estimate scaling differences between the *in-vivo* data and *ex-vivo* datasets related to the hardware, the phantom was imaged in the larger diameter gradient set using the larger FOV protocol

described in section 3.4.2. The system calibration protocol was used to calculate scaling factors for comparison with those from the smaller diameter set.

Structural MRI datasets were acquired for a cohort of wild-type mice (n=8) at 7.5 months using previously described *in-vivo*(125) and *ex-vivo*(119) imaging protocols. Total Brain Volumes (TBVs) were estimated by manually correcting brain masks generated automatically using a previously published multi-atlas label fusion algorithm(126). These volumes were then rescaled using the values from the appropriate gradient set calculated by the system calibration.

3.4.6 Post-Processing Correction

The MRI data (defined as the *source*) was transformed into the imaging space of the CT data (defined as the *target*) by rigid registration using the *reg_aladin* algorithm in NiftyReg. NiftySeg segmentation software was used to automatically generate a registration mask that encompassed the area within the outer casing of the phantom in the CT data. This prevented intensity changes outside of the grid section of the phantom affecting the registration. The *reg_f3d* algorithm(122) in NiftyReg was used to carry out a non-rigid registration to warp the MRI data, post rigid registration (*source*), to the CT data (*target*).

The *reg_f3d* algorithm(122) uses cubic B-splines to generate a deformation field. The local displacement of control points in an equally spaced lattice causes warping that modifies mapping between source and target images. The registration is assessed through Normalised Mutual Information as an indication of correspondence between images and warping is constrained through bending energy and elastic energy terms(123). Input parameters were optimized to generate a smooth deformation field. A spline grid spacing of 20 voxels was implemented and the weight of the linear elastic energy penalty term was increased to [0.01 0.01].

To investigate the reproducibility of the results, the phantom was imaged four times, back-to-back, and displacement fields were generated for each scan. The first acquisition was taken as a reference and the absolute displacement differences at each point were calculated in the X, Y, and Z orthogonal directions (Z is aligned with the axis of the scanner bore), for each subsequent acquisition.

3.5 Results

3.5.1 Phantom stability measurements

The structural stability of the phantom was assessed over a six month period from CT data acquired every month. The maximum change in scaling identified on any axis was 0.28%. Phantom length measurements showed no significant correlation between variables, which suggests that there were no gradual changes in the phantom structure over time. The comparison of manual measurements in the CT imaging data to those made using digital callipers at a single time point showed a mean percentage difference of 0.27±0.17%, indicating a close agreement. The temperature of the phantom recorded during an MRI acquisition ranged between 19.9 °C and 20.2 °C (melting point of PA 2200 is 184 °C).

3.5.2 System Calibration

Prior to the start of the study, the imaging gradients of the 9.4 T scanner had been calibrated using the scanner manufacturer's standard protocol described in the introduction. Details of this protocol are published in a user manual supplied with their structural phantom. By comparing the CT phantom images with 100 μm-resolution MRI data (acquired with the manufacturer's calibration) after rigid registration, marked discrepancies were observed between CT and MRI images (white and black structures, respectively, in Figure 19(a and b). Relative to CT, MRI images were globally compressed in the Y direction and expanded in the Z direction. This can be seen most clearly in a central section of the phantom, within the 40 mm DSV specified by the manufacturer, where gradient linearity is optimal (Figure 19b). Figure 19e demonstrates the magnitude of these global changes, which varied with direction (scaling*: X* = 100.4%*, Y* = 105.3%, *Z* = 97.6%). This experiment was defined as scaling time point -1.

Outside the 40 mm DSV, it was clear that discrepancies between MRI and CT data markedly increased due to gradient non-linearity. To reduce the impact of this distortion when comparing image distortion before and after calibration, dice coefficients were only calculated in a region of interest corresponding to the central section of the phantom, within the 40 mm DSV (Figure 19b). Correction of image distortion due to gradient non-linearity is the purpose of the *post-processing correction* evaluated later in the study.

The system was then calibrated using our proposed protocol (scaling time point 0), a new set of MRI data was acquired, and rigid registration to the CT data was repeated. The accordance between these data and CT prior to and following calibration (Figure 19) was assessed by comparing dice coefficients, *s*: in the central region of interest, *s* was 0.73 before calibration and 0.84 afterwards (0.57 and 0.67, respectively, over the whole FOV). Affine registration of the MRI data acquired after the system calibration to the CT data produced scaling factors of 99.6%, 99.9%, 100.5% in the *X*, *Y*, and *Z* axes (Figure 19e), which is a marked improvement over the pre-calibration values. The mean scaling factor error (relative to unity) across all axes after correction was reduced from 2.7% to 0.3%.

Using the same approach as described above, the mean and standard deviation of the scaling factors measured every month, for a total of six months, were 99.7±0.1%, 100±0.2%, and 100.1±0.1% in the *X, Y* and *Z* directions.

The scaling factors calculated by registering the MRI data acquired at an isotropic resolution of 40 µm to the CT data followed a very similar pattern to the 100 µm MRI data (Figure 19e). The mean percentage difference between the 40 µm and the 100 µm scaling factors taken across all time points was 0.52±0.23%.
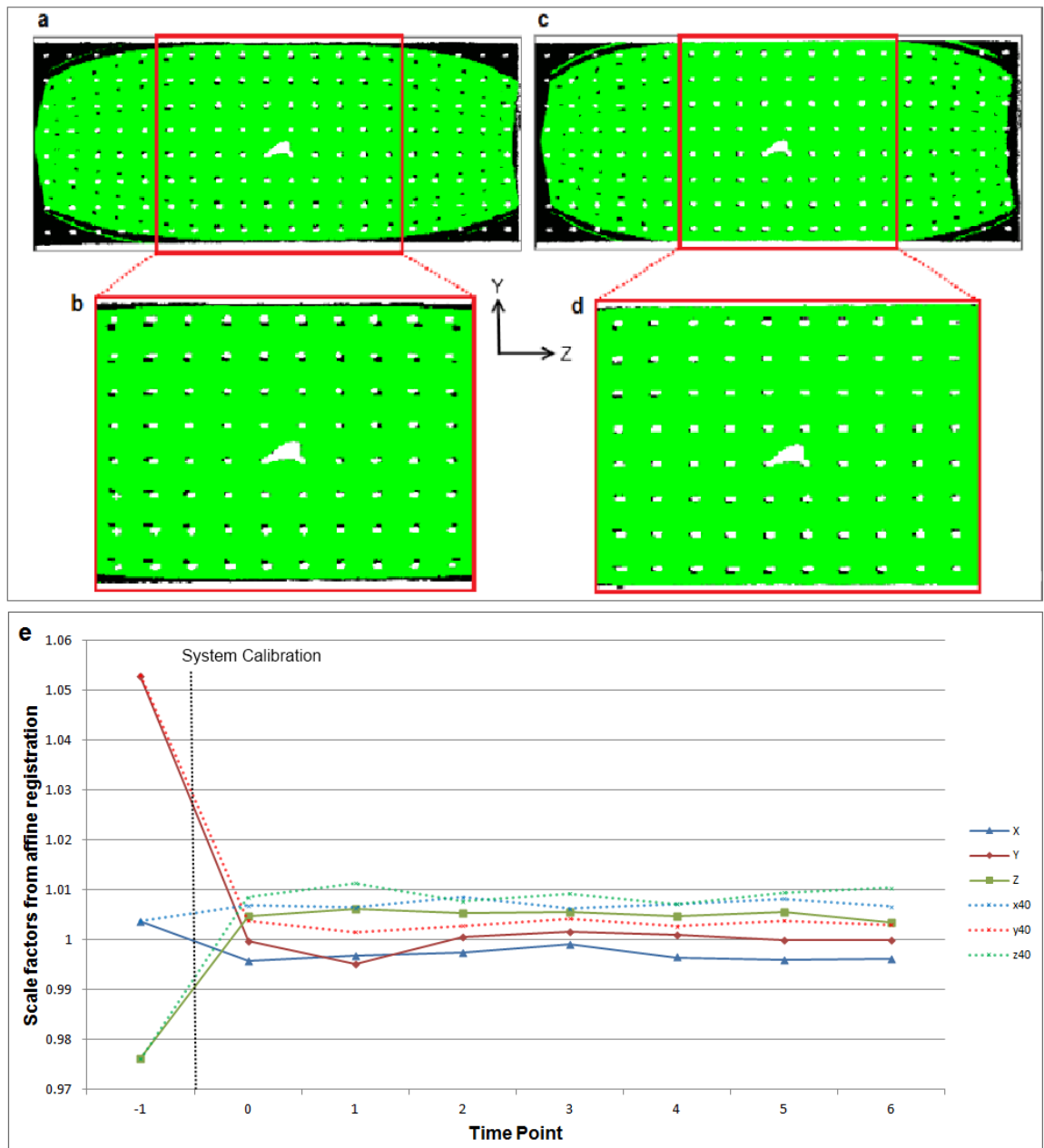
Figure 19. **Gradient scaling values before and after system calibration**

Sagittal slices of CT phantom images (white) overlaid on MRI images (filler inside phantom shown in green, phantom structure shown in black, 26x60 mm FOV) showing alignment before (a,b) and after (c,d) system calibration. The errors in the scaling factors (e) prior to calibration (time point -1) are reduced after system adjustment (TP 0) and the factors calculated using 100 μm data (X,Y,Z) are in good agreement with the 40 μm data (x40,y40,z40).

3.5.3 Post-Processing Correction

Alignment of MRI and CT data was further improved after non-rigid registration (Figure 20a), especially in regions further from the magnet isocentre. The dice coefficient calculated from the whole grid structure in the phantom increased from 0.62 before post-processing correction, to 0.88.

A displacement field, generated from the deformation field output by the non-rigid registration, shows the magnitude of voxel displacements applied to the MRI data to unwarp and register it to the CT data (Figure 19b-f). The displacements along the Z axis (Figure 19b) were less than 0.1 mm at a distance of less than ±10 mm from the isocentre. At a distance of ±20 mm, and greater, the displacements increase rapidly to more than 0.35 mm. The displacements along the X and Y axes show small displacements of less than 0.1 mm in central slices (Figure 19c,d) at distances of less than ±5 mm from the centre. For slices located further from the isocentre (in the Z direction) (Figure 19e,f), the magnitude of displacements markedly increases. Outside the central region of relatively low displacement, there is a rapid increase to values larger than 0.25 mm in the X and Y direction within the walls of the grid section of the phantom.

Within the central 40 mm DSV, where linearity is specified by the manufacturer, the maximum displacement was 0.72 mm, 0.87 mm and 0.6 mm in the X, Y, and Z axes, corresponding to a linearity of 3.6%, 4.35%, and 3% respectively. The maximum displacements in the phantom outside of this volume were 3.51 mm, 3.81 mm, and 2 mm in the X, Y and Z axes. The repeated generation of displacement fields to test reproducibility revealed the mean discrepancy between calculated displacements to be 11.8±10.2 µm across all axes for the whole FOV.
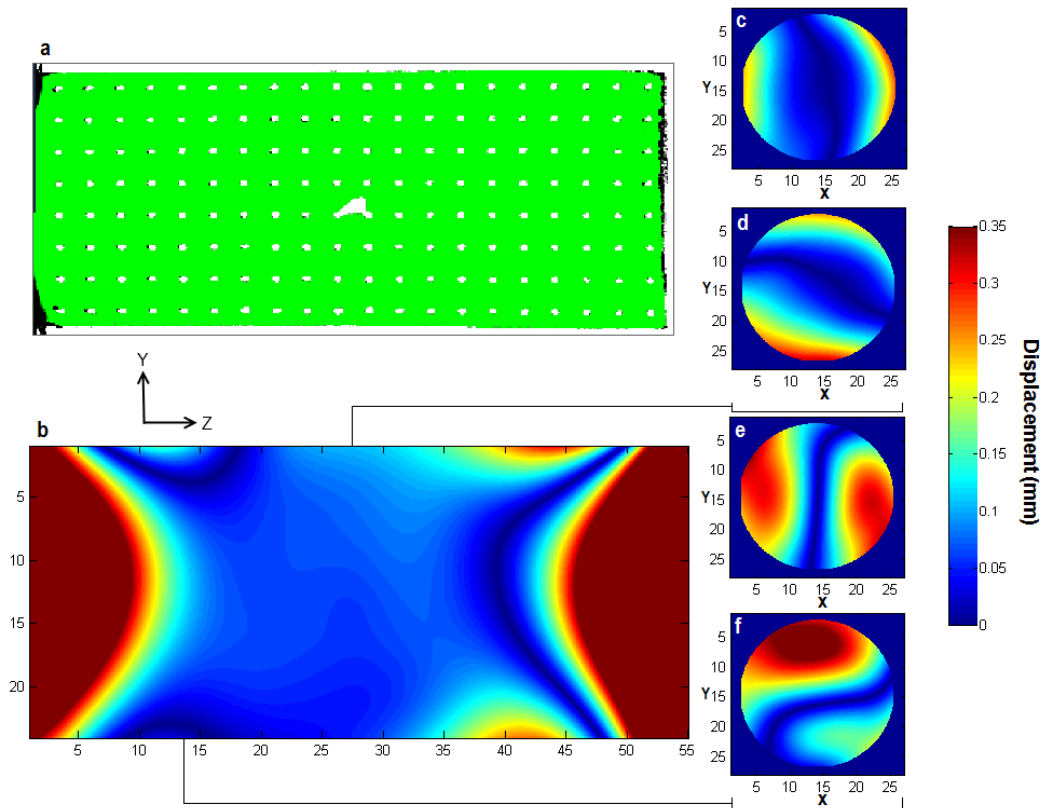
Figure 20.   **Displacement fields generated from post-processing correction**

Projection along the X axis from CT phantom data (white) overlaid on MRI images (filler inside phantom shown in green, phantom structure shown in black) show good alignment after post-processing correction (a). Displacement fields generated from the non-rigid registration show that Z displacements increase along the Z axis (b) as distance from the centre increases. Increased X and Y displacements are observed in the X (c) and Y (d) axes respectively for central slices. Slices taken further from the centre show these displacements in the X (e) and Y (f) directions increase more rapidly with distance from the slice centre.

3.5.4 MRI sequence comparison

Images acquired using the fast spin echo and gradient echo sequences were similar in appearance (Figure 21). Scaling factors calculated using a gradient echo sequence and a fast spin echo sequence showed a percentage difference of 0.06%, 0.02%, and 0.03% in the *X*, *Y*, and *Z* axes respectively. The mean displacement difference taken across the whole grid structure was 19±30 μm.
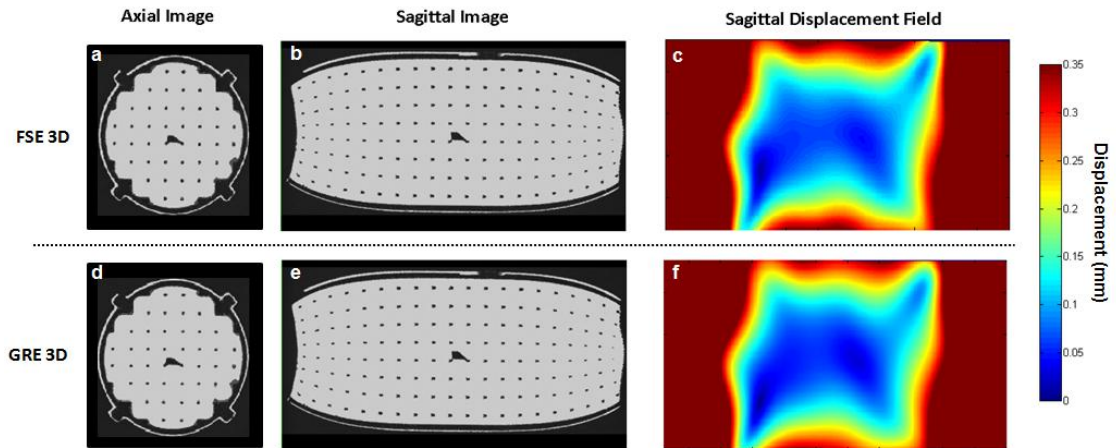
Figure 21.   **Sequence Comparison**

Representative axial and sagittal slices of MRI phantom images acquired using the FSE 3D sequence(a,b) and GRE 3D sequence(d,e). Displacement fields generated for each acquisition were of similar appearance (c,f).

3.5.5 Scaling of Total Brain Volume estimates

Scaling factors calculated for the larger diameter gradient set at the *in-vivo* imaging time point were 93.4%, 95.9%, and 92.1% in the *X,Y*, and *Z* axes respectively. The equivalent measurements for the *ex-vivo* data acquired in the small diameter gradient set were 99.5%, 99.9%, and 100.4% (Figure 22a). The percentage difference in the mean of the axis scaling factors between the small and large diameter sets was -17.4%.

The mean estimated total brain volume for the *in-vivo* samples was 634 mm^3 compared to 484 mm^3 in the *ex-vivo* data. This corresponded to a 30.8% larger mean volume measurement of the brains *in-vivo*. After adjustment of the individual volume measurements, this mean difference was reduced to 8% (Figure 22b).
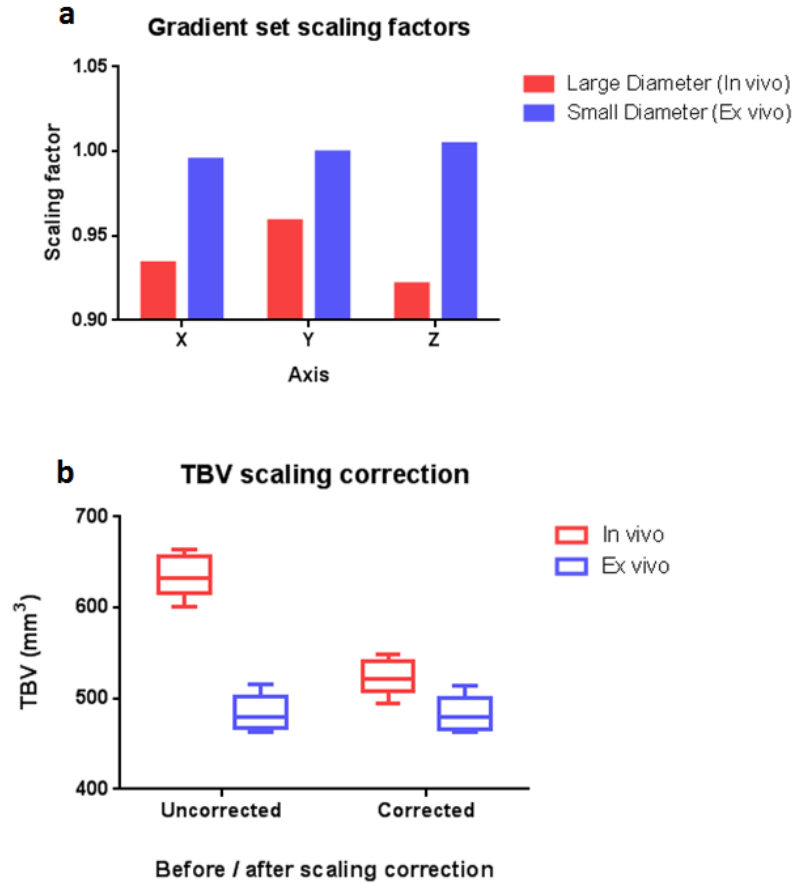
Figure 22.   **Scaling factor adjustments of TBV estimates**

Gradient scaling factors calculated using the system calibration protocol for large diameter and small diameter gradient sets(a) and TBV estimates for *in-vivo* and *ex-vivo* data before and after scaling correction.

3.6 Discussion

The precision and stability of a pre-clinical MRI system are of paramount importance when performing quantitative, comparative and longitudinal measurements in imaging subjects over time. A gradient calibration protocol has been developed, specific to pre-clinical imaging systems, that can quantify and correct for these errors. Moreover, it has been shown that, for the accuracy required for the detection of microscopic changes in tissue structure and size, significant measurement errors can be introduced through imperfect gradients, particularly when relying on calibration protocols with low acceptance limits. Our protocol is based on a 3D-printed geometric phantom, featuring a three-dimensional

grid structure. The plans for the phantom have been published online and can easily be adapted for individual RF coils and scanner bore sizes. The phantom design contains novel features such as an s-bend in the filling pipe to prevent air bubbles in the main cavity, and the ability to attach as a single piece directly to the RF coil to improve consistency in phantom positioning between measurements.

Monitoring of relative gradient scaling factors using MRI data has been reported previously(115). In this study, high-resolution CT and MRI imaging data were used to validate the structural stability of the phantom over time and provided a simple method for the absolute scaling of the system gradients. The ability to reduce errors in scaling values will improve accuracy of measurements acquired on the system and invites the possibility of reuse of control group data reducing animal numbers. A post-processing technique has been introduced for the correction of image distortions caused by gradient non-linearity.

Relative to the scanner manufacturer's standard calibration, the system calibration developed here reduced the mean gradient scaling factor error from 2.7% to 0.3%. Errors of the magnitude found prior to our calibration have the potential to be a significant confounder to detection of structural volume changes in the mouse brain, which can be less than 2% (109).

The calibration requires the acquisition of three-dimensional gradient echo data, and a comparison was made of the accuracy of acquiring at 40 and (more rapid) 100 μm isotropic resolution. There was close agreement between the scaling parameters calculated from gradient echo data acquired at two different resolutions and fast spin echo data, indicating that accurate system calibration can be performed using the gradient echo protocol with reduced scan time for inclusion in a routine QA protocol. Application of such a protocol on pre-clinical systems is clearly important, particularly given the magnitude of gradient errors that resulted from the manufacturer's standard calibration. A 5.3% scaling error was found in the *Y* direction prior to calibration, which, for example, would result in a 9.8% error in apparent diffusion coefficient (ADC) estimates, calculated from DWI data (due to the inverse square relationship between b-value and gradient magnitude). The scaling values, once corrected with our protocol, were stable over the six month period, indicating that it may be satisfactory to carry out as few as two system calibrations per annum.

Previous pre-clinical structural MRI studies have compared volumetric measurements from *in-vivo* and *ex-vivo* data sets (127,128) using multiple hardware configurations. To investigate effects of gradient scaling on TBV estimates, *in-vivo* and *ex-vivo* imaging was performed using different gradient sets for the same cohort of wild-type mice. The mean difference in scaling factor of 17.4% was shown to cause a 22.8% increase in the *in-vivo* volumes measured. After adjustment for scaling discrepancies, the difference in mean volume was reduced to 8% which may be due to dehydration and shrinkage of tissue caused by perfuse fixation for *ex-vivo* imaging(129,130). These results highlight the importance of gradient scaling measurements when comparing data acquired on different systems or hardware configurations.

The post processing correction showed that displacements near to the isocentre of the magnet, following calibration, can be less than 0.1 mm. The deviation from linearity of the small diameter gradient set used was specified by the manufacturer as ≤5% within a central 40 mm DSV region. The linearity, measured as the maximum spatial deviation as a percentage of the 20 mm DSV radius, was found to be within these limits in each axis. However, this tolerance corresponds to a maximum spatial deviation of 1 mm which may not be satisfactory for phenotyping applications and a correction may be required. Outside of this region, image distortion increases rapidly, with displacements of 0.3 mm and larger. With the application of non-rigid registration during post-processing, the dice coefficient improved by 26%. The strong correspondence between the CT data and the corrected MRI indicates that non-rigid registration approach is a robust solution to unwarping data in regions of large distortion.

The use of the generated deformation field may reduce distortions significantly, especially when imaging samples such as multiple embryos or anatomy that is positioned at a distance from the magnet isocentre. Therefore, the post-processing correction for gradient non-linearity can increase the effective FOV over which biological samples can be accurately imaged, markedly increasing the efficiency of high resolution scans that are often acquired overnight. Assuming satisfactory stability of the gradients, the deformation field from a single time point could be used to correct multiple datasets collected over a six month period for animal phenotyping studies (131).

In this study, MRI acquisition parameters were based on an *ex-vivo* murine structural neuroimaging sequence with the aim of correcting this data using the deformation field.

The use of a 3D gradient echo sequence to characterise gradient field distortion is in line with previous clinical studies(110,114,116,132,133) and the agreement of scaling factors calculated from data acquired at two resolutions and using a fast spin echo sequence indicate robustness of the methodology to changes in the read gradient magnitude and MRI sequence. The mean difference in displacements between the gradient echo and fast spin echo data is within a single standard deviation of the reproducibility data mean difference, suggesting that the warping, caused by non-linearity of the gradients, is dominating any sequence specific effects in the scenario investigated.

The deformation field could also be used to unwarp *in-vivo* data sets collected with the same imaging protocol although it should be noted that some variability in the accuracy of spatial displacement may be introduced by sample-dependent B_0 perturbations. These should be minimal in structural imaging and if necessary can be corrected for through the use of existing techniques (134). Minor deviations from the protocol described here may be necessary such as adjustments to the phantom dimensions to fit specific hardware configurations and an alteration of the composition of the phantom filler solution to optimize SNR for the particular pulse sequence used.

3.7 Conclusions

In this chapter, a complete protocol has been presented consisting of a system calibration of MRI gradients and a post-processing correction for non-linearities away from the magnet isocentre. The phantom design is open-source and can be adjusted as necessary for the specific imaging protocol, RF coil and scanner dimensions used. The NiftyReg software used for the system calibration and the post-processing correction is also freely available to download and has been used to perform absolute scaling of gradients and an image correction of distortions caused by gradient non-linearity. This simple step-by-step process can be integrated with or form the basis of a QA protocol that could be implemented during installation and as part of routine maintenance on any pre-clinical MRI system.

4 A Diffusion Tensor Imaging protocol for in-vivo multi-parametric MRI

4.1 Overview

In the previous chapter a gradient calibration protocol was developed to provide quality assurance for MR data acquired using the 9.4T MR system in CABI for the *in-vivo* measurement of phenotypic changes in mouse models of AD. The effects of gradient inaccuracies on MR measurements of anatomical volume and diffusion in tissue were discussed. Diffusion Tensor Imaging is an MRI technique sensitive to the diffusion of water molecules from which the microstructural organisation of tissue can be inferred. Changes to the diffusion environment may be indicative of white matter pathology, known to occur in neurodegenerative diseases.

In this chapter, a time efficient DTI acquisition is developed with the aim of inclusion in a multi-parametric protocol. The design and testing of this sequence is described and data is acquired *in-vivo* in the rTg4510 mouse model of tau pathology in AD. DTI parameter measurements in both grey matter and white matter regions of the rTg4510 are presented and compared to those of wild-type controls. Differences identified indicate the sensitivity of this DTI protocol to tau pathology and support its value within a multi-parametric MRI protocol to study mouse models of AD *in-vivo*.

4.2 Background

4.2.1 White matter pathology in AD

The tissue of the nervous system consists of regions of grey matter and white matter named for the colour exhibited by their parenchymal make up. Neuronal cell bodies (Figure 23c) in grey matter perform integrative functions or act as relays at junctions between synapses of axons and neighbouring cell bodies. The white matter is a network of myelinated axons grouped into bundles called tracts that enable communication across the central nervous system through the propagation of electrical signals known as action

potentials. Myelin sheaths wrap around the axons of neurons and are made up of membrane layers rich in phospholipids that are white in colour. They provide a layer of electrical insulation that increases the speed of transmission of action potentials. The millions of white matter tracts connect neurons across the nervous system to form a functional network. In the human brain, white matter lies centrally, beneath a layer of grey matter on the surface known as the cortex (Figure 23b).
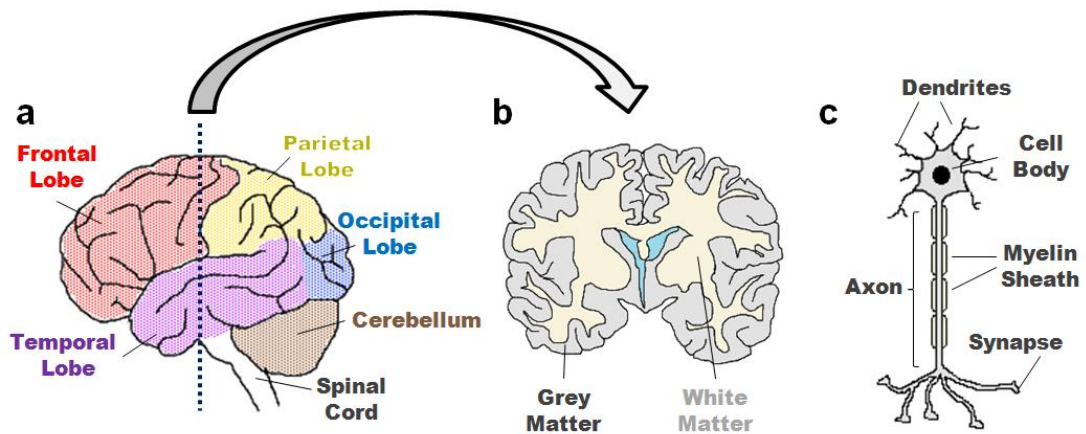
Figure 23.   **Anatomy of the human brain**

Schematics of the human brain with key parts labeled(a) , a coronal slice with grey matter and white matter regions indicated(b), and neuronal cell features depicted(c).

Damage to white matter that reduces nerve conduction will impact the ability and speed at which different parts of the brain communicate with each other, impairing sensory, motor and cognitive functions(135). Although AD is defined by the presence of Aβ and NFT pathology in grey matter regions, there is growing interest in white matter disease(WMD) which has been observed at neuropathological examination in over 50% of AD cases(136). Numerous white matter changes in AD have been reported in post mortem studies including decreased myelin density(136), decreased myelin basic protein(137), loss of oligodendrocytes(138), activation of microglia(139), ventricular ependyma and gliosis, and loss of myelinated axons(140). WMD in AD is mild and distributed throughout the brain, with the frontal lobes (Figure 23a) thought to be more severely affected(136). This presentation is unlike other AD-vascular type dementias where focal infarcts occur(141). It is currently unknown whether WMD is a direct result of protein misfolding and aggregation in AD or whether it is a secondary effect following connected regions of grey matter degeneration. The former scenario is described by 'Retrogenesis', a theory which

hypothesizes that white matter regions that myelinate later in development are the first to be affected by AD(142,143). The axons of these tracts have a smaller diameter and less oligodendrocytes associated with them when compared to earlier myelinating regions. In supporting a larger population of axons, a greater metabolic challenge may be placed on the oligodendrocytes making them more vulnerable to pathological processes(144). Alternatively, the white matter changes observed could be as a direct consequence of adjacent grey matter pathology, a process known as Wallerian Degeneration(145). The non invasive nature of DTI offers the possibility to spatially map sequential white matter changes in the AD brain over time and may provide insight into the primary cause of white matter disease.

4.2.2 DTI of white matter disease

The directional arrangement of hydrophobic myelin in the white matter of the brain is reflected by a highly anisotropic diffusion environment. Water molecules diffusing in this tissue will find their motion restricted by boundaries created by the walls of the myelin sheaths of axons aligned parallel to the orientation of the tract. Bulk diffusion over time will be reduced in directions perpendicular to tracts of densely packed fibres since spins will be impeded by these boundaries and will undergo a rather tortuous diffusion trajectory. The relative diffusion along the direction of the tract will be much larger due to the reduced obstructions encountered.

The ability of DTI to provide a multi-directional quantification of diffusion in three dimensions lends itself to the measurement of anisotropic diffusion in white matter. Values of Fractional Anisotropy(FA) and Mean Diffusivity (MD) calculated from the tensor can quantify the extent of anisotropy of diffusion and provide a measure of bulk diffusion in a voxel respectively. In the case of white matter voxels, the ellipsoid described by the tensor will have much greater diffusivity in the direction of the fibre tract - described by Axial Diffusivity(DA), than in the two directions perpendicular to it – described by Radial Diffusivity(DR)(146). By mapping these parameters, regional measurements can be taken in specific tracts of interest or fibre pathways can be traced using tractography image processing techniques(147).

As AD progresses, NFT pathology spreads sequentially to different grey matter regions of the brain as defined by Braak staging(11). Initially presenting in the transentorhinal region

of the temporal lobe including the entorhinal cortex and hippocampus, NFTs then become more widespread throughout the temporal lobe before severely affecting all neocortical association areas later in disease(11). Atrophy of grey matter in the hippocampus has also been shown to correlate with this time course of distribution of NFT pathology(37,148,149). The use of DTI to probe white matter tracts associated with regions implicated in these stages of disease may offer new insights into the link between neurodegeneration and WMD in AD.

In a study by Huang et al(150) reductions in FA and altered diffusivity relative to healthy controls were observed to be greatest in AD patients in the temporal lobe followed by lesser changes in the parietal and frontal lobes following a regional pattern that parallels NFT pathology. Furthermore, there was reduced DA and increased DR in the temporal white matter in patients with AD compared to reduced DA only in MCI cases. This was attributed to early axonal damage in MCI and a complete loss of myelinated axons in AD. The authors concluded that the white matter changes are most likely secondary, following perikaryal degeneration, consistent with wallarian degeneration. This hypothesis has been supported by other studies performing similar regional measurements (151,152) and correlating white matter damage measured by DTI with cognitive function(153,154).

The retrogenesis hypothesis suggests WMD is a primary effect that occurs due to the formation of plaques and tangles in tissue and to explore this possibility, DTI comparisons have been made between early and late myelinating fibre tracts during initial stages of AD. Studies supporting retrogenesis have reported lower FA values in late-myelinating pathways (uncinate fasciculus, ILF, SLF), limbic pathways (fornix/stria terminalus, cingulum), and commissural pathways (splenium of the corpus callosum, forceps major) with no significant differences identified for early-myelinating regions included in these studies(155,156). The anterior part(genu) of the corpus callosum myelinates later in life relative to the posterior part (splenium)(142) and studies have made comparisons between DTI measurements in these two structures. Although reduced FA in the splenium appears to be more prominent in AD(157), reductions in the genu have been reported in MCI patients(158,159) indicating sensitivity to changes in this prodromal stage of the disease. These findings suggest an increased vulnerability of later myelinating regions to AD. However, connections from these white matter structures to other parts of the brain, such

as those between the splenium and the temporal lobe(157,160) may mean that results are confounded by wallerian degeneration.

4.2.3 Potential of DTI as a disease biomarker

The utility of DTI as a tool to interpret the order in which WMD and neurodegeneration occur is challenging due to the difficulty in interpreting DTI parameters, conflicting results between studies, and the possibility of combined effects from multiple causes such as ischemic mechanisms, cerebrovascular disease and reactive gliosis(150). Through the consensus of a number of studies there is a growing body of evidence of widespread increased MD and reduced FA in AD brain(144,161,162). These differences have been observed in various white matter regions, using a number of acquisition protocols and analyses including ROI based, voxel-wise, and tract based. Changes in diffusivity have also been consistently observed in AD with increased DR thought to represent myelin damage that increases with disease progression and DA as a measure of axonal integrity, more sensitive to early disease(150). Correlation between DTI changes in white matter with both grey matter volume changes(163) and cognitive performances further support these parameters as indicators of disease progression(153,154).

Sensitivity to early disease has been assessed through DTI studies in MCI cohorts as well as cases of increased risk factor of AD including carriers of APOEe4 and parental family history. Patients diagnosed with MCI are considered to be in the prodomal phase of AD with increased risk of conversion. Changes in MD and FA are remarkably similar to those observed in AD patients although less widespread(161). DA has been suggested as a particularly sensitive marker to WMD in MCI(161) and that DTI measurements in the fornix may be as useful as hippocampal volume(164,165) as a biomarker in conversion of MCI to AD. In cohorts with an elevated risk factor of AD, reductions in FA in a number of white matter regions associated with AD have been observed in APOE e4 and subjects with a family history of late onset AD(166-168).

It should be noted that there are a number of studies that report a lack of group differences in AD and MCI compared to healthy controls(162). The source of these discrepancies are unclear with inconsistency in disease stage, low statistical power from small cohorts, and the variety of methods of data acquisition and analysis possible reasons.

The use of mouse models that mimic WMD found in AD may prove useful in controlling for some of these variables. The ability to image large numbers of subjects and generate corresponding histology to analyse microstructural changes and quantify pathological burden may provide crucial insights into how to best optimise DTI protocols for AD biomarker applications.

In comparison to white matter, DTI of grey matter is less commonly the subject of studies in AD literature. Often only MD measures are reported due to the lack of anisotropy in the tissue. An elevated MD has been reported in grey matter regions(169-171) as well as reduced FA in the hippocampus(171) and the thalamus(169).

4.2.4 DTI in mouse models

There may be multiple potential permutations of structural rearrangements in the tissue that give rise to a particular DTI contrast. The lack of specificity makes it difficult to attribute a known abnormality to an observed change in a parameter. MRI diffusion measurements in white matter originate from water molecules both within the axon and in the extracellular axonal spaces. There are multiple intra-axonal structures that may influence diffusion within this compartment. Both the axonal membrane and myelin sheath surrounding it act as barriers to diffusion, damage to which will cause changes to both intra and extra cellular diffusion environments(172). Alterations to any of these structures in pathology may occur in combination with unpredictable effects on diffusion. To be able to use DTI parameters as markers of specific microstructural alterations, their relationships to the biology must be fully understood.

DTI studies of mouse models that exhibit specific types of white matter abnormality may help to inform on root cause of signal changes. A number of studies have tried to draw parallels between diffusivity parameters and histology in simple models of white matter pathology. Studies in the shiverer mouse model of dysmyelination(98) and of demyelination using cuprizone treatment(173) suggest that reductions in myelination of the corpus callosum increase DR. In more subtle white matter pathology induced by hypoperfusion, mice exhibited a lower FA in the corpus callosum that correlated with measures of reduced myelin integrity(174). In some rodent models of axonal degeneration and injury, reduced DA has been observed in affected white matter regions(175,176). In

other studies including more complex models, these findings have not been replicated(177,178) highlighting the need for further investigation of these relationships.

Mouse models may also be used to better understand the relationship between DTI parameters and disease. The careful breeding and housing of transgenic mouse models of AD may reduce group variability through the control of external factors such as diet and exercise that can affect human studies. Histological analysis can be used to identify the physical tissue changes driving diffusion measurements and to draw correlations between DTI indices and presence of known pathologies in AD. The expedient progression of pathology in models allows rapid longitudinal studies of DTI measurements in early and late stages of pathology. Characterisation of the chronological order of myelination of white matter regions(179) will allow the testing of experimental paradigms to evaluate retrogenesis and wallerian degeneration hypotheses.

A number of studies have focussed on beta-amyloid models of AD with varying characteristic levels of pathological burden. Invariably, differences have been reported compared to wild-type controls but the nature of the changes in DTI parameters varies between studies. In the corpus callosum, both reductions(81,82) and increases in anisotropy(180) have been observed at late time points after the appearance of amyloid plaques. Likewise, grey matter FA increases(180) and decreases(181) have been reported for transgenic groups. Inconsistencies may be due to variations in mouse models, DTI protocols, ROIs, and image analysis methods between studies and without strong correlations with histology, the cause of differences is speculative.

4.3 Development of a time-efficient DTI protocol

4.3.1 Introduction and aims

The *in-vivo* imaging time for a mouse that is anaesthetised and then recovered is limited to protect for the toxic effects of prolonged anaesthesia. In the case of the phenotyping project licence (Phenotyping Transgenic Mice licence (PPL: 70/7474)) awarded to CABI by the UK Home Office, a maximum of 3 hours is specified. The aim of this work was to develop a methodological protocol for the acquisition of DTI data in the mouse brain at a

suitable resolution with sufficient SNR, which runs within an allocated portion of the total imaging time(3 hrs). As part of a multi-parametric MRI protocol that included 3D structural, ASL, and CEST, it was required that acquisition took no longer than 45 minutes.

To resolve white matter structures in the murine brain, a minimum in plane resolution of $200\mu m^2$ is required(182). When compared to human imaging, this high resolution requirement counteracts the SNR gain of the high field strength in dedicated small animal MRI scanners. Furthermore, the combined lengthening of T1 and shortening of T2 times at high field further reduce the amount of signal available for a given DTI scan time(182). *Ex-vivo* imaging offers a less time restricted alternative, however measurements may not represent *in-vivo* diffusion accurately due to the tissue fixation process required for *ex-vivo* sample preparation. Spin echo sequences have been used previously to measure diffusion in white matter of the mouse (183-185). The relatively long scan times of these protocols prohibit their use in this particular application where it is necessary to employ a rapid acquisition technique. Recently, multi-shot DW SE-EPI sequences have shown potential to provide high quality DTI data sets at high field with reduced imaging times (186,187).

Single shot spin echo EPI sequences allow very fast acquisition of images after a single excitation making them robust to motion artifacts relative to multi shot acquisitions. However, the signal decays with T2* dependence during the image readout and is highly sensitive to B_0 field inhomogeneities which can lead to distortion and signal loss at long TEs. In the brain, these are caused by discontinuities in bulk magnetic susceptibility at tissue boundaries where local magnetic field gradients are generated. Due to its size (and thus relatively high surface area to volume ratio), these effects make imaging in the mouse brain with EPI particularly challenging. Imaging at high field is favoured to capitalise on SNR increases, however susceptibility effects are worse(188). Compared to human brains, the mouse brain has a much larger surface to volume ratio meaning susceptibility effects in images spread to a larger proportion of the brain(189). There is also significant demand placed on the gradient hardware in the presence of a rapidly decaying signal, where high slew rates will be necessary to meet the resolution requirements.

As described in section 2.6.2, the distortion and signal loss caused by off resonances effects can be reduced by decreasing the number of PE steps per excitation required to traverse k-space in the PE direction. In a multi-shot acquisition, data acquired over multiple excitations are combined (commonly in a mesh pattern) to fill the whole of k-space in the

PE direction. This EPI technique places less stress on the gradient hardware whilst offering higher achievable resolution and reduced effects of field inhomogeneities and T2* decay. A multiple shot approach does necessitate acquiring data over multiple TRs which incur a penalty of increased scan time compared to the single shot method and motion between shots can introduce artifacts into the images.

In this section, a multi-shot DW SE-EPI sequence is optimised at 9.4T for the investigation of white matter changes in mouse models of AD as part of a multi-parametric MRI protocol. Steps taken to mitigate effects of common artifacts in multi-shot EPI sequences are described and the rationale behind choices of diffusion weighting parameters discussed. Preliminary *in-vivo* data is acquired and the accuracy of DTI measurements is evaluated through comparison to those reported in the literature.

4.3.2 Methods

4.3.2.1 DW SE-EPI protocol description

A four shot EPI sequence was developed for *in-vivo* imaging of the mouse brain based on a previously published protocol(187). Multi-shot EPI sequences are vulnerable to bulk motion. To prevent introduction of artifacts due to motion, the head of the anaesthetized mouse must be immobilized during imaging. This is usually achieved by securing the teeth of the animal using a bite bar and the use of ear bars to clamp a caudal section of the cranium. This method is very effective but was not compatible with the mouse bed and coil setup used in these experiments. A 72 mm inner diameter volume coil (Rapid Biomedical) was used for RF transmission and signal was received using a 4 channel array head coil (Rapid Biomedical). When the four channel array was attached to the mouse bed, a standard ear bar setup was not possible due to space restrictions, leaving only the bite bar and nose cone to secure the head. A nose cone attachment with arms that protruded outwards towards the caudal end of the mouse's head was designed and 3D printed by collaborators (Figure 24). Adjustable ear bars were inserted through holes drilled in the arms to secure the head from the sides. The polyamide (PA2200) material used for 3D printing is flexible and the dimensions of the head holder were such that they would flex inwards as the upper RF coils were secured adding further pressure.
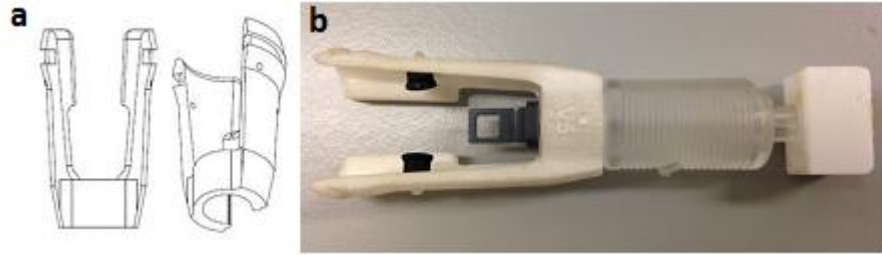
Figure 24.   Images of mouse head holder

CAD drawing of mouse head holder (a) and attached to nose cone with ear bars inserted (b).

It may not be possible to remove effects of respiratory motion through immobilization of the head and in this scenario, gating has been used previously to provide further improvements (190,191). Respiratory gating was added to a four shot EPI sequence to prevent acquisition during breaths. I achieved this by configuring the respiratory measurement equipment and by modifying the core EPI sequence code in VNMRJ. A respiratory pad (SA instruments) was used to monitor breathing of the animal and a gating output from the vendor software was read by the MR sequence prior to implementing each shot. The gate was configured to open between resps after a delay equal to 10% of the previous inter-resp period (Figure 25). It closed again after a time that was equal to 50% of the previous inter-resp period. The EPI pulse sequence code was amended to read the gate output at the start of each shot. If open, the sequence was played out and data acquired. If the start of the shot occurred during respiration, indicated by a closed gate, data was not acquired but all RF pulses and gradients would be played out as normal to retain the steady state of the MR signal with respect to T1 and T2* relaxation. Acquisition of the next shot would then occur at the next open gate reading.
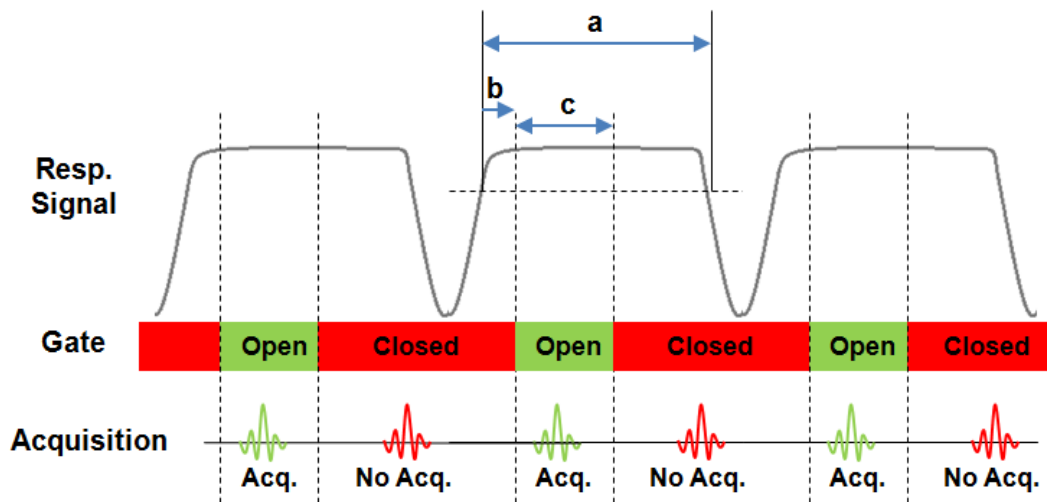
Figure 25. **Respiratory gating for EPI sequence**

SA instruments software detects an inter resp. period based on the gradient of the respiration signal(a). The gate is opened after a 10% inter-resp. period delay (b). The gate closes again after a further 50% of the inter-resp. period(c). Where the start of the pulse sequence for an EPI shot occurs while the gate is open, the echo is acquired. If the gate is closed, the echo is not acquired.

In acquiring each shot in an EPI sequence, gradients of alternating polarity are acquired to continually refocus the signal(Figure 10, section 2.6.1). Alterations to desired application of imaging gradients from sources such as eddy currents can cause a mismatch in adjacent lines of k-space. These may cause faint artifacts in the resulting images known as N/2 ghosts (section 2.6.2). To reduce these artifacts, timing delays were added to the pulse sequence to centre echoes in the acquisition window and calibration scans were acquired. Full triple reference scans were acquired prior to the EPI acquisition. These include a scan without phase encoding, one with inverted readout polarity and no phase encoding, and a scan with inverted readout polarity and phase encoding. To apply corrections using the reference scans, the phase of scans collected without phase encoding is negated and multiplied at each pixel with the phase encoded scans acquired with the corresponding gradient polarity. The two sets of modified phase encoded images are then summed at each pixel to give the final complex image.

To ensure sufficient directional diffusion sampling, gradients were applied in thirty directions (Table 1) spread equidistantly over a sphere using a Jones30 scheme(192). This scheme has been shown to produce low and rotationally invariant noise in FA estimates (193) required for robust estimation of tensor orientation and anisotropy at a b-value of

90

1000 s/mm^2 (194). Collecting diffusion data in a high number of directions limited the

acquisition to a single b-value due to time constraints. Previous studies have indicated a

difference in the optimal DTI b-value depending on diffusion environment in the tissue. In

estimating a single tensor in isotropic brain parenchyma, this has been found to be

approximately 1200 s/mm^2 (192).   When anticipating more anisotropic media such as

white matter tracts, a lower b-value has been suggested to be approximately 900 s/mm^2

(195). The final b-value after sequence optimization was 1050 s/mm^2 which falls between

the isotropic and anisotropic values indicated by the literature and is similar to that used in

previous studies *in-vivo* in the mouse(185,187). A single unweighted image was acquired

prior to collection of diffusion weighted images. To increase SNR, five signal averages were

collected for each image to give a scan time of 42 minutes and 41 seconds.

Order	Read	Phase	Slice
1	0	0	0
2	1	0	0
3	0.166	0.986	0
4	-0.11	0.664	0.74
5	0.901	-0.419	-0.11
6	-0.169	-0.601	0.781
7	-0.815	-0.386	0.433
8	0.656	0.366	0.66
9	0.582	0.8	0.143
10	0.9	0.259	0.35
11	0.693	-0.698	0.178
12	0.357	-0.924	-0.14
13	0.543	-0.488	-0.683
14	-0.525	-0.396	0.753
15	-0.639	0.689	0.341
16	-0.33	-0.013	-0.944
17	-0.524	-0.783	0.335
18	0.609	-0.065	-0.791
19	0.22	-0.233	-0.947
20	-0.004	-0.91	-0.415
21	-0.511	0.627	-0.589
22	0.414	0.737	0.535
23	-0.679	0.139	-0.721
24	0.884	-0.296	0.362
25	0.262	0.432	0.863
26	0.088	0.185	-0.979
27	0.294	-0.907	0.302
28	0.887	-0.089	-0.453
29	0.257	-0.443	0.859
30	0.086	0.867	-0.491
31	0.863	0.504	-0.025

Table 1.   Diffusion gradient directions

Unit vector directions for diffusion weighted gradients and the order they were applied in
the DW SE-EPI sequence.

In order to analyse the data, I wrote software in Matlab to construct tensors at each voxel using a least squares fit method.(196). Firstly, a gradient encoding matrix, g, is formed using the gradient unit vectors in Table 1. A b vector, b, is calculated using the acquired imaging data and the scalar b value using the equation(196)

$$b = \frac{-log_e.(\frac{I_{dw}}{I_{B0}})}{b}$$

Where I_{dw} is the intensity in the diffusion weighted images, I_{B0} is the intensity in the *b=0* images, and *b* is the scalar b-value. Once b has been calculated, it can be used with the gradient encoding matrix to solve the linear equation(196)

$$gx = b$$

to give x, which can be rearranged form the diffusion tensor matrix at each voxel. A least squares fit in matlab was used to solve the linear equation followed by an eigen decomposition of the diffusion tensor matrix. Eigen values were used to calculate MD, FA and radial and axial diffusivity following standard methods(98,197). Anatomical structures were delineated manually in the parameter maps produced to provide mean ROI estimates.

4.3.2.2 Protocol evaluation in a diffusion phantom

n-dodecane is a liquid alkane that has previously been identified as suitable for measuring the accuracy of DTI sequences(198). It has a well defined diffusion coefficient over a range of temperatures that can be used to test the accuracy of measurements using DTI. At room temperature, it is within the range of ADC values (0.5 x10^{-3}mm^2/s to 0.8 x10^{-3}mm^2/s) measured *in-vivo* in the corpus callosum of the developing mouse(185) and T1 and T2 values are close to those of human white matter.

A cylindrical diffusion phantom was constructed using 3 ml of Dodecane (Sigma-aldrich, UK) in a 5ml plastic syringe. It was imaged at 9.4T in a 26mm diameter birdcage RF coil used for signal transmission and reception. A temperature probe was attached to the outer surface of the phantom to monitor temperature during experiments (SA instruments). Images were acquired using the DW SE-EPI protocol described previously in a central region of the

phantom. A ROI was drawn in the centre of the phantom across all 16 slices (20 x 20 x 16 voxels) and the mean and standard deviation of the MD values was calculated to assess the accuracy of estimates, given the known diffusion coefficient of the phantom.

Misalignments of adjacent echoes in k-space caused by eddy currents can cause both distortions and translations in images. In DTI sequences, these effects may vary with the direction in which the diffusion weighting gradients are applied. The presence of these artifacts were investigated by applying the DW- SE-EPI protocol in the central slices of the dodecane phantom. The diffusion weighted image acquired first in the sequence was then subtracted from all other images to provide a set of difference images. The presence of spatial shifts or distortion should be visible by prominent intensity changes along the edges of the phantom.

4.3.2.3 Protocol evaluation *in-vivo*

All of the *in-vivo* imaging in the protocol evaluation was performed using C57BL/6 mice with a 9.4 T VNMRS horizontal bore scanner (Agilent Inc.). A 72 mm inner diameter volume coil (Rapid Biomedical) was used for RF transmission and signal was received using a 4 channel array head coil (Rapid Biomedical). Mice were anaesthetised under 2% isoflurane and positioned in a MRI compatible head holder to minimise motion artifacts. Anaesthesia was then maintained at 1.5% isoflurane in 100% O2 throughout imaging. Core temperature and respiration were monitored using a rectal probe and pressure pad (SA instruments). Mice were maintained at ~ 37 °C using heated water tubing and a warm air blower with a feedback system (SA instruments).

A four shot Spin Echo EPI sequence was used to acquire sixteen slices. The olfactory bulbs were used as an anatomical landmark to maintain consistency in slice positioning between animals(Figure 26). The FOV was 20×20 mm with a matrix size of 100×100 and a slice thickness of 0.5 mm. Diffusion gradients were applied in thirty directions with the following parameters G = 0.25 T/m, Δ = 9.3 ms, δ = 5.5 ms, and b = 1050 s/mm^2 to generate 30 diffusion weighted images in addition to a single unweighted b=0 image. Acquisition of 5 averages with a TR of 2000 ms and TE of 24 ms gave a total imaging time of 43 min.
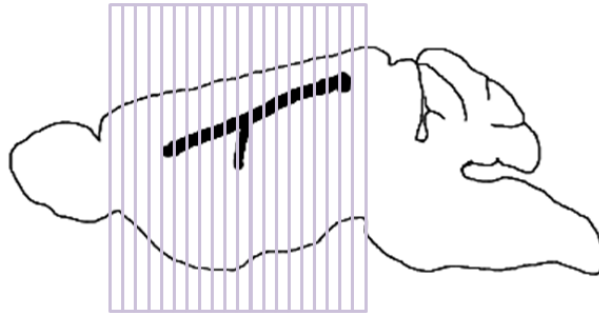
Figure 26. **Slice positioning for DW SE-EPI protocol**

Sagittal view of a mouse brain images with positioning of sixteen imaging slices overlaid. The junction between the olfactory bulbs and cortex was used as an anatomical landmark for the most rostral slice.

A single mouse was imaged to investigate the sensitivity of the DTI sequence to chemical shift and motion artifacts. Due to the low bandwidth in the phase encode direction, EPI sequences are highly susceptible to chemical shift artifacts(199). A frequency selective RF pulse was used to saturate the signal from fat to mitigate artifacts. The pulse was Gaussian shaped, non slice selective, and centred at 3.3ppm, the chemical shift of fat relative to water. Images were also collected *in-vivo* (n=1), without the saturation pulse to investigate the severity of chemical shift artifacts. An unweighted, single shot EPI image was acquired at the same resolution in a comparable imaging time (TR=8000ms, TE=24ms) to the multi shot sequence to compare distortion artifacts. Data was also acquired using the multi shot sequence to test the efficacy of the respiratory gating added to the sequence and customised head holder to reduce motion artifacts.

To investigate the accuracy of the DTI protocol *in-vivo*, data was acquired(n=1) and compared to previously published values for C57BL/6 mice during early development (P15 to P45)(185). The animal was imaged and DTI parameters were calculated using the protocol described earlier. To compare FA and MD measurements, mean values in ROIs in three regions were measured (Figure 27). A white matter region in the corpus callosum and a grey matter regions in the caudate putamen and in the somatosensory section of the cortex were manually segmented in three slices to replicate the ROIs in the previous study. Low SNR has been shown to reduce both precision and accuracy of DTI-based contrasts in FA(200). SNR calculations were made using the cortical ROI (Figure 27) by dividing the

94

mean signal intensity by the standard deviation of the signal measured in the four corners of the image.
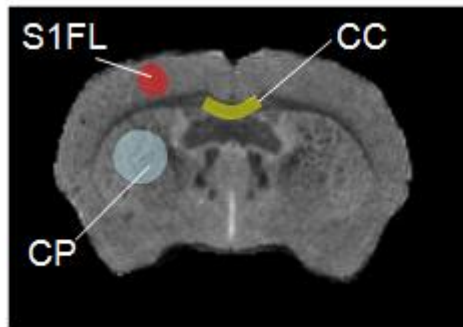
Figure 27.   ROIs for study comparison

ROIs in the corpus callosum (CC), the forelimb region of the somatosensory cortex (S1FL), and the Caudate Putamen(CP) are shown for calculation of mean diffusion parameter estimates and SNR (corpus callosum and cortex only).

4.3.3 Results

4.3.3.1 Protocol evaluation in a diffusion phantom

A dodecane diffusion phantom was used to investigate the accuracy of ADC estimates using the DW SE-EPI protocol as well as potential issues of echo misalignment. The mean and standard deviation of MD measurements at a b-value of 1050 s/mm^2 was 0.743±0.043 x10^{-3}mm^2/s. The measured temperature of the phantom during imaging was 18.5±0.3^{0}C. At this temperature, the MD was within the range of specified diffusion coefficient values previously published (0.708 x10^{-3}mm^2/s and 0.788 x10^{-3}mm^2/s measured at 15^{0}C and 20^{0}C respectively)(198).

Difference images were generated by subtracting the first diffusion weighted image from the other diffusion weighted images. In the case of eddy current induced distortion, it would be expected that visible differences would be observed at the periphery of the phantom. The signal magnitude observed in the difference images was very low compared to that in the raw diffusion weighted image (Figure 28). This is expected in such a phantom where diffusion should be isotropic and therefore attenuation of the signal should be equal in all weighting directions. Furthermore, the lack of noticeable signal at the edge of the

images of the phantom images indicate a lack of direction dependent distortion or translation of signal as might be produced in the presence of eddy currents in the gradient coils.

Figure 28.   Dodecane diffusion weighted difference images

The first DW images from a central slice of the phantom followed by difference images generated by subtracting this image from the twenty nine subsequent DW images. The DW value differences are very small compared to the DW signal magnitude and the lack of large differences around the periphery of phantom suggest the eddy current distortions are minimal.

The use of calibration scans can reduce the appearance of N/2 ghosting with the disadvantage of increasing scan time to acquire the extra data. Images of the dodecane phantom were acquired with and without a full triple reference scan (Figure 29). Ghosting was observed in the images acquired without a reference that disappeared when the full triple calibration scan was added to the sequence.
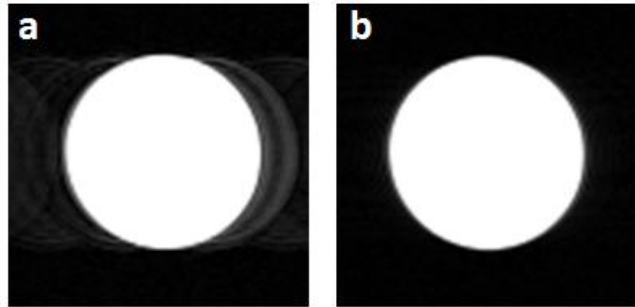
Figure 29.　　　**Effect of reference scan on EPI images**

SE-EPI images of n-dodecane phantom acquired with no reference scan (a) and with a full triple reference scan (b). Intensities were windowed [0 10000]. Ghosting is visible in the image acquired without the full triple reference scan.

4.3.3.2 Protocol evaluation *in-vivo*

EPI images were acquired *in-vivo* in a mouse to assess chemical shift artifacts and differences in distortion between single shot and multi shot images. Chemical shift artifacts were found to be present in the multi-shot EPI acquisitions (Figure 30a). These were markedly reduced by the addition of a fat saturation RF pulse (Figure 30b). Significant distortion in the phase encode direction was observed in images acquired using a single shot EPI sequence (Figure 30c). Mislocalisation of the MR signal resulted in a smearing across the image and a loss of contrast that is particularly apparent at the edges of the brain.
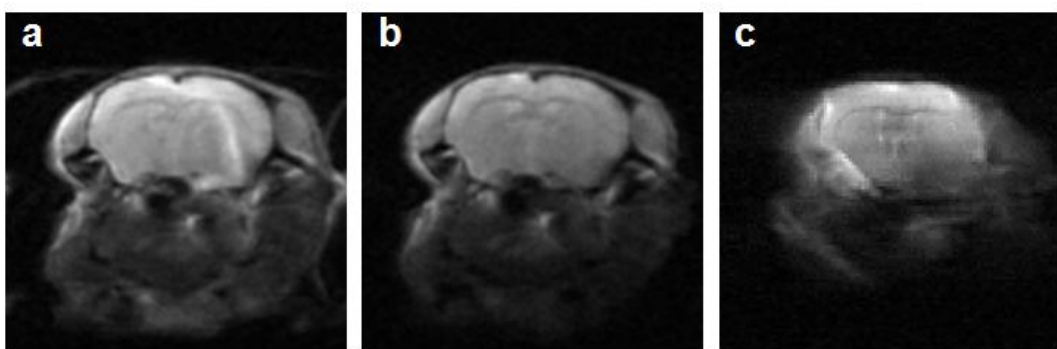
Figure 30.　　　**Multi-shot EPI with RF fat saturation**

Single image slice for four shot EPI acquisition, chemical shift artifacts are observed(a) that are removed by the addition of a fat saturation pre-excitation RF pulse(b). The single shot EPI acquisition(c) exhibits significant mislocalisation of signal in the phase encode direction (L to R).

97

Motion artifacts were evident in the multi-shot EPI images in the phase encode direction using only the manufacturer supplied nose cone to secure the mouse head(Figure 31a). Ghosting was most apparent in the diffusion weighted images(Figure 31a) which is likely to be due to the lower SNR and greater susceptibility to motion introduced by the diffusion gradients compared to the unweighted images. Marked improvements were observed in the images when respiratory gating was added to the EPI acquisition (Figure 31b) indicating that some of the motion was due to the breathing of the animal. A small time increase of a few minutes was caused by the necessity to repeat EPI shots that occurred during respiration. When using the head holder designed to immobilise the animals head, motion artifacts in images were further reduced without respiratory gating (Figure 31c).
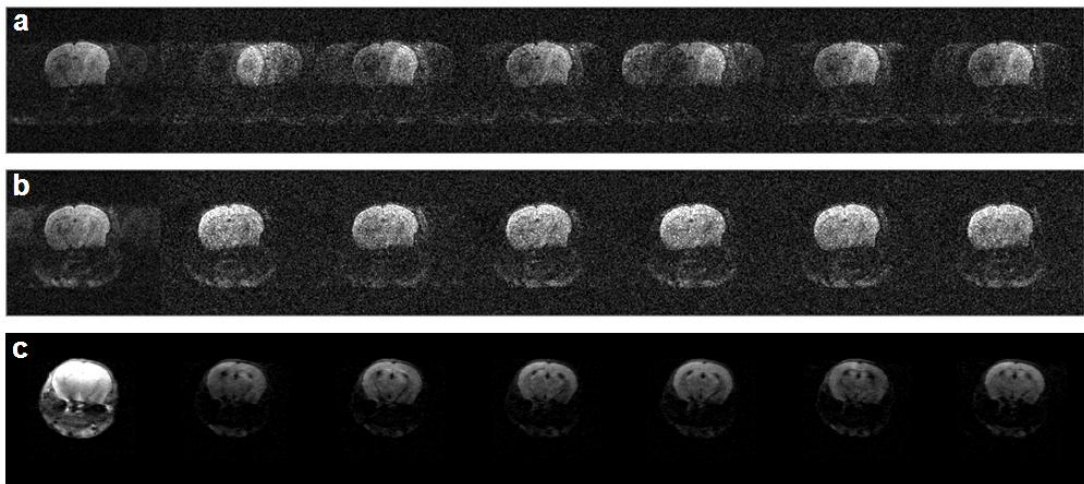
Figure 31.   **Respiratory motion artifacts in EPI images**

Single slice b=0 images and six diffusion weighted images acquired without (a) and with(b) respiratory gating(NSA=1)(without custom head holder). Artifacts were found to be reduced using the custom head holder with no respiratory gating(c) (NSA=5).

A single wild-type mouse was imaged *in-vivo* using the optimised DW SE-EPI protocol to compare SNR, and MD and FA in with previously published values in selected ROIs(185). Sixteen coronal images were generated for a single unweighted b=0 image, followed by thirty diffusion weighted images with gradients applied following a Jones30 scheme. Images were observed to be free from distortion and motion artifacts (Figure 32).
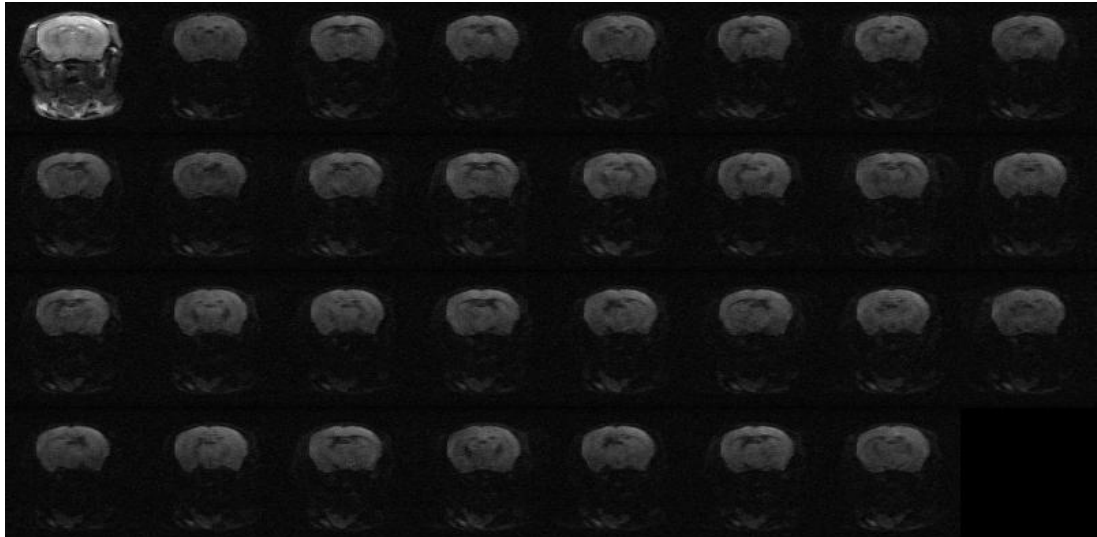
Figure 32. **DW SE-EPI in-vivo images**

Representative b=0 and thirty diffusion weighted images for a single coronal slice acquired in a wild-type mouse.

DTI parameter maps were generated from tensor calculations at each voxel in the images (Figure 33). It was observed, as expected, that MD values were greater in the CSF filled ventricular regions. White matter regions are clearly visible as areas of increased FA and DA and reduced DR in comparison to surrounding grey matter regions.
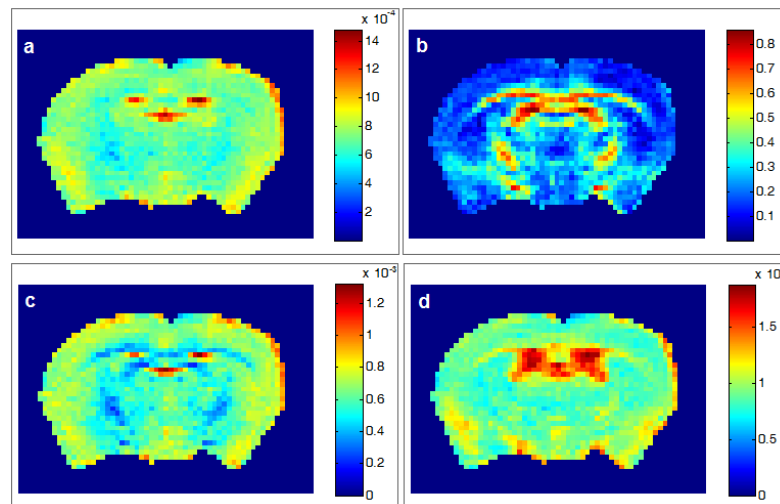
Figure 33. **DTI parameter maps**

Maps of MD (a), FA(b), DR(c), and DA(d) acquired *in-vivo* in the mouse brain (Diffusivity values given in mm^2/s). Increased MD can be observed in the ventricles(a) and white matter regions display increased FA(b) and reduced DR(c).

The SNR value calculated in the cortex of the b=0 images was 55 in the cortex. This equates to an SNR of 35 dB which is less than the value of 46 dB measured in the somatosensory cortex by Chahboune et al(185) which is likely due to differences in the imaging parameters used. In the diffusion weighted images, the mean SNR measured across all thirty diffusion weighting gradient directions in the cortex was 24.2±1.5.

The FA and MD measured in the corpus callosum ROI were 0.53±0.07 and 0.75± 0.11 x10^{-3}mm^{2}/s respectively. These estimates were in good agreement with values reported in the earlier study taken during early development. The values in the grey matter regions of the caudate putamen (FA = 0.19±0.05 / MD =0.75± 0.07 x10^{-3}mm^{2}/s) and the somatosensory region of the cortex (FA = 0.13±0.05 / MD =0.77± 0.07 x10^{-3}mm^{2}/s), also fell within the ranges of these parameters measured previously.

4.3.4 Discussion

In this section a multi-shot DW SE-EPI acquisition was optimised and tested for *in-vivo* acquisition in the mouse brain at 9.4T. The sequence runs in less than 43 minutes making it suitable for inclusion in an imaging protocol containing other MRI techniques to be performed within the maximum imaging time for an *in-vivo* murine recovery experiment. The protocol was evaluated through comparison of phantom and *in-vivo* diffusion measurements to published values and effects of artifacts known to plague this type of EPI acquisition were analysed.

Distortion experienced by single shot EPI acquisitions at high field can be seen clearly in Figure 30c, and are less apparent in the multi-shot sequence implemented. Artifacts in images caused by increased sensitivity to motion of multi shot sequences were reduced by introducing gating of the pulse sequence to acquire data between breaths in the respiratory cycle. However, a head holder was subsequently developed to immobilise the animal that proved to be a highly robust solution to motion artifacts. Consequently, the respiratory gating was removed from the sequence due to the extra scan time it incurred. The use of an RF pulse to saturate fat was successful in removing chemical shift artifacts in the phase encode direction.

The addition of a calibrated time delay was employed to reduce Nyquist or N/2 ghosting that can be caused by misalignments of consecutive echoes in k-space. Despite the increased time necessary to acquire them, it was found that full triple reference calibration scans provided a significant reduction in ghosting. The contribution of eddy currents in gradient coils due to the rapid switching of current in EPI sequences were investigated through the use of difference images in diffusion weighted images. Phantom images appeared to show minor changes in magnitude or spatial localisation in signal between images weighted by gradients applied in different directions. The gradient sets used in these experiments are self shielded to reduce eddy currents outside of the set. Effects of any remaining currents are reduced through the use of pre-emphasis or digital eddy current compensation that is employed by the console software. Post processing correction techniques can be employed which may involve registration and resampling to realign erroneous spatial localisation of signal in images. These were not employed in this study due to the apparent lack of severity of errors induced.

The accuracy of the DTI protocol was tested *in-vivo* and through the use of a diffusion phantom and parameter estimates were shown to be in good agreement with values previously published. Repeating the *in-vivo* experiments with a larger cohort of mice would have been desirable to provide a measure of precision of the technique. Although *in-vivo* SNR estimates in the cortex were lower than those reported, the values measured in both the b=0 and the diffusion weighted images were well above the noise floor(201). Furthermore, the increased number of DW gradient directions used in this protocol should reduce noise in FA estimates(193). Varying the number of gradient directions, b-value magnitude, and signal averages will have impacts on image SNR, accuracy of DTI parameter estimates, as well as scan time of this protocol and further investigation to establish optimal balance of these components would be beneficial.

4.4 Diffusion Tensor Imaging in a mouse model of Tau Pathology

4.4.1 Introduction

In recent years, tau has emerged as a potential target for therapeutic intervention in AD(25,26). Tau plays a critical role in the neurodegenerative process: aggregates of hyperphosphorylated tau forming neurofibrillary tangles (NFTs) are a major hallmark of AD and correlate with clinical disease progression(11). In the absence of amyloid-beta, NFTs are also implicated in several other neurodegenerative diseases (frontotemporal dementia with parkinsonism, progressive supranuclear palsy, corticobasal degeneration), further supporting the role of tau in the dementing process(202). The rTg4510, a mouse model of tauopathy has been developed that specifically expresses tau in the forebrain but without amyloid plaques, enabling dissection of the unique role of tau in AD pathology(203,204). Behavioural and histological studies of the rTg4510 mouse have demonstrated cognitive deficits in learning and motor tasks and marked atrophy of brain regions known to be selectively vulnerable to AD such as the hippocampus and frontal cortex(204).

In this study, diffusion tensor imaging (DTI) (a sensitive measure of local tissue inflammation and cellular integrity) was implemented to probe changes in microstructural compartmentation in the rTg4510 mouse. As part of a multi-parametric protocol, data was acquired in a limited scan time and sensitivity to tissue pathology in selected white and grey matter regions was evaluated against histological measures. Diffusion parameters were sampled in different sub regions of the corpus callosum. Differences identified between the earlier myelinating splenium(92) and the genu, may indicate a vulnerability to disease that is dependent on development.

It is shown that this DTI protocol can unambiguously discriminate tau pathology from healthy control subjects, providing a platform for the longitudinal assessment of experimental treatments in combination with other MRI techniques. Furthermore, we demonstrate that DTI metrics are sensitive to tau-pathology in regions of low NFT density, providing evidence that these data may inform the development of a multi-parametric imaging biomarker for early detection of tau pathology in the clinic.

4.4.2 Materials and Methods

4.4.2.1 Transgenic mice

Generation of homozygous rTg4510 transgenic mice has been reported previously(203). Female rTg4510 mice were licensed from the Mayo Clinic (Jacksonville Florida, USA) and bred for Eli Lilly by Taconic (Germantown, USA). Mice were imported to the UK for imaging studies at CABI. All studies were carried out in accordance with the United Kingdom Animals (Scientific Procedures) act of 1986.

4.4.2.2 Magnetic Resonance Imaging

All imaging was performed with a 9.4 T VNMRS horizontal bore scanner (Agilent Inc.). A 72 mm inner diameter volume coil (Rapid Biomedical) was used for RF transmission and signal was received using a 4 channel array head coil (Rapid Biomedical). Mice were anaesthetised under 2% isoflurane and positioned in a MRI compatible head holder to minimise motion artifacts. Anaesthesia was then maintained at 1.5% isoflurane in 100% O_2 throughout imaging. Core temperature and respiration were monitored using a rectal probe and pressure pad (SA instruments). Mice were maintained at ~37 °C using heated water tubing and a warm air blower with a feedback system (SA instruments).

In this study, rTg4510 and wild-type litter matched control mice at 8.5 months of age were imaged. DTI was conducted on N = 9 rTg4510 mice and N = 17 wild-type controls as part of a multi-parametric MRI protocol(125). The brains of each of the rTg4510 and wild-type(WT) mice were perfuse fixed for histology which was carried out by collaborators directly after imaging. The reported p-values are from standard t-tests for differences in parameters between the rTg4510 and WT groups, unless stated otherwise.

4.4.2.3 Diffusion Tensor Imaging (DTI)

A four shot Spin Echo EPI sequence was used to acquire sixteen slices as described in section 4.3. The olfactory bulbs were used as an anatomical landmark to maintain consistency in slice positioning between animals. The FOV was 20 × 20 mm with a matrix size of 100 × 100 and a slice thickness of 0.5 mm. Diffusion gradients were applied in thirty directions with the following parameters G = 0.25 T/m, Δ = 9.3 ms, δ = 5.5 ms, and b = 1050 s/mm^2 to generate diffusion weighted images in addition to a single unweighted b=0

image. Acquisition of 5 averages with a TR of 2000ms gave a total imaging time of 43min. Software written in Matlab was used to construct tensors at each voxel through a least squares solution approach (196). The parameters MD, FA as well as radial and axial diffusivity were calculated from the tensors following standard methods. Three slices posterior to the bregma were selected for comparison to histology in the unweighted images and ROIs were manually drawn in the corpus callosum and grey matter areas of the hippocampus, cortex and thalamus (Figure 34). White matter ROIs were also taken in single slices located in both a rostral and caudal location(Figure 34a) in the external capsule to compare measurements in the Genu and Splenium regions of the corpus callosum respectively. Mean Diffusivity and Fractional Anisotropy values were measured for all regions and radial and axial diffusivity were also calculated in white matter structures. Mean values were calculated for the ROIs in each group for comparison of the DTI parameters.
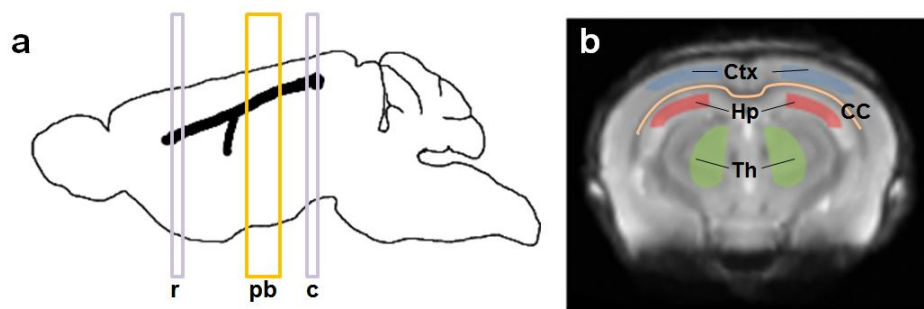
Figure 34. **DTI Regions of Interest**

Location of slices (a) in the rostral (a,r) and caudal (a, c) white matter of the external capsule, and in slices posterior to the bregma (a, pb) where ROIs(b) were drawn in the cortex(Ctx), Hippocampus(Hp), Thalamus(Th), and corpus callosum(CC)for comparison with histology.

4.4.2.4 Histology and Immunohistochemistry

Following *in-vivo* imaging, the brains were perfusion fixed and histology was performed by collaborators. Animals were terminally anaesthetised with Euthanal (0.1 mL) administered via intraperitoneal injection. The thoracic cavities were opened and the animals perfused through the left ventricle with 15–20 mL of saline (0.9%) followed by 50 mL of buffered formal saline at a flow rate of 3 mL per minute. Following perfusion, the animal was decapitated, defleshed, and the lower jaw removed. All brains were stored in-skull at 4 °C before being dispatched for histology.

Brain samples were then processed using the Tissue TEK® VIP processor (GMI Inc,MNUSA). After processing, sections were embedded in paraffin wax to allow coronal brain sections to be cut. Serial sections (6-8 µm) were taken using HM 200 and HM 355 (ThermoScientific Microm, Germany) rotary microtomes.

Immunohistochemistry (IHC) was performed using a primary antibody for tau phosphorylated at serine 409 (PG-5; 1:500 from Peter Davies, Albert Einstein College of Medicine, NY, USA). Secondary antibody was applied and slides were then incubated with avidin biotin complex (ABC) reagent for 5 min (M.O.M. kit PK-2200, Elite ABC rabbit kit PK-6101, or Elite RTU ABC PK-7100 Vector Labs). After rinsing, slides were treated with the chromogen 3,3′-diaminobenzidine (DAB; Vector Laboratories, SK-4100) to allow visualisation. The slides were then cover slipped, dried and digitised using an Aperio Scanscope XT (Aperio Technologies Inc., CA, USA).

4.4.3 Results

4.4.3.1 Regional correlations of diffusion parameters to NFT density

Immunohistochemistry was performed on each of the individual rTg4510 (n = 9) and WT (n = 17) control animals to estimate the density of PG-5 positive NFTs in cortical, hippocampal and thalamic regions (Figure 35). No PG-5 positive cells were observed in any of the control mice and quantitative measures were made in the hippocampus, cortex and thalamus for each rTg4510 mouse. There was high pathological burden detected in the cortex and hippocampus (mean NFT density = 229 cells/mm^2 and 83 cells/mm^2 respectively) of the transgenic group. The positive cell count observed in the thalamus was much lower in comparison (mean NFT density 2.3 cells/mm^2) (Figure 35).

The DTI measurements in the cortex and hippocampus, areas of high density of tau pathology, showed increased FA and MD in the transgenic group (Figure 36). Significant differences in both FA and MD were observed in the cortex. The FA in the transgenic and wild-type groups were 0.18±0.03 and 0.15±0.01 (p=2.1×10^{-4}) and the MD was 8.24±0.49x10-4 mm^2/s and 7.64±0.35x10-4 mm^2/s (p = 7.46 × 10^{-3}). The Hippocampus measurements of FA were 0.21±0.04 and 0.17±0.03 for the transgenic and wild-type groups respectively and the MD values were 9±0.49x10-4 mm^2/s and 7.7±0.59x10-4 mm^2/s, only

the MD group differences were significant ($p=4.75 \times 10^{-2}$). In the thalamus, a region of low tau pathology, a significant increase was observed in the MD only ($p=4.83 \times 10^{-2}$).
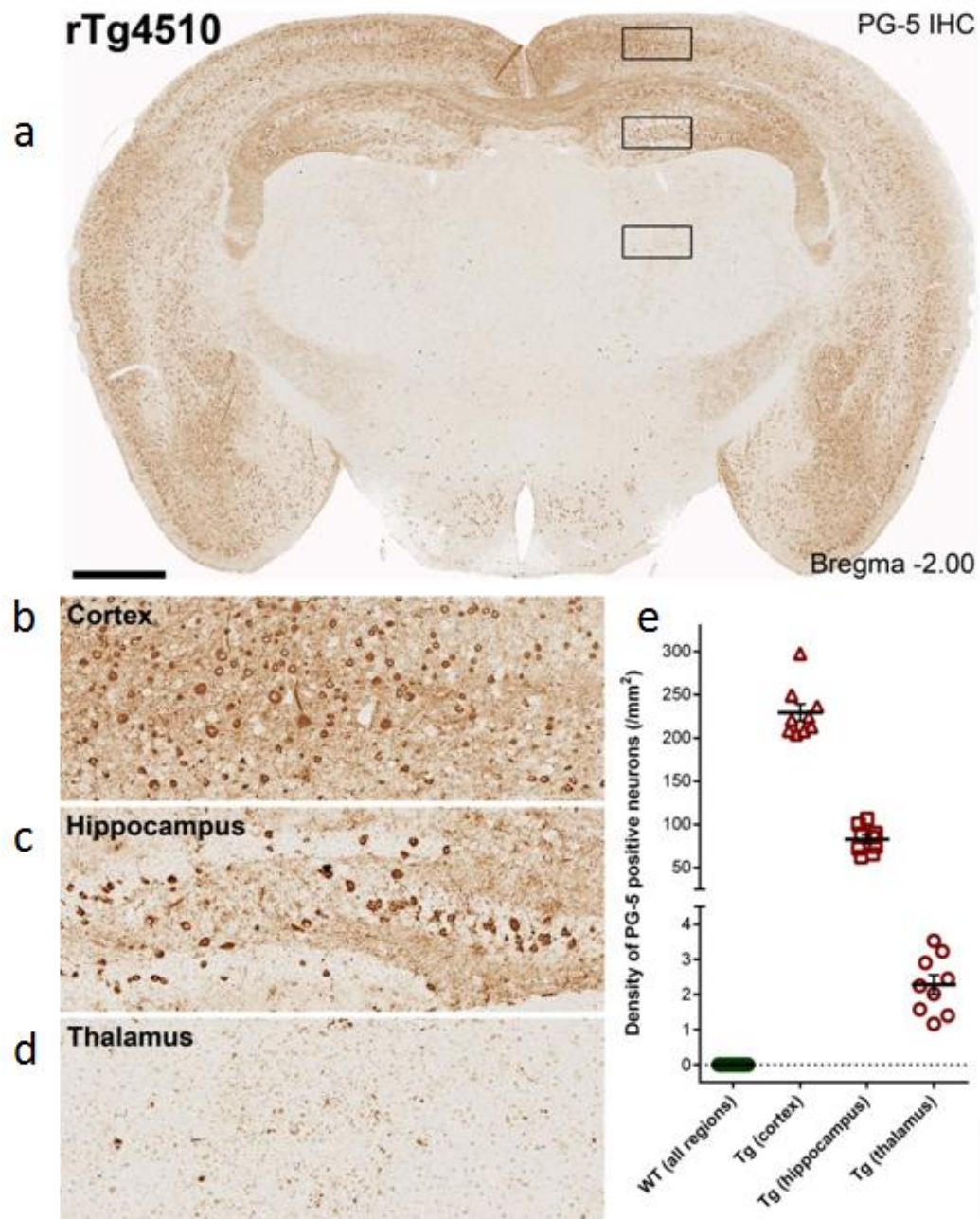
Figure 35.   **Immunohistochemistry to estimate regional PG-5 positive NFT density**

a) Single histology slice from a representative rTg4510 mouse with staining for PG-5 positive NFTs. Marked regional dependence of NFT density is observable (see inset(b-d) for example s of cortical, hippocampal and thalamic NFT distribution). E) Quantitative regional estimates of NFT density for each of the 17 WT and 9 rTg4510 mice that were used for MRI studies
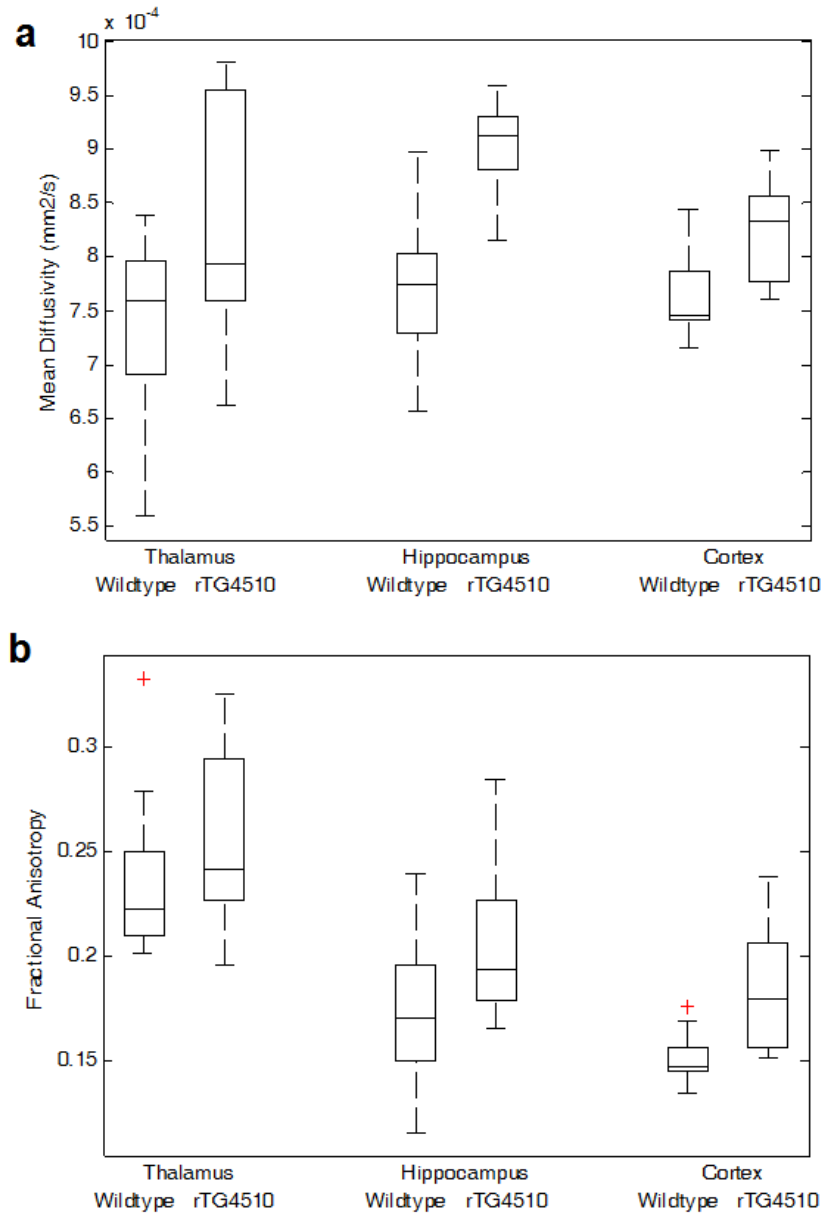
Figure 36.   **DTI measurements in Grey Matter regions**

Mean Diffusivity(a) and Fractional Anisotropy (b) in grey matter regions in WT and rTg4510 mice. A significant increase in MD was observed across all regions in the rTg4510. The cortex was the only grey matter regions to exhibit a significant increase in FA. Red crosses indicate outliers defined as values that lie greater than $\pm 2.7\sigma$ from the mean.

No significant correlations between DTI parameters and tau pathology measurements were observed within ROIs. Therefore, a secondary correlation analysis was performed in which regions were ranked based on their pathological burden. The cortex and hippocampus were ranked as "high" density while the thalamus was ranked as "low" density. The

relationship between percentage difference in MRI parameters from WT controls (ranked as 0 tau burden) and tau density was examined. A significant correlation of FA and MD to the ranked data was observed (Figure 37). There was a positive correlation of FA (Spearman's CC = 0.48, $p = 1 \times 10^{-5}$) and MD (Spearman's CC $= 0.57$, $p = 1.2 \times 10^{-7}$) to group ranked tau density. However, there was no statistical difference in the percentage difference from control between the cortex and hippocampus (the "high" ranked regions) in each of the MR measures, despite the cortex presenting with a threefold increase in NFT density relative to the hippocampus. This finding suggests a monotonic relationship exists between measures of MD and FA and NFT density within a degree of tau burden which dissociates between regions of "high" tau burden (the cortex and hippocampus) in the 8.5 month rTg4510 mice.
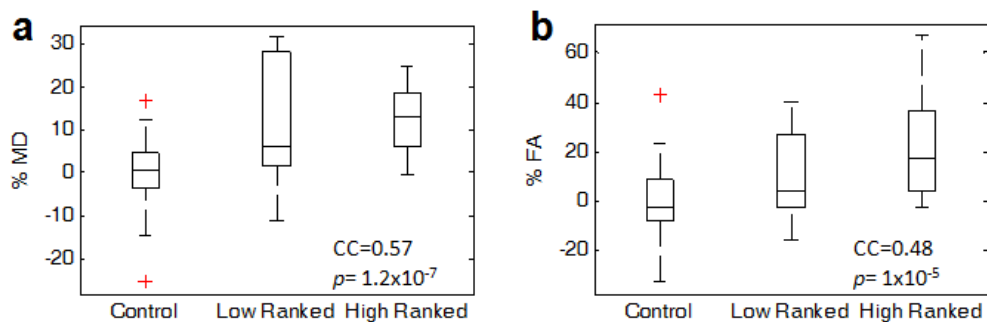
Figure 37.   **DTI correlates to histological ranking of tau density**

Percentage change (normalised to control) in a)MD and b) FA as a function of histological ranking of PG-5 positive NFT density. Spearman's non-parametric correlation coefficient was used to investigate a possible correlation of DTI measures to histological ranking (p-value and correlation coefficient (CC) reported in figure inset). Box plots represent median, interquartile range and range of quantitative MR estimates. Red crosses indicate outliers defined as values that lie greater than $\pm 2.7\sigma$ from the mean.

4.4.3.2 DTI of white matter regions of high pathology

DTI was employed to investigate microstructural changes in the white matter of the rTg4510 mice relative to the normal brain. Intensity of PG-5 staining in images of histology slices was used to calculate a staining density in the corpus callosum ROI as a ratio of the area of positive stain divided by the total area of the region. The staining density in the rTg4510 (3.5 ± 1.37) was significantly greater than that of the wild-type group (0.01 ± 0.01, $p = 6.12 \times 10^{-5}$). The mean ROI measurements of FA and MD in the corpus callosum taken posterior to the bregma showed significant differences between the transgenic and control

groups (Figure 38). The transgenic group exhibited a reduced FA of 0.32 ± 0.05 compared to the controls (0.48 ± 0.07, p = 4.5 × 10^{-6}, effect size = 2.7). In contrast, the MD of 9.4 ± 0.8 × 10^{-4} mm$_2$/s observed in the transgenic group was greater than in the controls (7.7 ± 0.4 × 10^{-4} mm$_2$/s, p = 6.3 × 10^{-8}, effect size = 3).
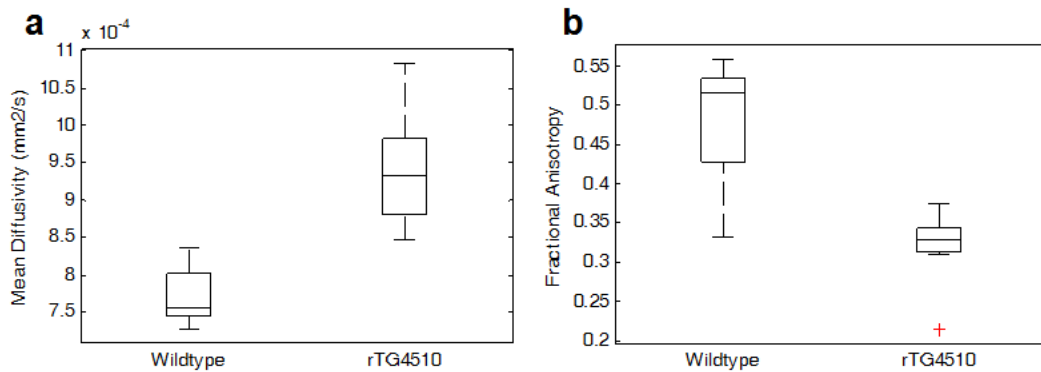
Figure 38.   **MD and FA measurements in the Corpus Callosum**

Mean Diffusivity (a) and Fractional Anisotropy measurements in the corpus callosum posterior to the bregma. MD is increased and FA is reduced in the rTg4510 group. Red crosses indicate outliers defined as values that lie greater than ±2.7σ from the mean.

Most marked was the change in radial diffusivity, where a clear discrimination between the wild-type and the transgenic groups was observed (p = 1.5 × 10^{-8}, effect size = 3.8) (Figure 39). No significant difference was observed in axial diffusivity values (rTg4510 = 11.1 ± 0.9 × 10^{-4} mm$_2$/s, control =10.7 ±0.9 × 10^{-4} mm^2/s, p = 0.36).
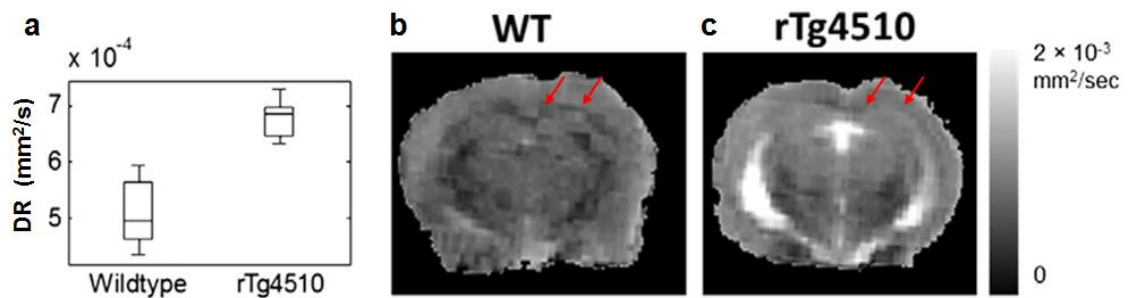
Figure 39.   **Radial Diffusivity in the corpus callosum**

Measurements of Radial Diffusivity in the corpus callosum posterior to bregma (a) showed elevated values in the rTg4510 group. Representative parameter maps are shown for a wild-type (b) and rTg4510(c) mouse. Red arrows highlight regions of reduced contrast in radial diffusivity between the corpus callosum and surrounding grey matter in the transgenic map.

4.4.3.3 Comparison of rostral and caudal regions in the corpus callosum

The measurements in regions of the genu and the splenium of the corpus callosum displayed a number of significant differences in DTI parameters between the wild-type and rTg4510 groups (Figure 40). In the rostral ROI containing the genu, there was a significant FA reduction in the rTg4510 (rTg4510 =0.31±0.07, control =0.51±0.1, p = 8.91×10^{-10}). DR and DA were also significantly different with increased DR (rTg4510 = $5.95 \pm 1.1 \times 10^{-4}$ mm^2/s, control =4.6 ±0.8 × 10^{-4} mm^2/s, p = 3.86×10^{-5}) and decreased DA measured in the rTg4510.

In the caudal ROI containing the Splenium of the corpus callosum, the DTI parameters followed a similar pattern to measurements taken for the histology comparison. There were significant increases observed in MD in the rTg4510 (rTg4510 = $7.58 \pm 1.1 \times 10^{-4}$ mm^2/s, control =6.58 ±0.8 × 10^{-4} mm^2/s, p = 3.6×10^{-4}) and DR (rTg4510 = $6.35 \pm 1.2 \times 10^{-4}$ mm^2/s, control =5.2 ±1.1 × 10^{-4} mm$_2$/s, p = 6.5×10^{-5}). Like the genu measurements, a reduced FA was observed in the rTg4510 (rTg4510 = 0.32 ± 0.1, control =0.41 ±0.2, p = 7.4 × 10^{-4}) decreased. DA was slightly increased in the transgenic groups but the difference was not significant(rTg4510 = $10.05 \pm 1.5 \times 10^{-4}$ mm^2/s, control =9.56 ±2.0 × 10^{-4} mm^2/s, p = 0.12).
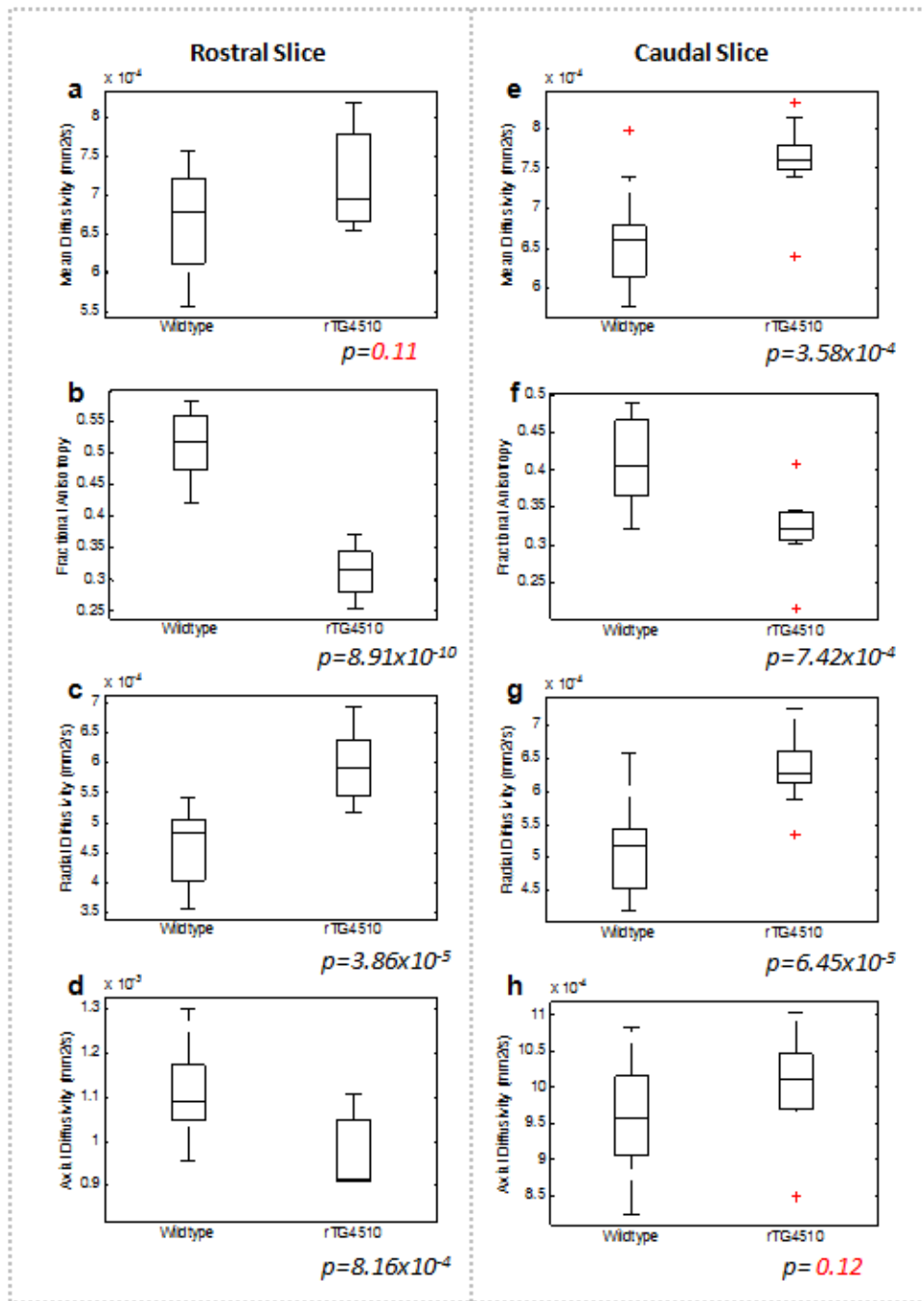
Figure 40. DTI in rostral and caudal slices

DTI parameter values measured in a rostral slice (a-d) and a caudal slice(e-h). MD (a,e), FA(b,f), DR(c,g) and DA(d,h) are presented for both slice ROIs. Calculated p-values are presented beneath box plots with group differences found not to be significant displayed in red. Red crosses indicate outliers defined as values that lie greater than ±2.7σ from the mean.

4.4.4 Discussion

In this study, a time efficient acquisition DTI protocol has been deployed to probe distinct aspects of AD pathophysiology in the rTg4510 mouse. The sensitivity of non-invasive DTI imaging to provide brain tissue correlates of tau pathology in white matter and in regions of high NFT density in the grey matter has been demonstrated. Increased MD was observed in a region of low NFT pathology highlighting the value of DTI for the identification of tau-driven pathological processes, suggesting its utility as a biomarker for the early assessment of novel tau therapeutics.

A number of clinical studies using DTI have observed increased MD and reduced FA in the white matter of the brains of AD patients when compared to healthy controls(18,65). These findings of increased MD and reduced FA in rTg4510 mice relative to wild-type controls are consistent with this and suggest that the aberrant white matter microstructure observed in AD may be, at least in part, a consequence of the tau pathology underlying the disease. The increase in radial diffusivity in the presence of unchanged axial diffusivity in the corpus callosum of the rTg4510 mice suggests a reduction in myelination, mirroring previous observations in sub regions of the corpus callosum in AD sufferers(39). These findings are highly concordant with an earlier longitudinal study by Sahara et al. that applied DTI methods to investigate the white matter of the rTg4510 model(205). Electron microscopy measures were performed and demonstrated the presence of tau inclusions in the white matter and subsequent micro-structural disorganisation relative to WT controls at later time points(205). The effects of amyloid plaques, the other hallmark pathology of AD, have been investigated in previous studies (81,82) where differences in DTI parameters have been observed at late time points after the appearance of amyloid plaques. Abnormal myelination patterns have been identified prior to appearance of NFTs and amyloid plaques in a mouse model exhibiting both pathologies(206).

To investigate the effects of tau pathology on white matter that matures at different stages of development, measurements were taken in the genu region of the corpus callosum and the earlier myelinating region of the splenium. Changes in the splenium mimicked those in the white matter region of high tau pathology, exhibiting reduced FA and increased MD and DR in the rTg4510. In the genu, reduced FA and increased DR was observed with greater significance than in the splenium and axial diffusivity was also significantly lower in than in the control group. No differences were detected in genu of the rTg4510 at this time

point in the study by Sahara et al.. The increased statistical significance of the diffusion changes in the genu compared to the splenium region of the external capsule may offer support to the retrogenesis hypothesis, that the later myelinating structures are affected more severely by pathology. However, the rostral location of the genu may make it more susceptible to the neurodegeneration that occurs preferentially in the forebrain(125,203,204) under the CaMKII promoter in the rTg4510. Additionally, it should be noted that a limitation of this study is the relatively late time point (8.5 months) may restrict evidence for specificity of DTI parameters to abnormal tau within and connected to the high ranked regions, as marked neurodegeneration is likely to have already occurred. Tracking the DTI changes from an early time point using this protocol alongside structural MRI atrophy measurements may provide more information on the temporal order of changes in white matter regions and their relationship with neuronal cell loss in connected grey matter tissue.

The MD findings in grey matter regions are in good agreement with previous studies that have detected elevated values in the brains of AD patients (169,171,207) and in mouse models exhibiting amyloid pathology at late stages of progression(82). In the previous longitudinal DTI study in the rTg4510 by Sahara et al(205), no differences in MD were observed in any of the ROIs at later time points. This may be due to the increased animal numbers as well as enhanced sensitivity of the DTI protocol used here. The positive correlation between the increased MD and the tau density ranking suggest that the disruption to the cytoarchitecture indicated by these increases may be driven by the pathology. Furthermore, the positive correlation of FA with tau density may indicate that the structural reorganisation that occurs may have directional specificity. FA has been found to be reduced in AD patients in the hippocampus (171) and the thalamus (169) which contradicts the findings in this study where the FA was increased significantly in the cortex and hippocampus in the transgenic mice and there is no significant difference in the thalamus. These differences may be due to the addition of amyloid-beta pathology present in the brains of AD patients or the inherent differences in murine grey matter tissue structure.

The thalamus of the rTg4510 mice was found to have relatively low NFT density (mean=2.3 cells/mm$_2$), mirroring human tissue at early Braak staging with low NFT density(208). We observed an increased MD in this region relative to WT controls. This finding suggests that

microstructural changes that occur with little pathology present can be detected in this brain region with DTI. These imaging changes may reflect very early local markers of tau pathology in the thalamus, but it cannot be ruled out that some of these differences may also be secondary to the large tau pathology in the forebrain structures, many of which are known to project to the thalamus. This may be important as we know that tau aggregates can transfer and propagate/spread within synaptic circuits(209,210). There is post-mortem evidence in AD for this regional spread(11) and more recent neuroimaging studies in human AD suggest "epicentres" (211) or "nodes" (212) that may link to network dysfunction.

Histological measures of pathological tau burden in the rTg4510 mice demonstrated a strong regional dependence of NFT density ranging from low (2.3 counts/mm$_2$ in the thalamus) to high (229 counts/mm$_2$ in the cortex) (Figure 35). This is to be expected as expression of tau is driven by a forebrain specific promoter in the rTg4510 mouse (87). We sought to exploit this marked dynamic range of NFT density (as quantified using PG-5, pS409 tau) between regions to investigate correlations between ranked tau burden and difference in MR parameters from control (to account for intrinsic regional differences). We observed significant correlations between the percentage change from control in MD and FA across regions free of NFTs (wild-type), low NFT density (rTg4510 thalamus) and high NFT density (rTg4510 cortex and hippocampus), indicating a monotonic relationship between NFT density and diffusion changes between different regions of varying tau load at this time point. This observation provides encouragement that DTI could be used to broadly classify regions of negligible, low and high NFT density for non-invasive staging of AD. The percentage change in MR parameters in rTg4510 from control were very similar between the cortex and hippocampus (high ranked data), despite the marked difference in the overall NFT density between these two brain regions. This may be a feature of the rTg4510 model at this time point or reflect the greater and more selective vulnerability (or different inherent composition) of the hippocampus, a region known to present with marked abnormality in AD patients. We observed limited within-region correlations of NFT density to other DTI parameters in grey matter which may be due to the relatively narrow distribution of NFT density within each region (Cortex: 229 (±28), Hippocampus: 82.9 (±15), Thalamus: 2.3 (±0.8)(PG-5 positive neurons per mm^2)) at this time point.

4.5 Conclusions

This study has demonstrated the value of non-invasive DTI MRI for sensitive detection of tau pathology in the rTg4510 model of AD. These novel data represent a platform for future longitudinal and therapeutic evaluation studies in this model. The time efficient acquisition has been integrated into a multi-parametric protocol and merits application in clinical populations to investigate the pattern of MR changes in regions known to follow the well-defined stages of NFT progression. Estimates of diffusion can detect changes in healthy tissue in a region of low NFT density (2.3 cells/mm^2) which provides promise for the use of these markers to identify and track subjects early in the Alzheimer's disease continuum.

White matter DTI measurements showed significant changes in the corpus callosum of the rTg4510. Reductions in FA and increases in DR were observed in all measurements and may be attributed to a reduction in the presence of hydrophobic myelin in this tract suggested in a previous study using Electron Microscopy(205). However, the microstructural rearrangements that occur in disease may not always be straight forward and there have been studies that call into question the specificity of FA and DR to abnormalities in myelination(177,178). Quantitative Magnetic Susceptibility Mapping(QSM) is an MRI technique sensitive to the diamagnetic properties of myelin and has shown increased sensitivity over DTI to the maturation of white matter tracts in the developing mouse brain(213). In the following chapter, a protocol is developed and applied in the rTg4510 to investigate the sensitivity of QSM to tau pathology.

5 Quantitative Susceptibility Mapping in the rTg4510 mouse model

5.1 Overview

In the last chapter, an SNR time efficient DTI protocol was developed for integration into a multi-parametric MRI protocol and applied to the rTg4510 mouse model of AD. Differences in diffusion parameters relative to wild-type controls indicated a reduction in the directional diffusion of spins in white matter tracts which may be due to degradation of the myelin sheaths of axons. Neuroinflammation and oxidative stress in AD are associated with NFT pathology and dysfunction of oligodendrocytes - myelin generating glial cells. Disruption to the homeostasis of iron in the brain may be a trigger for neuroinflammation and excess accumulation of iron in the basal ganglia has been observed(214). Quantitative Susceptibility Mapping (QSM) is an emerging MRI technique that has demonstrated sensitivity to the concentration of myelin(diamagnetic) and iron(paramagnetic) which may represent an early biomarker of AD.

In this chapter, a QSM protocol is developed and data is collected both *in-vivo* and *ex-vivo* in the rTg4510 and WT controls. Firstly, the phase data from a previously acquired *ex-vivo* dataset was processed and used to carry out a pilot experiment to identify regions of reduced magnetic susceptibility contrast between white matter and grey matter.   Gradient echo acquisitions were then optimised for collection of both *in-vivo* and *ex-vivo* data and a post processing software pipeline was developed to generate susceptibility maps from this data. Magnetic susceptibility and T2* estimates in regions of interest in rTg4510s and wild-type controls are presented and discussed.

5.2 Background

5.2.1 Introduction

Despite its role in a variety of metabolic processes, iron can take on a reactive ferrous form in the body that may lead to tissue damage in the brain caused by the generation of biologically toxic Reactive Oxygen Species(ROS) (215,216). The storage of iron, in its ferric form, is disrupted in Alzheimer's Disease where deposition occurs in excess of the global increases associated with healthy ageing(217). Abnormal accumulation has been shown to occur in the iron rich regions of the basal ganglia(214) and co localised with plaque and tangle pathology(216). Oxidative stress is associated with the dysfunction of oligodendrocytes in AD(218) and the consequent breakdown of axonal sheaths in white matter tracts may lead to the release of myelin-associated iron(219). It has been hypothesized that a breakdown in iron homeostasis is responsible for an increase in the harmful redox-active iron population(216). The use of chelating agents to target these reactive species has shown neuroprotective value in mouse models of AD(220). However, a causal relationship between iron accumulation and the pathobiological cascade in AD has not been demonstrated. *In-vivo* biomarkers sensitive to tissue iron concentration may play a key role in tracking the progressive iron accumulation that occurs in AD pathogenesis and provide a means by which to measure the efficacy of therapeutics.

5.2.2 Role of Iron in Neurodegenerative disease

Iron is crucial for the healthy function of neural tissue, it is involved in DNA synthesis, mitochondrial respiration, myelin synthesis, and the synthesis and metabolism of neurotransmitters. It occurs in ferric (Fe^{3+}) and ferrous (Fe^{2+}) forms that constitute a redox couple, important in its functions of electron and oxygen transport. Iron is absorbed from food in the gastrointestinal tract and is transported through the body in the bloodstream. It enters the brain by passing through the vascular endothelial cells of the blood brain barrier into the extracellular space. It can then be taken up by neurons, microglia, astrocytes and oligodendrocytes and is stored in the brain in its ferric form bound within the proteins ferritin and neuromelanin. Iron levels need to be tightly regulated in the brain but homeostasis can become disturbed during neuroinflammation which is thought to increase iron levels in neurons and microglia(221). Ferritin containing reactive microglia

have been found to be present alongside neuroinflammatory AD pathology(222) as well as reactive astrocytes, known to express haemochromatosis, a protein linked with congenital iron overload(220). Increased iron levels are associated with ROS generated through the Fenton reaction between hydrogen peroxide and ferrous iron. Oxidative stress can be caused if ROS exceed a cells detoxification level leading to cell death.

The ability to spatially map iron stores *in-vivo* would provide insight into their link with pathology in AD. The insoluble beta-amyloid plaques and neurofibrillary tangles of tau that form in the AD brain have both been found to contain iron(223,224). The Amyloid Precursor Protein(APP) gene is a known to be mutated in familial forms of AD and its genetic translation has been shown to be highly sensitive to intracellular iron concentration(225). Genetic studies indicate an association between several iron related genes and AD risk factor(226). Furthermore, previous studies investigating the appearance and location of plaques in transgenic mouse models of familial forms of AD have shown a co localisation with iron deposition(216). Aggregation and phosphorylation of tau and iron accumulation has been observed in a mouse model over expressing heme oxygenase(HO-1), which is a haem degrading enzyme that is upregulated in the hippocampus and temporal cortex of patients with AD and MCI(216). Additionally, in vitro experiments have shown that aggregation of phosphorylated tau can be mediated by transitions of iron between its ferric and ferrous forms(227). Iron accumulation has also been observed in MAPT knockout mice due to impairment of APP mediated iron export(228). Iron accumulation in mouse models that over express tau forming NFT pathology(such as the rTg4510) have not been characterised.

5.2.3 Iron measurement in-vivo using MRI

The relationship between excess iron deposition and ROS in the brain suggests that iron measurement may act as a surrogate marker of oxidative stress(229). The interaction of iron with magnetic fields is due to its paramagnetic susceptibility and is therefore, theoretically, detectable in tissue by MRI. The magnetic properties of haemoglobin in the blood are mostly due to the presence of heme iron. The transition from oxyhemoglobin to deoxyhemoglobin during oxygen consumption increases the paramagnetism of the heme iron ions and the balance of oxyhemoglobin/deoxyhemoglobin forms the basis of the BOLD effect in fMRI(230). Non-heme iron is found in cells throughout the body and in the brain is distributed heterogeneously with greater density found in regions associated with

movement such as the globus pallidus, the putamen, the caudate nucleus, and the red nuclei(231). The variations in tissue concentration generate measureable changes in the local susceptibility that can be measured using MRI(231). Non-heme iron stored as ferritin and hemosiderin (found in broken down blood products) are the only types present in great enough concentrations to be detected(232).

Perturbations in the B_0 field caused by materials with high magnetic susceptibility have a shortening effect on the relaxation time constants of the transverse MR signal. Hypointensities in T2 and T2* weighted images have been observed in brain regions such as the basal ganglia, a structure associated with a greater iron content (229,233). Iron may also cause hyper intensities in T1 weighted images due to shortening of the longitudinal relaxation time(231). A more quantitative correlate of iron concentration in tissue can be gained by measurement of transverse relaxation constants T2, T2', and T2*, where T2* is a combination of spin-spin relaxation(T2), and reversible relaxation(T2') caused by in homogeneities in the main magnetic field(see Equation 11). T2 measurement is robust from background susceptibility effects and is reduced in the presence of high iron content in tissue(234). However, its sensitivity to changing water content in tissue may affect iron estimates, especially in the presence of inflammation(231). This issue can be overcome using field dependent rate increase (FDRI) technique which requires T2 measurements at two different magnetic field strengths(235).

The reversible relaxation constant, T2', is directly related to signal phase and shortening of this parameter is thought to more accurately relate to iron in brain tissue when compared with T2(231,236). Increased scan times are necessary for the acquisition of both T2 and T2* relaxation datasets to calculate T2' and its relatively small magnitude make it vulnerable to noisy estimates due to field inhomogeneities. Consequently, T2* measurements are more frequently used(229). T2* incorporates T2 and T2' relaxation mechanisms and the errors in iron estimation associated with them. Nevertheless, values correlate well with post mortem measurements of iron in human brain samples(237) and data can be acquired using a simple multi echo gradient echo acquisition that is fast and widely available making this the most established MRI method for this application(233). The techniques described so far use the magnitude of the MRI signal to provide a measure that is sensitive to magnetic susceptibilities of materials that are both paramagnetic and diamagnetic relative to water. Calcifications and myelin in white matter are diamagnetic

and like iron will have the effect of reducing transverse relaxation constants. Using the phase of the signal from gradient echo acquisitions, it is possible to discriminate between tissue types that are either diamagnetic or paramagnetic relative to water.

The phase of the transverse MR signal in a gradient echo acquisition is directly related to the magnetic field experienced by the spins. The interaction with the B_0 field is dependent on the bulk magnetic susceptibility of the tissue and is proportional to off resonance effects on signal phase. The polarity of the phase of the complex signal allows differentiation between positive and negative susceptibility effects on the signal and the size of the phase shift has been shown to correlate with iron concentration in the brain(238). Phase measurement at a voxel is complicated by the non local effects from sources at other locations within the volume of tissue imaged, peripheral air/tissue/bone interfaces at the edge of the brain, as well as any other sources of field inhomogeneity such as poor shimming of the B_0 field. The latter two sources are known as background field contributions and can cause severe distortion artifacts and signal drop out in affected regions. The relationship between magnetic susceptibility and field strength means artifacts related to magnetic susceptibility are exacerbated in high field applications. Furthermore, signal phase is only defined between the values of $\pm\pi$ radians and the occurrence of values outside of this range cause aliasing, known as phase wrapping in the reconstructed images.

Image post-processing methods can be used to remove wraps and background field contributions and the resulting phase images can then be combined with magnitude images to generate Susceptibility Weighted Images(SWI). SWI enhances T2* contrast with phase information to improve visualisation of small blood vessels within the brain(239), Cerebral Microbleeds (CMBs)(240), as well as identification of iron and improved grey matter/white matter contrast(241). To remove the effects on phase estimates from non local contributions that persist in SWI, a further post-processing step is applied that requires deconvolution of the phase map with a magnetic dipole field. This technique is known as Quantitative Susceptibility Mapping. Magnetic susceptibility estimates using QSM correlate well with iron measurement at post mortem(242). Unlike relaxometry techniques, QSM provides contrast between diamagnetic tissue such as calcifications and myelin, and paramagnetic iron through negative and positive susceptibility values respectively. One drawback of this method is that the deconvolution calculation is ill-posed

and consequently requires regularisation to reduce noise and streaking artifacts. The susceptibility estimates are dependent on the centre frequency used in acquisition and values are given relative to reference tissue regions that often vary between studies. Additionally, there are a number of alternative methods for the QSM processing of phase data reported in the literature with few comparisons made between them. These inconsistencies are due, in part, to the novelty of the QSM technique. Non-local contributions that cause blooming artifacts in T2* maps may impact accuracy and mean that QSM offers an improved estimation of iron concentration(103,243). Conveniently, both can be generated from the same multi-echo gradient echo acquisition enabling QSM to be validated against the more established T2* method.

In early studies of iron deposition in AD, focal hypointensities were observed around beta-amyloid plaques in *ex-vivo* T2* weighted images(244), and lower regional intensities in the putamen and red nucleus were found in AD patients(245). Relative to healthy subjects, regional quantitative measurements of T2 have shown reductions in the caudate putamen(246) as well in the cortex, and globus pallidus(231) and a recent study found reductions in T2* in the pulvinar nucleus(247) in AD patients. MRI phase contrast studies also suggest increased iron concentrations in the caudate putamen as well as in the hippocampus, frontal and parietal regions in the cortex(248,249). In a recent QSM study of AD the increased magnetic susceptibility measured in the putamen of patients was as statistically significant as the differences in atrophy of the hippocampus in this region, a measure seen as the 'gold standard' MRI biomarker in AD(250).

High resolution T2 and T2* weighted imaging of APP and PS1 mouse models of AD have been used to visualise beta-amyloid plaques and study their distribution *in-vivo*. Hypointensities observed were validated using histological stains sensitive to iron and beta-amyloid(72-78). Studies have also shown T2 shortening in amyloid pathology models where no iron was detected, suggesting this effect may be due to other plaque characteristics, especially in younger mice(251,252). T2 is thought to better delineate these plaques than T2* which may overestimate their size, and T2 relaxation has shown a longitudinal relationship with plaque load in the hippocampus and cortex of mice(253). T2* and T1 shortening has been observed in plaque-containing structures of the brain in APP/PS1 mice but not in pathology free regions (78,254). Studies using phase based methods include the visualisation of plaques using SWI(255) and CMBs using QSM(256).

Thus far, QSM group comparisons have only been applied in the ArcBeta model of AD with significant differences observed longitudinally(257) but not in a cross sectional study(256). There have been no studies using MRI to investigate iron accumulation in models of tau pathology of AD.

5.2.4 Motivation and aims

Despite the link between iron and tau pathology in neurodegeneration, there have been no attempts to use MRI as a measure of non invasive iron quantification to explore this relationship. In this chapter, a QSM protocol is developed and applied in the rTg4510 mouse *in-vivo*. Previous work has shown that reactive microglia and astrocytes, associated with neuroinflammation and iron accumulation, are present in higher quantities in this model than in controls(258,259). Abnormalities in myelination in the corpus callosum have been observed using DTI and EM in previous studies(125,205) and aggregated tau protein has been found to be present in oligodendrocytes(260). I hypothesized that QSM might provide a sensitive *in-vivo* method to alterations in myelin and potentially iron accumulation that may be occurring in the rTg4510. T2* and high resolution *ex-vivo* measurements are presented with histological staining of markers of tissue inflammation and white matter integrity to aid the interpretation of *in-vivo* findings.

5.3 An ex vivo pilot study of contrast enhanced QSM in the rTg4510

5.3.1 Introduction

Quantitative susceptibility maps can be generated from the phase of MRI data acquired using a gradient echo sequence. High resolution gradient echo imaging of the *ex-vivo* mouse brain has been previously optimised in CABI for the study of structural changes in disease(119). Protocols have been designed to maximise contrast between white matter and grey matter in fixed tissue. Voxel sizes of the order of 40μm x 40μm x 40μm have been achieved using a 12 hr "overnight scan" enabling fine structures in the mouse brain to be resolved. To achieve this resolution, gadolinium, a paramagnetic contrast agent is added to the fixative which shortens the longitudinal relaxation time constant for the tissue and permits a reduced time to repeat for enhanced SNR efficiency per unit time. The selective uptake of contrast agent in grey matter provides an added benefit of increased CNR between grey matter and white matter(261).

The effects on magnetic susceptibility of *ex-vivo* mouse brain tissue caused by the addition of gadolinium to the perfuse fixation process was the subject of a recent study by Dibb et al (261). As the concentration of the contrast agent was increased, an increased difference in magnetic susceptibility between white matter and grey matter tissue was observed. It was suggested that this may be due to a barrier to penetration created by the myelin sheaths in white matter restricting the uptake of Gd molecules to the extracellular space. This produces a relatively lower Gd content per unit volume of tissue in white matter compared to the grey matter. Gd is paramagnetic and therefore the greater concentration in grey matter generates an increased magnetic susceptibility relative to the white matter.

As a preliminary investigation into magnetic susceptibility in the rTg4510, data from a previous volumetric study was used(data acquired by a collaborator). This data was acquired at high resolution using brains doped with Gadolinium. I hypothesized that disrupted white matter in the rTg4510(205) may be less resilient to penetration from the paramagnetic contrast agent, thus reducing differences between QSM estimates between grey and white matter in this animal modal (relative to healthy controls). Deformation

fields generated from the non-rigid registration of the magnitude data were used to transform magnetic susceptibility maps into a common space for analysis. A voxel-wise group comparison was used to identify differences in magnetic susceptibility between the rTg4510 and controls. This automatic technique expedited analysis, removing the time consuming process of manual segmentation.

5.3.2 Methods

5.3.2.1 Magnetic Resonance Imaging

Imaging data was acquired previously by collaborator to perform a high resolution tensor based morphometry(TBM) comparison of the rTg4510 mouse with Wild-type controls. 10 rTg4510 mice and 8 wild-type littermates were culled at 7.5 months and perfuse-fixed with 0.9% saline (15 – 20 mL) followed by 10% Buffered Formalin (50 mL) doped with Magnevist (8 mM). High resolution *ex-vivo* images of three brains were acquired simultaneously at 9.4T (Agilent Inc. Palo Alto, CA, USA) by securing brains in a purpose built holder. A 35 mm diameter birdcage RF coil was used for RF transmission and signal detection using a gradient echo sequence with the following parameters: FOV = 32 mm x 25 mm x 25 mm; resolution = 40 µm x 40 µm x 40 µm; TR = 17 ms; TE = 4.54 ms; flip angle = 51°; NSA= 6. Total imaging time was approx. 11 h and was typically performed "overnight".

5.3.2.2 Magnetic susceptibility mapping and non-rigid registration

The post processing of the MRI data involved reconstruction of phase data and generation of magnetic susceptibility maps using a combination of software that I developed alongside algorithms made freely available by other research groups online. Corresponding magnitude data had already been reconstructed and registered by a collaborator for TBM using an automated software pipeline. The deformation fields from this registration were used to transform magnetic susceptibility maps into this common space for voxel-wise group analysis. The data processing protocol is described in the flowchart in Figure 41.
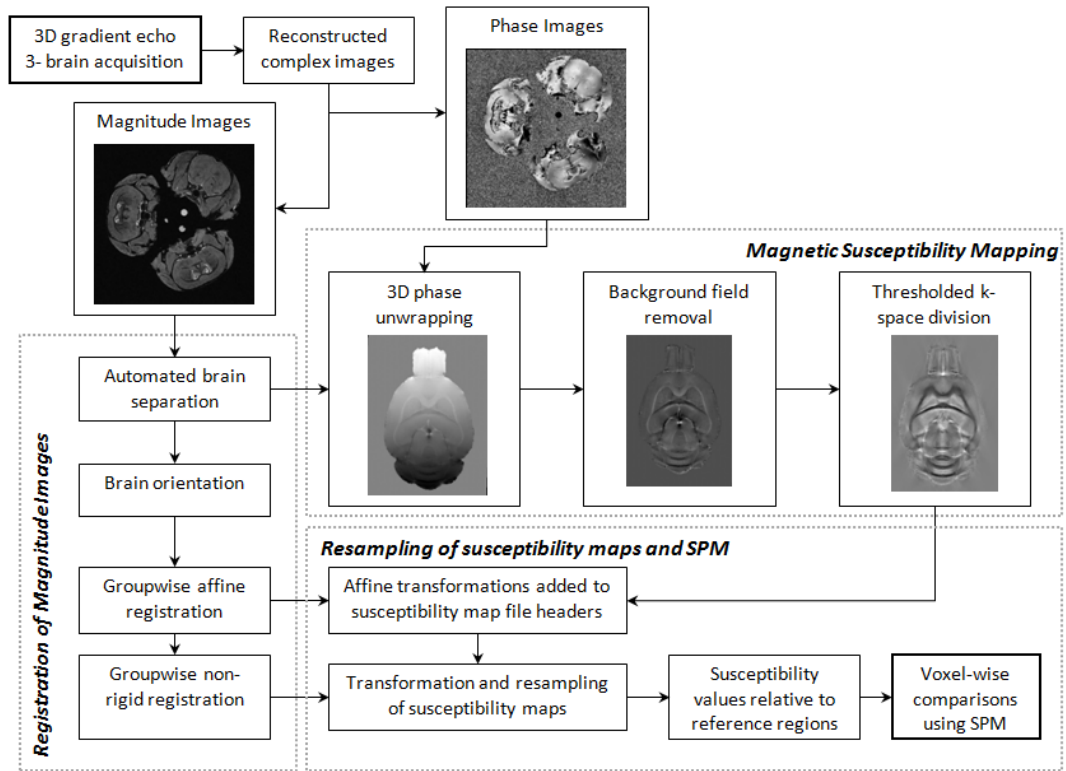
Figure 41.   **Flowchart of image processing**

Flowchart detailing the post processing of the gradient echo to register magnetic susceptibility maps into the same space for voxel-wise analysis in SPM.

The first step of the registration pipeline performs automatic separation of the three brains in each reconstructed magnitude image. This separation was then applied by a collaborator to the corresponding phase images and I then conducted susceptibility mapping processing on these individual brains. FSL Prelude (*fsl.fmrib.ox.ac.uk/fsl/fsl-4.1.9/fugue/prelude.html)* was used to perform spatial unwrapping of the phase images. The background field effects were then removed using the Projection on to Dipole Fields method (*PDF.m*, MEDI toolbox, Cornell MRI Research Lab) (107,262). Susceptibility maps were calculated by thresholded k-space division (TKD)(101) using a low truncation value $t_F=1$ to limit streaking effects in the final susceptibility maps. This was to limit artifacts that might be caused by large susceptibility differences at tissue boundaries due to the Gadolinium contrast agent in the fixative.

After the brain separation, further steps to register the magnitude images were carried out by a collaborator (Figure 41). These included the automatic orientation to a standard atlas

126

followed by an intensity non-uniformity correction (N3 algorithm(263)) before automatic skull stripping using the STAPLE algorithm(264) which also generated masks for each brain. Group-wise registration was then performed using NiftyReg software(120,122). Firstly, all subjects were rigidly aligned to a randomly chosen target member of the group followed by five iterations of affine registration producing a matrix describing the transformation of the registration for each brain. Finally, there were 20 iterations of non-rigid registration (NRR). After each iteration, the intensity average image was found and used as the target for the subsequent registration. Deformation fields describing the transformation from the affine registration were generated for each brain.

To register susceptibility maps, I applied the rigid, affine, and non-rigid transformations from corresponding magnitude image registrations to the susceptibility maps. Firstly, the orientation matrix was added to the header of the nifty file containing the susceptibility map. Next this header matrix was multiplied by the affine registration matrix to combine transformations. Using niftyreg software, the modified affine matrix in the file header was used to transform the susceptibility map in the file before a further transformation was applied using the deformation field generated from the non-rigid registration. The combination of affine and non-rigid transformations in niftyreg ensured that resampling was performed only once on the data in the final step.

Prior to group comparisons, all susceptibility values were calculated relative to a reference to account for differences in centre frequency in the MR acquisitions. The mean susceptibility in the grey matter of each mouse brain was used as a reference and was subtracted from each voxel value. A grey matter mask (Figure 42) was generated automatically for this purpose by intensity thresholding in the magnitude atlas image.

Figure 42.　　　　**Grey Matter Mask**

Axial slice of grey matter mask used to generate reference magnetic susceptibility values.

5.3.2.3 Statistical Parametric Mapping

Statistical Parametric Mapping (SPM) (SPM, *http://www.fil.ion.ucl.ac.uk/spm/*) was used to investigate susceptibility differences between the wild-type and transgenic groups. Images were smoothed to with a 0.1 mm FWHM Gaussian kernel to account for registration error and to bring image values closer to a normal distribution. A two sample, two-tailed, t-test at each voxel was carried out for statistical significance. The results were corrected for multiple comparisons using the False Discovery Rate(FDR) method (q=0.05)(265).

5.3.3 Results

Marked, region-specific, increases in susceptibility were observed in a rostral section of the corpus callosum (less diamagnetic in the rTg4510) as shown in the Statistical Parametric Map in Figure 43(a - c). Mean images of the registered susceptibility maps were calculated for the wild-type (Figure 43d-f) and rTg4510 mice (Figure 43g-i). In both the coronal and axial slices presented in Figure 43, a reduction of white matter contrast is observed from visual inspection of the rTg4510 susceptibility maps in regions that correspond to increases in the comparative SPMs. This appears to be due to an increase in the mean susceptibility in these white matter regions in the rTg4510. Increased magnetic susceptibility was also observed in the striatum (more paramagnetic in the rTg4510) (Figure 43b).
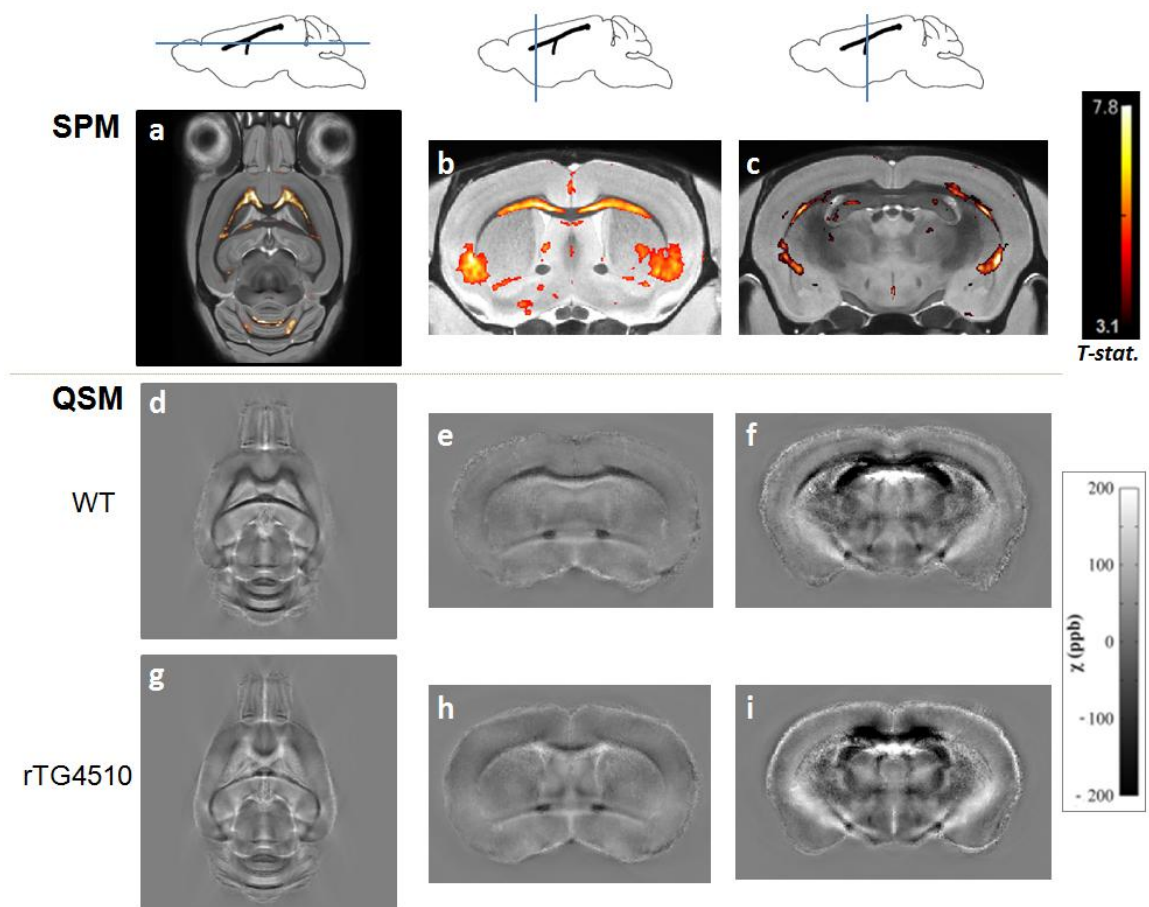
Figure 43.   Increases in magnetic susceptibility in the rTg4510

SPM (FDR corrected,q=0.05) overlaid on magnitude image atlas(a-c), showing increases in magnetic susceptibility in the corpus callosum and anterior commissure (less diamagnetic), and the striatum(more paramagnetic) in the rTg4510 mice in comparison to WT. Corresponding slices in mean magnetic susceptibility images display greater contrast between the white matter and grey matter in the external capsule in the WT mice (d-f) in comparison to the rTg4510 mice (g-i).

To investigate the possibility of registration errors causing the loss of contrast in the white matter, magnitude images were inspected. The visible reduction in contrast in the corpus callosum in the mean susceptibility maps (Figure 44a) of the rTg4510 mice was not observed in the mean magnitude image (Figure 44b). This finding was replicated in an unregistered susceptibility map and magnitude image in a representative mouse (Figure 44 c,d).
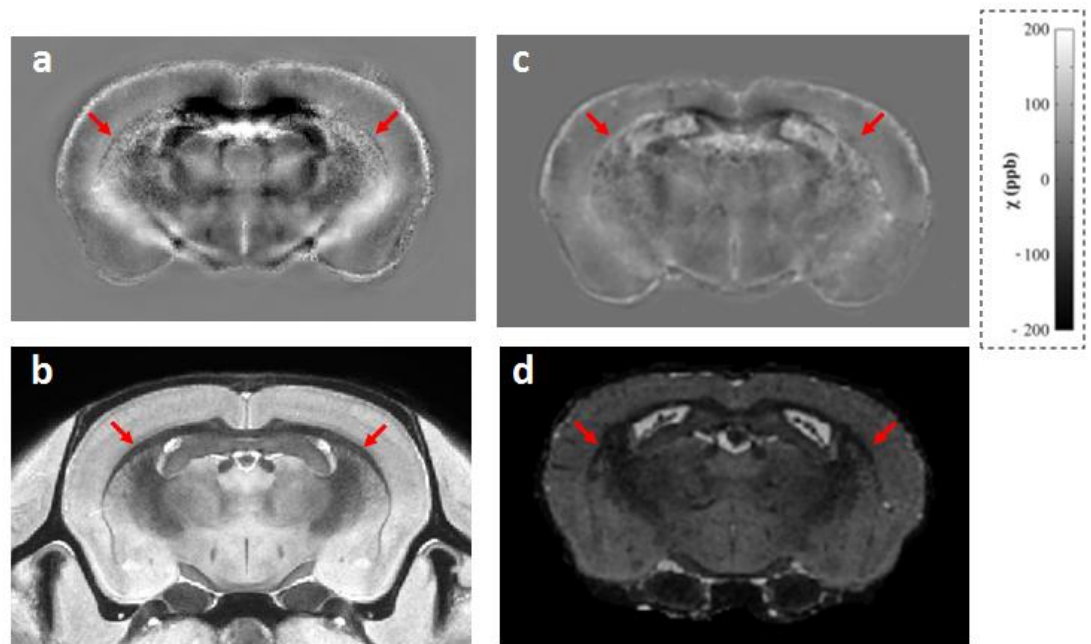
Figure 44.   **White matter contrast in mean images**

Contrast between white matter and grey matter reduced in the rTg4510 mean susceptibility maps (a) was not observed in the corresponding mean magnitude images(b). This finding was consistent with comparisons between susceptibility maps in individual rTg4510 mice (c), and magnitude images (d) prior to registration.

Decreased magnetic susceptibility was detected in various regions throughout the rTg4510 brain. Most notable, bilateral changes appeared to co localise to the motor cortex, striatum, the amygdala, the substantia nigra and the dentate gyrus (Figure 45).
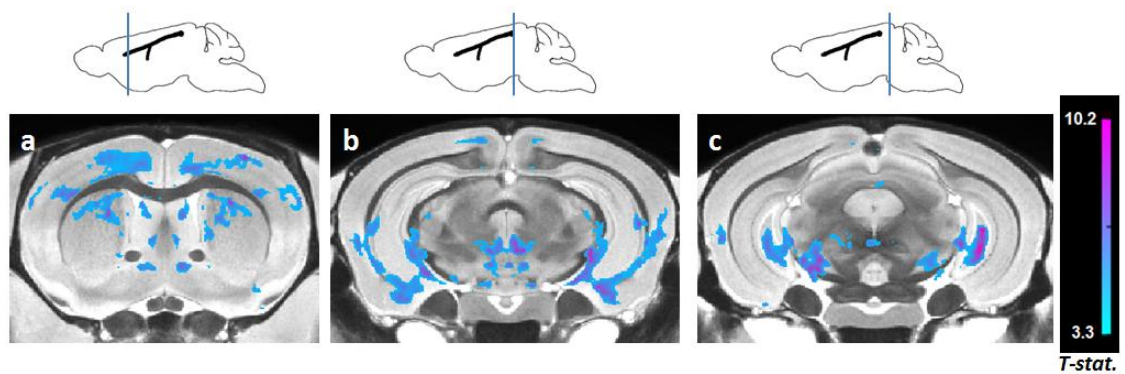
Figure 45.   **Decreased magnetic susceptibility in the rTg4510**

SPM (FDR corrected, p<0.05) overlaid on magnitude image atlas, indicating decreases in magnetic susceptibility in the rTg4510 mice. Significant bilateral decreases were observed in the rTg4510 in regions including the motor cortex and caudate putamen (a), the nucleus of the posterior commissure and the amygdala(b), and the substantia nigra and the polymorph layer of the dentate gyrus(c).

Histological staining (n=1) was carried out by collaborators in a coronal slice in the frontal cortex to identify any abnormalities in the regions of increased susceptibility (Figure 43 b). White matter integrity was probed using a stain consisting of solochrome cyanin sensitive to myelin combined with cresyl violet, a neuronal counter stain. To identify reactive microglia and astroctyes that are thought to mediate neuroinflammation(221), a GFAP and an IBA-1 stain were also used. In comparison to the WT, the solochrome staining in the genu of the corpus callosum showed a more disorganised arrangement of cell bodies and myelin with large gaps evident in the rTg4510(Figure 46d,e). This was accompanied by an increased density of reactive microglia in this region (Figure 46b,f,g). Astrocytic staining was also more dense across the corpus callosum in the rTg4510(Figure 46c), with increased activity also observed in the striatum(Figure 46h,i).
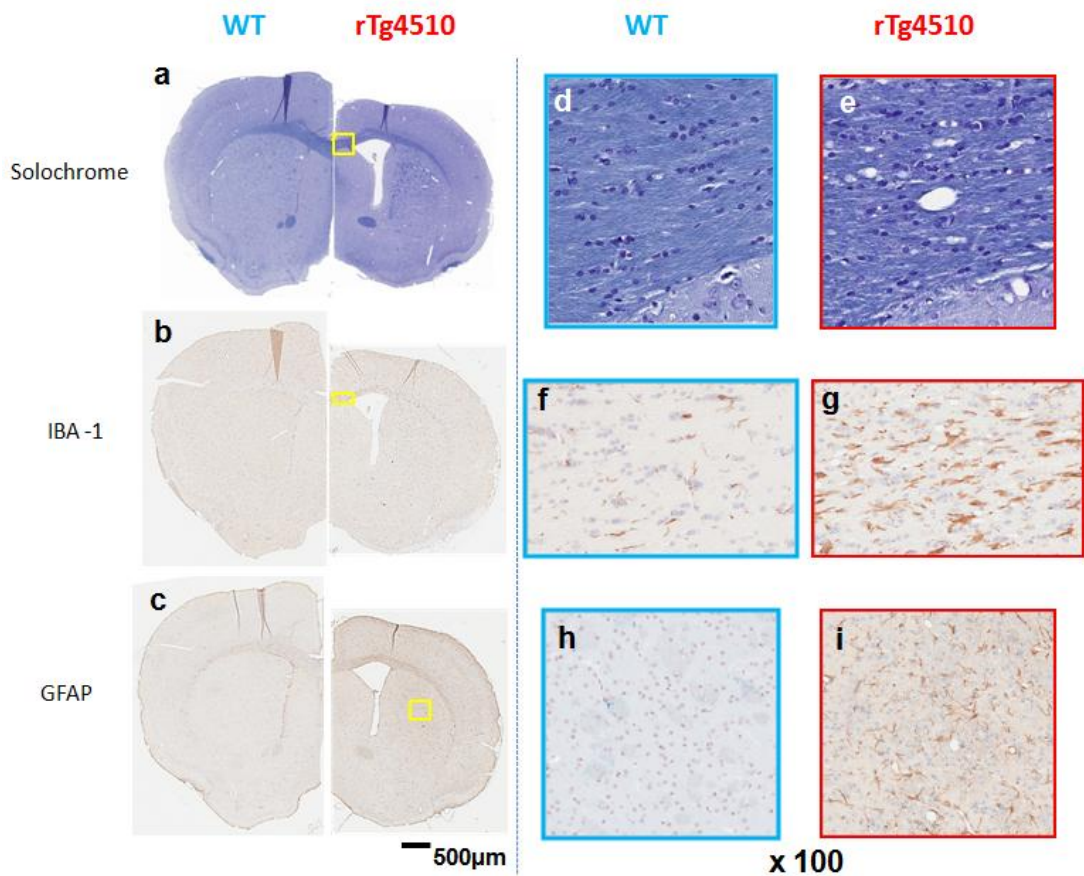
Figure 46.   Histology in rTg4510

Solochrome cyanin / cresyl violet(a), IBA-1(b), and GFAP(c) staining of a coronal slice 0.74mm rostral to the bregma for a WT(left) and rTg4510(right) mouse. ROIs are magnified at x100 for inspection of the corpus callosum(d,e,f,g) and the striatum(h,i)

5.3.4 Discussion

Magnetic susceptibility maps of the *ex-vivo* mouse brain were registered using the transformations from the non-rigid registration of the magnitude data. Significant relative increases in susceptibility in the white matter of the rTg4510 mouse were observed using a voxel-wise group comparison. A loss of contrast was evident from visual inspection of the QSM maps between the white matter of the corpus callosum and the surrounding grey matter. This may be due to a reduction in diamagnetic myelin, which has been shown to be disorganised in this model in histology and in previous studies(205). In the previous chapter, increased diffusion perpendicular to the direction of the white matter in the rTg4510 tracts was observed, with greater significance observed in the rostral regions of the brain. This further indicates the possibility of reduced myelination which has also been observed using EM(205). However, rather than a decrease in diamagnetic tissue present, it may be the case that an increase in paramagnetic components are being observed. The increased presence of reactive microglia and astrocytes suggest neuroinflammation in the corpus callosum and striatum and have been linked to iron accumulation(220,221), as has the presence of NFT pathology(224) which is present in these regions in the rTg4510 at the age imaged(203). In this study, only a single animal from each group was analysed histologically. Staining for gliosis and iron in a greater number of animals would enable a more quantitative group analysis to be conducted as well tests for correlations with MRI parameters.

The use of gadolinium in the preparation of the *ex-vivo* tissue may have amplified the QSM changes in the rTg4510 and possibly masked the underlying pathological changes. The neurodegeneration that occurs in this model may cause damage to tissue in the rTg4510 that alters the uptake of the paramagnetic contrast agent. In the case of the rostral white matter, a greater concentration of Gd may be present due to disruption to myelin sheaths which may be responsible or be contributing to the increased magnetic susceptibility in the rTg4510. Interestingly, a loss of contrast with grey matter was not observed in the magnitude images which might be expected if an increased signal in the white matter were generated by the T1 shortening effect of an elevated Gd concentration. Since there is marked atrophy in the rTg4510 at the timepoint imaged, an irregular distribution of the contrast agent may also be the cause of both paramagnetic increase and decreases

observed in the striatum as well as decreases in magnetic susceptibility in other grey matter regions.

This preliminary study indicates that there may be changes in the magnetic susceptibility of tissue in the rTg4510 mouse model of Tau pathology that are detectable using QSM. It is unclear whether group differences stem from differences in the magnetic susceptibility in the tissue or alterations to contrast agent distribution. The following sections of this chapter attempt to answer this question by optimising and performing QSM in *ex-vivo* rTg4510 tissue omitting Gadolinium from the perfuse fixation process. This data is also used to validate data collected using an *in-vivo* protocol which suffers from a lower SNR and is acquired at a lower spatial resolution.

5.4 Development of gradient echo acquisitions for QSM in the mouse

5.4.1 Introduction

The biological interpretation of the differences in magnetic susceptibility in the rTg4510 relative to controls identified in the last section was confounded by the presence of Gadolinium. In order to repeat this experiment without contrast agent, the parameters of the gradient echo sequence used to acquire data must be adjusted to allow for the different MR relaxation properties of the tissue. The expected increase in the longitudinal relaxation constant will cause a reduction in the MRI signal at an echo time given the same time to repeat. The goal of the design of a gradient echo sequence for QSM is to provide pristine phase data. The precision of this data can be estimated by the uncertainty or variance of the estimated phase. Greater variance may reflect noisy estimates that will propagate through the susceptibility processing and manifest as artifacts in the maps produced. The variance of the phase is inversely proportional to the SNR of the magnitude of the MRI signal(104) as described by the formula(266)

$$\sigma_{phase} = \frac{1}{SNR_{mag}}$$

Equation 62

Where σ_{phase} is the standard deviation of the phase in radians and SNR_{mag} is the signal to noise ratio of the magnitude of the MRI signal. So by maximising the SNR of the signal magnitude, the uncertainty in phase estimation and noise in the susceptibility maps produced will be reduced. In spoiled gradient echo sequences, commonly used for QSM, the signal S_{SGRE} is given by the following equation(90)

$$S_{SGRE} = \frac{M_0 \, \sin\theta \, (1 - e^{-TR/T_1})}{(1 - \cos\theta \, e^{-TR/T_1})} . e^{-TE/T_2^*}$$

Equation 63

Where M_0 is the longitudinal equilibrium magnetisation and θ is the flip angle, known as the Ernst Angle when maximum signal is generated. This relationship can be used calculate the Ernst Angle in tissue of given T1 and T2* for a given TE and TR. Selection of TR will

depend on the total scan time, desired resolution and FOV of the acquisition and the number of signal averages taken. Longer TRs allow longitudinal relaxation to occur over a greater time period and more signal available for RF excitation. For a 3D spoiled GRE (SGRE) acquisition, the longest TR possible will be calculated by the division of the scan time limit by the number of excitations necessary to cover the FOV at the desired resolution. However, SNR is proportional to the square root of the number of signal averages(NSA)(266), assuming uncorrelated noise between transients, and TR will need to be reduced if extra averages are collected. This additional factor can be added to the equation above to incorporate the trade off between TR and NSA to calculate the Ernst Angle and provide optimal SNR as follows to select the SGRE sequence parameters that will yield lowest phase uncertainty.

$$SNR_{SGRE} = \left[\frac{M_0 \, \sin\theta \, (1 - e^{-TR/T_1})}{(1 - \cos\theta \, e^{-TR/T_1})} . e^{-TE/T_2^*} \right] . \sqrt{NSA}$$

Equation 64

The phase contrast generated by off resonance due to magnetic susceptibility will increase with time after excitation. Optimal phase CNR is achieved when the echo time is equal to the T2* of the tissue imaged (267,268). Where limitations due to scan time or spatial distortion at later echo times in T2* weighted sequences require earlier acquisition, a minimum of TE = T2*/2 may be used to provide an acceptable CNR for QSM applications(104). In this section, the T2* measured in the white matter in the corpus callosum of *ex-vivo* mice, was used to calculate the Ernst Angle that would maximise magnitude SNR and provide the most accurate phase estimates for QSM. T1 and T2* mapping of fixed *ex-vivo* mouse brains provided regional estimates that could be used in Equation 64 to simulate different combinations of TR and NSA within a 12hr overnight scan.

A main aim of this thesis is to investigate the potential of new pre-clinical MRI techniques for *in-vivo* imaging of AD mouse models for inclusion in a multi-parametric protocol. To this end, the mapping of relaxation parameters and Ernst angle calculations were also carried out to calculate optimal sequence parameters for an *in-vivo* acquisition. Phase estimation *in-vivo* is complicated by the presence of flow, most prominent in blood vessels. The flow of spins in the direction of an applied magnetic field gradient will cause them to accumulate phase and may lead to an error in signal phase as well as mislocalisation of signal in phase encoding directions. To improve accuracy of phase estimates, first order

gradient moment nulling was added to the SGRE sequence to provide flow compensation in three dimensions.

5.4.2 Methods

The experimental methods in this section are described in three parts: T1 and T2* mapping and regional estimates in *ex-vivo* and *in-vivo* animal cohorts; ernst angle simulations; and development and testing of a flow compensated 3D SGRE sequence.

5.4.2.1 T1 and T2* mapping and regional estimates

Animals

Ex-vivo animals had been culled at 8 months and perfuse fixed previously by collaborators as described in section 5.3.2.1 with the exception of the addition of Magnevist contrast agent which was omitted. The de-skulled brains of wild-type rTg4510 littermates (n=3) were rehydrated in 50ml PBS (Sigma-Aldrich, UK) for three weeks to increase proton density and T2 in the tissue(for increased SNR)(184,269,270). They were transferred to 20ml syringes filled with 10ml of proton MR signal-free, non-viscous Fomblin perfluoropolyether (PFS-1, Solvay Solexis SpA., Bollate, Italy) and imaged individually in a 26mm diameter birdcage coil (Rapid Biomedical GmbH, Germany) at 9.4T (Agilent 9.4 T VNMRS 20 cm horizontal-bore system / Agilent Inc. Palo Alto, CA, USA).

For *in-vivo* experiments, wild-type littermates (n=8) of a J20 AD mouse model were imaged at 15.5 months. Mice were secured in a cradle under anaesthesia with 1-2% isoflurane in 100% oxygen using a custom-built head holder to reduce motion. Body temperature was maintained at 36 – 37.5 °C using a water-heating system and warm air fan. Core body temperature and respiratory rate were monitored using a temperature probe and pressure pad (SA Instruments, NY). Scans were performed on an Agilent 9.4 T VNMRS 20 cm horizontal-bore system (Agilent Inc. Palo Alto, CA, USA). A 72 mm birdcage radiofrequency (RF) coil was used for RF transmission and a 2 channel mouse brain surface coil (RAPID, Germany) was used for signal detection.

T1 mapping and image acquisition

A single slice 4-shot segmented spin echo echo-planar imaging (EPI) readout was implemented with the following parameters: slice thickness = 0.5 mm, FOV =15 × 15 mm, matrix size = 100 × 100, slice selective inversion pulse width = 100 mm, 16 inversion times, TR=16.6 seconds. For the *ex-vivo* acquisition, TI = 9, 14, 22, 34, 52, 81, 126, 196, 304, 471, 732, 1140, 1760, 2700, 4300, and 6600ms, TE = 11 ms. For the *in-vivo* acquisition, TI = 30, 44, 65, 96, 141, 208, 306, 451, 664, 979, 1442, 2124, 3129, 4609, 6789, and 10000 ms, and TE=13ms. T1 maps were calculated using a conventional three parameter fit(271) at each pixel across magnitude values for all TIs using a non linear least squares curve algorithm in matlab.   Mean T1 values were calculated for each mouse in ROIs in the cortex and hippocampus.

T2* Mapping and image acquisition

A Spoiled 3D Gradient Recalled Multi-Echo sequence was used to acquire data for both *in-vivo* and *ex-vivo* T2* mapping.   The *ex-vivo* dataset was acquired with the following parameters 16 TEs (TE1 = 2.27ms, ΔTE=2.37ms), TR = 600ms, flip angle =44^0, NSA=3 at a resolution of 80μm x 80μm x 80μm , FOV = 18mm x 12mm x 12mm. Eight echoes were acquired for the *in-vivo* data: TE1 = 2.33ms and ΔTE=2.3ms, with a flip angle of 27^0 and TR=210ms, at a resolution of 150μm x 150μm x 150μm (FOV = 15mm x 15mm x 15mm). T2* estimates were calculated at each voxel using a non linear least square fitting algorithm in matlab using a two parameter fit function. ROIs were drawn in the cortex and corpus callosum and mean T2* values were calculated.

5.4.2.2 Ernst angle simulations

The T1 and T2* measured in the corpus callosum was used to optimise values of flip angle, TR, and NSA using Equation 64. Software was written in matlab to estimate maximum SNR and optimal flip angle for varying TR and NSA. For the *ex-vivo* scan, a time limit of 11 hrs was necessary to complete the scan within an overnight time slot on the 9.4T MRI scanner in CABI. At the desired resolution of resolution of 80μm x 80μm x 80μm and FOV = 18mm x 12mm x 12mm, the maximum TR was 1000ms for a single average. To optimise SNR, simulations were run for ten to one signal averages by varying the TR (100, 111.11, 125, 142.86, 166.66, 200, 250, 333.33, 500, and 1000 ms respectively) to complete in the desired scan time. Each TR/NSA combination was run for integer flip angles from 1 to 90

degrees) with the measured T1/T2* in the white matter (952ms and 32ms respectively) with TE=T2*.

The target time for the *in-vivo* scan was to run in approximately an hour, at a 150μm x 150μm x 150μm resolution FOV = 18mm x 18mm x 18mm, a single average could be taken with TR=250ms. To optimise SNR, simulations were run for ten to one signal averages by varying the TR (25, 28, 31, 36, 42, 50, 62.5, 83, 125, and 250ms respectively) to complete in the desired scan time. Each TR/NSA combination was run for integer flip angles from 1 to 90 degrees with the measured *in-vivo* T1/T2* in the white matter (1533ms and 29ms respectively). Due to poor SNR and distortion at late echo times, TE = T2*/2 of white matter was used for *in-vivo* simulations which is preferred in situations when TE = T2* cannot be achieved (104).

5.4.2.3 Flow compensation development and testing

To reduce error in phase estimates caused by flow in the *in-vivo* acquisitions, first order gradient moment nulling was added to the gradient echo sequence to provide flow compensation in three dimensions. Bipolar gradients were added to null the first moment for slice select, readout, and both phase encoding gradients. I achieved this by modifying the core 3D GRE sequence code in VNMRJ. As shown in Figure 47, the nulling of the slice select gradient is carried out by addition of a bipolar gradient immediately after the slice select gradient and nulling of readout and phase encoding gradients was implemented simultaneously, immediately before the start of the readout rephase gradient. Bipolar gradients were trapezoidal in shape and magnitudes and duration were calculated using equations previously published(272). These values were not 'hard coded' and calculated based on the imaging gradient dimensions generated by VNMRJ. This flexibility means that the bipolar gradients are automatically adjusted in this sequence if the user changes any sequence parameters such as the TE and enables easy portability of this functionality into other 3D sequence code.
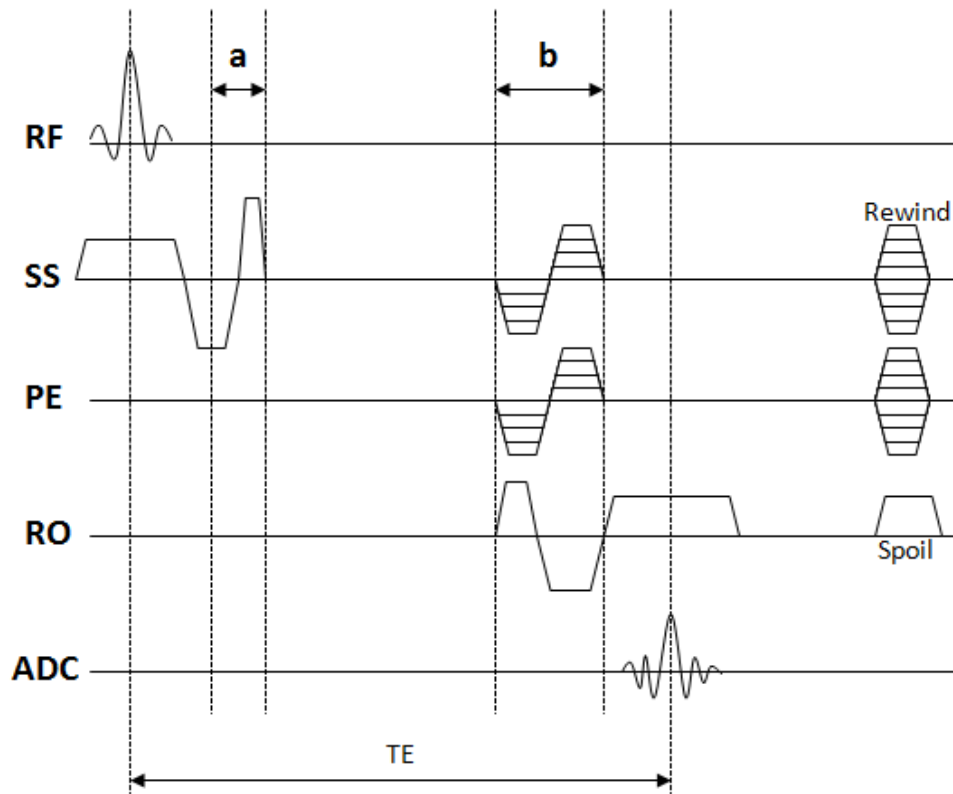
Figure 47. **Flow compensation gradient diagram**

Sequence diagram showing the placement of bipolar gradients to implement first order gradient moment nulling. Slice select gradient is nulled using the bipolar gradient in interval a, and all other bipolar gradients are implemented in interval b, prior to read refocus gradient.

A flow phantom (Figure 51a) was constructed to test the 3D gradient moment nulling added to the sequence. A section of plastic tubing of 2.5mm inner diameter was embedded in a 20ml falcon tube filled agar (1%). The ends of the tubing were connected at each end to a water heating system (Haake Circulator DC30 with B3 bath, Thermo Haake, Newington NH, USA). The system was configured to pump water through the tubing at a flow rate of 12.5 l/min at room temperature. The effects of phase accumulation of the flowing spins can be observed in MRI phase images as disruptions to wrapping in the direction perpendicular to flow(266). The phantom was imaged in a 26mm diameter birdcage coil (Rapid Biomedical GmbH, Germany) with a 3D gradient echo sequence with the following parameters: TE = 18.5ms, TR=250ms, flip angle =29, FOV = 18mm x 18mm x 18mm, matrix = 96 x 32 x 32. Data was acquired without flow compensation with water

flow on and off to observe the effects on phase. This experiment was then repeated with flow compensating gradients implemented in the sequence.

5.4.3 Results

5.4.3.1 T1 and T2* mapping and regional estimates

Parameter maps of T1 and T2* in *ex-vivo* and *in-vivo* mice are shown in Figure 48. Mean values in ROIs were in good agreement with published relaxation measurements at 9.4T (273,274). *Ex-vivo* estimates of T1 in the cortex and corpus callosum were 1063±66 ms and 952±32 ms respectively. T2* values measured were 65±3ms in the cortex and 32±7 ms in the corpus callosum. *In-vivo* measurements of T1 were higher than their *ex-vivo* equivalents. Unlike the cortex, where the T1 (1917±109 ms) was similar to reported values(274), a reduced T1 was found in the corpus callosum (1533±107 ms) possibly due to discrepancies in the age and breed of the mice used. The T2* measured in the cortex (37±2ms) and in the white matter (29±2ms) were lower than the *ex-vivo* estimates and similar to previous high field measurements(275).
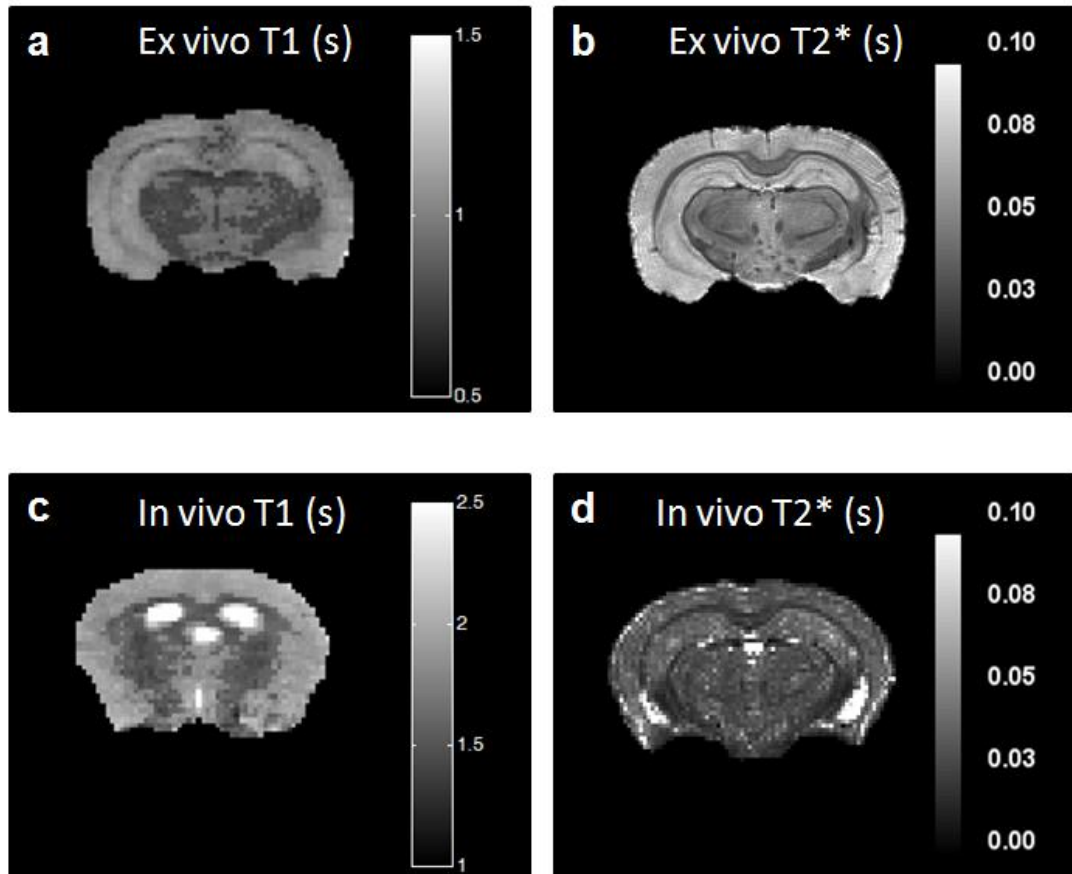
Figure 48.   **Ex vivo and In-vivo T1 and T2* maps**

Single slice coronal images of *Ex-vivo* (a,b) and *In-vivo* (c,d) T1 and T2* maps.

5.4.3.2 Ernst angle calculations

The simulated SNR calculated in the *ex-vivo* data using the relaxation parameters calculated for white matter (T1 =952 ms, T2*=32ms) is shown in Figure 49. The optimal flip angle decreased as TR was reduced in the simulation and SNR was found to increase with the number of averages (Figure 49a). The percentage gain in SNR decreased with the addition of each average (Figure 49b). The SNR increased by 3.1% by increasing NSA from 1 to 2. However, increasing the number of signal averages beyond 5 resulted in percentage increases of less than 0.1%. In light of such minimal gains in SNR, it was decided to limit NSA to 5 so as to maintain as long a TR as possible. This maximises the scanner "dead time" built into each repetition, reducing heating in the scanner coils and amplifiers(276). The combination of 5 signal averages with a TR of 200ms gave and optimal flip angle of 36 degrees in white matter and 34 degrees in grey matter in simulations (Figure 49c).
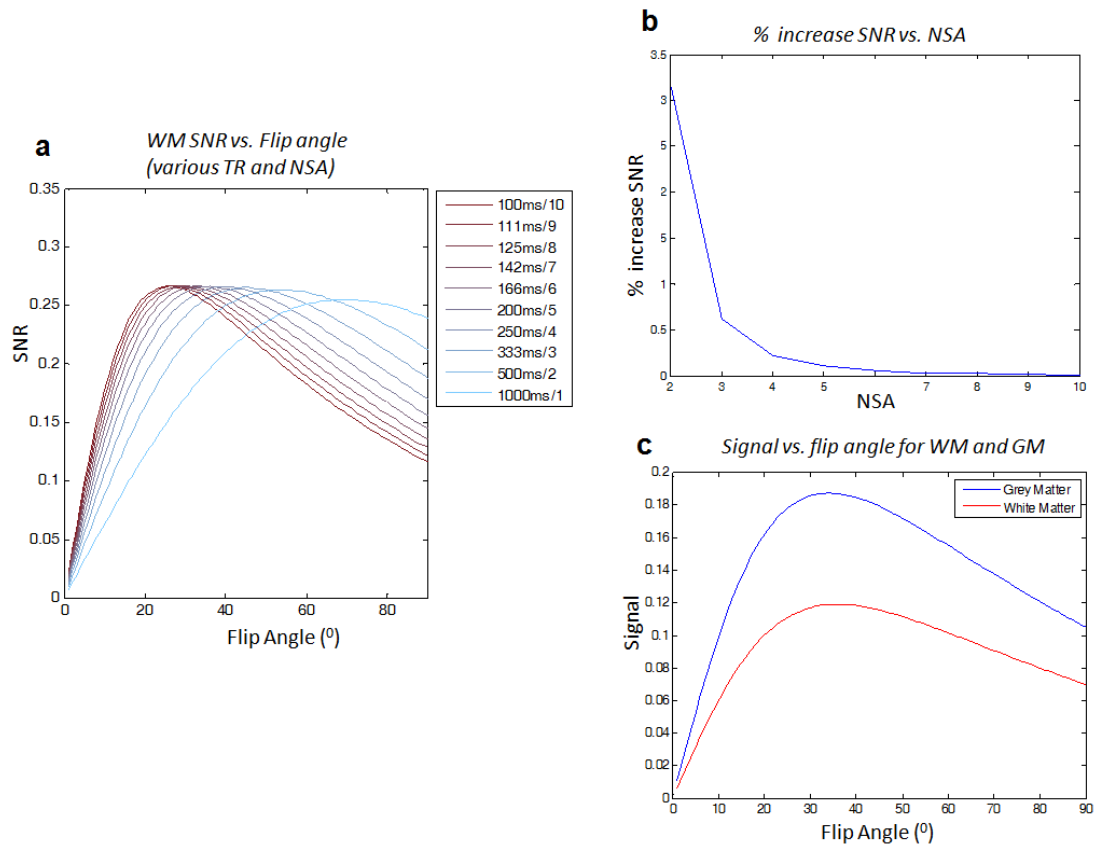
Figure 49.   **Ex vivo signal estimates**

Simulations using the gradient echo equation to estimate SNR for different TR and NSA combinations using white matter relaxation parameters(a). The percentage gain in SNR decreases with increasing NSA(b). Signal for grey matter and white matter is plotted against flip angle for TR =200ms and NSA = 5(c).

The simulated SNR calculated in the *in-vivo* data using the relaxation parameters calculated for white matter (T1 =1533 ms, T2*=29ms) is shown in Figure 50. The flip angle at which maximum SNR is achieved, decreased as TR was reduced in the simulation and there was only a slight gain in SNR observed for the extra averages acquired (Figure 50a).   The percentage increase in SNR by taking two averages over a single average was less than 0.1%.   The signal in grey matter and white matter was simulated for a single average and a TR of 250ms indicating an optimal flip angle of 32 degrees in white matter and 29 degrees in grey matter (Figure 50b).   *In-vivo* data acquired (n=1) with at a TE of 15ms repeated at multiple flip angles was in good agreement with simulations indicating a maximum signal at a flip angle of 32 degrees in white matter (Figure 50c).
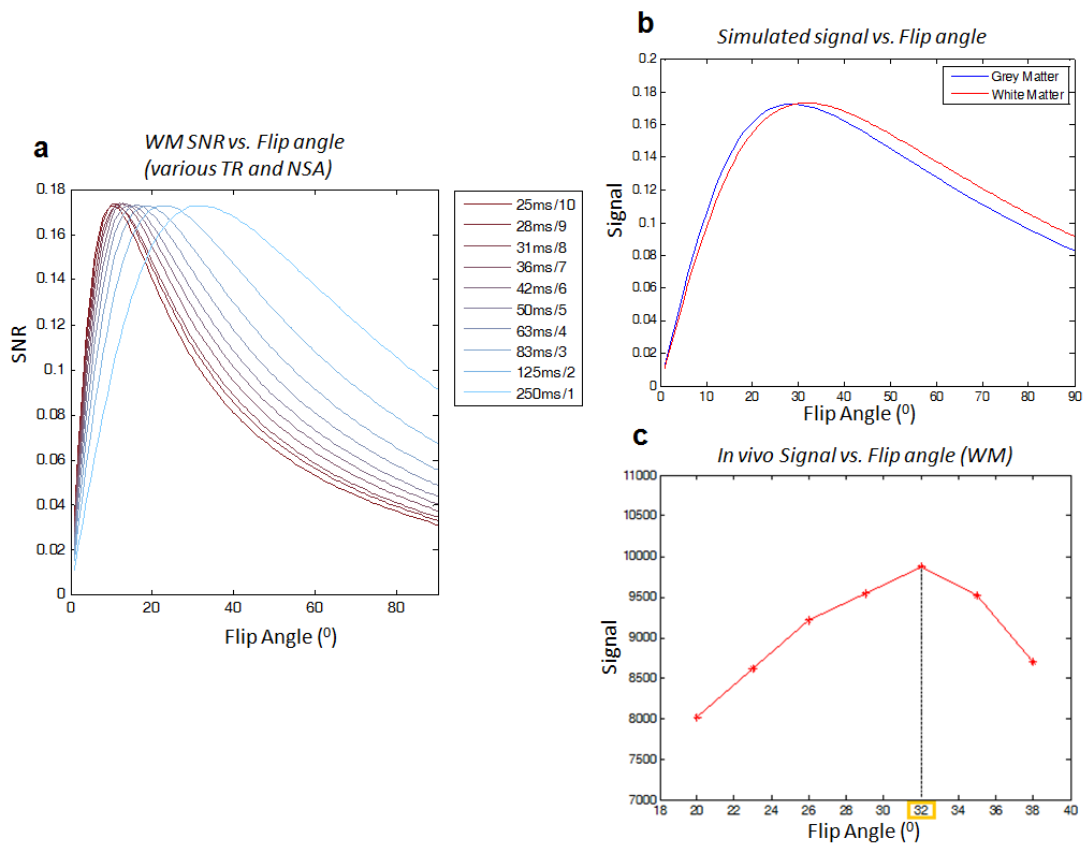
Figure 50.   In-vivo signal estimates

Simulations using the gradient echo equation to estimate SNR for different TR and NSA combinations using white matter signal relaxation parameters(a). Simulated signal for grey matter and white matter is plotted against flip angle for TR =250ms and NSA = 1(b). *In-vivo* measurements of white matter signal plotted against flip angle(c).

5.4.3.3 Flow compensation development and testing

Magnitude images of a cross section of the flow phantom indicate the flowing water region within the water bath tubing surrounded by agar (Figure 51a). When the water bath flow is turned off, the phase images display complete phase wrap lines that pass through the water tube horizontally across images (Figure 51 b,c). When the flow was turned on, the wrap lines are disturbed in the flowing section of the phantom as the phase of spins in the flowing water accumulate phase in the direction of flow (Figure 51d). This accumulation was corrected and the artifacts markedly reduced when the flow compensation gradients are turned on and complete phase wrap lines can be observed in the presence of flow (Figure 51e).

143
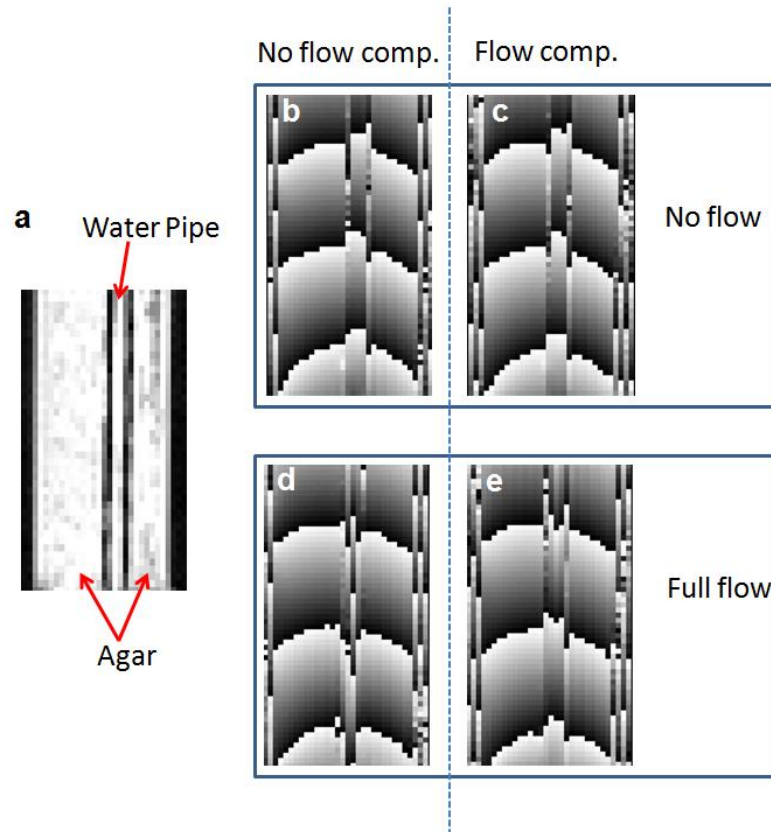
Figure 51. **Flow compensation phantom**

Magnitude image of flow phantom(a) with phase images of the same slice where the water is not flowing (b,c) and when the flow is switched on(d,e). The effect on the phase of the flowing water can be observed by the disruption to the wrapping pattern(d) that is corrected by addition of flow compensation gradients(e).

5.4.4 Discussion

In this section, ernst angle simulations were carried out to optimise the SNR of the signal magnitude of a 3D spoiled gradient recalled echo sequence both *in-vivo* and *ex-vivo*. T1 and T2* mapping was conducted to provide estimates in white matter and grey matter regions that could be used to calculate the flip angle to generate greatest signal at the desired echo time. Optimal values for TR and NSA were calculated for given scan times to maximise SNR.

The signal relaxation values used in simulations were generated through T1 and T2* mapping and ROI estimates. These were in good agreement with values reported in previous studies(261,274,275). The T1 estimates were greater *in-vivo* than *ex-vivo* which

may be due to both differences in the imaging temperature and fixation effects. The *in-vivo* imaging was conducted at body temperature compared to the room temperature at which *ex-vivo* imaging was carried out. There is a known increasing relationship between spin-lattice relaxation and temperature(277). T1 has also been shown to be reduced in tissue fixed using aldehydes thought to be due to the chemical reactions that occur during fixation(269). Increases in temperature and use of formaldehyde fixative have been shown to also decrease T2(269,277). However, it has been shown that the reduction due to fixative can be reversed through rehydration of tissue using PBS(269) as carried out in this study. The increased T2* observed in the *ex-vivo* tissue is contradictory to the expected decrease in the T2 component due to temperature. The use of smaller voxels and improved field homogeneity reduce dephasing of the transverse MR signal(278) and in addition to greater tissue hydration may be responsible for the elevated T2* measurements in the *ex-vivo* data.

To maximise phase SNR, the *ex-vivo* simulations used an echo time equal to the T2* of white matter. At this echo time, maximum magnitude SNR was produced with a flip angle of 36 degrees, a TR of 200ms and five signal averages. An echo time of half of the T2* measured in white matter was used in the *in-vivo* ernst angle simulations and a maximum SNR was calculated at a flip angle of 32 degrees for a single average with a TR of 250ms. This simulated experiment was in good agreement with empirical data collected. First order gradient moment nulling improves phase estimation of spins moving with a constant velocity. However, it should be noted that there may be extra phase components not accounted for from the acceleration of spins (caused by turbulent flow in vessels) and inconsistent field gradients in the direction of movement. Techniques to correct for these effects have been reported and are a subject of current research (279,280). Nevertheless, the flow compensation implemented here will improve phase estimation caused by mislocalisation of signal and accumulation of spins due to motion at a constant velocity(104,279,281). Spoiled gradient recalled echo acquisitions that include this flow compensation, in combination with the optimised parameters from the ernst angle simulations carried out in this chapter, should provide ideal data for QSM under these *in-vivo / ex-vivo* experimental conditions.

5.5 In-vivo and Ex vivo QSM in the rTg4510

5.5.1 Introduction

Quantitative Susceptibility Mapping has been shown previously to correlate to iron concentrations in tissue(242,282) and myelin in white matter(213,275), both of which are thought to be altered in AD(161,216). In a recent clinical study, significant increases in magnetic susceptibility were detected in AD patients relative to controls in the putamen, a sub region of the striatum(250). There have been few studies in mouse models of AD but in common with T2* studies of iron, none have been performed in mice exhibiting tau pathology. The magnetic susceptibility findings and histology in the preliminary study in section 5.3.3 suggest that QSM may be sensitive to white matter damage and neuroinflammation in grey matter regions in the rTg4510. The loss of contrast between rostral white matter and surrounding grey matter that was visually apparent in the mean magnetic susceptibility maps may be due to reduced myelin. This is supported by the increased radial diffusivity and reduced FA measured in the genu region of the corpus callosum of the rTg4510 presented in chapter 4. Furthermore, abnormalities in myelination in the rTg4510 have been observed at 4 months of age using electron microscopy(205). Magnetic susceptibility measurements have been shown to be more specifically related to myelin concentration than measures of diffusion using DTI(213). QSM may therefore provide a non invasive method to measure myelin content in tissue and to track early white matter damage *in-vivo* in the rTg4510.

The increased presence of reactive microglia and astrocytes known to occur in regions of NFT pathology in the rTg4510(70,87) were observed in the corpus callosum and striatum in section 5.3.3. Gliosis is associated with oxidative stress and the accumulation of iron which may be responsible for the increases in magnetic susceptibility in these regions. The rTg4510 may provide the opportunity to further understand the relationship between iron accumulation and tau pathology in the absence of plaques. Measurement of iron concentration *in-vivo* using QSM may constitute a novel biomarker of neuroinflammation in the rTg4510 and a means by which to test iron chelating therapeutics.

In this study, the sensitivity of QSM to NFT pathology in the rTg4510 is investigated. *In-vivo* and *ex-vivo* data are acquired using the gradient echo acquisitions optimised in the

previous section. Commonly used methods for phase unwrapping and background field removal are evaluated and a QSM post processing software pipeline is developed. Magnetic susceptibility maps are generated and group comparisons are made between rTg4510 mice and wild-type controls. Regions of interest were selected to be comparable to those used in the DTI study (Figure 34, section 4.4.2.3) and based on the voxel-wise increases detected in the striatum and rostral section of the corpus callosum in the pilot study(Figure 43, section 5.3.3). T2* mapping estimates were taken in corresponding regions and comparisons are presented between QSM measurements and this more established MRI method of estimation of iron concentration *in-vivo*.

5.5.2 Methods

Animals

Generation of homozygous rTg4510 transgenic mice has been reported previously(203). Female rTg4510 mice were licensed from the Mayo Clinic (Jacksonville Florida, USA) and bred for Eli Lilly by Taconic (Germantown, USA). Mice were imported to the UK for imaging studies at CABI. All studies were carried out in accordance with the United Kingdom Animals (Scientific Procedures) act of 1986.

Imaging

All imaging was performed with a 9.4 T VNMRS horizontal bore scanner (Agilent Inc.). *In-vivo* imaging was conducted on N = 10 rTg4510 mice and N = 10 wild-type controls. A 72 mm inner diameter volume coil (Rapid Biomedical) was used for RF transmission and signal was received using a 2 channel array head coil (Rapid Biomedical). Mice were anaesthetised under 2% isoflurane and were immobilised by securing the head using a bite bar within the anaesthesia nose cone and ear bars that protruded inward from the sides of the mouse bed apparatus (Rapid Biomedical). Anaesthesia was then maintained at 1.5% isoflurane in 100% O_2 throughout imaging. Core temperature and respiration were monitored using a rectal probe and pressure pad (SA instruments). Mice were maintained at ~37 °C using heated water tubing and a warm air blower with a feedback system (SA instruments). Shimming was performed using an automatic 3D gradient echo shim function (VNMRJ, Agilent Inc.) with a voxel containing the cortex (linewidths were 47±7 Hz). Data for QSM was collected using a 3D single echo spoiled gradient recalled echo sequence with flow compensation in three dimensions. Subsequently, a multi-echo sequence was

run without flow compensation to acquire data for T2* mapping. Parameters for both sequences are provided in Table 2.

In preparation for *ex-vivo* imaging, perfusion fixation was carried out by laboratory collaborators. Animals were terminally anaesthetised with Euthanal administered via intraperitoneal injection immediately after *in-vivo* imaging. Fixation was then carried out by perfusion through the left ventricle: first with 15 – 20 mL of saline (0.9%) and heparin; second with 50 mL of buffered formal saline, at a flow rate of 3 mL per minute. Brains were then removed and stored in-skull at 4 $^{\circ}$C in buffered formal saline. After 4 weeks, brains were transferred to PBS (50ml refreshed weekly, Sigma-Aldrich) for rehydration (184,269,270) for a further 3 weeks. *Ex-vivo* imaging was conducted on N = 8 rTg4510 mice and N = 8 wild-type controls using a 3D spoiled GRE acquisition with parameters given in Table 2. Brains were secured individually in a 20ml Syringe filled with 10ml proton MR signal-free, non-viscous Fomblin perfluoropolyether (PFS-1, Solvay Solexis SpA., Bollate, Italy) prior to imaging in a 26mm diameter birdcage coil (Rapid Biomedical GmbH, Germany) at 9.4T. Shimming was conducted using a pulse a collect sequence generating a linewidth of 47±5 Hz.

Parameter	*In-vivo* Single Echo	*In-vivo* Multi Echo	*Ex-vivo* Multi Echo
TR (ms)	250	250	200
minTE/dTE/maxTE (ms)	15	2.31/2.46/29.32	3.05/3.92/46.21
FA (^{0})	32	32	36
NE	1	12	12
Averages	1	1	5
Scan time	1hr,2s	1hr,2s	10hr,45min,2s
Spectral width (Hz)	50000	100000	73529
FOV (mm)	18x18x18	18x18x18	18x17.2x14.4
Matrix	120x120x120	120x120x120	225x215x180
Iso. Resolution (µm)	150	150	80

Table 2.   Spoiled GRE sequence parameters

Registration and mask generation

With the exception of the preliminary brain separation step, a group wise registration of the magnitude images was conducted by collaborators using an automated pipeline described in section 5.3.2.2. Masks of the brain were generated automatically for generation of susceptibility maps which were then transformed back into the atlas space using deformation fields from the non-rigid registration. Mean susceptibility images were generated in this space for WT and rTg4510 groups.

QSM pipeline optimisation

Reconstruction of the phase of the *in-vivo* data involves a preliminary processing step where phase data from the two receive array coils is combined to remove phase shifts between channels. This was achieved using a global offset correction technique(283). The offset was calculated as the mean difference in phase between the two coils calculated in a ROI measuring 10x10x10 voxels in the centre of the brain. The receiver offset was then removed by global subtraction of the mean difference calculated from each voxel of one coil. The coil phases with the offset removed were then combined by weighted average. The magnitude at each voxel provided the weighting to suppress noise(283).

There are a number of methods by which to generate magnetic susceptibility maps from reconstructed phase data. All involve three basic stages: phase unwrapping; background field removal; and magnetic susceptibility calculated through dipole inversion. More information on these standard methods can be found in section 2.8. Comparisons were made between algorithms that are freely available to download and commonly used in the literature. Evaluation was done both qualitatively though visual observation of artifacts in processed data and quantitatively by calculating the standard deviation and CNR of the processed phase in ROIs. A rostral slice was chosen for the quantitative analysis and ROIs were drawn manually in the corpus callosum and cortex across five slices in five wild-type mice selected at random from the cohort imaged (the analysis was repeated in rTg4510 mice to ensure no bias in the processing methodology had been introduced). The CNR in the phase was calculated as

$$CNR = \frac{\overline{wm} - \overline{gm}}{0.5 * (\sigma_{wm} + \sigma_{gm})}$$

Equation 65

149

where $\overline{wm}$ and $\overline{gm}$ are the mean of the white matter and grey matter regional measurements and σ_{wm} and σ_{gm} are the standard devations of the voxels within an ROI.

Two commonly used phase unwrapping algorithms are path based and laplacian based techniques. Phase data was unwrapped in 3D using algorithms downloaded online from the MEDI toolbox (Cornell MRI Research Lab). For path based unwrapping, the *unwrapPhase.m* algorithm was used and *unwrapLaplacian.m* was implemented for laplacian unwrapping. Background field removal comparisons were made for the projection onto dipole fields (PDF) (*PDF.m*, MEDI toolbox, Cornell MRI Research Lab) (107,262) and Variable Sophisticated Harmonic Artifact Reduction for Phase data (VSHARP)(284,285) methods. The kernel width used in the VSHARP method equates to the diameter of a spherical mean value filter used. The diameter chosen is a trade-off between the amplification of phase error using small widths and the increased erosion of data around the periphery of the brain using wider kernals(285). To prevent erosion of white matter structures, the kernel width was limited to k=3 voxels for the *in-vivo* data and k=9 for the *ex-vivo* data. Once the field maps were optimised, the dipole inversion step was performed using thresholded k-space division. The k-space filter threshold was varied between values of 2 and 10.

The multi echo sequence used to collect the *ex-vivo* data required a further step of optimisation where field maps and susceptibility maps were compared to select the echo to use for QSM group comparisons. A frequency field map may be generated by fitting phase values from a multi echo sequence across time. To investigate the possibility of generating field maps by combining phase data from difference echoes in the *ex-vivo* data, phase was unwrapped across echo times voxel by voxel using the *unwrap* function in matlab before linear fitting using a least squares algorithm. The gradient of the linear fit at each voxel was used to generate a field map of frequencies prior to susceptibility mapping by TKD.

QSM and T2* group comparisons

The outcome of the post processing optimisation experiments were used to develop a QSM pipeline for the *in-vivo* and *ex-vivo* data sets. After coil combination, *in-vivo* phase data were unwrapped using the laplacian method before background field removal using VSHARP (k=3 voxels). TKD was performed on the field map using a threshold t=5. *Ex-vivo*

QSMs were generated by path based unwrapping of the fourth echo followed by VSHARP background field removal (k=7 voxels) and TKD using a threshold t=5. Susceptibility values at each voxel were then calculated for all QSMs relative to the mean susceptibility of the whole brain, calculated using the masks from the registration. T2* estimates were calculated at each voxel across all echoes using a non linear least square fitting algorithm in matlab using a two parameter fit function.

Mean QSM and T2* estimates were calculated for within the ROIs shown in Figure 52. Regions in the corpus callosum and striatum in a rostral part of the brain were chosen based on the increases in susceptibility in the rTg4510 in these regions in the pilot study(Figure 43, section 5.3.3). In the previous chapter, NFT pathology was quantified histologically in a caudal region of the brain(Figure 35, section 4.4.3.1), and corresponding ROIs in these slices were taken in the QSM and T2* data. ROIs were drawn manually on the magnitude atlas image using Amira software and then back propagated by a collaborator on to the susceptibility maps in their original space using deformation fields from the non rigid registration. Errors in segmentation propagation were corrected manually using Amira software. The reported p-values are from standard t-tests for differences in parameters between the rTg4510 and WT groups, unless stated otherwise.
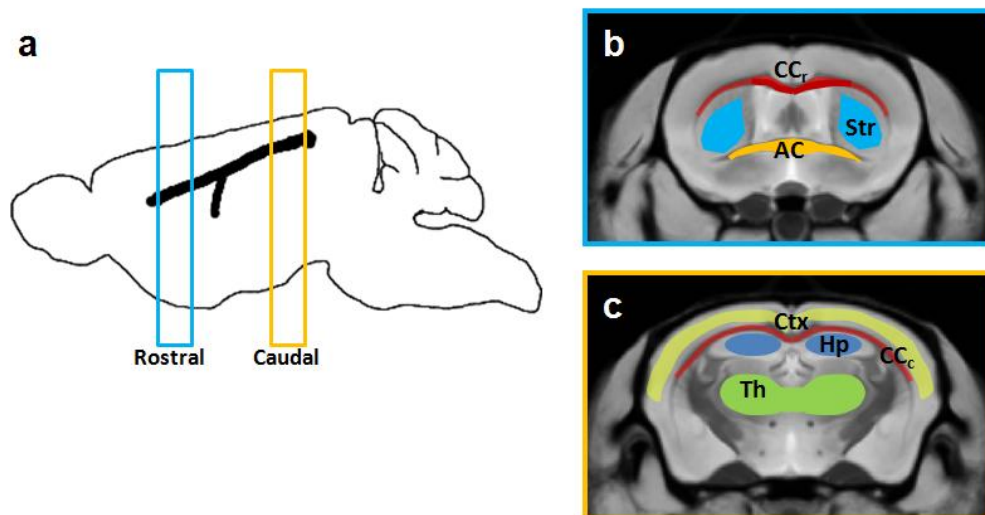
Figure 52.   ROIs for group comparisons

ROIs were drawn in rostral and caudal sections of the brain(a). In the rostral section(b), the corpus callosum CC_r, Striatum, Str, and Anterior Commissure, AC, were segmented. In the Caudal section (C) regions were drawn in the Cortex, Ctx, the Hippocampus, Hp, the Thalamus, Th, and the Corpus Callosum, CC_c.

5.5.3 Results

5.5.3.1 QSM optimisation

5.5.3.1.1 Optimisation of ex-vivo QSM post processing

To compare phase unwrapping methods in randomly selected wild-type mice (n=5), laplacian and path based region growing algorithms were combined with PDF and VSHARP(k=3) to generate field maps. Reduced variations and artifacts were observed for both background field removal unwrapping using the region growing algorithm (Figure 53 a,b). In the field maps where laplacian unwrapping was used (Figure 53 c,d) the PDF method fails to remove variations across the brain and there are ripples and more local dipolar artifacts observed in the VSHARP image.
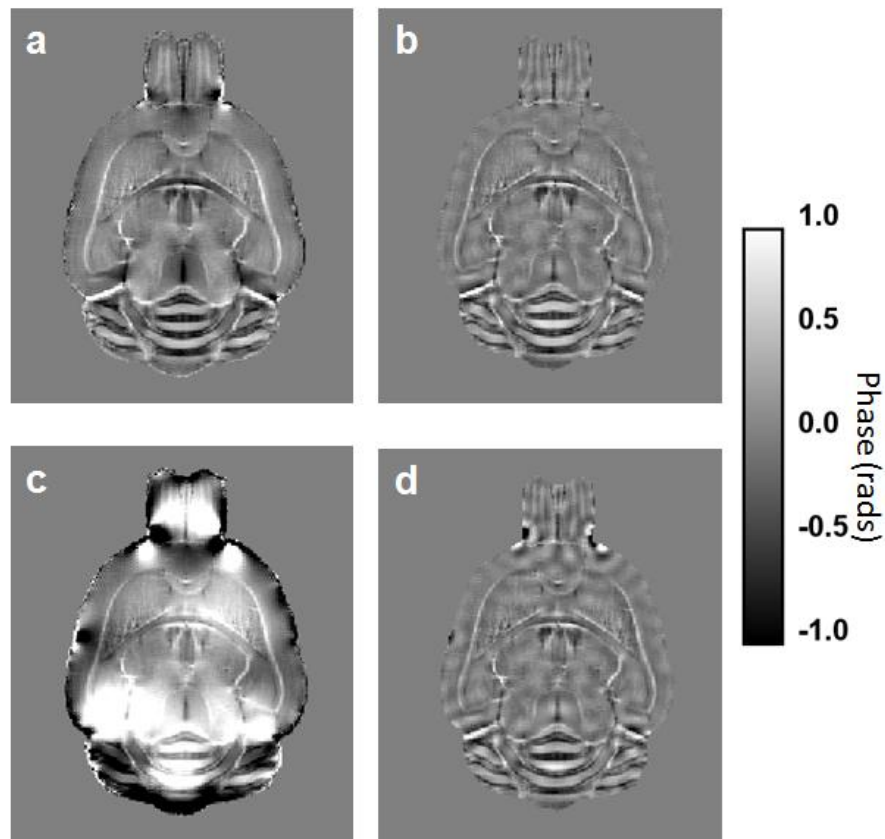
Figure 53.   Phase unwrapping comparison

Axial images showing a path based region growing unwrapping algorithm combined with PDF background field removal(a) and the VSHARP method(b). Images are also shown for Laplacian unwrapping combined with PDF background field removal(c) and the VSHARP method(d).

To compare PDF and VSHARP background removal techniques, ROIs were taken in the cortex and corpus callosum to measure mean standard deviation of the phase of the voxels in the ROI and mean CNR for the mice in these regions in the field map of the fifth echo. The phase was unwrapped using the region growing algorithm and the background field contributions were removed using VSHARP with kernel widths of 3, 5, 7, and 9 as well as PDF. In the corpus callosum, the phase standard deviation increased as the kernel was widened, and was even larger using the PDF method (Figure 54a). The contrast between grey matter and white matter was also greater at larger kernel widths and the CNR is greatest at k=9 voxels using VSHARP (Figure 54b). The larger the kernel width, the more of the periphery of the brain is eroded using the VSHARP method, and at a width of 9 voxels, the white matter of the external capsule was eroded in some mice particularly in the rTg4510 mice where there is significant atrophy in the cortex at the age studied. A kernel size of 7 voxels was selected as optimal since the CNR is similar to that achieved with a width of 9 (Figure 54b) and is greater than with the PDF method. The improved contrast and uniformity within the cortex was observed in the field maps at this kernel size (Figure 54d) compared to smaller kernals where ripples remain in the cortex (Figure 54c) and PDF where dipolar artifacts are observed near the olfactory bulbs(Figure 54e).
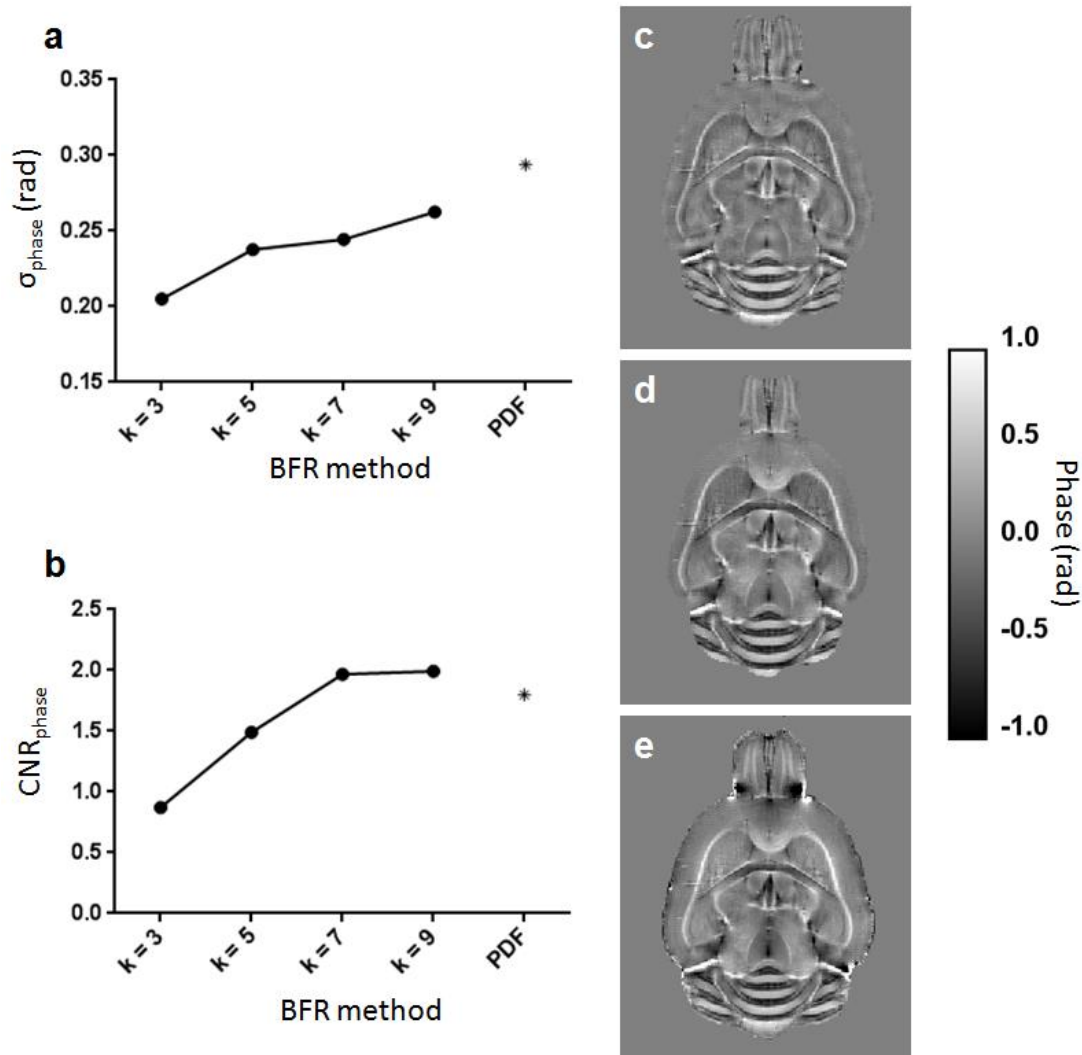
Figure 54.   **Ex vivo BFR comparison**

Comparison of mean phase standard deviation in the corpus callosum(a) for VSHARP field removal with kernel sizes 3 to 7 and PDF method. CNR between WM and GM is at a maximal with the VSHARP method and a kernel size of 9(b). Example phase field maps are shown for VSHARP k=3(c),7(d) and PDF(e).

The SNR of the phase signal in white matter is maximum at TE=T2*, however, the SNR of the signal sampled is reduced due to T2* decay at longer echo times which may increase variability and error in phase estimates. Field maps and susceptibility maps were generated for each mouse and values of phase variability and CNR was measured in the grey matter and white matter ROIs for both sets of data. The field maps were generated by unwrapping using the region growing algorithm before field removal using VSHARP (k=7). QSMs were calculated by TKD using a threshold t_F=5. Mean variability in the corpus

callosum ROI increased with echo time and CNR in both the field maps and susceptibility maps peaked at the fourth echo (Figure 55a-c). At this echo, susceptibility maps appeared to have greater contrast and less noise than those generated for earlier and later echoes(Figure 55d-f).
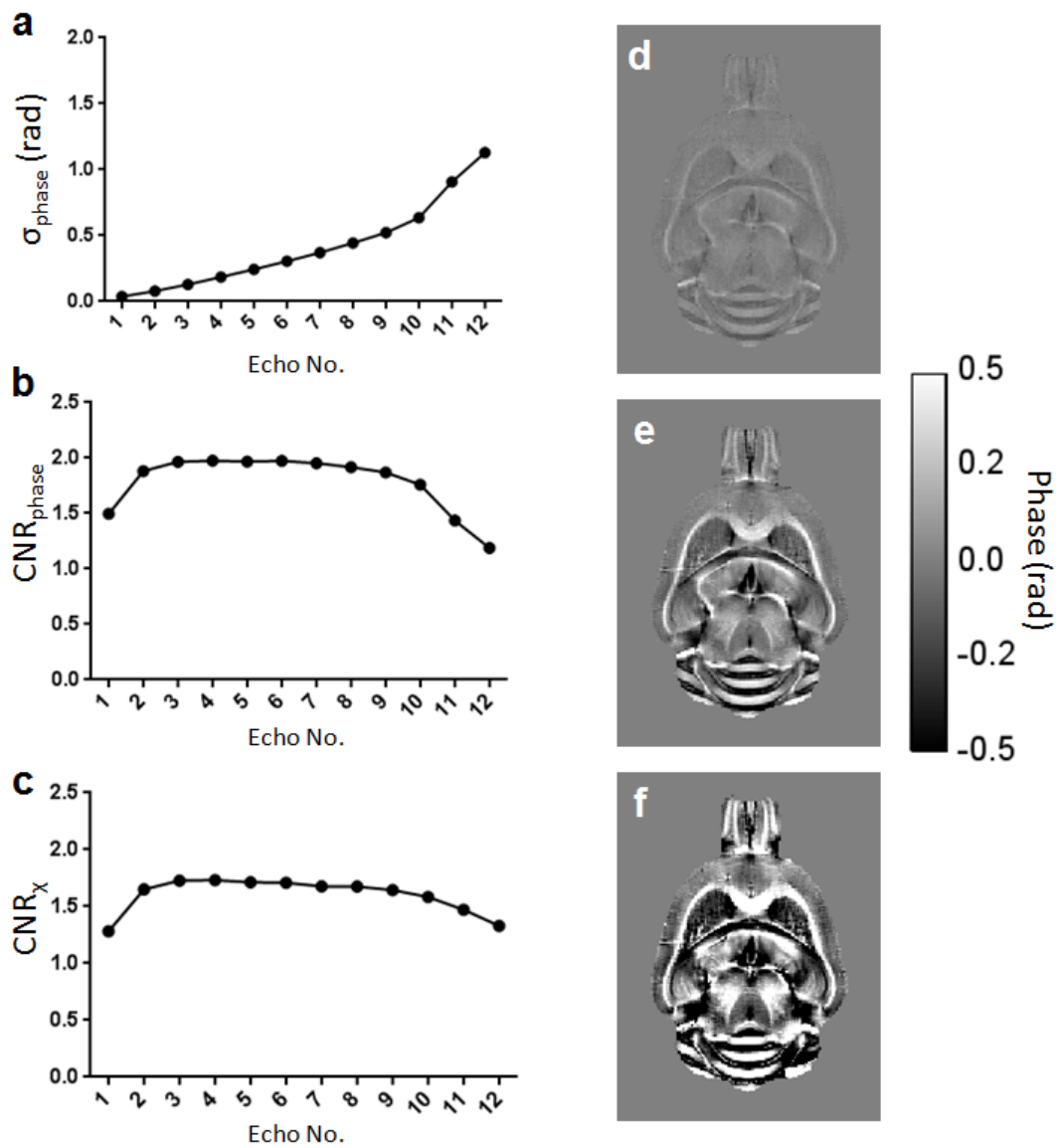
Figure 55.   Ex vivo echo comparison

a)Phase s.d. vs echo, b) CNR in field map vs echo, c) CNR in susceptibility map vs echo, and field maps of echo=1, 4,and 10 respectively (path based unwrapping with vSHARP BFR(k=7) TKD threshold =5)(d,e,f). CNR calculated between grey matter and white matter ROIs.

The final optimisation step involved selection of a TKD threshold value, t_F. At larger values of t_F, less data is removed through truncation of the k-space filter and a better estimate of the susceptibility is expected, however more noise will be included in the inversion generating artifacts in the susceptibility maps. Mean values of susceptibility in the white matter regions are shown in Figure 56a. The values appear to decrease, converging towards a minimum value as the t_F value increases. Conversely, the variability in the susceptibility values increase with t_F value (Figure 56b). The CNR of the grey matter and white matter regions reaches a maximum value at t_F=6, although there is a minimal increase from t_F=5(Figure 56c). The increased CNR is evident in susceptibility maps generated from larger t_F values (Figure 56d,e). At Echo 4, t=5, susceptibility in the corpus callosum was -28±2ppb, and in the cortex was -3.6±1.3ppb, and the mean difference of white matter relative to grey matter was -31±3ppb. This is in reasonable agreement with a previous study at 9.4T which reported a mean difference value of -29.8ppb between white matter and grey matter in control mice(286). To ensure that the optimisation did not bias the post processing towards the wild-type animals, measurements were taken in a randomly selected group of rTg4510 mice (n=5). ROIs were taken in the corpus callosum and cortex and CNR in susceptibility maps was measured for each echo and for multiple t_F values, repeating the wild-type experiments described above. The results were in good agreement with those from the WT group with CNR peaking in susceptibility maps at the fourth echo collected and at a TKD threshold equal to 5(data not shown).
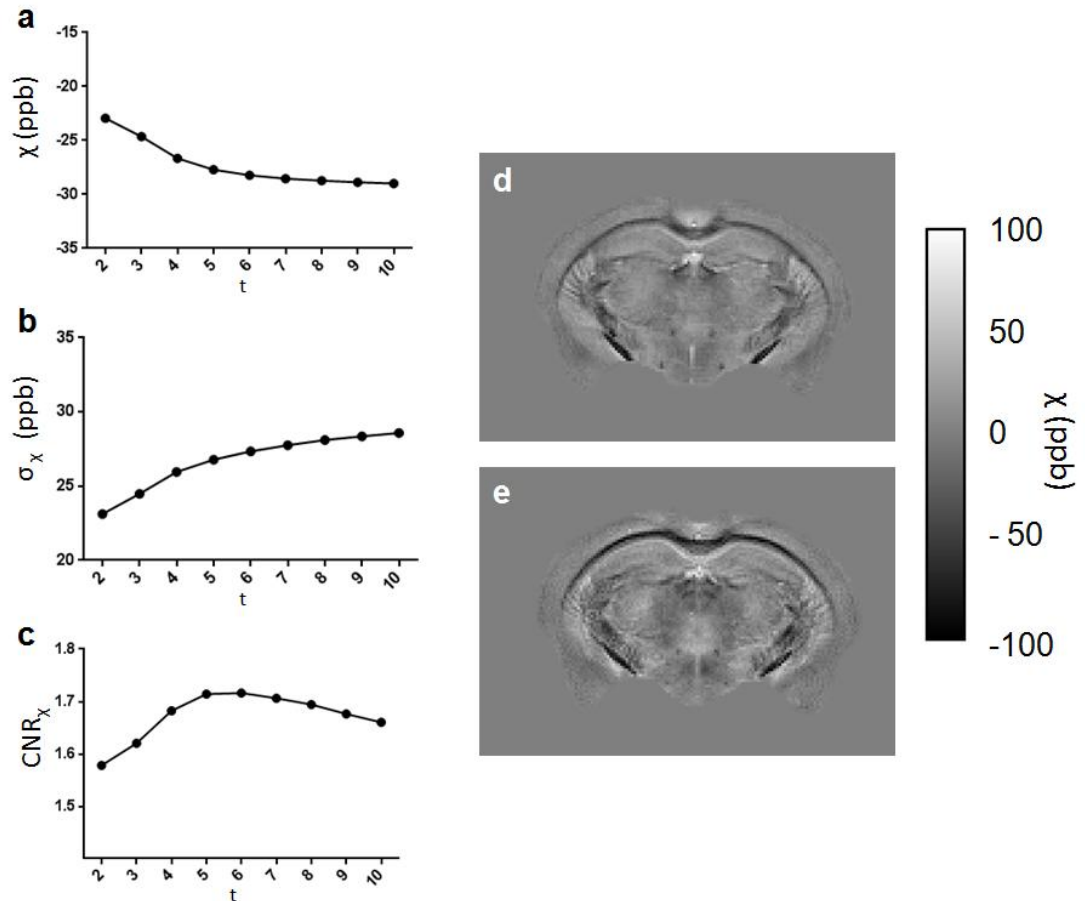
Figure 56. **Ex vivo t_F value comparison**

Mean susceptibility in corpus callosum vs t value(a), s.d. of susceptibility in corpus callosum(b), susceptibility CNR of white matter grey matter vs t value(c). Examples of susceptibility maps at t=2(d) and t=10(e) respectively showing increased contrast but increased noise from streaking artifacts.

5.5.3.1.2 Optimisation of in-vivo QSM pipeline

The phase data was reconstructed from the *in-vivo* imaging data and after coil combination, post processing algorithms were compared through mean measurements in ROIs in n=5 WT animals as in the *ex-vivo* optimisation. Firstly, phase unwrapping was done using both laplacian and path based methods and the background field was removed using PDF and VSHARP techniques. For the VSHARP method, the kernel size was restricted to three voxels due to the significant erosion of the cortex at larger widths. The variability in the field map phase was much reduced using the VSHARP field removal method (Figure 57a). The use of laplacian phase unwrapping with VSHARP produced the lowest standard deviation in the phase. Additionally, the CNR in the field maps between the white matter

and grey matter ROIs was greatest using this combination of techniques (Figure 57b). Example field maps for a single mouse are shown in Figure 57c.
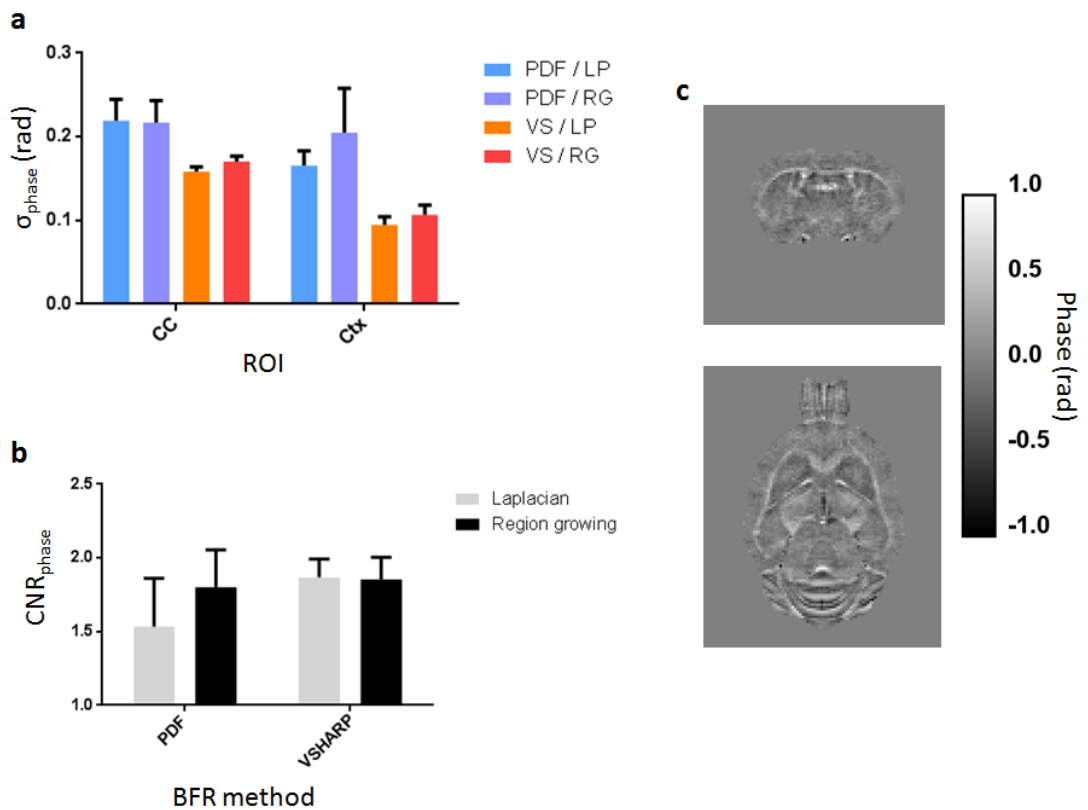
Figure 57.   **In-vivo field mapping comparison**

Comparison of phase variation for various phase unwrapping and field removal combinations in the cc and ctx (a). CNR in the field map for the same combinations(b). Field maps in coronal and axial plane with laplacian unwrapping and VSHARP field removal(c).

The field maps generated from laplacian phase unwrapping with VSHARP background field removal were used to calculate susceptibility maps using TKD with different filter threshold values. In both ROIs, mean susceptibility estimates peaked in magnitude at t_F=5 whereas the standard deviation of the susceptibility values increased with t_F value(Figure 58a-d). Calculating the mean CNR in the susceptibility maps using the ROIs indicated a maximum value was reached at t_F=5 before decreasing at larger threshold values(Figure 58e). Mean susceptibility in the white matter ROI at t_F=5 was -29±1ppb and in the cortex the susceptibility was 3±1ppb. Literature values are given to a reference which is rarely reported but the mean susceptibility difference of white matter relative to grey matter is -32±1 ppb which is similar to the difference in a

previously published *in-vivo* paper at 9.4T(256) (cc= -59.9±7.3ppb, cortex = -33.9±7.3ppb, mean diff = -25.1ppb – values relative to CSF). To ensure optimisation did not bias the WT group, transgenic mice were selected randomly from the cohort (n=5) and CNR between grey matter and white matter ROIs in the susceptibility maps was measured over the same range of threshold values. Susceptibility CNR peaked at 0.79 in the transgenic mice at threshold values of t_F=4 and t_F = 5.
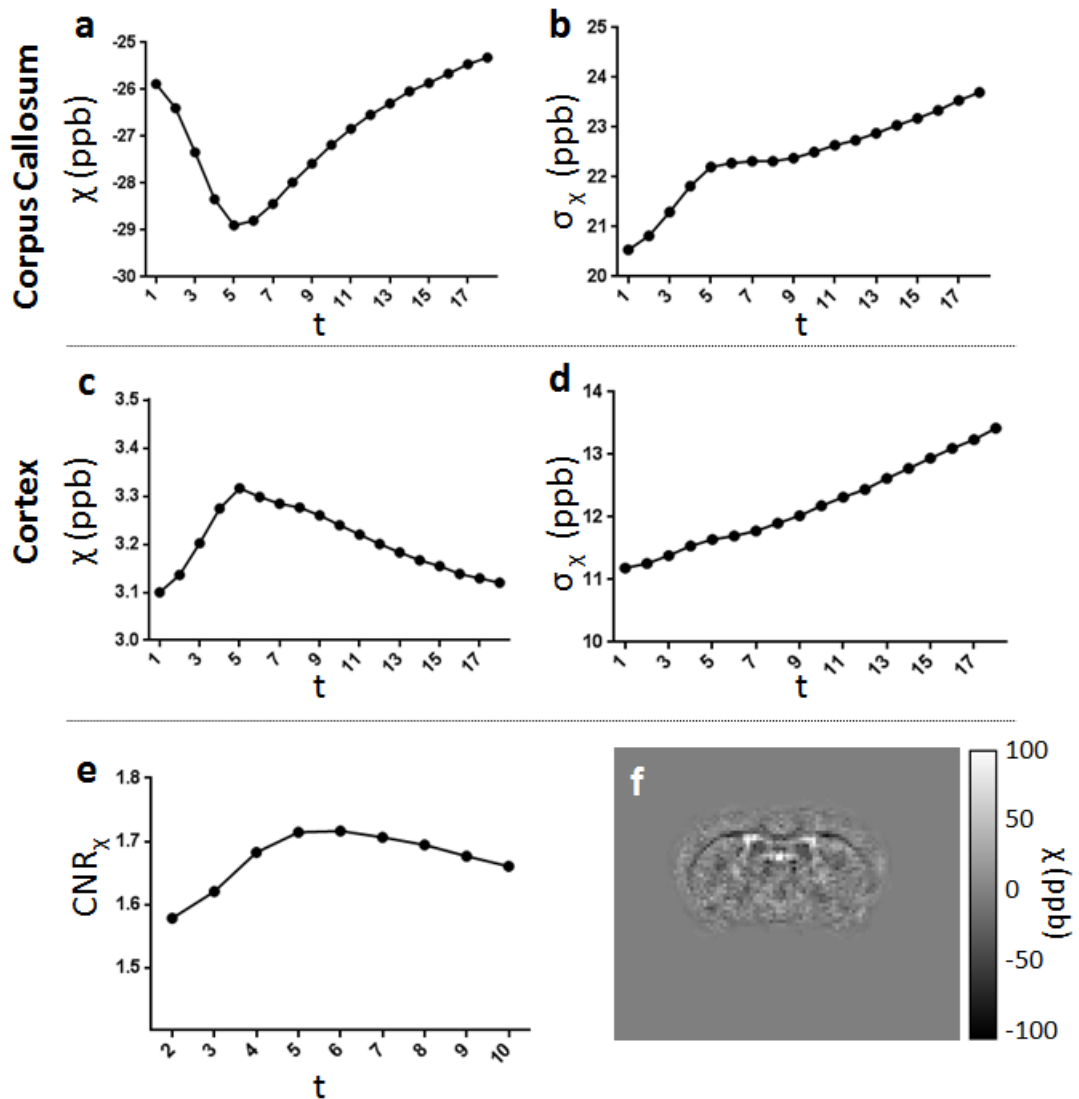
Figure 58.   **In-vivo t_F value comparison**

Mean and s.d. susceptibility in the cc (a,b), and mean and s.d. susceptibility in the cortex(c,d), and susceptibility CNR between grey matter and white matter (e) and a representative susceptibility map(f)

5.5.3.1.3 QSM using multiple echo data

To combine multiple echo data with the aim of improving SNR in the field maps and subsequent susceptibility maps, the reconstructed ex vivo phase datasets were unwrapped temporally, voxel by voxel across the twelve TEs collected. After this unwrapping step, spatial phase wraps were observed in the phase data at each echo (Figure 59a). By performing a least squares linear fit at each voxel, the gradient of the fit was used to produce a frequency field map and the background field contributions were removed using the VSHARP method (k=7) (Figure 59b). Maps of R^2 of the fit were calculated (Figure 59c) and low values appeared to form coherent patterns that appeared to coincide with areas of large phase gradients in the phase images after temporal unwrapping(Figure 59a). Plotting the phase values vs echo number for a voxel in one of these regions of poor fit, showed that the unwrapping had failed (Figure 59d). As a result of the unwrapping and fitting errors in these regions, increased noise and artifacts can be observed in the susceptibility maps generated using multiple echoes compared to single echo data (Figure 59e,f). In an attempt to improve the phase fitting, spatial unwrapping of the individual echoes was done both prior and post temporal unwrapping with no observed improvement in the susceptibility maps.   For this reason, QSM mapping using a multi-echo, temporal unwrapping approach was not pursued further and QSM maps were generated from data acquired at a single echo (informed by optimisation steps described above). Multi-echo magnitude data were used to estimate T2* (the more established biomarker of tissue iron concentration) for comparison to QSM metrics generated from simultaneously-acquired data.
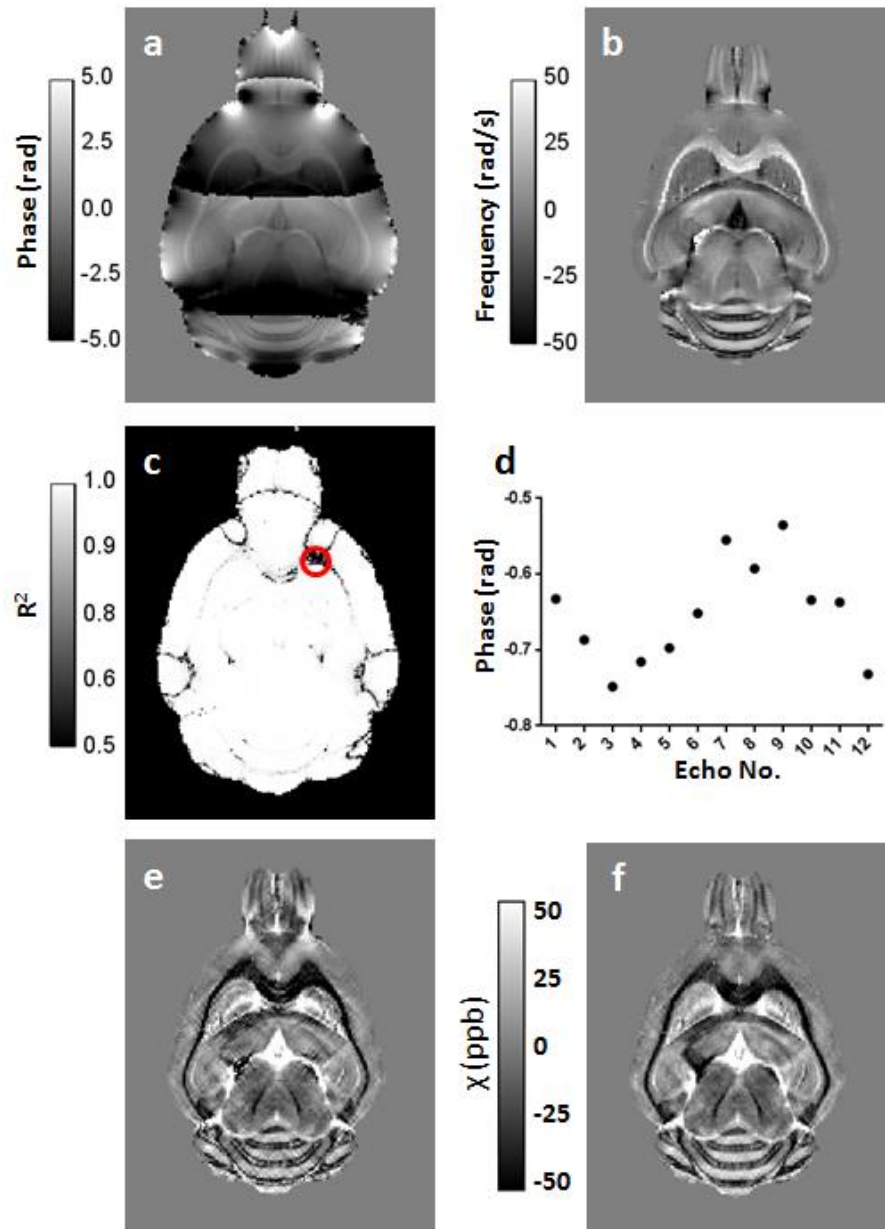
Figure 59.   **Ex vivo multi-echo QSM**

a)Residual wraps remain after temporal unwrapping of echoes(image shows 12th echo) b)field map generated by linear fit of unwrapped phase and background field removal c) map of R squared values for linear fits d) errors in temporal unwrapping from a single voxel within regions marked in c e) and f) are the multi echo susceptibility map and single echo susceptibility map respectively.

5.5.3.2 QSM group comparisons

Deformation fields from the non rigid registration of the magnitude data were applied to the QSMs and T2* maps of the individual mice to transform them into the same space. Mean maps of the registered data were then calculated separately for the WT(*in-vivo* : n=10, *ex-vivo*: n=8) and rTg4510(*in-vivo* : n=10, *ex-vivo*: n=8) groups. An axial slice of each of the mean QSM and T2* maps for both the *ex-vivo* and *in-vivo* datasets is shown in Figure 60. The anatomical structures are better delineated in the *ex-vivo* data owing in part to its finer resolution compared to the *in-vivo* maps. In a rostral section of the external capsule, a marked reduction in contrast with the surrounding cortical grey matter is observed in the rTg4510 QSMs (Figure 60b,d). This does not occur in the corresponding T2* maps (Figure 60f,h). A global reduction in intensity in the grey matter of the *in-vivo* T2* maps indicate a shortening of relaxation time compared to the *ex-vivo* data (Figure 60e-h).
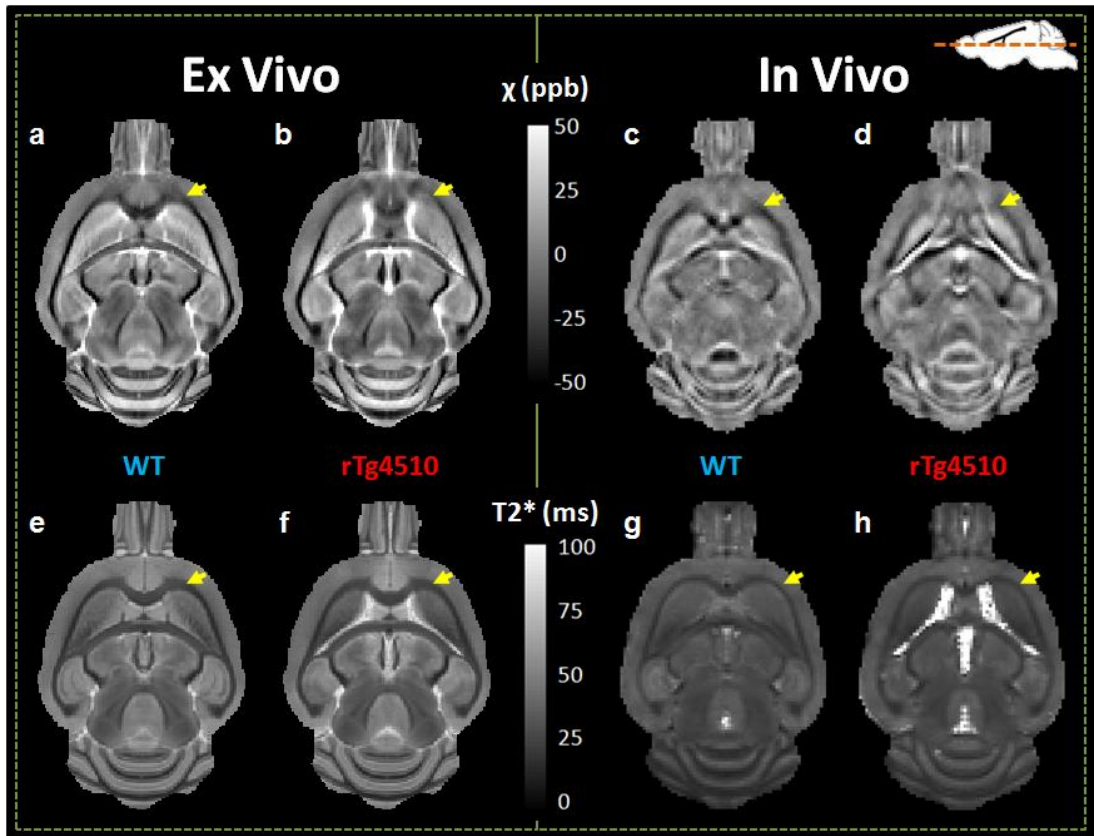
Figure 60.   **Mean QSM and T2* images**

Mean QSM (a-d) and T2*(e-h) images for registered *ex-vivo* (a,b,e,f) and *in-vivo* (c,d,g,h) datasets. A reduction in the white matter / grey matter contrast(yellow arrows) can be seen in a rostral section of the external capsule in the rTg4510 QSMs that is not apparent in the T2* maps.

Regional mean estimates of quantitative measures were generated by delineation of ROIs in atlas magnitude images before transformation back into the original image space of each animal where maps were segmented. Regional values of magnetic susceptibility and T2* for the WT group are provided in Figure 61. There was good agreement between the *ex-vivo* and *in-vivo* susceptibility in the deeper grey matter structures whereas an increase was observed in the hippocampus and the cortex in the *ex-vivo* data (p≤0.01, individual t-tests, FDR corrected q(<0.05)). The T2* was elevated in all grey matter regions in the *ex-vivo* data(p≤ 0.0001).
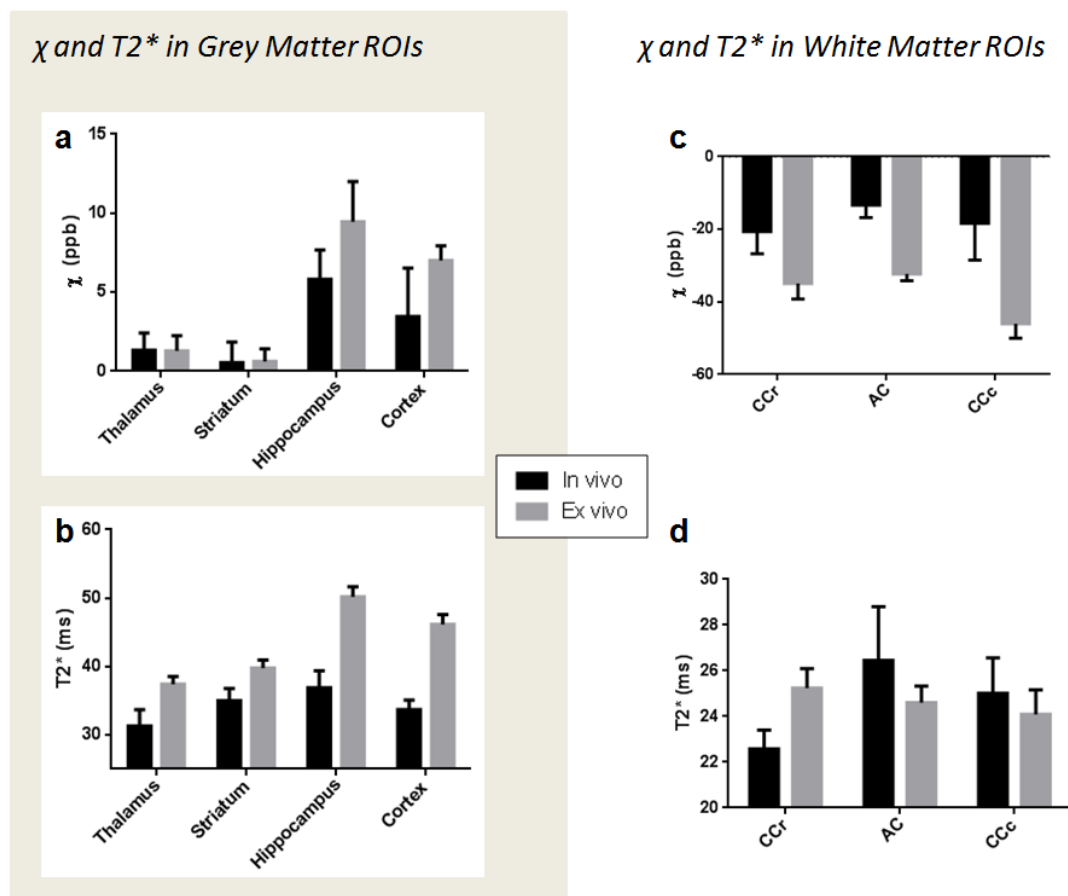
Figure 61. **Magnetic Susceptibility and T2* regional estimates**

In-vivo and *Ex-vivo* mean magnetic susceptibility and T2* values for grey matter(a,b) and white matter(c,d). ROIs calculated for wild-type mice.

In comparisons between grey matter regions in WT mice, the *in-vivo* susceptibility was increased in the Hippocampus compared to the Thalamus (p≤0.01, one way ANOVA) and Striatum (p≤0.001), and in the *ex-vivo* data, susceptibility was significantly greater in the

163

Hippocampus and the Cortex compared to the thalamus($p \leq 0.0001$ for both) and striatum($p \leq 0.001$ and $p \leq 0.0001$ respectively). There were differences between all regions in the T2* *ex-vivo* data, the pattern of greater values in the hippocampus and cortex regions was similar to that observed in the QSM data. These regions also exhibited differences, of lower significance, in the *in-vivo* data with the exception of the thalamus and cortex, and the hippocampus and striatum. Interestingly the striatum T2* was greater than that for the thalamus ($p \leq 0.05$), with no difference in the magnetic susceptibility between these regions.

In white matter ROIs, the *ex-vivo* data was found to have a larger negative susceptibility ($p \leq 0.0001$, t-tests, FDR corrected ($q \leq 0.05$)), the rostral corpus callosum ($p \leq 0.0001$) was the only region with different T2* to the *in-vivo* data(T2* significantly increased in *ex-vivo*) . The *in-vivo* magnetic susceptibility in this region was diamagnetic compared to the anterior commissure ($p \leq 0.05$, ANOVA) and in the *ex-vivo* data, susceptibility in the caudal corpus callosum more diamagnetic compared to both the more rostral measurement($p \leq 0.0001$), and the anterior commissure($p \leq 0.001$). The rostral corpus callosum T2* measurements were significantly different to the anterior commissure and the caudal corpus callosum regions for both *in-vivo*(T2* increased, $p \leq 0.01$ for both) and *ex-vivo* (T2* decreased, $p \leq 0.05$,$p \leq 0.001$ respectively) data.

Differences in magnetic susceptibility and T2* in rTg4510s relative to WT controls were most significant in the striatum. In both the *in-vivo*, and *ex-vivo* datasets, an increased paramagnetic susceptibility and reduced T2* was calculated for the rTg4510 (Figure 62a,d). This region appears hyperintense in the mean *ex-vivo* QSMs (Figure 62b,c). In the Hippocampus, an increased magnetic susceptibility was also observed in both *in-vivo* and *ex-vivo* data, with no differences in T2*. A shortening of T2* in the cortex was observed in the *in-vivo* data only. The *ex-vivo* measurements of susceptibility were elevated in the rTg4510 thalamus with a reduced T2*, findings that were not replicated *in-vivo* where magnetic susceptibility was found to be decreased with no change in T2*.
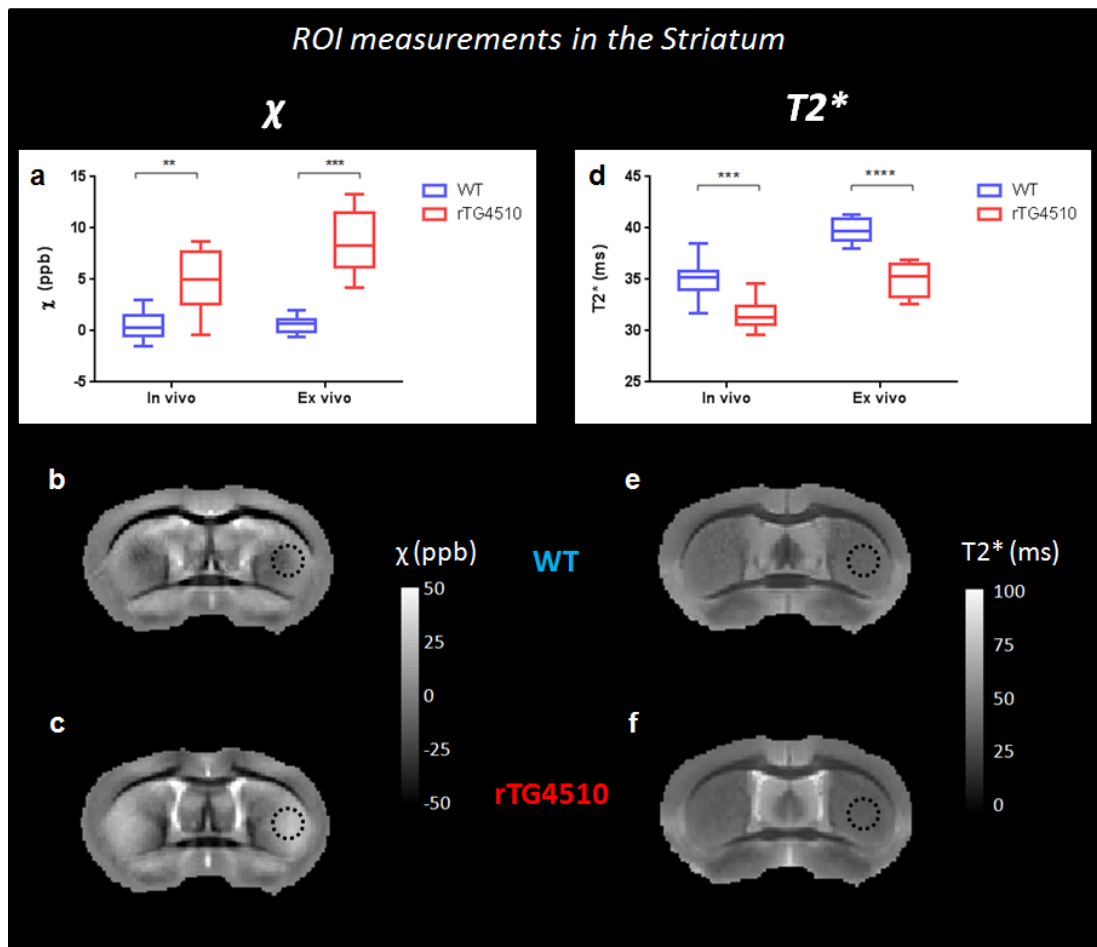
Figure 62.   **Magnetic susceptibility and T2* in the striatum**

In-vivo and *ex-vivo* magnetic susceptibility(a) and T2*(d) values in the striatum for WT and rTg4510 cohorts. Coronal slices of mean *ex-vivo* QSMs(b,c) show hyperintensity in the striatum (black circle) with corresponding slices of *ex-vivo* T2* maps(e,f).

An increased magnetic susceptibility was detected in the diamagnetic rostral region of the corpus callosum of the rTg4510s relative to WT controls. This was consistent across both *in-vivo* and *ex-vivo* datasets and was evident as a loss in grey matter / white matter contrast in both the mean average images(Figure 60b,d) and coronal slices in unregistered representative QSMs(Figure 63b,c). No significant changes were observed in T2* values and differences in representative T2* maps were less apparent (Figure 63e,f). Other white matter measurements did not exhibit differences in rTg4510 values, although T2* was reduced in the anterior commissure in the *ex-vivo* data. T2* and QSM values for all regions are listed in Table 3.
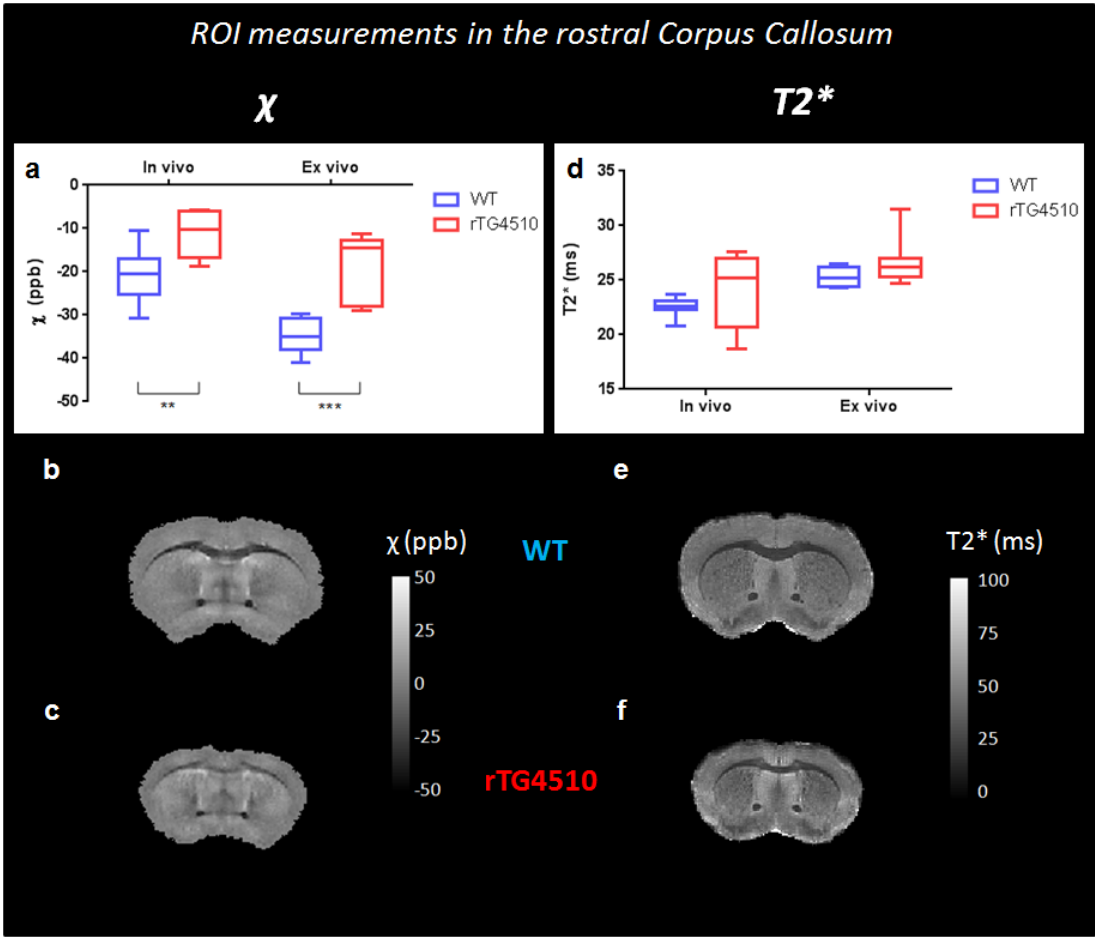
Figure 63. **Magnetic susceptibility and T2* in the corpus callosum**

Measurements of magnetic susceptibility (a) and T2*(d) in the rostral ROI of the corpus callosum for WT and rTg4510 mice(*in-vivo* and *ex-vivo*). Reductions in grey matter / white matter contrast were apparent in QSMs(b,c) but not in T2* maps(e,f) when comparing a coronal slice for a single representative(unregistered) WT and rTg4510 *ex-vivo*.

χ (ppb)	Ex vivo		In-vivo	
ROI	**WT**	**rTg4510**	**WT**	**rTg4510**
Striatum	0.61 ± 0.81	8.71 ± 3.21	0.54 ± 1.31	4.85 ± 3.09
Hippocampus	9.45 ± 2.55	13.60 ± 2.91	5.82 ± 1.86	11.11 ± 4.84
Cortex	7.01 ± 0.92	2.72 ± 5.37	3.46 ± 3.06	1.40 ± 1.79
Thalamus	1.30 ± 0.97	3.03 ± 1.31	1.33 ± 1.09	-0.45 ± 1.2
CCr	-34.92 ± 4.29	-18.73 ± 7.6	-20.55 ± 6.15	-11.22 ± 5.21
AC	-32.32 ± 1.88	-31.58 ± 3.33	-13.33 ± 3.45	-9.42 ± 5.34
CCc	-46.01 ± 3.97	-48.70 ± 8.88	-18.31 ± 10.14	-17.10 ± 4.43
T2* (ms)				
Striatum	39.79 ± 1.14	35.08 ± 1.61	34.99 ± 1.82	31.58 ± 1.42
Hippocampus	50.16 ± 1.51	50.39 ± 2.39	36.89 ± 2.48	36.62 ± 2.55
Cortex	46.14 ± 1.44	45.13 ± 1.81	33.67 ± 1.4	32.01 ± 1.8
Thalamus	37.41 ± 1.1	35.57 ± 1	31.25 ± 2.44	31.72 ± 0.59
CCr	25.23 ± 0.86	26.67 ± 2.1	22.58 ± 0.82	24.20 ± 3.2
AC	24.60 ± 0.73	22.89 ± 0.81	26.46 ± 2.35	25.27 ± 2.08
CCc	24.08 ± 1.07	23.54 ± 1.25	25.02 ± 1.54	24.73 ± 1.72

Table 3.   ***ROI magnetic susceptibility and T2* estimates***
List of mean and standard deviation of regional measures of magnetic susceptibility and T2*. Abbreviations for white matter regions : CCr – rostral corpus callosum, AC - anterior commissure, CCc caudal corpus callosum.

5.5.4 Discussion

The rTg4510 mouse model develops NFT pathology associated with AD without beta-amyloid plaques. The increased presence of reactive microglia and astrocytes has been observed in this model previously using histological stains(70,87). Their presence in brain tissue is associated with neuroinflammation in AD(287) and may be related to increased iron levels that give rise to ROS causing oxidative stress. The aggregation of insoluble Tau protein found in tangled form in AD has been shown to be mediated by iron (227). QSM and the more established T2* MRI techniques have been shown to be sensitive to iron content in the brain(233). In this work, QSM and T2* were used to non invasively probe the magnetic susceptibility in the rTg4510 brain both *in-vivo* and *ex-vivo*. Magnetic susceptibility increases relative to WT controls were identified in both grey matter and white matter regions and may indicate sensitivity to iron content *in-vivo*. QSM in the

rTg4510 may therefore present a non invasive method by which to dissect the relationship between iron and tau pathology in AD.

At high field, contributions from background susceptibility sources are increased(188) which may affect phase estimates throughout the mouse brain due to its large surface area to volume ratio. Neurodegenerative mouse models such as the rTg4510 may be affected disproportionately since marked atrophy may make delineation of structures difficult and may decrease the size of the shim voxel relative to controls. Compared to *ex-vivo* acquisition, additional error may be introduced into *in-vivo* datasets from increased noise and motion artifacts, primarily of physiological origin that fluctuate with the cardiorespiratory cycle(128,288) as well as from partial volume effects due to the lower resolution attainable. Furthermore, the use of oxygen to deliver anaesthetic may alter in vivo blood oxygen saturation levels, shown to cause changes in the magnetic susceptibility in and around blood vessels(289). This might suggest a fairer group comparison can be achieved using *ex-vivo* data. However, tissue fixation processes and the difference in imaging temperature will alter relaxation properties(269,277) and measurements may not reflect *in-vivo* values. *Ex-vivo* T2* measurements were increased (relative to *in-vivo*) in all grey matter regions in the WT animals in this study. This may have been caused by fixation and rehydration processes, known to alter the T2 properties of the *ex-vivo* tissue(269). Relative to *in-vivo* tissue, rehydration of *ex-vivo* tissue may have increased tissue water content, lengthening T2 relaxation. There may also be reduced dephasing effects from the use of smaller voxel sizes. Interestingly, this increase was not observed in the white matter regions which may be due to a decrease in water uptake during *ex-vivo* rehydration or partial volume errors in the *in-vivo* analysis. The *in-vivo* voxel size used is large relative to the white matter structures in the mouse brain and incorporation of grey matter into ROIs is inevitable. This may be reflected by the greater standard deviation of the *in-vivo* data compared to the *ex-vivo* data and may have produced inflated T2* estimates. In group comparisons, regional T2* differences in the rTg4510 relative to controls were in good agreement between *in-vivo* and *ex-vivo* datasets. This suggests that any T2* effects of *ex-vivo* tissue processing were consistent between transgenic and wild-type mice.

T2* star has been used previously to estimate iron concentrations in the brain and is regarded as an established technique for this purpose(233). Both *in-vivo* and *ex-vivo* rTg4510 datasets showed a reduced T2* in the striatum, a region that is known to develop

tangle pathology at the age imaged(204). The hippocampus and cortex also have a high density of NFTs present in the tissue whereas the thalamus is less affected(87,125,204). Although the rTg4510 exhibited differences in T2* in the cortex and relatively low pathology region of the thalamus, no differences were detected in the hippocampus. This suggests that relationships between iron deposition(as inferred by T2* measurement) and tau pathology(estimated by histological assessment of NFT density) may not be straight forward in the rTg4510 model or that other factors are complicating the interpretation of T2* changes in the tissue.

The QSM results support the notion of iron deposition in the striatum which was paramagnetic in the rTg4510s relative to controls. This increase in magnetic susceptibility would cause more rapid spin dephasing in the transverse plane, expediting decay of the signal as reflected by the T2* shortening observed. As with the T2* comparisons, differences in the striatum were the most marked of the measured grey matter regions. In a recent QSM study in humans, AD patients were found to have particularly elevated magnetic susceptibility in the putamen, a sub region of the striatum(250). Iron concentration in the healthy brain is particularly high in the basal ganglia structures, including the striatum, and abnormally high accumulation occurs in AD(214). These findings in the rTg4510 specifically implicate tau as playing a key role in the dysfunction of iron storage in this brain region. Iron-containing microglia have been identified in the hippocampus of AD patients(222) which may be responsible for the elevated magnetic susceptibility in the rTg4510. A lack of T2* differences in this region may highlight the enhanced sensitivity of the QSM technique to iron. The NFT histology in the rTg4510 in chapter 4 (Figure 35, section 4.4.3.1) showed greatest burden in the cortex, a region in where no QSM differences were detected in comparison to wild-type controls. Similar to the T2* measurements, regional magnetic susceptibility estimates do not appear to have an obvious relationship with NFT density in the rTg4510 at the time point measured.

The decreased diamagnetism of the rostral region of the corpus callosum of the rTg4510 may be due to abnormal myelination. The contrast with grey matter in this region is driven by myelination of white matter, and similar losses in contrast have been observed in mouse models of dysmyelination. However, a reduction in diamagnetic material may cause the same effect as an increase in paramagnetic material in elevating the negative magnetic susceptibility of white matter. Oligodendrocytes maintain myelination of axons and have

been shown to contain iron, which may increase in disease. GFAP and IBA-1 staining in this region previously has also shown increased reactive microglia and astrocytes, also implicated in the elevation of iron and neuroinflammation.

In chapter 4, reduced FA and increased radial diffusivity, findings suggestive of abnormal myelination in white matter, were observed in the rTg4510 mice at 8.5 months of age. The significance was greater for these group differences in the rostral corpus callosum in comparison to a caudal region. The reduced diamagnetism detected in the rostral white matter ROI of the rTg4510 in this study was not observed in the caudal section. Although findings of reactive microglia in section 5.3.3 mean that an increase in paramagnetic iron cannot be ruled out, these results may reflect a disruption to myelination that is amplified in the rostral white matter in the rTg4510. The magnetic susceptibility of the white matter in the WT mice measured in these regions was found to be more diamagnetic in the caudal section. This may suggest that there is greater myelination in the caudal part of the corpus callosum. Relative to the rostral section, the caudal corpus callosum is known to myelinate earlier in development(179) which may be the source of the observed resilience to pathology in accordance with retrogenesis theory.

The advantage of QSM over T2* in its ability to provide contrast between tissue types of paramagnetic and diamagnetic magnetic susceptibility can be seen in the myelin driven(213) negative susceptibility of the white matter versus the positive values in the grey matter regions(Table 3). There were few regions where group differences were identified in both the QSM and T2* data. An increased magnetic susceptibility and decreased T2* was observed in the rTg4510 relative to wild-type controls in the *in-vivo* and *ex-vivo* data in the striatum and in the *ex-vivo* data only in the thalamus. This is to be expected since the susceptibility effects of a paramagnetic increase in tissue may cause more rapid dephasing of the MR signal in the transverse plane, reducing relaxation time. The agreement of QSM group differences with the more established T2* measurement method lends credence to this novel technique. In contrast, *in-vivo* and *ex-vivo* increases in magnetic susceptibility were observed in the rTg4510 in the rostral corpus callosum and hippocampus in the absence of T2* changes. QSM is thought to be more directly related to iron content and tissue composition than T2* (which includes T2 effects)(101) which may explain the apparent improved sensitivity to changes in the rTg4510. These measurements

can be acquired using a single pulse sequence and the differing mechanisms that drive their contrast highlight the complementary nature of the two techniques (101,290).

The data acquired for *in-vivo* T2* mapping and QSM were collected using two separate 3D gradient echo sequences run sequentially. T2* mapping was conducted using multi-echo data and a single echo sequence was used to acquire data for QSM, with the addition of flow compensating gradients to improve phase estimates. Modification of the multi echo sequences to include first order gradient moment nulling(104) would enable simultaneous *in-vivo* acquisition of data for both measures and scan time could be reduced using EPI for inclusion in a multi-parametric protocol. Additionally, further optimisation of the acquisition parameters and inclusion of recently developed phase unwrapping techniques such as CAMPUS(268) or non-linear field map estimation(291) may remove errors and reduce noise in field maps generated from multi echo data and improve the quality of magnetic susceptibility maps produced.

5.6 Conclusions

In this chapter, T2* mapping and QSM was conducted in a mouse model of AD exhibiting tau pathology for the first time. The results indicate that both techniques are sensitive to alterations in the bulk magnetic susceptibility of tissue *in-vivo* in the rTg4510. Further work to estimate iron and myelin content in post mortem tissue will be conducted using histopathological staining techniques and may help to determine the pathological basis for these differences. Preliminary data, enhanced by contrast agent, showed increased magnetic susceptibility in white and grey matter regions of the rTg4510 illustrating the sensitivity of QSM to altered states in both tissue types. These findings were replicated both *ex-vivo*, without contrast agent, and *in-vivo* using optimised acquisitions and post processing QSM protocols. Histological markers of neuroinflammation suggested oxidative stress possibly caused by a disruption to iron homeostasis in grey matter regions of the rTg4510 where differences in T2* and QSM were detected. Both T2* and QSM findings support the possibility of excess iron accumulation in the striatum of the rTg4510, and may provide a disease biomarker that may or may not be directly related to NFT burden. The additional benefit of simultaneous acquisition means that these complementary measurements can be acquired in a relatively short scan time.

6 Thesis summary, discussion, and conclusions

The long road to the development of a cure for Alzheimer's Disease has now been tread for over a century with the urgency of this endeavour building as more and more people are left to face the tragic decline into dementia. In Chapter 1, major scientific breakthroughs that have improved our basic understanding of the disease were described along with the promising diagnostic tools in development to aid early diagnosis and disease staging. An emphasis was placed on the crucial role of mouse models of AD in the development of new biomarkers, the dissection of different aspects of the pathogenesis, in addition to the testing of potential therapies. There is a variety of emerging MRI techniques that can be used to probe different aspects of tissue vitality *in-vivo*. The benefits of their combination into so called 'multi-parametric' protocols have already been realised in a small number of studies and may provide a more comprehensive characterisation of AD. As such, the application of multi-parametric MRI protocols to mouse models of AD may spawn novel imaging-based correlates of the condition and help unlock new mechanisms of disease.

The Centre of Advanced Biomedical Imaging(CABI) and pharmaceutical manufacturer Eli Lilly has forged a collaborative relationship with a mission to develop treatments targeting the tangle pathology in AD. Integral to this effort is the development and evaluation of a pre-clinical multi-parametric MRI protocol sensitive to NFT accumulation in the rTg4510 mouse model of AD. The staging of the progression of tau pathology through these measurements will provide a test bed for the evaluation of drug efficacy in longitudinal studies. Ensuring the accuracy and precision of MRI data is paramount to achieving this goal. In chapter 3, a protocol was developed to both calibrate and monitor imaging gradients of the 9.4T MRI scanner in CABI. In addition, a post-processing technique was implemented to correct for spatial gradient non-linearity away from the magnet iso-centre. The use of structural MRI to measure volumetric changes is an established biomarker in AD and has formed the cornerstone of early multi-parametric MRI studies that have also included DTI protocols(42,43,46,70). Prior to correction, gradient scaling errors were calculated that could give rise to a 2.7% overestimation in volumes and 9.8% errors in diffusion measurements. These errors were greatly reduced after adjustments were made

to gradient scaling values on the MRI scanner, based on calculations using the new calibration method. Measurements were also used to rescale structural MRI data sets to remove effects of scaling discrepancies between different gradient sets used in the acquisitions. This highlighted the importance of consideration of this source of systematic error in studies utilising multiple hardware setups. The stability of scaling values across time points was measured and the temporal monitoring of gradients has since been employed alongside longitudinal studies in CABI to identify any fluctuations that may occur.

The incorporation of the gradient calibration protocol developed here into quality assurance procedures implemented in pre-clinical laboratories should be trivial. The phantom design can be 3D printed with standard materials and has been made open source(https://www.ucl.ac.uk/cabi/publications/open_source) and the software used for post processing is freely available to download(http://cmic.cs.ucl.ac.uk/home/software/). The versatility of the protocol was demonstrated through acquisition of data using different pulse sequences and at multiple resolutions. Accurate calibration and system monitoring was shown to be possible using a relatively low resolution scan to reduce scan time to four hours. Hopefully this work will raise awareness of the importance of accurate gradient calibration in pre-clinical systems and provide a useful resource for the pre-clinical imaging community.

This gradient calibration technique has formed the bedrock of the CABI/Eli Lilly multi-parametric MRI protocol, essential to the acquisition of quantitative data. In Chapter 4, a DTI protocol was developed for longitudinal study of the rTg4510 mouse. Sitting alongside other quantitative MR methodologies, a portion of time for the DTI acquisition was allocated from the three hour anaesthesia duration limit stipulated for *in-vivo* imaging of mice. A SNR and time efficient SE-EPI DTI pulse sequence was optimised to acquire data of suitable resolution to generate accurate estimates of diffusion measures in white matter regions in the mouse brain. Steps were taken to reduce motion artifacts, known to plague multi-shot EPI acquisitions, and DTI parameter estimates were evaluated against published phantom and *in-vivo* values. The optimised pulse sequence, which was forty three minutes in duration, was then used to acquire DTI data alongside other MRI measures in a single timepoint multi-parametric study in rTg4510 mice and wild-type controls.

DTI parameters measured in the rTg4510 group were significantly different to controls in a number of regions. Measurements in the thalamus, a region of low NFT density, indicated

an increased MD in the rTG4510 mice, indicating the sensitivity of this technique to tissue changes inflicted by mild pathology. In the more severely affected regions of the hippocampus and cortex, FA and MD were also elevated relative to controls indicating a microstructural rearrangement in this tissue that causes a greater diffusion of spins with increased directional specificity. Furthermore, a positive correlation was found between regional MD and FA estimates and ranking of hyperphosphorylated tau density. The rTg4510 displays neurodegeneration at the time point imaged and tau pathology has been shown previously to correlate with tissue atrophy(13-16). Therefore caution must be taken when interpreting these results, since it may be the case that these DTI measurements are also sensitive to other biological changes associated with tissue atrophy in this model.

The DTI measurements in white matter regions mirror the reduced anisotropic diffusion observed AD patients. In combination with the increased radial diffusivity and unchanged axial diffusivity in the rTg4510 relative to controls, this may indicate reduced myelination of axons in the white matter tracts of the corpus callosum(98,173,174). Electron microscopy observations in a previous study indicated myelin abnormalities as early as 4 months in the rTg4510(205) and further DTI investigations in younger mice would inform on the ability of this technique to detect effects of tau pathology at earlier stages of pathogenesis. The retrogenesis hypothesis states that later myelinating regions of white matter in neurodevelopment are more vulnerable to damage in AD. The DTI changes in the rTg4510 suggest that this may indeed be the case since they were of greater statistical significance in the later myelinating rostral section compared to the caudal section of the corpus callosum. However, the promoter driven expression of mutated tau in this model is directed to the forebrain and more rostral sections of white matter may be exposed to higher levels of tangle pathology. It is important to recognise that, as with all animal models, the rTg4510 does not capture all aspects of the human condition. There is no amyloid pathology and the regional and temporal pattern of NFT progression deviates from Braak staging. Nonetheless it does enable the study of unique tau pathology to better understand it's role in AD pathogenesis.

The changes in microstructure inferred by DTI that were observed in the corpus callosum of the rTg4510 were further investigated in Chapter 5 using a recently described MRI technique, Quantitative Susceptibility Mapping. QSM provides an estimate of the bulk magnetic susceptibility of tissue and is thought to be a more direct measure of the myelin

content in white matter tissue relative to DTI(213). In this final results chapter, QSM protocols were developed and optimised for *in-vivo* and *ex-vivo* acquisition and post processing. Regional estimates of magnetic susceptibility were conducted in the rTg4510 and wild-type controls in the first application of QSM in a mouse model of tauopathy. The QSM measurements in a rostral region of the corpus callosum were increased in the rTg4510 mice which may reflect a relative decrease in myelin content in agreement with DTI findings in chapter 4. There were no differences detected in this region in T2* measurements and unlike QSM no reduction in contrast was visually apparent between rostral white matter and surrounding grey matter. Like DTI, T2* measurements are modulated by a number of mechanisms besides myelin content in tissue. Quantification of myelin using histological measures alongside QSM measures in white matter would allow better definition of the relationship observed. It is also possible that the increases in magnetic susceptibility observed in the corpus callosum could be due to the increased presence of paramagnetic materials such as iron in the tissue.

The basal ganglia is known to contain structures that are iron rich relative to the rest of the brain and are particularly vulnerable to pathological iron accumulation in AD(214). The striatum, a constituent part of this system, was found to have increased magnetic susceptibility in the rTg4510. Reductions in T2*, the more established method of *in-vivo* iron estimation, supported this finding. These T2* and QSM findings are in good agreement with clinical studies of AD(250) and may indicate that iron deposition in the striatum may be related to tangle pathology. QSM values in the hippocampus, a region previously shown exhibit iron accumulation in AD(222), were also paramagnetic in the rTG4510 relative to controls. The lack of findings in the cortex, a region of high NFT pathology in the rTg4510, indicates that possible iron driven changes may not be caused by iron co localised with NFTs. Increased histological staining for reactive astrocytes and microglia were visually apparent in the corpus callosum and striatum. The increased magnetic susceptibility in the rTg4510 in this region may indicate that rather than tau pathology, neuroinflammation and associated iron accumulation may be responsible for these changes.

The work in this thesis has laid the foundations for three MRI techniques important to the development of multi-parametric protocols for the *in-vivo* imaging of AD mouse models. A complete protocol for the system calibration of MRI gradients in pre-clinical scanners has

been made open source and available to the imaging community. The sensitivity of DTI, QSM and T2* measurements to effects of NFT accumulation in the brain has been demonstrated. This work could be further extended through longitudinal studies using these proven biomarkers alongside detailed histological analysis in the rTg4510 as well as in other mouse models to elucidate the relationships iron and myelin have with tangle pathology and their roles in neurodegenerative diseases.

References

1. Goedert M, Spillantini MG. A Century of Alzheimer's Disease. Science 2006;314(5800):777-781.
2. Hardy J. A Hundred Years of Alzheimer's Disease Research. Neuron 2006;52(1):3-13.
3. Redlich E. Über miliare Sklerose der Hirnrinde bei seniler Atrophie. Jahrb Psychiat Neurol 1898;17:208-216.
4. Schottky J. Über präsenile Verblödungen. Z f d g Neur u Psych 1932;140(1):333-397.
5. Perry G, Avila J, Kinoshita J, Smith MA. Alzheimer's Disease: A Century of Scientific and Clinical Research (" Alzheimer 100") A Special Issue of JAD. Journal of Alzheimer's Disease 2006;9:1.
6. Alzheimer A. Über eigenartige Krankheitsfälle des späteren Alters. Z f d g Neur u Psych 1911;4(1):356-385.
7. Terry RD, Gonatas NK, Weiss M. Ultrastructural Studies in Alzheimer's Presenile Dementia. The American Journal of Pathology 1964;44(2):269-297.
8. Kidd M. Paired Helical Filaments in Electron Microscopy of Alzheimer's Disease. Nature 1963;197(4863):192-193.
9. Glenner GG, Wong CW. Alzheimer's disease and Down's syndrome: Sharing of a unique cerebrovascular amyloid fibril protein. Biochemical and Biophysical Research Communications 1984;122(3):1131-1135.
10. Thinakaran G, Koo EH. Amyloid Precursor Protein Trafficking, Processing, and Function. Journal of Biological Chemistry 2008;283(44):29615-29619.
11. Braak H, Braak E. Neuropathological stageing of Alzheimer-related changes. Acta Neuropathologica 1991;82(4):239-259.
12. Braak H, Braak E. Staging of alzheimer's disease-related neurofibrillary changes. Neurobiology of Aging 1995;16(3):271-278.
13. Vemuri P, Whitwell JL, Kantarci K, Josephs KA, Parisi JE, Shiung MS, Knopman DS, Boeve BF, Petersen RC, Dickson DW, Jack CR, Jr. Antemortem MRI based STructural Abnormality iNDex (STAND)-scores correlate with postmortem Braak neurofibrillary tangle stage. NeuroImage 2008;42(2):559-567.
14. Jack CR, Jr., Dickson DW, Parisi JE, Xu YC, Cha RH, O'Brien PC, Edland SD, Smith GE, Boeve BF, Tangalos EG, Kokmen E, Petersen RC. Antemortem MRI findings correlate with hippocampal neuropathology in typical aging and dementia. Neurology 2002;58(5):750-757.
15. Csernansky JG, Hamstra J, Wang L, McKeel D, Price JL, Gado M, Morris JC. Correlations between antemortem hippocampal volume and postmortem neuropathology in AD subjects. Alzheimer Dis Assoc Disord 2004;18(4):190-195.
16. Whitwell JL, Josephs KA, Murray ME, Kantarci K, Przybelski SA, Weigand SD, Vemuri P, Senjem ML, Parisi JE, Knopman DS, Boeve BF, Petersen RC, Dickson DW, Jack CR, Jr. MRI correlates of neurofibrillary tangle pathology at autopsy: a voxel-based morphometry study. Neurology 2008;71(10):743-749.
17. Reitz C, Mayeux R. Alzheimer disease: epidemiology, diagnostic criteria, risk factors and biomarkers. Biochemical pharmacology 2014;88(4):640-651.
18. Jack CR. Alzheimer Disease: New Concepts on Its Neurobiology and the Clinical Role Imaging Will Play. Radiology 2012;263(2):344-361.
19. Organisation(2012) WH. Dementia Fact Sheet. (362).

20. Lundkvist J, Halldin M, Sandin J, Nordvall G, Forsell P, Svensson S, Jansson L, Johansson G, Winblad B, Ekstrand J. The battle of Alzheimer disease - the beginning of the future Unleashing the potential of academic discoveries. Frontiers in Pharmacology 2014;5.

21. Wu Y-T, Fratiglioni L, Matthews FE, Lobo A, Breteler MMB, Skoog I, Brayne C. Dementia in western Europe: epidemiological evidence and implications for policy making. The Lancet Neurology.

22. Strooper BD, Gutiérrez LC. Learning by Failing: Ideas and Concepts to Tackle γ-Secretases in Alzheimer's Disease and Beyond. Annual Review of Pharmacology and Toxicology 2015;55(1):419-437.

23. Ghosh AK, Tang J. Prospects of β-Secretase Inhibitors for the Treatment of Alzheimer's Disease. ChemMedChem 2015;10(9):1463-1466.

24. Sakai K, Boche D, Carare R, Johnston D, Holmes C, Love S, Nicoll JR. Aβ immunotherapy for Alzheimer's disease: effects on apoE and cerebral vasculopathy. Acta Neuropathologica 2014;128(6):777-789.

25. Ittner A, Bertz J, Suh LS, Stevens CH, Götz J, Ittner LM. Tau-targeting passive immunization modulates aspects of pathology in tau transgenic mice. Journal of Neurochemistry 2015;132(1):135-145.

26. Herrmann A, Spires–Jones T. Clearing the way for tau immunotherapy in Alzheimer's disease. Journal of Neurochemistry 2015;132(1):1-4.

27. Blennow K, Hampel H, Zetterberg H. Biomarkers in Amyloid-[beta] Immunotherapy Trials in Alzheimer/'s Disease. Neuropsychopharmacology 2014;39(1):189-201.

28. Clark CM, Sheppard L, Fillenbaum GG, et al. Variability in annual mini-mental state examination score in patients with probable alzheimer disease: A clinical perspective of data from the consortium to establish a registry for alzheimer's disease. Archives of Neurology 1999;56(7):857-862.

29. Ihl R, Frölich L, Dierks T, Martin E-M, Maurer K. Differential validity of psychometric tests in dementia of the Alzheimer type. Psychiatry Research 1992;44(2):93-106.

30. Dubois B, Feldman HH, Jacova C, DeKosky ST, Barberger-Gateau P, Cummings J, Delacourte A, Galasko D, Gauthier S, Jicha G, Meguro K, O'Brien J, Pasquier F, Robert P, Rossor M, Salloway S, Stern Y, Visser PJ, Scheltens P. Research criteria for the diagnosis of Alzheimer's disease: revising the NINCDS–ADRDA criteria. The Lancet Neurology 2007;6(8):734-746.

31. Buerger K, Ewers M, Pirttilä T, Zinkowski R, Alafuzoff I, Teipel SJ, DeBernardis J, Kerkman D, McCulloch C, Soininen H, Hampel H. CSF phosphorylated tau protein correlates with neocortical neurofibrillary pathology in Alzheimer's disease. Brain 2006;129(11):3035-3041.

32. Shafaati M, Solomon A, Kivipelto M, Björkhem I, Leoni V. Levels of ApoE in cerebrospinal fluid are correlated with Tau and 24S-hydroxycholesterol in patients with cognitive disorders. Neuroscience Letters 2007;425(2):78-82.

33. Green AJE, Harvey RJ, Thompson EJ, Rossor MN. Increased tau in the cerebrospinal fluid of patients with frontotemporal dementia and Alzheimer's disease. Neuroscience Letters 1999;259(2):133-135.

34. Süssmuth SD, Tumani H, Ecker D, Ludolph AC. Amyotrophic lateral sclerosis: disease stage related changes of tau protein and S100 beta in cerebrospinal fluid and creatine kinase in serum. Neuroscience Letters 2003;353(1):57-60.

35. Jack CR, Petersen RC, Xu YC, Waring SC, O'Brien PC, Tangalos EG, Smith GE, Ivnik RJ, Kokmen E. Medial temporal atrophy on MRI in normal aging and very mild Alzheimer's disease. Neurology 1997;49(3):786-794.

36. Fox NC, Scahill RI, Crum WR, Rossor MN. Correlation between rates of brain atrophy and cognitive decline in AD. Neurology 1999;52(8):1687.

37. Jack CR, Dickson DW, Parisi JE, Xu YC, Cha RH, O'Brien PC, Edland SD, Smith GE, Boeve BF, Tangalos EG, Kokmen E, Petersen RC. Antemortem MRI findings correlate with hippocampal neuropathology in typical aging and dementia. Neurology 2002;58(5):750-757.

38. Jack Jr CR, Knopman DS, Jagust WJ, Petersen RC, Weiner MW, Aisen PS, Shaw LM, Vemuri P, Wiste HJ, Weigand SD, Lesnick TG, Pankratz VS, Donohue MC, Trojanowski JQ. Tracking pathophysiological processes in Alzheimer's disease: an updated hypothetical model of dynamic biomarkers. The Lancet Neurology 2013;12(2):207-216.

39. Di Paola M, Di Iulio F, Cherubini A, Blundo C, Casini AR, Sancesario G, Passafiume D, Caltagirone C, Spalletta G. When, where, and how the corpus callosum changes in MCI and AD: A multimodal MRI study. Neurology 2010;74(14):1136-1142.

40. Sabbagh JJ, Kinney JW, Cummings JL. Alzheimer's disease biomarkers: Correspondence between human studies and animal models. Neurobiology of Disease 2013;56(0):116-130.

41. Celone KA, Calhoun VD, Dickerson BC, Atri A, Chua EF, Miller SL, DePeau K, Rentz DM, Selkoe DJ, Blacker D, Albert MS, Sperling RA. Alterations in Memory Networks in Mild Cognitive Impairment and Alzheimer's Disease: An Independent Component Analysis. The Journal of Neuroscience 2006;26(40):10222-10231.

42. Cherubini A, Spoletini I, Péran P, Luccichenti G, Di Paola M, Sancesario G, Gianni W, Giubilei F, Bossù P, Sabatini U, Caltagirone C, Spalletta G. A multimodal MRI investigation of the subventricular zone in mild cognitive impairment and Alzheimer's disease patients. Neuroscience Letters 2010;469(2):214-218.

43. Mesrob L, Sarazin M, Hahn-Barma V, Souza LCd, Dubois B, Gallinari P, Kinkingn¨¦hun S. DTI and Structural MRI Classification in Alzheimer¡¯s Disease. Advances in Molecular Imaging 2012;Vol.02No.02:9.

44. den Heijer T, der Lijn Fv, Vernooij MW, de Groot M, Koudstaal PJ, der Lugt Av, Krestin GP, Hofman A, Niessen WJ, Breteler MMB. Structural and diffusion MRI measures of the hippocampus and memory performance. NeuroImage 2012;63(4):1782-1789.

45. Dyrba M, Grothe M, Kirste T, Teipel SJ. Multimodal analysis of functional and structural disconnection in Alzheimer's disease using multiple kernel SVM. Human brain mapping 2015;36(6):2118-2131.

46. Walhovd KB, Fjell AM, Amlien I, Grambaite R, Stenset V, Bjørnerud A, Reinvang I, Gjerstad L, Cappelen T, Due-Tønnessen P, Fladby T. Multimodal imaging in mild cognitive impairment: Metabolism, morphometry and diffusion of the temporal–parietal memory network. NeuroImage 2009;45(1):215-223.

47. Henkelman RM. Systems Biology through Mouse Imaging Centers: Experience and New Directions. Annual Review of Biomedical Engineering 2010;12(1):143-166.

48. Hall AM, Roberson ED. Mouse models of Alzheimer's disease. Brain Research Bulletin 2012;88(1):3-12.

49. Mucke L, Masliah E, Yu G-Q, Mallory M, Rockenstein EM, Tatsuno G, Hu K, Kholodenko D, Johnson-Wood K, McConlogue L. High-Level Neuronal Expression of Aβ1–42 in Wild-Type Human Amyloid Protein Precursor Transgenic Mice: Synaptotoxicity without Plaque Formation. The Journal of Neuroscience 2000;20(11):4050-4058.

50. Duff K, Eckman C, Zehr C, Yu X, Prada C-M, Perez-tur J, Hutton M, Buee L, Harigaya Y, Yager D, Morgan D, Gordon MN, Holcomb L, Refolo L, Zenk B, Hardy J, Younkin S. Increased amyloid-[beta]42(43) in brains of mice expressing mutant presenilin 1. Nature 1996;383(6602):710-713.

51. Savonenko A, Xu GM, Melnikova T, Morton JL, Gonzales V, Wong MPF, Price DL, Tang F, Markowska AL, Borchelt DR. Episodic-like memory deficits in the APPswe/PS1dE9 mouse model of Alzheimer's disease: Relationships to β-amyloid deposition and neurotransmitter abnormalities. Neurobiology of Disease 2005;18(3):602-617.

52. Dubois A, Hérard A-S, Delatour B, Hantraye P, Bonvento G, Dhenain M, Delzescaux T. Detection by voxel-wise statistical analysis of significant changes in regional cerebral glucose uptake in an APP/PS1 transgenic mouse model of Alzheimer's disease. NeuroImage 2010;51(2):586-598.

53. Holcomb L, Gordon MN, McGowan E, Yu X, Benkovic S, Jantzen P, Wright K, Saad I, Mueller R, Morgan D, Sanders S, Zehr C, O'Campo K, Hardy J, Prada C-M, Eckman C, Younkin S, Hsiao K, Duff K. Accelerated Alzheimer-type phenotype in transgenic mice carrying both mutant amyloid precursor protein and presenilin 1 transgenes. Nat Med 1998;4(1):97-100.

54. Lewis J, McGowan E, Rockwood J, Melrose H, Nacharaju P, Van Slegtenhorst M, Gwinn-Hardy K, Murphy MP, Baker M, Yu X. Neurofibrillary tangles, amyotrophy and progressive motor disturbance in mice expressing mutant (P301L) tau protein. Nature genetics 2000;25(4):402-405.

55. Lewis J, Dickson DW, Lin W-L, Chisholm L, Corral A, Jones G, Yen S-H, Sahara N, Skipper L, Yager D, Eckman C, Hardy J, Hutton M, McGowan E. Enhanced Neurofibrillary Degeneration in Transgenic Mice Expressing Mutant Tau and APP. Science 2001;293(5534):1487-1491.

56. Roberson ED, Scearce-Levie K, Palop JJ, Yan F, Cheng IH, Wu T, Gerstein H, Yu GQ, Mucke L. Reducing endogenous tau ameliorates amyloid β-induced deficits in an Alzheimer's disease mouse model. Science 2007;316(5825):750-754.

57. Dujardin S, Colin M, Buée L. Animal models of tauopathies and their implications for research/translation into the clinic. Neuropathology and Applied Neurobiology 2014:n/a-n/a.

58. Klunk WE, Lopresti BJ, Ikonomovic MD, Lefterov IM, Koldamova RP, Abrahamson EE, Debnath ML, Holt DP, Huang G-f, Shao L, DeKosky ST, Price JC, Mathis CA. Binding of the Positron Emission Tomography Tracer Pittsburgh Compound-B Reflects the Amount of Amyloid-β in Alzheimer's Disease Brain But Not in Transgenic Mouse Brain. The Journal of Neuroscience 2005;25(46):10598-10606.

59. Toyama H, Ye D, Ichise M, Liow J-S, Cai L, Jacobowitz D, Musachio J, Hong J, Crescenzo M, Tipre D, Lu J-Q, Zoghbi S, Vines D, Seidel J, Katada K, Green M, Pike V, Cohen R, Innis R. PET imaging of brain with the β-amyloid probe, [11C]6-OH-BTA-1, in a transgenic mouse model of Alzheimer's disease. European Journal of Nuclear Medicine and Molecular Imaging 2005;32(5):593-600.

60. Manook A, Yousefi BH, Willuweit A, Platzer S, Reder S, Voss A, Huisman M, Settles M, Neff F, Velden J, Schoor M, von der Kammer H, Wester H-J, Schwaiger M, Henriksen G, Drzezga A. Small-Animal PET Imaging of Amyloid-Beta Plaques with [11C]PiB and Its Multi-Modal Validation in an APP/PS1 Mouse Model of Alzheimer's Disease. PLoS ONE 2012;7(3):e31310.

61. Choi SR, Golding G, Zhuang Z, Zhang W, Lim N, Hefti F, Benedum TE, Kilbourn MR, Skovronsky D, Kung HF. Preclinical Properties of 18F-AV-45: A PET Agent for Aβ Plaques in the Brain. Journal of Nuclear Medicine 2009;50(11):1887-1894.

62. Poisnel G, Dhilly M, Moustié O, Delamare J, Abbas A, Guilloteau D, Barré L. PET imaging with [18F]AV-45 in an APP/PS1-21 murine model of amyloid plaque deposition. Neurobiology of Aging 2012;33(11):2561-2571.

63. Fodero-Tavoletti MT, Okamura N, Furumoto S, Mulligan RS, Connor AR, McLean CA, Cao D, Rigopoulos A, Cartwright GA, O'Keefe G, Gong S, Adlard PA, Barnham KJ, Rowe CC, Masters CL, Kudo Y, Cappai R, Yanai K, Villemagne VL. 18F-THK523: a novel in vivo tau imaging ligand for Alzheimer's disease. Brain 2011;134(4):1089-1100.

64. Maeda J, Zhang M-R, Okauchi T, Ji B, Ono M, Hattori S, Kumata K, Iwata N, Saido TC, Trojanowski JQ, Lee VM-Y, Staufenbiel M, Tomiyama T, Mori H, Fukumura T, Suhara T, Higuchi M. In Vivo Positron Emission Tomographic Imaging of Glial Responses to Amyloid-β and Tau Pathologies in Mouse Models of Alzheimer's Disease and Related Disorders. The Journal of Neuroscience 2011;31(12):4720-4730.

65. Sabbagh JJ, Kinney JW, Cummings JL. Alzheimer's disease biomarkers: Correspondence between human studies and animal models. Neurobiology of Disease 2013;56:116-130.

66. Redwine JM, Kosofsky B, Jacobs RE, Games D, Reilly JF, Morrison JH, Young WG, Bloom FE. Dentate gyrus volume is reduced before onset of plaque formation in PDAPP mice: A magnetic resonance microscopy and stereologic analysis. Proceedings of the National Academy of Sciences 2003;100(3):1381-1386.

67. Syková E, Voříšek I, Antonova T, Mazel T, Meyer-Luehmann M, Jucker M, Hájek M, Or M, Bureš J. Changes in extracellular space size and geometry in APP23 transgenic mice: A model of Alzheimer's disease. Proceedings of the National Academy of Sciences of the United States of America 2005;102(2):479-484.

68. Van Broeck B, Vanhoutte G, Pirici D, Van Dam D, Wils H, Cuijt I, Vennekens Kl, Zabielski M, Michalik A, Theuns J, De Deyn PP, Van der Linden A, Van Broeckhoven C, Kumar-Singh S. Intraneuronal amyloid β and reduced brain volume in a novel APP T714I mouse model for Alzheimer's disease. Neurobiology of Aging 2008;29(2):241-252.

69. Weiss C, Venkatasubramanian PN, Aguado AS, Power JM, Tom BC, Li L, Chen KS, Disterhoft JF, Wyrwicz AM. Impaired Eyeblink Conditioning and Decreased Hippocampal Volume in PDAPP V717F Mice. Neurobiology of Disease 2002;11(3):425-433.

70. Yang D, Xie Z, Stephenson D, Morton D, Hicks CD, Brown TM, Sriram R, O'Neill S, Raunig D, Bocan T. Volumetric MRI and MRS provide sensitive measures of Alzheimer's disease neuropathology in inducible Tau transgenic mice (rTg4510). NeuroImage 2011;54(4):2652-2658.

71. Lau JC, Lerch JP, Sled JG, Henkelman RM, Evans AC, Bedell BJ. Longitudinal neuroanatomical changes determined by deformation-based morphometry in a mouse model of Alzheimer's disease. NeuroImage 2008;42(1):19-27.

72. Zhang J, Yarowsky P, Gordon MN, Di Carlo G, Munireddy S, van Zijl PCM, Mori S. Detection of amyloid plaques in mouse models of Alzheimer's disease by magnetic resonance imaging. Magnetic Resonance in Medicine 2004;51(3):452-457.

73. Helpern JA, Lee S-P, Falangola MF, Dyakin VV, Bogart A, Ardekani B, Duff K, Branch C, Wisniewski T, de Leon MJ, Wolf O, O'Shea J, Nixon RA. MRI assessment of neuropathology in a transgenic mouse model of Alzheimer's disease. Magnetic Resonance in Medicine 2004;51(4):794-798.

74. Jack CR, Garwood M, Wengenack TM, Borowski B, Curran GL, Lin J, Adriany G, Gröhn OHJ, Grimm R, Poduslo JF. In vivo visualization of Alzheimer's amyloid

plaques by magnetic resonance imaging in transgenic mice without a contrast agent. Magnetic Resonance in Medicine 2004;52(6):1263-1271.

75. Lee SP, Falangola MF, Nixon RA, Duff K, Helpern JA. Visualization of β-amyloid plaques in a transgenic mouse model of Alzheimer's disease using MR microscopy without contrast reagents. Magnetic Resonance in Medicine 2004;52(3):538-544.

76. Vanhoutte G, Dewachter I, Borghgraef P, Van Leuven F, Van der Linden A. Noninvasive in vivo MRI detection of neuritic plaques associated with iron in APP[V717I] transgenic mice, a model for Alzheimer's disease. Magnetic Resonance in Medicine 2005;53(3):607-613.

77. Wengenack TM, Reyes DA, Curran GL, Borowski BJ, Lin J, Preboske GM, Holasek SS, Gilles EJ, Chamberlain R, Marjanska M, Jack Jr CR, Garwood M, Poduslo JF. Regional differences in MRI detection of amyloid plaques in AD transgenic mouse brain. NeuroImage 2011;54(1):113-122.

78. Meadowcroft MD, Connor JR, Smith MB, Yang QX. MRI and Histological Analysis of Beta-Amyloid Plaques in Both Human Alzheimer's Disease and APP/PS1 Transgenic Mice. Journal of Magnetic Resonance Imaging 2009;29(5):997-1007.

79. Weidensteiner C, Metzger F, Bohrmann ABB, Kuennecke B, von Kienlin M. Cortical hypoperfusion in the B6.PS2APP mouse model for Alzheimer's disease: Comprehensive phenotyping of vascular and tissular parameters by MRI. Magnetic Resonance in Medicine 2009;62(1):35-45.

80. Faure A, Verret L, Bozon B, El Tannir El Tayara N, Ly M, Kober F, Dhenain M, Rampon C, Delatour B. Impaired neurogenesis, neuronal loss, and brain functional deficits in the APPxPS1-Ki mouse model of Alzheimer's disease. Neurobiology of Aging 2011;32(3):407-418.

81. Song S-K, Kim JH, Lin S-J, Brendza RP, Holtzman DM. Diffusion tensor imaging detects age-dependent white matter changes in a transgenic mouse model with amyloid deposition. Neurobiology of Disease 2004;15(3):640-647.

82. Sun S-W, Song S-K, Harms MP, Lin S-J, Holtzman DM, Merchant KM, Kotyk JJ. Detection of age-dependent brain injury in a mouse model of brain amyloidosis associated with Alzheimer's disease using magnetic resonance diffusion tensor imaging. Experimental Neurology 2005;191(1):77-85.

83. Dedeoglu A, Choi J-K, Cormier K, Kowall NW, Jenkins BG. Magnetic resonance spectroscopic analysis of Alzheimer's disease mouse brain that express mutant human APP shows altered neurochemical profile. Brain Research 2004;1012(1–2):60-65.

84. Choi J-K, Jenkins BG, Carreras I, Kaymakcalan S, Cormier K, Kowall NW, Dedeoglu A. Anti-inflammatory treatment in AD mice protects against neuronal pathology. Experimental Neurology 2010;223(2):377-384.

85. Kim J, Choi I-Y, Michaelis ML, Lee P. Quantitative in vivo measurement of early axonal transport deficits in a triple transgenic mouse model of Alzheimer's disease using manganese-enhanced MRI. NeuroImage 2011;56(3):1286-1292.

86. Santacruz K, Lewis J, Spires T, Paulson J, Kotilinek L, Ingelsson M, Guimaraes A, DeTure M, Ramsden M, McGowan E. Tau suppression in a neurodegenerative mouse model improves memory function. Science 2005;309(5733):476-481.

87. Ramsden M, Kotilinek L, Forster C, Paulson J, McGowan E, SantaCruz K, Guimaraes A, Yue M, Lewis J, Carlson G, Hutton M, Ashe KH. Age-Dependent Neurofibrillary Tangle Formation, Neuron Loss, and Memory Impairment in a Mouse Model of Human Tauopathy (P301L). The Journal of Neuroscience 2005;25(46):10637-10647.

88.   Perez P, Hall G, Kimura T, Ren Y, Bailey R, Lewis J, Febo M, Sahara N. In vivo functional brain mapping in a conditional mouse model of human tauopathy (taup301l) reveals reduced neural activity in memory formation structures. Molecular Neurodegeneration 2013;8(1):9.

89.   Gadian DG. NMR and its applications to living systems: Oxford University Press Oxford; 1995.

90.   Bernstein MA, King KF, Zhou XJ. Handbook of MRI pulse sequences: Elsevier; 2004.

91.   McRobbie DW, Moore EA, Graves MJ, Prince MR. MRI from Picture to Proton: Cambridge university press; 2006.

92.   Schmitt F, Stehling MK, Turner R. Echo-planar imaging: Springer Science & Business Media; 1998.

93.   Johansen-Berg H, Behrens TE. Diffusion MRI: from quantitative measurement to in vivo neuroanatomy: Academic Press; 2013.

94.   Bihan DL. Molecular diffusion, tissue microdynamics and microstructure. NMR in Biomedicine 1995;8(7):375-386.

95.   Doran M, Hajnal JV, Bruggen NV, King MD, Young IR, Bydder GM. Normal and Abnormal White Matter Tracts Shown by MR Imaging using Directional Diffusion Weighted Sequences. Journal of computer assisted tomography 1990;14(6):865-873.

96.   Basser PJ, Mattiello J, LeBihan D. MR diffusion tensor spectroscopy and imaging. Biophysical Journal 1994;66(1):259-267.

97.   Basser PJ, Mattiello J, Lebihan D. Estimation of the Effective Self-Diffusion Tensor from the NMR Spin Echo. Journal of Magnetic Resonance, Series B 1994;103(3):247-254.

98.   Song S-K, Sun S-W, Ramsbottom MJ, Chang C, Russell J, Cross AH. Dysmyelination Revealed through MRI as Increased Radial (but Unchanged Axial) Diffusion of Water. NeuroImage 2002;17(3):1429-1436.

99.   Salomir R, de Senneville BD, Moonen CTW. A fast calculation method for magnetic field inhomogeneity due to an arbitrary distribution of bulk susceptibility. Concepts in Magnetic Resonance Part B: Magnetic Resonance Engineering 2003;19B(1):26-34.

100. Marques JP, Bowtell R. Application of a Fourier-based method for rapid calculation of field inhomogeneity due to spatial variation of magnetic susceptibility. Concepts in Magnetic Resonance Part B: Magnetic Resonance Engineering 2005;25B(1):65-78.

101. Shmueli K, de Zwart JA, van Gelderen P, Li T-Q, Dodd SJ, Duyn JH. Magnetic susceptibility mapping of brain tissue in vivo using MRI phase data. Magnetic Resonance in Medicine 2009;62(6):1510-1522.

102. Schweser F, Deistung A, Sommer K, Reichenbach JR. Toward online reconstruction of quantitative susceptibility maps: Superfast dipole inversion. Magnetic Resonance in Medicine 2013;69(6):1581-1593.

103. Wang Y, Liu T. Quantitative susceptibility mapping (QSM): Decoding MRI data for a tissue magnetic biomarker. Magnetic Resonance in Medicine 2015;73(1):82-101.

104. Haacke EM, Liu S, Buch S, Zheng W, Wu D, Ye Y. Quantitative susceptibility mapping: current status and future directions. Magnetic Resonance Imaging 2015;33(1):1-25.

105. Schofield MA, Zhu Y. Fast phase unwrapping algorithm for interferometric applications. Opt Lett 2003;28(14):1194-1196.

106. Li W, Wu B, Liu C. Quantitative susceptibility mapping of human brain reflects spatial variation in tissue composition. NeuroImage 2011;55(4):1645-1656.

107. Liu T, Khalidov I, de Rochefort L, Spincemaille P, Liu J, Tsiouris AJ, Wang Y. A novel background field removal method for MRI using projection onto dipole fields (PDF). NMR in Biomedicine 2011;24(9):1129-1136.
108. Wang Y. 2nd ISMRM Phase Contrast and Quantitative Susceptibility Mapping Workshop proceedings. ISMRM 2013.
109. Lerch JP, Yiu AP, Martinez-Canabal A, Pekar T, Bohbot VD, Frankland PW, Henkelman RM, Josselyn SA, Sled JG. Maze training in mice induces MRI-detectable brain shape changes specific to the type of learning. NeuroImage 2011;54(3):2086-2095.
110. Wang D, Doddrell DM, Cowin G. A novel phantom and method for comprehensive 3-dimensional measurement and correction of geometric distortion in magnetic resonance imaging. Magnetic Resonance Imaging 2004;22(4):529-542.
111. Wu YC, Alexander AL. A method for calibrating diffusion gradients in diffusion tensor imaging. J Comput Assist Tomogr 2007;31(6):984-993.
112. Bammer R, Markl M, Barnett A, Acar B, Alley MT, Pelc NJ, Glover GH, Moseley ME. Analysis and generalized correction of the effect of spatial gradient field distortions in diffusion-weighted imaging. Magnetic Resonance in Medicine 2003;50(3):560-569.
113. Gunter JL, Bernstein MA, Borowski BJ, Ward CP, Britson PJ, Felmlee JP, Schuff N, Weiner M, Jack CR. Measurement of MRI scanner performance with the ADNI phantom. Medical Physics 2009;36(6):2193-2205.
114. Doran SJ, Charles-Edwards L, Reinsberg SA, Leach MO. A complete distortion correction for MR images: I. Gradient warp correction. Phys Med Biol 2005;50(7):1343-1361.
115. Yoshimaru E, Totenhagen J, Alexander GE, Trouard TP. Design, manufacture, and analysis of customized phantoms for enhanced quality control in small animal MRI systems. Magnetic Resonance in Medicine 2014;71(2):880-884.
116. Baldwin LN, Wachowicz K, Thomas SD, Rivest R, Fallone BG. Characterization, prediction, and correction of geometric distortion in 3 T MR images. Medical Physics 2007;34(2):388-399.
117. Stanescu T, Jans HS, Wachowicz K, Fallone BG. Investigation of a 3D system distortion correction method for MR images. Journal of Applied Clinical Medical Physics 2010;11(1):200-216.
118. Schenck JF. The role of magnetic susceptibility in magnetic resonance imaging: MRI magnetic compatibility of the first and second kinds. Medical Physics 1996;23(6):815-850.
119. Cleary JO, Wiseman FK, Norris FC, Price AN, Choy M, Tybulewicz VLJ, Ordidge RJ, Brandner S, Fisher EMC, Lythgoe MF. Structural correlates of active-staining following magnetic resonance microscopy in the mouse brain. NeuroImage 2011;56(3):974-983.
120. Ourselin S, Roche A, Subsol G, Pennec X, Ayache N. Reconstructing a 3D structure from serial histological sections. Image and Vision Computing 2001;19(1–2):25-31.
121. Ourselin S, Stefanescu R, Pennec X. Robust Registration of Multi-modal Images: Towards Real-Time Clinical Applications. In: Dohi T, Kikinis R, editors. Medical Image Computing and Computer-Assisted Intervention — MICCAI 2002. Volume 2489, Lecture Notes in Computer Science: Springer Berlin Heidelberg; 2002. p 140-147.
122. Modat M, Ridgway GR, Taylor ZA, Lehmann M, Barnes J, Hawkes DJ, Fox NC, Ourselin S. Fast free-form deformation using graphics processing units. Computer Methods and Programs in Biomedicine 2010;98(3):278-284.

123. Modat M. http://sourceforge.net/p/niftyreg/git/ci/master/tree/.

124. Dice LR. Measures of the Amount of Ecologic Association Between Species. Ecology 1945;26(3):297-302.

125. Wells JA, O'Callaghan JM, Holmes HE, Powell NM, Johnson RA, Siow B, Torrealdea F, Ismail O, Walker-Samuel S, Golay X, Rega M, Richardson S, Modat M, Cardoso MJ, Ourselin S, Schwarz AJ, Ahmed Z, Murray TK, O'Neill MJ, Collins EC, Colgan N, Lythgoe MF. In vivo imaging of tau pathology using multi-parametric quantitative MRI. NeuroImage 2015;111(0):369-378.

126. Ma D, Cardoso MJ, Modat M, Powell N, Wells J, Holmes H, Wiseman F, Tybulewicz V, Fisher E, Lythgoe MF, Ourselin S. Automatic Structural Parcellation of Mouse Brain MRI Using Multi-Atlas Label Fusion. PLoS ONE 2014;9(1):e86576.

127. Zhang J, Peng Q, Li Q, Jahanshad N, Hou Z, Jiang M, Masuda N, Langbehn DR, Miller MI, Mori S, Ross CA, Duan W. Longitudinal characterization of brain atrophy of a Huntington's disease mouse model by automated morphological analyses of magnetic resonance images. NeuroImage 2010;49(3):2340-2351.

128. Oguz I, Yaxley R, Budin F, Hoogstoel M, Lee J, Maltbie E, Liu W, Crews FT. Comparison of Magnetic Resonance Imaging in Live vs. Post Mortem Rat Brains. PLoS ONE 2013;8(8):e71027.

129. Fox CH, Johnson FB, Whiting J, Roller PP. Formaldehyde fixation. J histochem Cytochem 1985;33(8):845-853.

130. Ma Y, Smith D, Hof PR, Foerster B, Hamilton S, Blackband SJ, Yu M, Benveniste H. In vivo 3D digital atlas database of the adult C57BL/6J mouse brain by magnetic resonance microscopy. Frontiers in Neuroanatomy 2008;2.

131. Cleary JO, Modat M, Norris FC, Price AN, Jayakody SA, Martinez-Barbera JP, Greene NDE, Hawkes DJ, Ordidge RJ, Scambler PJ, Ourselin S, Lythgoe MF. Magnetic resonance virtual histology for embryos: 3D atlases for automated high-throughput phenotyping. NeuroImage 2011;54(2):769-778.

132. Wang D, Strugnell W, Cowin G, Doddrell DM, Slaughter R. Geometric distortion in clinical MRI systems: Part II: correction using a 3D phantom. Magnetic Resonance Imaging 2004;22(9):1223-1232.

133. Wang D, Strugnell W, Cowin G, Doddrell DM, Slaughter R. Geometric distortion in clinical MRI systems: Part I: evaluation using a 3D phantom. Magnetic Resonance Imaging 2004;22(9):1211-1221.

134. Stefan AR, Simon JD, Elizabeth MC-E, Martin OL. A complete distortion correction for MR images: II. Rectification of static-field inhomogeneities by similarity-based profile mapping. Physics in Medicine and Biology 2005;50(11):2651.

135. Fields RD. Change in the Brain's White Matter. Science 2010;330(6005):768-769.

136. Sjöbeck M, Haglund M, Englund E. Decreasing myelin density reflected increasing white matter pathology in Alzheimer's disease—a neuropathological study. International Journal of Geriatric Psychiatry 2005;20(10):919-926.

137. Wang D-S, Bennett DA, Mufson EJ, Mattila P, Cochran E, Dickson DW. Contribution of changes in ubiquitin and myelin basic protein to age-related cognitive decline. Neuroscience Research 2004;48(1):93-100.

138. Sjöbeck M, Haglund M, Englund E. White matter mapping in Alzheimer's disease: A neuropathological study. Neurobiology of Aging 2006;27(5):673-680.

139. Gouw AA, Seewann A, Vrenken H, van der Flier WM, Rozemuller JM, Barkhof F, Scheltens P, Geurts JJG. Heterogeneity of white matter hyperintensities in

Alzheimer's disease: post-mortem quantitative MRI and neuropathology; 2008. 3286-3298 p.

140. Scheltens P, Barkhof F, Leys D, Wolters EC, Ravid R, Kamphorst W. Histopathologic correlates of white matter changes on MRI in Alzheimer's disease and normal aging. Neurology 1995;45(5):883-888.

141. Englund E. Neuropathology of White Matter Lesions in Vascular Cognitive Impairment. Cerebrovascular Diseases 2002;13(suppl 2)(Suppl. 2):11-15.

142. Bartzokis G. Age-related myelin breakdown: a developmental model of cognitive decline and Alzheimer's disease. Neurobiology of Aging 2004;25(1):5-18.

143. Reisberg B, Franssen EH, Souren LEM, Auer SR, Akram I, Kenowsky S. Evidence and mechanisms of retrogenesis in Alzheimer's and other dementias: Management and treatment import. American Journal of Alzheimer's Disease and Other Dementias 2002;17(4):202-212.

144. Štěpán-Buksakowska I, Keller J, Laczó J, Rulseh A, Hort J, Lisý J, Charvát F, Roček M, Hořínek D. Diffusion tensor imaging in Alzheimer disease and mild cognitive impairment. Neurologia i neurochirurgia polska 2012;46(5):462-471.

145. Coleman M. Axon degeneration mechanisms: commonality amid diversity. Nat Rev Neurosci 2005;6(11):889-898.

146. Basser PJ. Inferring microstructural features and the physiological state of tissues from diffusion-weighted images. NMR in Biomedicine 1995;8(7):333-344.

147. Catani M, Howard RJ, Pajevic S, Jones DK. Virtual in Vivo Interactive Dissection of White Matter Fasciculi in the Human Brain. NeuroImage 2002;17(1):77-94.

148. Silbert LC, Quinn JF, Moore MM, Corbridge E, Ball MJ, Murdoch G, Sexton G, Kaye JA. Changes in premorbid brain volume predict Alzheimer's disease pathology. Neurology 2003;61(4):487-492.

149. Gosche KM, Mortimer JA, Smith CD, Markesbery WR, Snowdon DA. Hippocampal volume as an index of Alzheimer neuropathology: Findings from the Nun Study. Neurology 2002;58(10):1476-1482.

150. Huang J, Friedland RP, Auchus AP. Diffusion Tensor Imaging of Normal-Appearing White Matter in Mild Cognitive Impairment and Early Alzheimer Disease: Preliminary Evidence of Axonal Degeneration in the Temporal Lobe. American Journal of Neuroradiology 2007;28(10):1943-1948.

151. Zhang Y, Schuff N, Du A-T, Rosen HJ, Kramer JH, Gorno-Tempini ML, Miller BL, Weiner MW. White matter damage in frontotemporal dementia and Alzheimer's disease measured by diffusion MRI; 2009. 2579-2592 p.

152. Bozzali M, Falini A, Franceschi M, Cercignani M, Zuffi M, Scotti G, Comi G, Filippi M. White matter damage in Alzheimer's disease assessed in vivo using diffusion tensor magnetic resonance imaging. Journal of Neurology, Neurosurgery & Psychiatry 2002;72(6):742-746.

153. Duan J-H, Wang H-Q, Xu J, Lin X, Chen S-Q, Kang Z, Yao Z-B. White matter damage of patients with Alzheimer's disease correlated with the decreased cognitive function. Surg Radiol Anat 2006;28(2):150-156.

154. Nakata Y, Sato N, Nemoto K, Abe O, Shikakura S, Arima K, Furuta N, Uno M, Hirai S, Masutani Y, Ohtomo K, Barkovich AJ, Aoki S. Diffusion abnormality in the posterior cingulum and hippocampal volume: correlation with disease progression in Alzheimer's disease. Magnetic Resonance Imaging 2009;27(3):347-354.

155. Stricker NH, Schweinsburg BC, Delano-Wood L, Wierenga CE, Bangen KJ, Haaland KY, Frank LR, Salmon DP, Bondi MW. Decreased white matter integrity

in late-myelinating fiber pathways in Alzheimer's disease supports retrogenesis. NeuroImage 2009;45(1):10-16.

156. Choi SJ, Lim KO, Monteiro I, Reisberg B. Diffusion Tensor Imaging of Frontal White Matter Microstructure in Early Alzheimer's Disease: A Preliminary Study. Journal of Geriatric Psychiatry and Neurology 2005;18(1):12-19.

157. Sexton CE, Kalu UG, Filippini N, Mackay CE, Ebmeier KP. A meta-analysis of diffusion tensor imaging in mild cognitive impairment and Alzheimer's disease. Neurobiology of Aging 2011;32(12):2322.e2325-2322.e2318.

158. Chen T-F, Chen Y-F, Cheng T-W, Hua M-S, Liu H-M, Chiu M-J. Executive dysfunction and periventricular diffusion tensor changes in amnesic mild cognitive impairment and early Alzheimer's disease. Human brain mapping 2009;30(11):3826-3836.

159. Wang L, Goldstein FC, Veledar E, Levey AI, Lah JJ, Meltzer CC, Holder CA, Mao H. Alterations in Cortical Thickness and White Matter Integrity in Mild Cognitive Impairment Measured by Whole-Brain Cortical Thickness Mapping and Diffusion Tensor Imaging. American Journal of Neuroradiology 2009;30(5):893-899.

160. Zarei M, Johansen-Berg H, Smith S, Ciccarelli O, Thompson AJ, Matthews PM. Functional anatomy of interhemispheric cortical connections in the human brain. Journal of Anatomy 2006;209(3):311-320.

161. Goveas J, O'Dwyer L, Mascalchi M, Cosottini M, Diciotti S, De Santis S, Passamonti L, Tessa C, Toschi N, Giannelli M. Diffusion-MRI in neurodegenerative disorders. Magnetic Resonance Imaging 2015;33(7):853-876.

162. Stebbins G, Murphy C. Diffusion tensor imaging in Alzheimer's disease and mild cognitive impairment. Behavioural neurology 2009;21(1-2):39-49.

163. Agosta F, Pievani M, Sala S, Geroldi C, Galluzzi S, Frisoni GB, Filippi M. White Matter Damage in Alzheimer Disease and Its Relationship to Gray Matter Atrophy. Radiology 2011;258(3):853-863.

164. Mielke MM, Okonkwo OC, Oishi K, Mori S, Tighe S, Miller MI, Ceritoglu C, Brown T, Albert M, Lyketsos CG. Fornix integrity and hippocampal volume predict memory decline and progression to Alzheimer's disease. Alzheimer's & Dementia 2012;8(2):105-113.

165. Nowrangi MA, Lyketsos CG, Leoutsakos J-MS, Oishi K, Albert M, Mori S, Mielke MM. Longitudinal, region-specific course of diffusion tensor imaging measures in mild cognitive impairment and Alzheimer's disease. Alzheimer's & Dementia 2013;9(5):519-528.

166. Honea RA, Vidoni E, Harsha A, Burns JM. Impact of APOE on the Healthy Aging Brain: A Voxel-Based MRI and DTI Study. Journal of Alzheimer's disease : JAD 2009;18(3):553-564.

167. Persson J, Lind J, Larsson A, Ingvar M, Cruts M, Van Broeckhoven C, Adolfsson R, Nilsson L-G, Nyberg L. Altered brain white matter integrity in healthy carriers of the APOE ε4 allele: A risk for AD? Neurology 2006;66(7):1029-1033.

168. Bendlin BB, Ries ML, Canu E, Sodhi A, Lazar M, Alexander AL, Carlsson CM, Sager MA, Asthana S, Johnson SC. White matter is altered with parental family history of Alzheimer's disease. Alzheimer's & Dementia 2010;6(5):394-403.

169. Rose SE, Janke PhD AL, Chalk JB. Gray and white matter changes in Alzheimer's disease: A diffusion tensor imaging study. Journal of Magnetic Resonance Imaging 2008;27(1):20-26.

170. Kantarci K, Jack CR, Xu YC, Campeau NG, O'Brien PC, Smith GE, Ivnik RJ, Boeve BF, Kokmen E, Tangalos EG, Petersen RC. Mild cognitive impairment and

Alzheimer disease: regional diffusivity of water. Radiology 2001;219(1):101-107.

171. Fellgiebel A, Wille P, Müller MJ, Winterer G, Scheurich A, Vucurevic G, Schmidt LG, Stoeter P. Ultrastructural Hippocampal and White Matter Alterations in Mild Cognitive Impairment: A Diffusion Tensor Imaging Study. Dementia and Geriatric Cognitive Disorders 2004;18(1):101-108.

172. Beaulieu C. The basis of anisotropic water diffusion in the nervous system – a technical review. NMR in Biomedicine 2002;15(7-8):435-455.

173. Song S-K, Yoshino J, Le TQ, Lin S-J, Sun S-W, Cross AH, Armstrong RC. Demyelination increases radial diffusivity in corpus callosum of mouse brain. NeuroImage 2005;26(1):132-140.

174. Holland PR, Bastin ME, Jansen MA, Merrifield GD, Coltman RB, Scott F, Nowers H, Khallout K, Marshall I, Wardlaw JM, Deary IJ, McCulloch J, Horsburgh K. MRI is a sensitive marker of subtle white matter pathology in hypoperfused mice. Neurobiology of Aging 2011;32(12):2325.e2321-2325.e2326.

175. Song S-K, Sun S-W, Ju W-K, Lin S-J, Cross AH, Neufeld AH. Diffusion tensor imaging detects and differentiates axon and myelin degeneration in mouse optic nerve after retinal ischemia. NeuroImage 2003;20(3):1714-1722.

176. Zhang J, Jones M, DeBoy CA, Reich DS, Farrell JAD, Hoffman PN, Griffin JW, Sheikh KA, Miller MI, Mori S, Calabresi PA. Diffusion Tensor Magnetic Resonance Imaging of Wallerian Degeneration in Rat Spinal Cord after Dorsal Root Axotomy. The Journal of Neuroscience 2009;29(10):3160-3171.

177. Herrera JJ, Chacko T, Narayana PA. Histological correlation of diffusion tensor imaging metrics in experimental spinal cord injury. Journal of Neuroscience Research 2008;86(2):443-447.

178. Drobyshevsky A, Derrick M, Wyrwicz AM, Ji X, Englof I, Ullman LM, Zelaya ME, Northington FJ, Tan S. White matter injury correlates with hypertonia in an animal model of cerebral palsy. J Cereb Blood Flow Metab 2006;27(2):270-281.

179. Vincze A, Mázló M, Seress L, Komoly S, Ábrahám H. A correlative light and electron microscopic study of postnatal myelination in the murine corpus callosum. International Journal of Developmental Neuroscience 2008;26(6):575-584.

180. Qin Y-Y, Li M-W, Zhang S, Zhang Y, Zhao L-Y, Lei H, Oishi K, Zhu W-Z. In vivo quantitative whole-brain diffusion tensor imaging analysis of APP/PS1 transgenic mice using voxel-based and atlas-based methods. Neuroradiology 2013;55(8):1027-1038.

181. Müller H-P, Kassubek J, Vernikouskaya I, Ludolph AC, Stiller D, Rasche V. Diffusion Tensor Magnetic Resonance Imaging of the Brain in APP Transgenic Mice: A Cohort Study. PLoS ONE 2013;8(6):e67630.

182. Zhang J. Diffusion tensor imaging of white matter pathology in the mouse brain. Imaging in medicine 2010;2(6):623-632.

183. Sun S-W, Liang H-F, Trinkaus K, Cross AH, Armstrong RC, Song S-K. Noninvasive detection of cuprizone induced axonal damage and demyelination in the mouse corpus callosum. Magnetic Resonance in Medicine 2006;55(2):302-308.

184. Zhang J, Jones MV, McMahon MT, Mori S, Calabresi PA. In vivo and ex vivo diffusion tensor imaging of cuprizone-induced demyelination in the mouse corpus callosum. Magnetic Resonance in Medicine 2012;67(3):750-759.

185. Chahboune H, R. Ment L, B. Stewart W, Ma X, Rothman DL, Hyder F. Neurodevelopment of C57B/L6 mouse brain assessed by in vivo diffusion tensor imaging. NMR in Biomedicine 2007;20(3):375-382.

186. Zerbi V, Kleinnijenhuis M, Fang X, Jansen D, Veltien A, Van Asten J, Timmer N, Dederen PJ, Kiliaan AJ, Heerschap A. Gray and white matter degeneration

revealed by diffusion in an Alzheimer mouse model. Neurobiology of Aging 2013;34(5):1440-1450.

187. Harsan L-A, Paul D, Schnell S, Kreher BW, Hennig J, Staiger JF, von Elverfeldt D. In vivo diffusion tensor magnetic resonance imaging and fiber tracking of the mouse brain. NMR in Biomedicine 2010;23(7):884-896.

188. Guilfoyle DN, Hrabe J. Interleaved snapshot echo planar imaging of mouse brain at 7.0 T. NMR in Biomedicine 2006;19(1):108-115.

189. Grieve SM, Blamire AM, Styles P. The effect of bulk susceptibility on murine snapshot imaging at 7.0 T: A comparison of snapshot imaging techniques. Magnetic Resonance in Medicine 2000;43(5):747-755.

190. Boska MD, Hasan KM, Kibuule D, Banerjee R, McIntyre E, Nelson JA, Hahn T, Gendelman HE, Mosley RL. Quantitative diffusion tensor imaging detects dopaminergic neuronal degeneration in a murine model of Parkinson's disease. Neurobiology of Disease 2007;26(3):590-596.

191. Wang S, Wu EX, Tam CN, Lau H-F, Cheung P-T, Khong P-L. Characterization of White Matter Injury in a Hypoxic-Ischemic Neonatal Rat Model by Diffusion Tensor MRI. Stroke 2008;39(8):2348-2353.

192. Jones DK, Horsfield MA, Simmons A. Optimal strategies for measuring diffusion in anisotropic systems by magnetic resonance imaging. Magnetic Resonance in Medicine 1999;42(3):515-525.

193. Skare S, Hedehus M, Moseley ME, Li T-Q. Condition Number as a Measure of Noise Performance of Diffusion Tensor Data Acquisition Schemes with MRI. Journal of Magnetic Resonance 2000;147(2):340-352.

194. Jones DK. The effect of gradient sampling schemes on measures derived from diffusion tensor MRI: A Monte Carlo study†. Magnetic Resonance in Medicine 2004;51(4):807-815.

195. Armitage PA, Bastin ME. Utilizing the diffusion-to-noise ratio to optimize magnetic resonance diffusion tensor acquisition strategies for improving measurements of diffusion anisotropy. Magnetic Resonance in Medicine 2001;45(6):1056-1065.

196. Batchelor PG, Atkinson D, Hill DLG, Calamante F, Connelly A. Anisotropic noise propagation in diffusion tensor MRI sampling schemes. Magnetic Resonance in Medicine 2003;49(6):1143-1151.

197. Le Bihan D, Mangin J-F, Poupon C, Clark CA, Pappata S, Molko N, Chabriat H. Diffusion tensor imaging: Concepts and applications. Journal of Magnetic Resonance Imaging 2001;13(4):534-546.

198. Tofts PS, Lloyd D, Clark CA, Barker GJ, Parker GJM, McConville P, Baldock C, Pope JM. Test liquids for quantitative MRI measurements of self-diffusion coefficient in vivo. Magnetic Resonance in Medicine 2000;43(3):368-374.

199. Le Bihan D, Poupon C, Amadon A, Lethimonnier F. Artifacts and pitfalls in diffusion MRI. Journal of Magnetic Resonance Imaging 2006;24(3):478-488.

200. Farrell JAD, Landman BA, Jones CK, Smith SA, Prince JL, van Zijl PCM, Mori S. Effects of signal-to-noise ratio on the accuracy and reproducibility of diffusion tensor imaging–derived fractional anisotropy, mean diffusivity, and principal eigenvector measurements at 1.5T. Journal of Magnetic Resonance Imaging 2007;26(3):756-767.

201. Dietrich O, Heiland S, Sartor K. Noise correction for the exact determination of apparent diffusion coefficients at low SNR. Magnetic Resonance in Medicine 2001;45(3):448-453.

202. Lee VM-Y, Goedert M, Trojanowski JQ. NEURODEGENERATIVE TAUOPATHIES. Annual Review of Neuroscience 2001;24(1):1121-1159.

203. Ramsden M, Kotilinek L, Forster C, Paulson J, McGowan E, SantaCruz K, Guimaraes A, Yue M, Lewis J, Carlson G. Age-dependent neurofibrillary tangle formation, neuron loss, and memory impairment in a mouse model of human tauopathy (P301L). J Neurosci 2005;25:10637 - 10647.

204. Santacruz K, Lewis J, Spires T, Paulson J, Kotilinek L, Ingelsson M, Guimaraes A, DeTure M, Ramsden M, McGowan E. Tau suppression in a neurodegenerative mouse model improves memory function. Science 2005;309:476 - 481.

205. Sahara N, Perez PD, Lin W-L, Dickson DW, Ren Y, Zeng H, Lewis J, Febo M. Age-related decline in white matter integrity in a mouse model of tauopathy: an in vivo diffusion tensor magnetic resonance imaging study. Neurobiology of Aging 2014;35(6):1364-1374.

206. Desai MK, Sudol KL, Janelsins MC, Mastrangelo MA, Frazer ME, Bowers WJ. Triple-transgenic Alzheimer's disease mice exhibit region-specific abnormalities in brain myelination patterns prior to appearance of amyloid and tau pathology. Glia 2009;57(1):54-65.

207. Kantarci K, Jack CR, Xu YC, Campeau NG, O'Brien PC, Smith GE, Ivnik RJ, Boeve BF, Kokmen E, Tangalos EG, Petersen RC. Mild Cognitive Impairment and Alzheimer Disease: Regional Diffusivity of Water. Radiology 2001;219(1):101-107.

208. Whitwell JL, Josephs KA, Murray ME, Kantarci K, Przybelski SA, Weigand SD, Vemuri P, Senjem ML, Parisi JE, Knopman DS, Boeve BF, Petersen RC, Dickson DW, Jack CR. MRI correlates of neurofibrillary tangle pathology at autopsy: A voxel-based morphometry study. Neurology 2008;71(10):743-749.

209. Clavaguera F, Bolmont T, Crowther RA, Abramowski D, Frank S, Probst A, Fraser G, Stalder AK, Beibel M, Staufenbiel M, Jucker M, Goedert M, Tolnay M. Transmission and spreading of tauopathy in transgenic mouse brain. Nat Cell Biol 2009;11(7):909-913.

210. de Calignon A, Polydoro M, Suárez-Calvet M, William C, Adamowicz David H, Kopeikina Kathy J, Pitstick R, Sahara N, Ashe Karen H, Carlson George A, Spires-Jones Tara L, Hyman Bradley T. Propagation of Tau Pathology in a Model of Early Alzheimer's Disease. Neuron 2012;73(4):685-697.

211. Zhou J, Gennatas Efstathios D, Kramer Joel H, Miller Bruce L, Seeley William W. Predicting Regional Neurodegeneration from the Healthy Brain Functional Connectome. Neuron 2012;73(6):1216-1227.

212. Raj A, Kuceyeski A, Weiner M. A Network Diffusion Model of Disease Progression in Dementia. Neuron 2012;73(6):1204-1215.

213. Argyridis I, Li W, Johnson GA, Liu C. Quantitative magnetic susceptibility of the developing mouse brain reveals microstructural changes in the white matter. NeuroImage 2014;88(0):134-142.

214. Bartzokis G, Tishler TA. MRI evaluation of basal ganglia ferritin iron and neurotoxicity in Alzheimer's and Huntingon's disease. Cellular and molecular biology (Noisy-le-Grand, France) 2000;46(4):821-833.

215. Abbaspour N, Hurrell R, Kelishadi R. Review on iron and its importance for human health. Journal of Research in Medical Sciences : The Official Journal of Isfahan University of Medical Sciences 2014;19(2):164-174.

216. Ward RJ, Zucca FA, Duyn JH, Crichton RR, Zecca L. The role of iron in brain ageing and neurodegenerative disorders. The Lancet Neurology 2014;13(10):1045-1060.

217. Connor JR, Snyder BS, Beard JL, Fine RE, Mufson EJ. Regional distribution of iron and iron-regulatory proteins in the brain in aging and Alzheimer's disease. Journal of Neuroscience Research 1992;31(2):327-335.

218. Cai Z, Xiao M. Oligodendrocytes and Alzheimer's disease. International Journal of Neuroscience 2015:1-8.

219. Bartzokis G, Lu PH, Mintz J. Human brain myelination and amyloid beta deposition in Alzheimer's disease. Alzheimer's & Dementia 2007;3(2):122-125.

220. Zecca L, Youdim MBH, Riederer P, Connor JR, Crichton RR. Iron, brain ageing and neurodegenerative disorders. Nat Rev Neurosci 2004;5(11):863-873.

221. Urrutia P, Aguirre P, Esparza A, Tapia V, Mena NP, Arredondo M, González-Billault C, Núñez MT. Inflammation alters the expression of DMT1, FPN1 and hepcidin, and it causes iron accumulation in central nervous system cells. Journal of Neurochemistry 2013;126(4):541-549.

222. Zeineh MM, Chen Y, Kitzler HH, Hammond R, Vogel H, Rutt BK. Activated iron-containing microglia in the human hippocampus identified by magnetic resonance imaging in Alzheimer disease. Neurobiology of Aging 2015;36(9):2483-2500.

223. Lovell MA, Robertson JD, Teesdale WJ, Campbell JL, Markesbery WR. Copper, iron and zinc in Alzheimer's disease senile plaques. Journal of the Neurological Sciences 1998;158(1):47-52.

224. Good PF, Perl DP, Bierer LM, Schmeidler J. Selective accumulation of aluminum and iron in the neurofibrillary tangles of Alzheimer's disease: A laser microprobe (LAMMA) study. Annals of Neurology 1992;31(3):286-292.

225. Rogers JT, Randall JD, Cahill CM, Eder PS, Huang X, Gunshin H, Leiter L, McPhee J, Sarang SS, Utsuki T, Greig NH, Lahiri DK, Tanzi RE, Bush AI, Giordano T, Gullans SR. An Iron-responsive Element Type II in the 5′-Untranslated Region of the Alzheimer's Amyloid Precursor Protein Transcript. Journal of Biological Chemistry 2002;277(47):45518-45528.

226. Crespo ÂC, Silva B, Marques L, Marcelino E, Maruta C, Costa S, Timóteo Â, Vilares A, Couto FS, Faustino P, Correia AP, Verdelho A, Porto G, Guerreiro M, Herrero A, Costa C, de Mendonça A, Costa L, Martins M. Genetic and biochemical markers in patients with Alzheimer's disease support a concerted systemic iron homeostasis dysregulation. Neurobiology of Aging 2014;35(4):777-785.

227. Yamamoto A, Shin RW, Hasegawa K, Naiki H, Sato H, Yoshimasu F, Kitamoto T. Iron (III) induces aggregation of hyperphosphorylated τ and its reduction to iron (II) reverses the aggregation: Implications in the formation of neurofibrillary tangles of Alzheimer's disease. Journal of Neurochemistry 2002;82(5):1137-1147.

228. Lei P, Ayton S, Finkelstein DI, Spoerri L, Ciccotosto GD, Wright DK, Wong BXW, Adlard PA, Cherny RA, Lam LQ, Roberts BR, Volitakis I, Egan GF, McLean CA, Cappai R, Duce JA, Bush AI. Tau deficiency induces parkinsonism with dementia by impairing APP-mediated iron export. Nat Med 2012;18(2):291-295.

229. Daugherty A, Raz N. Appraising the Role of Iron in Brain Aging and Cognition: Promises and Limitations of MRI Methods. Neuropsychol Rev 2015:1-16.

230. Ogawa S, Lee T-M, Kay AR, Tank DW. Brain magnetic resonance imaging with contrast dependent on blood oxygenation. Proceedings of the National Academy of Sciences 1990;87(24):9868-9872.

231. Haacke EM, Cheng NYC, House MJ, Liu Q, Neelavalli J, Ogg RJ, Khan A, Ayaz M, Kirsch W, Obenaus A. Imaging iron stores in the brain using magnetic resonance imaging. Magnetic Resonance Imaging 2005;23(1):1-25.

232. Schenck JF. Imaging of brain iron by magnetic resonance: T2 relaxation at different field strengths. Journal of the Neurological Sciences 1995;134, Supplement:10-18.

233. Langkammer C, Ropele S, Pirpamer L, Fazekas F, Schmidt R. MRI for Iron Mapping in Alzheimer's Disease. Neurodegenerative Diseases 2014;13(2-3):189-191.
234. Siemonsen S, Finsterbusch J, Matschke J, Lorenzen A, Ding X-Q, Fiehler J. Age-Dependent Normal Values of T2* and T2′ in Brain Parenchyma. American Journal of Neuroradiology 2008;29(5):950-955.
235. Bartzokis G, Mintz J, Sultzer D, Marx P, Herzberg JS, Phelan CK, Marder SR. In vivo MR evaluation of age-related increases in brain iron. American Journal of Neuroradiology 1994;15(6):1129-1138.
236. Ordidge RJ, Gorell JM, Deniau JC, Knight RA, Helpern JA. Assessment of relative brain iron concentrations using T2-weighted and T2*-weighted MRI at 3 Tesla. Magnetic Resonance in Medicine 1994;32(3):335-341.
237. Langkammer C, Krebs N, Goessler W, Scheurer E, Ebner F, Yen K, Fazekas F, Ropele S. Quantitative MR Imaging of Brain Iron: A Postmortem Validation Study. Radiology 2010;257(2):455-462.
238. Ogg RJ, Langston JW, Haacke EM, Steen RG, Taylor JS. The correlation between phase shifts in gradient-echo MR images and regional brain iron concentration. Magnetic Resonance Imaging 1999;17(8):1141-1148.
239. Reichenbach JR, Venkatesan R, Schillinger DJ, Kido DK, Haacke EM. Small vessels in the human brain: MR venography with deoxyhemoglobin as an intrinsic contrast agent. Radiology 1997;204(1):272-277.
240. Nandigam RNK, Viswanathan A, Delgado P, Skehan ME, Smith EE, Rosand J, Greenberg SM, Dickerson BC. MR Imaging Detection of Cerebral Microbleeds: Effect of Susceptibility-Weighted Imaging, Section Thickness, and Field Strength. American Journal of Neuroradiology 2009;30(2):338-343.
241. Haacke EM, Xu Y, Cheng Y-CN, Reichenbach JR. Susceptibility weighted imaging (SWI). Magnetic Resonance in Medicine 2004;52(3):612-618.
242. Langkammer C, Schweser F, Krebs N, Deistung A, Goessler W, Scheurer E, Sommer K, Reishofer G, Yen K, Fazekas F, Ropele S, Reichenbach JR. Quantitative susceptibility mapping (QSM) as a means to measure brain iron? A post mortem validation study. NeuroImage 2012;62(3):1593-1599.
243. Li J, Chang S, Liu T, Wang Q, Cui D, Chen X, Jin M, Wang B, Pei M, Wisnieff C, Spincemaille P, Zhang M, Wang Y. Reducing the object orientation dependence of susceptibility effects in gradient echo MRI through quantitative susceptibility mapping. Magnetic Resonance in Medicine 2012;68(5):1563-1569.
244. Benveniste H, Einstein G, Kim KR, Hulette C, Johnson GA. Detection of neuritic plaques in Alzheimer's disease by magnetic resonance microscopy. Proceedings of the National Academy of Sciences of the United States of America 1999;96(24):14079-14084.
245. Parsey RV, Krishnan KRR. Quantitative analysis of T2 signal intensities in Alzheimer's Disease. Psychiatry Research: Neuroimaging 1998;82(3):181-185.
246. Bartzokis G, Sultzer D, Cummings J, et al. IN vivo evaluation of brain iron in alzheimer disease using magnetic resonance imaging. Archives of General Psychiatry 2000;57(1):47-53.
247. Moon W-J, Kim H-J, Roh HG, Choi JW, Han S-H. Fluid-Attenuated Inversion Recovery Hypointensity of the Pulvinar Nucleus of Patients with Alzheimer Disease: Its Possible Association with Iron Accumulation as Evidenced by the T2* Map. Korean J Radiol 2012;13(6):674-683.
248. Zhu W-z, Zhong W-d, Wang W, Zhan C-j, Wang C-y, Qi J-p, Wang J-z, Lei T. Quantitative MR Phase-corrected Imaging to Investigate Increased Brain Iron Deposition of Patients with Alzheimer Disease. Radiology 2009;253(2):497-504.

249. van Rooden S, Versluis MJ, Liem MK, Milles J, Maier AB, Oleksik AM, Webb AG, van Buchem MA, van der Grond J. Cortical phase changes in Alzheimer's disease at 7T MRI: A novel imaging marker. Alzheimer's & Dementia 2014;10(1):e19-e26.

250. Acosta-Cabronero J, Williams GB, Cardenas-Blanco A, Arnold RJ, Lupson V, Nestor PJ. *In Vivo* Quantitative Susceptibility Mapping (QSM) in Alzheimer's Disease. PLoS ONE 2013;8(11):e81093.

251. Falangola MF, Dyakin VV, Lee SP, Bogart A, Babb JS, Duff K, Nixon R, Helpern JA. Quantitative MRI reveals aging-associated T2 changes in mouse models of Alzheimer's disease. NMR in Biomedicine 2007;20(3):343-351.

252. El Tayara NET, Volk A, Dhenain M, Delatour B. Transverse relaxation time reflects brain amyloidosis in young APP/PS1 transgenic mice. Magnetic Resonance in Medicine 2007;58(1):179-184.

253. Braakman N, Matysik J, van Duinen SG, Verbeek F, Schliebs R, de Groot HJM, Alia A. Longitudinal assessment of Alzheimer's β-amyloid plaque development in transgenic mice monitored by in vivo magnetic resonance microimaging. Journal of Magnetic Resonance Imaging 2006;24(3):530-536.

254. El Tannir El Tayara N, Delatour B, Le Cudennec C, Guégan M, Volk A, Dhenain M. Age-related evolution of amyloid burden, iron load, and MR relaxation times in a transgenic mouse model of Alzheimer's disease. Neurobiology of Disease 2006;22(1):199-208.

255. Nakada T, Matsuzawa H, Igarashi H, Fujii Y, Kwee IL. In vivo visualization of senile-plaque-like pathology in Alzheimer's disease patients by mr microscopy on a 7T system. Journal of Neuroimaging 2008;18(2):125-129.

256. Klohs J, Deistung A, Schweser F, Grandjean J, Dominietto M, Waschkies C, Nitsch RM, Knuesel I, Reichenbach JR, Rudin M. Detection of cerebral microbleeds with quantitative susceptibility mapping in the ArcAbeta mouse model of cerebral amyloidosis. J Cereb Blood Flow Metab 2011;31(12):2282-2292.

257. Klohs J, Politano IW, Deistung A, Grandjean J, Drewek A, Dominietto M, Keist R, Schweser F, Reichenbach JR, Nitsch RM, Knuesel I, Rudin M. Longitudinal Assessment of Amyloid Pathology in Transgenic ArcAβ Mice Using Multi-Parametric Magnetic Resonance Imaging. PLoS ONE 2013;8(6):e66097.

258. Maphis N, Xu G, Kokiko-Cochran ON, Jiang S, Cardona A, Ransohoff RM, Lamb BT, Bhaskar K. Reactive microglia drive tau pathology and contribute to the spreading of pathological tau in the brain; 2015.

259. Yoshiyama Y, Higuchi M, Zhang B, Huang S-M, Iwata N, Saido Takaomi C, Maeda J, Suhara T, Trojanowski JQ, Lee VMY. Synapse Loss and Microglial Activation Precede Tangles in a P301S Tauopathy Mouse Model. Neuron 2007;53(3):337-351.

260. Ren Y, Lin W-L, Sanchez L, Ceballos C, Polydoro M, Spires-Jones TL, Hyman BT, Dickson DW, Sahara N. Endogenous Tau Aggregates in Oligodendrocytes of rTg4510 Mice Induced by Human P301L Tau. Journal of Alzheimer's Disease 2014;38:589-600.

261. Dibb R, Li W, Cofer G, Liu C. Microstructural origins of gadolinium-enhanced susceptibility contrast and anisotropy. Magnetic Resonance in Medicine 2014;72(6):1702-1711.

262. de Rochefort L, Liu T, Kressler B, Liu J, Spincemaille P, Lebon V, Wu J, Wang Y. Quantitative susceptibility map reconstruction from MR phase data using bayesian regularization: Validation and application to brain imaging. Magnetic Resonance in Medicine 2010;63(1):194-206.

263. Sled JG, Zijdenbos AP, Evans AC. A nonparametric method for automatic correction of intensity nonuniformity in MRI data. Medical Imaging, IEEE Transactions on 1998;17(1):87-97.

264. Jorge Cardoso M, Leung K, Modat M, Keihaninejad S, Cash D, Barnes J, Fox NC, Ourselin S. STEPS: Similarity and Truth Estimation for Propagated Segmentations and its application to hippocampal segmentation and brain parcelation. Medical Image Analysis 2013;17(6):671-684.

265. Genovese CR, Lazar NA, Nichols T. Thresholding of Statistical Maps in Functional Neuroimaging Using the False Discovery Rate. NeuroImage 2002;15(4):870-878.

266. Haacke EM, Brown R, Thompson M, Venkatesan R. Magnetic resonance imaging: physical principles and sequence design. 1999. New York: A John Wiley and Sons.

267. Wu B, Li W, Avram AV, Gho S-M, Liu C. Fast and tissue-optimized mapping of magnetic susceptibility and T2* with multi-echo and multi-shot spirals. NeuroImage 2012;59(1):297-305.

268. Feng W, Neelavalli J, Haacke EM. Catalytic multiecho phase unwrapping scheme (CAMPUS) in multiecho gradient echo imaging: Removing phase wraps on a voxel-by-voxel basis. Magnetic Resonance in Medicine 2013;70(1):117-126.

269. Shepherd TM, Thelwall PE, Stanisz GJ, Blackband SJ. Aldehyde fixative solutions alter the water relaxation and diffusion properties of nervous tissue. Magnetic Resonance in Medicine 2009;62(1):26-34.

270. Benveniste H, Blackband S. MR microscopy and high resolution small animal MRI: applications in neuroscience research. Progress in Neurobiology 2002;67(5):393-420.

271. Barral JK, Gudmundson E, Stikov N, Etezadi-Amoli M, Stoica P, Nishimura DG. A Robust Methodology for In Vivo T(1) Mapping. Magnetic resonance in medicine : official journal of the Society of Magnetic Resonance in Medicine / Society of Magnetic Resonance in Medicine 2010;64(4):1057-1067.

272. Bernstein MA, Shimakawa A, Pelc NJ. Minimizing TE in moment-nulled or flow-encoded two-and three-dimensional gradient-echo imaging. Journal of Magnetic Resonance Imaging 1992;2(5):583-588.

273. Dibb R, Li W, Cofer G, Liu C. Microstructural origins of gadolinium-enhanced susceptibility contrast and anisotropy. Magnetic Resonance in Medicine 2014:n/a-n/a.

274. van de Ven RCG, Hogers B, van den Maagdenberg AMJM, de Groot HJM, Ferrari MD, Frants RR, Poelmann RE, van der Weerd L, Kiihne SR. T1 relaxation in in vivo mouse brain at ultra-high field. Magnetic Resonance in Medicine 2007;58(2):390-395.

275. Lee J, Shmueli K, Kang B-T, Yao B, Fukunaga M, van Gelderen P, Palumbo S, Bosetti F, Silva AC, Duyn JH. The contribution of myelin to magnetic susceptibility-weighted contrasts in high-field MRI of the brain. NeuroImage 2012;59(4):3967-3975.

276. Ivanov EN, Pogromsky AY, Van Den Brink JS, Rooda JE. Optimization of duty cycles for MRI scanners. Concepts in Magnetic Resonance Part B: Magnetic Resonance Engineering 2010;37B(3):180-192.

277. Rieke V, Pauly KB. MR Thermometry. Journal of magnetic resonance imaging : JMRI 2008;27(2):376-390.

278. Chavhan GB, Babyn PS, Thomas B, Shroff MM, Haacke EM. Principles, Techniques, and Applications of T2*-based MR Imaging and Its Special Applications. Radiographics 2009;29(5):1433-1449.

279. Xu B, Liu T, Spincemaille P, Prince M, Wang Y. Flow compensated quantitative susceptibility mapping for venous oxygenation imaging. Magnetic Resonance in Medicine 2014;72(2):438-445.

280. Wu D, Liu S, Buch S, Ye Y, Dai Y, Haacke EM. A fully flow-compensated multiecho susceptibility-weighted imaging sequence: The effects of acceleration and background field on flow compensation. Magnetic Resonance in Medicine 2015:n/a-n/a.

281. Deistung A, Dittrich E, Sedlacik J, Rauscher A, Reichenbach JR. ToF-SWI: Simultaneous time of flight and fully flow compensated susceptibility weighted imaging. Journal of Magnetic Resonance Imaging 2009;29(6):1478-1484.

282. Bilgic B, Pfefferbaum A, Rohlfing T, Sullivan EV, Adalsteinsson E. MRI estimates of brain iron concentration in normal aging using quantitative susceptibility mapping. NeuroImage 2012;59(3):2625-2635.

283. Hammond KE, Lupo JM, Xu D, Metcalf M, Kelley DAC, Pelletier D, Chang SM, Mukherjee P, Vigneron DB, Nelson SJ. Development of a robust method for generating 7.0 T multichannel phase images of the brain with application to normal volunteers and patients with neurological diseases. NeuroImage 2008;39(4):1682-1692.

284. Schweser F, Deistung A, Lehr BW, Reichenbach JR. Quantitative imaging of intrinsic magnetic tissue properties using MRI signal phase: An approach to in vivo brain iron metabolism? NeuroImage 2011;54(4):2789-2807.

285. Wu B, Li W, Guidon A, Liu C. Whole brain susceptibility mapping using compressed sensing. Magnetic Resonance in Medicine 2012;67(1):137-147.

286. Liu C, Li W, Johnson GA, Wu B. High-field (9.4 T) MRI of brain dysmyelination by quantitative mapping of magnetic susceptibility. NeuroImage 2011;56(3):930-938.

287. Akiyama H, Barger S, Barnum S, Bradt B, Bauer J, Cole GM, Cooper NR, Eikelenboom P, Emmerling M, Fiebich BL, Finch CE, Frautschy S, Griffin WST, Hampel H, Hull M, Landreth G, Lue LF, Mrak R, Mackenzie IR, McGeer PL, O'Banion MK, Pachter J, Pasinetti G, Plata–Salaman C, Rogers J, Rydel R, Shen Y, Streit W, Strohmeyer R, Tooyoma I, Van Muiswinkel FL, Veerhuis R, Walker D, Webster S, Wegrzyniak B, Wenk G, Wyss–Coray T. Inflammation and Alzheimer's disease. Neurobiology of Aging 2000;21(3):383-421.

288. Jack CR, Wengenack TM, Reyes DA, Garwood M, Curran GL, Borowski BJ, Lin J, Preboske GM, Holasek SS, Adriany G, Poduslo JF. In Vivo Magnetic Resonance Microimaging of Individual Amyloid Plaques in Alzheimer's Transgenic Mice. The Journal of Neuroscience 2005;25(43):10041-10048.

289. Fernández-Seara MA, Techawiboonwong A, Detre JA, Wehrli FW. MR susceptometry for measuring global brain oxygen extraction. Magnetic Resonance in Medicine 2006;55(5):967-973.

290. Deistung A, Schäfer A, Schweser F, Biedermann U, Turner R, Reichenbach JR. Toward in vivo histology: A comparison of quantitative susceptibility mapping (QSM) with magnitude-, phase-, and R2⁎-imaging at ultra-high magnetic field strength. NeuroImage 2013;65:299-314.

291. Liu T, Wisnieff C, Lou M, Chen W, Spincemaille P, Wang Y. Nonlinear formulation of the magnetic field to source relationship for robust quantitative susceptibility mapping. Magnetic Resonance in Medicine 2013;69(2):467-476.